

Effects of the Pole-Slot Combination on a Surface Permanent Magnet Generator for Wind Applications

JORDAN KILMARTIN

Bachelor of Engineering (Robotics)/ Master of Engineering (Electronics)

Supervisor: Dr. Amin Mahmoudi

October 2016



Submitted to the School of Computer Science, Engineering, and Mathematics in the Faculty of Science and Engineering at Flinders University in partial fulfilment of the requirements for the degree of Bachelor of Engineering (Robotics), Master of Engineering (Electronics)

Contents

Table of Figures.....	4
Abstract.....	8
Declaration of Academic Integrity.....	9
Acknowledgements.....	9
Chapter 1 Introduction.....	10
1.1 Background.....	11
1.2 Problem Statement.....	13
1.3 Objectives.....	14
1.4 Methodology.....	14
1.5 Limitations.....	15
1.6 Scope.....	15
1.7 Thesis Outline.....	16
Chapter 2 Literature Review.....	17
2.1 Introduction.....	18
2.2 Wind Turbine Generator Machine Design.....	18
2.3 Pole-Slot Combination.....	20
2.4 Gap Statement.....	23
2.5 Contribution.....	23
Chapter 3 Design Aspects and Justification.....	24
3.1 Pole-Slot Combination.....	25
3.2 Flux Direction.....	25
3.3 Stator-Rotor Configuration.....	26
3.4 Field Excitation.....	26
3.5 Magnet Orientation.....	27
3.6 Magnet Shape.....	27
3.7 Pole Pitch.....	28
3.8 Windings.....	29
3.9 Dimensions.....	29
3.10 Power Rating.....	30
3.11 Rated Speed.....	31
3.12 Thermal Considerations.....	31
3.13 Final Design.....	31
3.13.1 Rotor.....	32
3.13.2 Stator.....	33
3.13.3 Stator Slot.....	34

3.13.4 Core Steel.....	35
3.13.5 Winding.....	36
3.13.6 Permanent Magnets	37
3.13.7 Material Consumption.....	38
3.13.8 Pole-Slot Combinations	39
Chapter 4 Testing and Results	40
4.1 System Analysis Methods.....	41
4.1.1 Maxwell RMXprt.....	41
4.1.2 Maxwell 2D/3D FEA	42
4.1.3 Simplorer Systems Modelling.....	43
4.2 Magnetic Analysis.....	44
4.2.1 Magnetic Flux Density.....	45
4.2.2 Magnetic Field Flux Line Representation	46
4.2.3 Magnetic Flux Linkage	47
4.2.4 Air Gap Flux Density	50
4.2.5 Summary of Magnetic Analysis Findings	53
4.3 Open Circuit Analysis.....	55
4.3.1 Cogging Torque Measurement.....	55
4.3.2 Induced EMF Measurement.....	60
4.3.3 Core Losses.....	64
4.3.4 Summary of Open Circuit Analysis Findings	65
4.4 Load Test – Three-Phase Operation	66
4.4.1 Resistive Load	67
4.4.2 Variable Resistance Load.....	76
4.4.3 Variable Speed Analysis	79
4.4.4 Summary of Three-Phase Load Analysis Findings.....	82
4.5 Load Test – DC Operation	83
4.5.1 Resistive Load	84
4.5.2 Variable Resistance Load.....	92
4.5.3 Variable Speed Analysis	95
4.5.4 Summary of DC Analysis Findings	97
4.6 Load Test – Battery Charging Configuration.....	98
4.6.1 Setup Notes.....	98
4.6.2 Preliminary Simulations	99
4.6.3 48V Battery Configuration.....	101
4.6.4 Summary of Battery Load Analysis Findings	108
4.7 Design Summary and Evaluation.....	109

Chapter 5 Prototyping.....	112
5.1 Introduction.....	113
5.2 Alternative Build Design.....	113
5.2.1 Identification of Suitable Motor.....	114
5.2.2 Motor Modelling.....	116
5.2.3 Motor Conversion.....	118
5.2.4 Test Rig Design.....	120
5.2.5 Generator Testing and Results.....	123
5.3 Further Conversion.....	128
5.3.1 Pole-Slot Combination of Prototype.....	128
5.4 NdFeB Prototype Preliminary Simulations.....	129
5.4.1 Open Circuit Tests.....	129
5.4.2 Battery Tests.....	130
5.4.3 Summary of NdFeB Conversion Analysis.....	133
Chapter 6 Conclusions and Future Direction.....	134
6.1 Conclusion.....	135
6.2 Key Findings.....	135
6.3 Further Direction.....	137
References.....	138
Bibliography.....	141
Appendices.....	142
Appendix A: Flux Density Contour Plots.....	143
Appendix B: Magnetic Field Strength Vector Plots.....	148
Appendix C: Flux Line Plots.....	152
Appendix D: Cogging Torque Plots.....	155
Appendix E: Total Harmonic Distortion Calculations.....	157
Appendix F: Three-Phase Resistive Load Test.....	165
Appendix G: Rectified Output Load Resistive Test.....	175
Appendix H: Maxwell 2D Meshing Result.....	185
Appendix J: Simplorer Circuit Diagram.....	186

Table of Figures

Figure 1: Global cumulative installed wind capacity from 2000-2015 [1]	11
Figure 2: Wind resource map of Australia with average wind speed measured at a height of 80m [5]	12
Figure 3: (left) Axial-flux Generator (right) Radial-flux Generator	25
Figure 4: (left) Surface PM machine (right) Internal PM machine	27
Figure 5: (left) Pole pitch of 90° (right) Pole pitch of 180°	28
Figure 6: Pole embrace parametric analysis for 20-pole machine	28
Figure 7: (left) Distributed windings (right) Double-layer concentrated windings	29
Figure 8: Wind speed rose representing average wind speed in Ceduna 10m above ground level [6]	30
Figure 9: Dimensioned drawing of the rotor (not to scale)	32
Figure 10: Dimensioned drawing of the stator and stator slot (not to scale)	33
Figure 11: Stator slot detail view (not to scale)	34
Figure 12: Stator slot dimension reference diagram	34
Figure 13: Detailed slot dimensions	34
Figure 14: BH Curve of steel_1010	35
Figure 15: Final proposed machines for testing	39
Figure 16: RMXprt generator diagram after parameter specification	41
Figure 17: (left) Maxwell 2D model (right) Maxwell 3D Model	42
Figure 18: Simplified block diagram of cosimulation process	43
Figure 19: Maxwell/Simplorer Cosimulation with rectifier and battery load	43
Figure 20: (Top) No-load flux density plots (bottom) full-load flux density plots for the five different machines	45
Figure 21: Flux line plots for the five machines (full figures in Appendix C)	46
Figure 22: Magnified view of magnet junctions	46
Figure 23: Relationship between sinusoidal flux linkage and induced voltage	47
Figure 24: No-load flux linkage plots for the five machines	48
Figure 25: Full-load flux linkage plots for the 5 different machines	49
Figure 26: Comparison of flux linkage of one phase for full-load (blue) and no-load (red) operation	49
Figure 27: (Top) Airgap flux density (bottom) Airgap flux density showing stator slot positions	50
Figure 28: (left) Average airgap flux density (right) Maximum airgap flux density	51
Figure 29: Arc of the magnetic flux density measurements for a rotating stator	51
Figure 30: Measured airgap flux density for the five machines	52
Figure 31: Average airgap flux density over a 90° mechanical rotation	52
Figure 32: Summarised figures for the no-load magnetic analysis	54
Figure 33: Cogging torque plots for the machines showing waveform shape	56
Figure 34: Cogging torque plots for the machines showing magnitude variations between machines	57
Figure 35: Summary of cogging torque values at 200 rpm	57
Figure 36: Inverse of the LCM of the number of poles and slots	59
Figure 37: Estimated cogging torque using scaling factor	59
Figure 38: Induced EMF waveforms and spectral representation	61
Figure 39: Summary of the THD measurements	62
Figure 40: Harmonic factors for the third, fifth, and seventh harmonics	62
Figure 41: Summary of the peak and RMS voltages of the EMF in the open circuit tests	63
Figure 42: Calculated crest factors for the open circuit tests	63
Figure 43: (left) Core losses with separated loss components (right) Alternating flux frequency	64
Figure 44: Simplorer simulation block diagram	66
Figure 45: (top) Acceleration profile of the simulation (bottom) Torque curve generated with acceleration	67
Figure 46: Torque plots for the three-phase resistive loads using individual y-axis scales	68
Figure 47: (left) Average torque measurements (right) Comparison between torque ripple and cogging torque	68
Figure 48: RMS voltage and current measurements from one phase	69
Figure 49: (left) Open circuit crest factors (right) Loaded crest factors	69
Figure 50: Summary of THD values calculated for the source current waveform	70
Figure 51: Harmonic factor for the 3rd, 5th, and 7th harmonics	70
Figure 52: Current waveforms and spectral plots for the purely resistive load	71
Figure 53: Measured electrical power dissipated in the load (*Note: 6-pole machine is a different scale)	72
Figure 54: (left) Average load power (right) peak-to-peak ripple in the power waveform	72
Figure 55: Measured mechanical power supplied to the machine	73
Figure 56: (left) Average mechanical power supplied (right) Percentage mechanical power ripple	73
Figure 57: Calculated efficiency of the machines	74

Figure 58: Reduction in voltage caused by the addition of the load	74
Figure 59: Summary of graphs for the three-phase load test.....	75
Figure 60: Plot of the RMS values of the output from the machines as the load is varied	76
Figure 61: Load power plot for the three-phase variable load test.....	77
Figure 62: Maximum power outputs over the load range at rated speed.....	77
Figure 63: Efficiency curves for the machine variants using a variable resistance load	78
Figure 64: Torque curves for the machine variants from the variable speed test.....	79
Figure 65: RMS voltage values for the machine variants from the variable speed test.....	80
Figure 66: Measured RMS load voltage at different speeds	80
Figure 67: Electrical power measurements for the machine variants from the variable speed test.....	81
Figure 68: Output power for 200 rpm and 600 rpm	81
Figure 69: Simulation block diagram using a three-phase rectifier and a resistive load	83
Figure 70: Torque plots for the three-phase resistive loads using individual y-axis scales.....	84
Figure 71: (left) Average torque measurements (right) Comparison between torque ripple and cogging torque.....	84
Figure 72: Average voltage and current measurements from the load.....	85
Figure 73: Calculated percentage output ripple	85
Figure 74: Summary of THD values calculated for the source current waveform.....	86
Figure 75: Harmonic factor for the 3 rd , 5 th , and 7 th harmonics.....	86
Figure 76: Current waveforms and spectral plots for the rectifier load	87
Figure 77: Measured electrical power dissipated in the load	88
Figure 78: (left) Average load power (right) Percentage ripple in the power waveform	88
Figure 79: Measured mechanical power supplied to the machine	89
Figure 80: (left) Average mechanical power supplied (right) Percentage mechanical power ripple	89
Figure 81: Calculated efficiency of the machines	90
Figure 82: Reduction in voltage caused by the addition of the load	90
Figure 83: Summary of graphs presented for the rectifier resistive load tests	91
Figure 84: Peak voltage of the machine variants for a variable resistance	92
Figure 85: Steady state output voltage of the rectifier	92
Figure 86: Load power of the machine variants for a variable resistance.....	93
Figure 87: Maximum power delivered to the load at rated speed.....	93
Figure 88: Efficiency of the machine variants for a variable resistance	94
Figure 89: Plot of the average voltage over the speed range.....	95
Figure 90: Average load voltage at rated speed and at 600 rpm.....	95
Figure 91: Plot of the load power generated by the machine variants for the variable load tests	96
Figure 92: Output power at rated speed and at maximum operating speed	96
Figure 93: Simplorer cosimulation setup with a battery load.....	98
Figure 94: Electrical power delivered to the load.....	99
Figure 95: Charging time at rated speed.....	99
Figure 96: Efficiency of the machines for the four different battery voltages	100
Figure 97: THD of the machines for the four different battery voltages.....	100
Figure 98: Torque plots for the three-phase resistive loads using individual y-axis scales.....	101
Figure 99: (left) Average torque measurements (right) Comparison between torque ripple and cogging torque.....	101
Figure 100: Average current measurements through the load.....	102
Figure 101: Calculated percentage output ripple	102
Figure 102: Summary of THD values calculated for the source current waveform.....	103
Figure 103: Harmonic factors for the 3 rd , 5 th , and 7 th harmonics.....	103
Figure 104: Current waveforms and spectral plots for the rectifier load	104
Figure 105: Measured electrical power dissipated in the load	105
Figure 106: (left) Average load power (right) Percentage ripple in the power waveform	105
Figure 107: Measured mechanical power supplied to the machine	106
Figure 108: (left) Average mechanical power supplied (right) Percentage mechanical power ripple	106
Figure 109: Calculated efficiency of the machines	107
Figure 110: (left) Blown-up diagram of the SmartDrive (right) front view of the SmartDrive [28].....	114
Figure 111: Picture showing the plastic coating of the stator, with exposed iron at the tips [28]	116
Figure 112: (left) 3D motor model (right) SmartDrive motor [28].....	116
Figure 113: Induced phase voltage simulated under open circuit conditions.....	117
Figure 114: Simulated cogging torque of the SmartDrive in mNm	117
Figure 115: Regrouped stator with rotor and shaft attached	119
Figure 116: (left) 3D mock-up of testing rig (right) implemented build.....	120
Figure 117: Tachometer in the setup used for speed measurement.....	121
Figure 118: Three-phase incandescent bulb load.....	122

Figure 119: Three-phase resistive load	122
Figure 120: Three-phase bridge rectifier.....	122
Figure 121: Plots of the phase voltage as obtained by measurements and simulation.....	123
Figure 122: Measured single phase load voltage from the three-phase load.....	124
Figure 123: Measure load current from a single phase in the three phase load.....	124
Figure 124: Load power calculated for the three-phase resistive test	125
Figure 125: Measured voltage over 3Ω load with rectified output	126
Figure 126: Measured current over 3Ω load with rectified output.....	126
Figure 127: Calculated power over 3Ω load with rectified output.....	127
Figure 128: Peak voltage measured in open circuit tests for the F&P NdFeB generator variants.....	129
Figure 129: Cogging torque measured in open circuit tests for the F&P NdFeB generator variants	129
Figure 130: Load power simulated for the variants of the NdFeB SmartDrive	130
Figure 131: Torque simulated for the variants of the NdFeB SmartDrive.....	130
Figure 132: Efficiency simulated for the variants of the NdFeB SmartDrive	131
Figure 133: Total harmonic distortion for the F&P generator with various battery voltages.....	132
Figure 134: Winding current waveform and spectral plot for increasing battery voltage	132
Figure 135: Flux density contour plot with corresponding flux linkage plot for a 6-pole machine.....	143
Figure 136: Flux density contour plot with corresponding flux linkage plot for a 14-pole machine	144
Figure 137: Flux density contour plot with corresponding flux linkage plot for a 20-pole machine	145
Figure 138: Flux density contour plot with corresponding flux linkage plot for a 24-pole machine	146
Figure 139: Flux density contour plot with corresponding flux linkage plot for a 26-pole machine	147
Figure 140: Vector representation of the magnetic field strength inside the 6-pole machine	149
Figure 141: Vector representation of the magnetic field strength inside the 14-pole machine	149
Figure 142: Vector representation of the magnetic field strength inside the 20-pole machine	150
Figure 143: Vector representation of the magnetic field strength inside the 24-pole machine	150
Figure 144: Vector representation of the magnetic field strength inside the 26-pole machine	151
Figure 145: Flux line representation for a 6-pole machine.....	152
Figure 146: Flux line representation for a 14-pole machine.....	152
Figure 147: Flux line representation for a 20-pole machine.....	153
Figure 148: Flux line representation for a 24-pole machine.....	153
Figure 149: Flux line representation for a 26-pole machine.....	154
Figure 150: Stacked plot of the cogging torque waveforms for the five machine variants using individual scales	156
Figure 151: Open circuit phase voltage waveform generated at 200 rpm	157
Figure 152: (top) Open circuit waveform voltages (bottom) Waveform spectrum.....	158
Figure 153: (top) Open circuit waveform voltages (bottom) Waveform spectrum.....	159
Figure 154: (top) Open circuit waveform voltages (bottom) Waveform spectrum.....	160
Figure 155: (top) Open circuit waveform voltages (bottom) Waveform spectrum.....	161
Figure 156: (top) Open circuit waveform voltages (bottom) Waveform spectrum.....	162
Figure 157: Overlay of the measured voltage waveform (blue) and a pure sine wave (red).....	163
Figure 158: Spectral plots obtained in ANSYS (top) and MATLAB (bottom)	163
Figure 159: (left) Quantisation error (right) Correctly displayed fundamental at 40 Hz	164
Figure 160: Collected plots from the three-phase resistive test for a 6-pole machine.....	165
Figure 161: (top) Load current waveform (bottom) Amplitude spectrum.....	166
Figure 162: Collected plots from the three-phase resistive test for a 14-pole machine	167
Figure 163: (top) Load current waveform (bottom) Amplitude spectrum.....	168
Figure 164: Collected plots from the three-phase resistive test for a 20-pole machine	169
Figure 165: (top) Load current waveform (bottom) Amplitude spectrum.....	170
Figure 166: Collected plots from the three-phase resistive test for a 24-pole machine	171
Figure 167: (top) Load current waveform (bottom) Amplitude spectrum.....	172
Figure 168: Collected plots from the three-phase resistive test for a 26-pole machine	173
Figure 169: (top) Load current waveform (bottom) Amplitude spectrum.....	174
Figure 170: Collected plots from the rectifier test with resistive load [6-pole machine]	175
Figure 171: (top) Load current waveform (bottom) Amplitude spectrum)	176
Figure 172: Collected plots from the rectifier test with resistive load [14-pole machine].....	177
Figure 173: (top) Load current waveform (bottom) Amplitude spectrum)	178
Figure 174: Collected plots from the rectifier test with resistive load [20-pole machine].....	179
Figure 175: (top) Load current waveform (bottom) Amplitude spectrum.....	180
Figure 176: Collected plots from the rectifier test with resistive load [24-pole machine].....	181
Figure 177: (top) Load current waveform (bottom) Amplitude spectrum.....	182
Figure 178: Collected plots from the rectifier test with resistive load [26-pole machine].....	183
Figure 179: (top) Load current waveform (bottom) Amplitude spectrum.....	184

Figure 180: Meshing result for the 18-slot 24-pole machine	185
Figure 181: Three-phase load test setup in Simplorer	186
Figure 182: Three-phase bridge rectifier and resistive load	187
Figure 183: Three-phase bridge rectifier and battery load.....	187

Abstract

This paper discusses the design and analysis of a 1 kW, outer-rotor, surface permanent magnet generator for household wind turbine applications. Five machine designs are presented with differing pole numbers. The designs are studied in detail using finite element analysis. Analysis includes the open circuit operation of the machine as well as loaded conditions. The loads considered are a three-phase resistive load, a rectifier with resistive load, and a rectifier with a battery load. The study measures generator characteristics such as flux density, back-emf, cogging torque, ripple torque, output power, total harmonic distortion, and losses. The results of the analysis are used to correlate the pole-slot combination and the output characteristics of the permanent magnet generator. The analysis is performed using ANSYS RMXprt, ANSYS Maxwell 2D/3D, and ANSYS Simplorer. The final 18-slot, 20-pole design offers high efficiency with low cogging torque. The machine can provide 1.4 kW to a 48V battery at the rated speed of 200 rpm. As a standalone chapter, a Fisher & Paykel SmartDrive outer-rotor, direct-drive motor was salvaged and converted into a generator. Preliminary analysis and testing are performed on the converted motor. The experimental results in this section are limited.

Declaration of Academic Integrity

I certify that this thesis does not incorporate without acknowledgment any material previously submitted for a degree or diploma in any university; and that to the best of my knowledge and belief it does not contain any material previously published or written by another person except where due reference is made in the text.

Signed:  20/02/2017

Acknowledgements

I would like to acknowledge my family for providing support and guidance through this project, the writing was vastly improved from their input. I am also very grateful to my friends who supported me and helped me.

I would also like to acknowledge my supervisor, Dr. Amin Mahmoudi, for his help during this project.

Chapter 1

Introduction



1.1 Background

In the modern age, renewable energy is experiencing an unprecedented rise in investment, and global capability [1]. Figure 1 below shows how the global cumulative wind capacity has increased significantly in the last 15 years. The driving factors behind this growth include faltering confidence in the fossil fuel industry, and an increasing awareness of the environmental effects of using non-renewable energy.

One of the fastest growing and most mature renewable technologies is large-scale wind power [2]. Its flexibility in location, with minimal environmental impact has been instrumental in its widespread adoption.

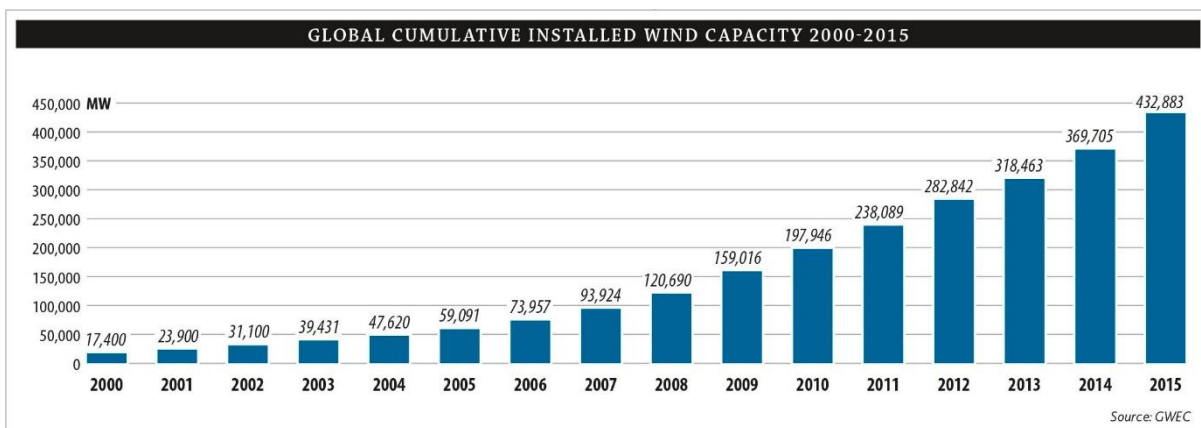


Figure 1: Global cumulative installed wind capacity from 2000-2015 [1]

In recent years, scaled down versions of this technology have become objects of interest for environmentalists as a way of generating household levels of power for self-sufficiency [3]. Household solar has already been promoted as an alternative energy supply to reduce grid power consumption, and wind power may now be next in the line of affordable household-scale renewable power plants.

South Australia has ideal conditions for household wind power due to its spread out, rural communities, and large wind resources [4]. Wind power is more suitable for open rural areas due to reduced wind turbulence. The increased cost of grid connection infrastructure in rural areas is another advantage of standalone renewable power systems. Ideal conditions such as these exist in southern coastal regions such as the Fleurieu, Eyre, and Yorke Peninsulas. Inland South Australia also offers superb wind resources [4]. The potential wind resources are illustrated in Figure 2 below, showing the average wind speeds across Australia.

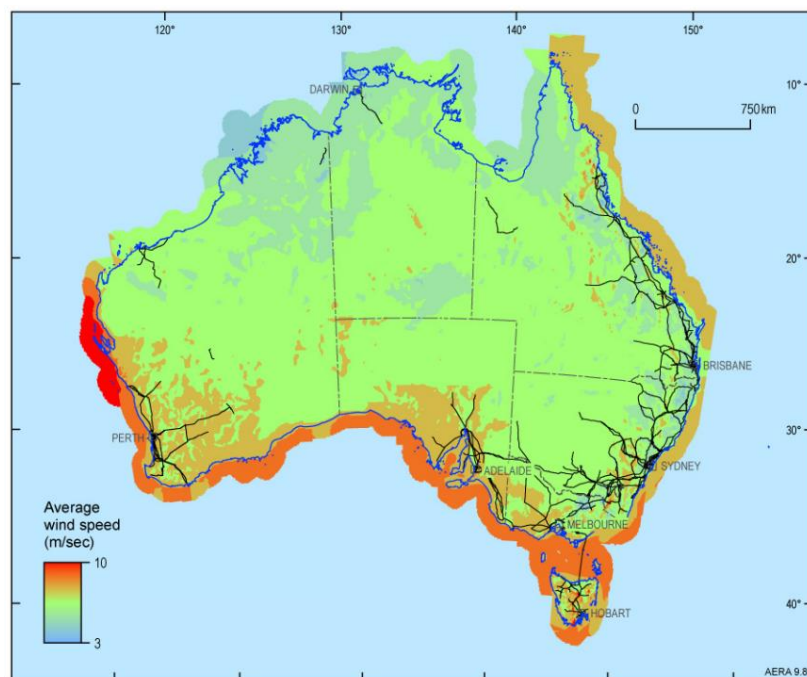


Figure 2: Wind resource map of Australia with average wind speed measured at a height of 80m [5]

1.2 Problem Statement

A household-scale renewable energy plant to supplement, or fully provide, the power needs of people living in rural areas with high wind power capability in South Australia would benefit consumers, while contributing to reduced greenhouse gas emissions.

However, small-scale wind turbine designs have not been investigated as thoroughly as large-scale generators, leading to designs that have significant potential for improvement. A turbine generator with reduced cogging torque, reduced torque ripple, lower maintenance requirements, or higher efficiency would be a desirable improvement. These characteristics are essential for an effective, marketable machine.

A topology with favourable characteristics for wind applications is the direct-drive (DD) permanent magnet generator (PMG). This type of machine can be highly economical, with reduced maintenance due to the absence of a gearbox, and high efficiency from the use of permanent magnets. However, this type of machine typically exhibits high cogging torque. Cogging torque is the torque generated due to the interactions between the permanent magnets and the core steel. High levels of cogging torque can reduce machine lifetime, and increase required start-up wind speed. One of the main objectives would be to significantly reduce cogging torque.

A relevant area of research is the pole-slot combination of a surface permanent magnet machine. This is defined as the number of slots and the number of magnetic poles used in the design. The pole-slot combination of a permanent magnet machine has been shown to directly affect the cogging torque, total harmonic distortion, and output power for several machine topologies.

To optimise the design of the proposed PMG design, and to research the effects of the pole-slot combination, five different machine designs are proposed with unique pole numbers. The measured characteristics of the machine, such as efficiency, and cogging torque, are used to determine the effectiveness of the optimised solution.

1.3 Objectives

- To design a 1kW outer-rotor, surface permanent magnet generator suitable for wind applications
- To determine the effect of the pole-slot combination on the output characteristics of the machine
- To design and build a prototype in order to validate the simulations using experimental results

1.4 Methodology

The research is performed primarily using Finite Element Analysis (FEA) simulation. The electrical machine simulation is performed using standard techniques and programs. The software used for the simulation of the generator is ANSYS Maxwell RMXprt, Maxwell 2D, and Maxwell 3D. These are industry standard simulation programs specifically designed for transient and magnetostatic analysis of electrical machines. Basic power electronics will also be simulated in conjunction with the generator, in order to test its functionality in a variety of different setups. The electronics are simulated in ANSYS Simplorer, and is connected to Maxwell using the transient cosimulation feature of the programs. Additional analysis scripts, such as the total harmonic distortion measurement, are written using MATLAB.

Due to budgetary constraints, the prototyping stage does not use the proposed design. In lieu of this, a standalone chapter presents the conversion of an outer-rotor direct-drive motor into a generator. Preliminary analysis is undertaken on the converted machine. The experimental setup tests the converted generator under a variety of different load conditions, with the results compared to the preliminary simulations.

1.5 Limitations

The main limitation of this project is the number of designs used. It is desirable to use more variations of the pole-slot combination to establish a stronger link between the number of poles and the output characteristics. However, it will not be practical to simulate and perform in-depth analysis on more than the five different designs proposed.

Due to the computationally expensive nature of 3D simulations, and the number of designs being tested, most simulations are performed in 2D.

The experimental analysis of the designed generator is expected to be expensive, and a limitation is the budget for the materials and testing equipment. Due to the low budget, the prototyping and testing is not expected to be comprehensive.

1.6 Scope

The scope of this project includes the design, and analysis of a surface permanent magnet generator, with a testing regime suitable to determine the effect of the slots per pole and phase on output characteristics of the machine. The scope includes basic modelling of electronic loads and rectification modules using ideal components. However, development of any further electronic control or power conversion modules are out of the scope of the project. The construction of other wind turbine system components, such as the blade assembly, tower, and generator housing is also out of the project scope. Up to five variants of the generator should be simulated.

1.7 Thesis Outline

Chapter 1: Introduction

Chapter 1 gives an overview of the background and motivation of the project. The problem statement, methodology, limitations, and scope of the project is presented. The chapter ends with the thesis outline.

Chapter 2: Literature Review

Chapter 2 contains a literature review that informed the evaluation process that guided the direction of research and determined areas in which a unique contribution could be made. The literature review contains a synopsis on several academic papers concerned with the design of permanent magnet generators for wind applications. The review concludes with a gap statement to summarise the perceived research gap, and the proposed contributions.

Chapter 3: Design Aspects and Justification

Chapter 3 presents the common design aspects of an electrical machine. A brief description and a justification is given for the design choices. The chapter concludes with the final design for the proposed generator.

Chapter 4: Testing and Results

Chapter 4 begins with an explanation of the software used to simulate the generator system. The details and results of the magnetostatic, open-circuit and load analyses are then. The conclusion of this chapter summarises the results and findings of the tests.

Chapter 5: Prototyping

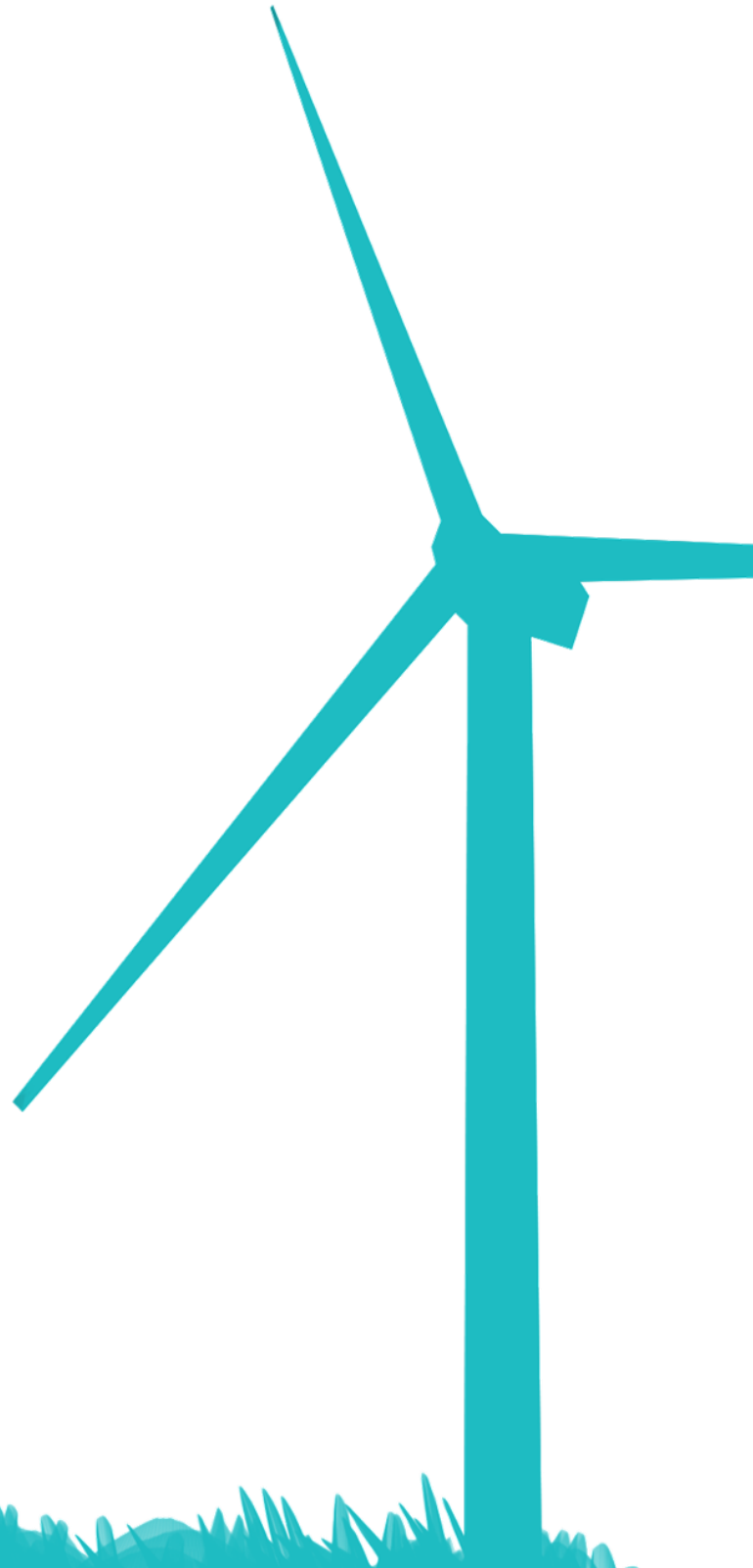
Chapter 5 is a standalone chapter that presents the process of converting an outer-rotor direct-drive Fisher & Paykel SmartDrive motor into a generator with similar characteristics as the proposed design. Analysis and experimental measurements are presented for this machine.

Chapter 6: Conclusions and Future Work

Chapter 6 presents the conclusions drawn from the results of the research. The chapter concludes with details of future direction, and further work that could build upon the results of the project.

Chapter 2

Literature Review



2.1 Introduction

Electrical machines have been widely studied for decades. Interconnected design aspects of an electrical machine has resulted in numerous unique generator designs, each with its own advantages and disadvantages. Due to the application-specific nature of electrical machines, there is no objectively optimised machine, and no systematic approach to designing one. This literature review begins with papers discussing general design and analysis methods for generators used in wind applications. The second part of the review focuses on determining any research gaps in papers discussing the pole-slot combinations in electrical machines.

2.2 Wind Turbine Generator Machine Design

Although most papers consider singular aspects of electrical machine design, there are several that provide a broad scope, touching on the most common design techniques. Dorell et al. [7] provides practical information on a wide range of design techniques, while textbook sources such as written by Pyrhönen, Jokinen, and Hrabovcova [8], and Ferreira and van der Merwe [9] provide a solid theoretical background, with rigorous mathematical working.

An optimised electrical machine design is subjective, and is based on its application. Sources focused on machine design for wind power generation, such as books written by Rekioua [10], and Anaya-Lara [11] provide a wealth of information on the subject of wind generator design.

For more specific details there are several relevant papers describing the design and analysis of low-power wind turbines. Choi, Jang, and Song [12] present design, FEA, prototyping methodology, and experimental analysis for a low-power 400W permanent magnet generator (PMG) for wind applications. The design is a grid connected, direct-drive turbine rated for 400W at 450rpm. The study describes some design methods concerning the dimensions of the rotor, stator, and magnet, with a cursory description of the cogging torque. The study uses FEA analysis to determine magnetostatic properties, and uses experimental analysis of a prototype to evaluate the design.

Choi, Jang, and Song provide a good reference for design methodology of several generator characteristics. However, it does not describe the FEA process and does not provide any information on slots per pole and phase. Additionally, the design is rated at 450rpm, which may be unreasonably fast for a direct-drive wind turbine generator, and so the stated efficiency of 92% may not be achievable in a practical situation.

Lepa and Kilk [13] describe a similar direct-drive machine with 20 poles and 54 slots, rated at 650W. The analysis is first performed mathematically using a reluctance network, and then using Finite Element Analysis (FEA). The main objectives of this study are to analyse the magnetic fields in the generator, and to compare FEA results with a prototype. The results of the study show that the simulations are adequately accurate for analysing the magnetic fields and the generator performance. This study uses a regular inner-rotor topology, and does not explore any novel concepts. The design process of the slots per pole and phase is explained minimally.

Kilk and Kudrjavnsev [14] describe the study of a 5kW outer-rotor PMG for wind applications. The paper covers design, prototyping, and testing. The design stage makes use of analytical techniques as well as FEA. The design has a focus on slot skewing as a method of cogging torque reduction. The results of the paper present the differences between actual and simulated results, showing that the simulated results are accurate. However, the generator designed has a power output larger than a household turbine. The machine uses 70 slots with 32 poles, and the design is for a vertical axis wind turbine rather than a horizontal axis wind turbine.

2.3 Pole-Slot Combination

Review of a large number of studies describing the electrical machine design process shows that there is minimal explanation regarding the selection of the pole-slot combination, and few papers focused on researching the subject. The pole-slot combination is defined as the number of poles and number of slots used in the machine. In some studies this is also referred to as the slots per pole and phase (SPP). This is commonly measured using the ratio, q , which is defined as the ratio between the number of slots, and the number of poles multiplied by the number of phases.

$$q = \frac{N_s}{2p \times N_\phi}$$

Where q is the slots per pole and phase, p is the number of pole pairs ($2p$ is the number of poles), N_s is the number of slots, and N_ϕ is the number of phases. This parameter can be crucial in the performance of a machine. Specific studies that focus on this aspect are discussed below.

Gandzha, Sogrin, and Kiessh [15] analyse two different motors with an SPP value of 0.3 and 1. The motors are high speed (≈ 1000 rpm), permanent magnet, outer-rotor designs. The analysis is performed using FEA in ANSYS Maxwell. The results show that a low fractional number of slots per pole and phase is a viable design choice, and offers advantages of reduced cogging torque, torque ripple, and copper losses. This paper is highly relevant due to the low value of SPP, and the use of an outer-rotor configuration.

The results obtained by Gandzha et al. are limited as the paper only considers two different variations of the motor: an 18-slot, 20-pole (SPP = 0.3) machine, and a 60-slot, 20-pole (SPP = 1.0) machine. The two different sets of results provide insufficient data to draw a conclusion. Additionally, modifying the number of slots significantly alters the structure of the motor, as it directly affects the slot dimensions and the coil dimensions. This increases the number of variables in the experiment, and therefore makes the causation between modifying the SPP and the resultant changes in output more tenuous. This paper uses a very low power 25 W motor, which is significantly different to the 1 kW generator design proposed.

Tang, Soong, Liew, and Ertugrul [16] present the analysis of the effects of SPP on a number of different surface permanent magnet machines. The two main designs use a 36-slot stator, and a 12-slot stator, with several different combinations of pole pairs. The results are presented at a rated speed of 6,000 rpm and are generated using 2D FEA. The relevant conclusions show that machines using distributed windings with integer values of SPP have increased peak values of cogging torque and torque ripple.

The research methodology and results presented by Tang et al. are highly relevant and similar to the methodology proposed in this thesis. The main points of difference are in the machine topology, speed, and range of SPP. The machine presented by Tang et al. is inner-rotor, designed for high-speed (≈ 6000 rpm) operation, and covers a minimum SPP of 0.375.

In another research paper aimed at the design and analysis of a permanent magnet generator, Rucker [17] describes the design process of a large 16 MW PMG for naval applications. The author uses analytical methods in MATLAB in order to calculate generator parameters, and uses PSIM to model the electronics. Among other analyses this paper covers the effect of the pole number on characteristics of the machine such as the Total Harmonic Distortion (THD), the weight, and the overall losses. The results show that an increased number of poles reduces losses in the power electronics, reduces THD, increases machine losses, and can reduce weight.

The results obtained by Rucker are in the context of a large, inner-rotor, MW turbine, with SPP values higher than 1. The paper does not make any reference to the varied values of SPP for the tests. The type of PM generator is also designed for high speed, and is therefore not applicable to direct-drive wind turbine designs.

Sun et al. [18] investigate the effect of the pole and slot combination on noise and vibration. The machine used is a 2 kW, internal permanent magnet synchronous machine, rated for 2500 rpm and using an inner rotor configuration. The SPP is varied between 0.375 and 0.5. The analysis is carried out using FEA. The results show that noise is reduced when the SPP has a numerator of unity. Although this paper discusses low values of SPP there are significant differences in the machine topology and speed range used.

The results are somewhat relevant. However, the study is based on a low-torque, high speed machine, which is designed for a geared system, and the main focus of the research is based on vibration.

Zhang and Wang [19] study the effects of different pole-slot combinations on the torque and output power of a 1.5 MW PM wind turbine. The generators are analysed using FEA. The study concludes that lower SPP results in higher average power output, reduced power ripple, and reduced positioning torque. The results are limited as they only use a range of combinations with SPP between 0.8 and 1.25.

Liu et al. [20] study the effect of SPP on the output torque of a 2 MW PM wind turbine generator. The study uses a combination of FEA and equivalent magnetic circuit theory for analysis. The study concludes that, as the slots per pole and phase decreases, the THD increases, and the cogging torque decreases. However, overall torque ripple is increased due to harmonic distortion in the back-EMF. Similarly to previous studies, this does not cover the proposed research area as it focuses on large, inner-rotor, MW generators and only uses SPP between 0.8 and 1.6.

Hannon, Sergeant, and Dupré [21] study high-speed, direct-drive, PM synchronous motors. Specifically, the torque output compared to number of pole pairs, SPP, and coil throw. The results are obtained from FEA simulations using ANSYS Maxwell. The conclusions show that a higher ratio of slots per pole and phase contribute to decreased torque ripple. This study is aimed at higher SPP values from 1 to 6 in higher speed machines, and does not cover the proposed research area.

Choi, Park, and Jang [22] use a 5kW, 7000 rpm, 6-pole internal permanent magnet machine with varying slot numbers, in order to determine the effect on the THD, torque ripple, and d-/q-axis inductance. The results are obtained using finite element analysis, with experimental validation using prototypes of selected machine designs. The results show that the cogging torque, torque ripple, and THD increase as the slots per pole and phase decreases. This does not cover the research gap as the study only investigates SPP of 1, 1.5, and 2.

2.4 Gap Statement

Review of the literature of the specified generator topology has identified an area where a unique contribution can be made. The pole-slot combination of an electrical machine is an important parameter of the electrical machine, but has limited research for the proposed topology. For outer-rotor PMGs there is potential to use larger numbers of surface mounted magnets, and the effect of this is not widely studied. Research papers concerning the pole-slot combination typically used low numbers of poles, such that the SPP was above 0.5. There are few papers that included designs with SPP below 0.5.

2.5 Contribution

This project aims to study the effect on the electrical machine output when greatly increasing the number of poles, thus, varying the SPP to very low values. This analysis is performed in the context of a direct-drive generator designed for a wind turbine. The design is proposed to be a direct-drive, outer-rotor, surface permanent magnet generator.

Chapter 3

Design Aspects and Justification



3.1 Pole-Slot Combination

The pole-slot combination is an important part of the design and is the main focus of this project. To test the pole-slot combination, the number of slots is kept constant, and the number of poles is varied over several proposed machine designs. The number of slots should ideally have a large number of numerical factors, and should also be a factor of three, as this is a three-phase machine. This is to ensure a large number of applicable pole-slot combinations. The proposed design uses 18 slots. 18 slots is divisible by 3, 6, and 9, and therefore offers many potential pole-slot combinations.

With a constant number of slots, the change in pole number has a great effect on the cogging torque, and is directly related to the frequency of the output voltage. Low-resolution simulations are performed on all applicable pole numbers from 6 up to 40 poles. At higher pole numbers the simulations showed increasingly poor results of the machines, and so machines with greater than 40 poles are not considered. The final pole numbers are 6, 14, 20, 24, and 26.

3.2 Flux Direction

The flux topology refers to the different directions of the working magnetic flux, and is named based upon the orientation of the working flux with respect to the axis of rotation. There are two main categories: axial flux, and radial flux, as shown in Figure 3 below. A third topology, transverse flux, is increasing in prevalence, but is still classified as more of a novelty.

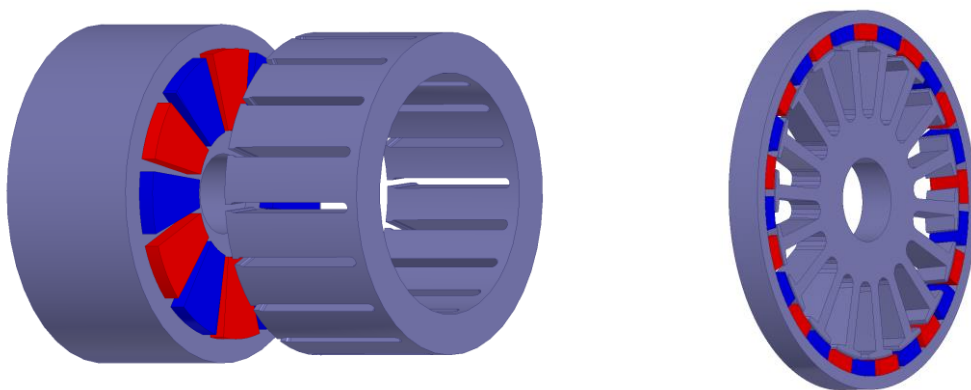


Figure 3: (left) Axial-flux Generator (right) Radial-flux Generator

The proposed design is a radial flux machine as it has advantages in manufacturability, and it is the most common and proven design.

3.3 Stator-Rotor Configuration

The conventional configuration for the stator and rotor is the inner-rotor topology. As the name suggests, the rotor is situated inside the stator. This topology is simple and effective. However, outer-rotor topologies have several advantages over the conventional design, especially for wind turbine applications.

Outer-rotor direct-drive configurations can have the blade assembly mounted directly to the rotor. The steel used for the mounting will also double as rotor back iron, reducing the total amount of iron required. The outer-rotor configuration also provides centrifugal force which will aid the adhesion of the magnets. This reduces the effort required to secure the surface mounted magnets. The outer-rotor configuration is chosen for the design.

3.4 Field Excitation

The field excitation refers to the method of setting up the magnetic field in the machine. There are two main excitation methods: electrical excitation and permanent magnet excitation.

Electrical excitation passes current through coils of copper wire in order to create a magnetic field, similar to the operation of a solenoid. The disadvantage of this method is that it causes more generator losses setting up the field due to the current passing through the resistance of the coils. The advantage of electrical excitation is the control afforded to the user. As the strength of the magnetic field is related to the amount of current through the field coils, the magnetic field strength can be controlled accordingly. This can be used to control the induced Electromotive Force (EMF).

The second method uses permanent magnets to set up the magnetic field. This method is more efficient as it excludes the copper losses caused by the field coils. Some losses may occur in the magnets due to eddy currents, but the net efficiency is typically increased. The main disadvantage of permanent magnet excitation is that the voltage is directly dependent on the rotational speed during operation, which leads to reduced control over the output voltage. This can have potential drawbacks in fault situations, and can be more dangerous.

A permanent magnet configuration is used for the proposed design. Permanent magnet generators have been shown to be very efficient, and can be used to design simpler machines.

3.5 Magnet Orientation

For permanent magnet generators there are two main classes for magnet orientation: surface permanent magnet (SPM) machines, and internal permanent magnet (IPM) machines. The SPM and IPM rotors are shown in Figure 4.

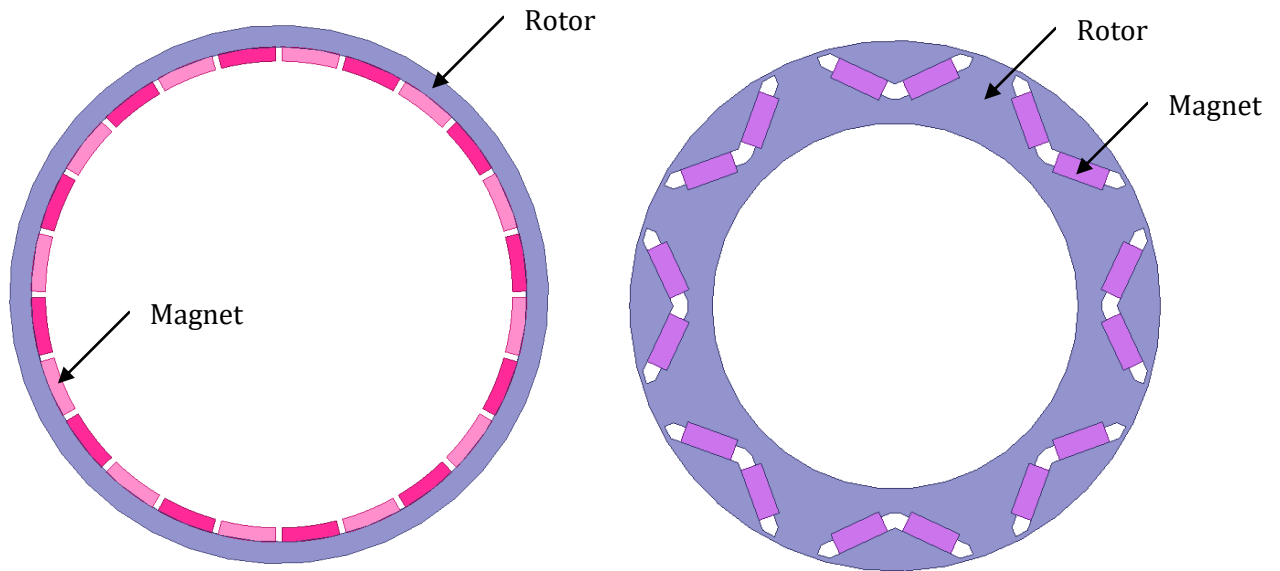


Figure 4: (left) Surface PM machine (right) Internal PM machine

For an outer-rotor configuration, surface permanent magnets offer the most efficient use of space, and are used for the proposed design.

3.6 Magnet Shape

The magnet shape defines the dimensions of the magnet and general shape. The shape of the magnet can be extremely important in the design of the machine as it affects the direction the magnetic flux. Shaped magnets usually feature a slight curve that can reduce the cogging torque at the cost of slightly reduced power output.

For simplicity, the magnets used are basic rectangular types. In future, the design may be improved by shaping these magnets. Curving magnets is a known method for reducing cogging torque.

3.7 Pole Pitch

The pole pitch describes the circumferential coverage of the magnets. For a value of 180° the magnets are continuous around the circumference. For a value of 90° , the magnet covers half of the available circumference, as shown in Figure 5 below.

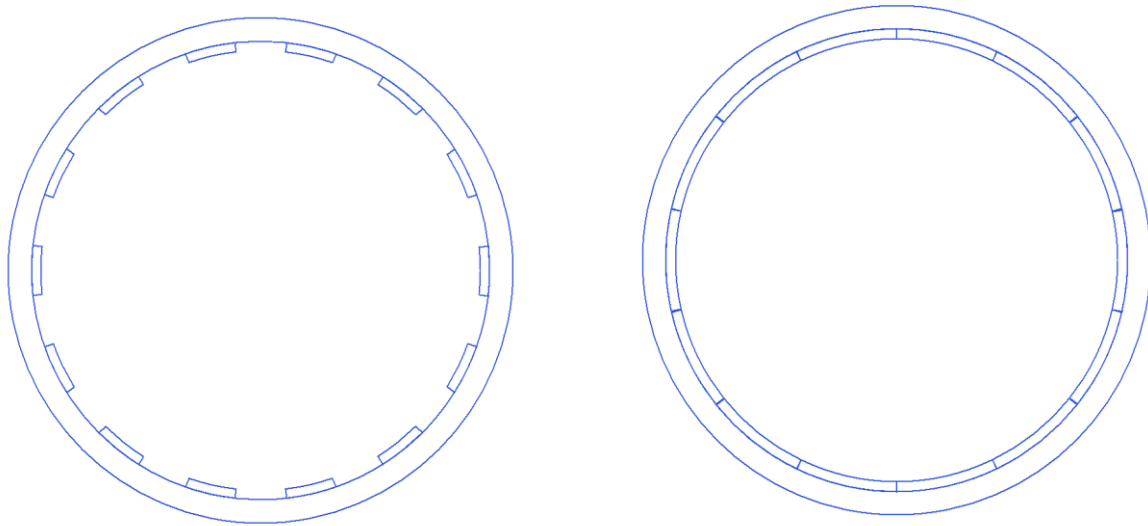


Figure 5: (left) Pole pitch of 90° (right) Pole pitch of 180°

Parametric simulations are performed in RMXprt to determine the effect of the pole pitch on the system, and therefore optimise its value. The RMXprt variable is called pole embrace, where a value of 1.0 is equivalent to 180° pole pitch. The parametric analysis for the 20-pole machine is presented in Figure 6. This shows the sweep of the pole embrace from 0.75 to 0.95 (135° to 171°) and the corresponding results on the output. A value of 0.88 (158.4°) is used as it displayed favourable characteristics over all five machine designs.

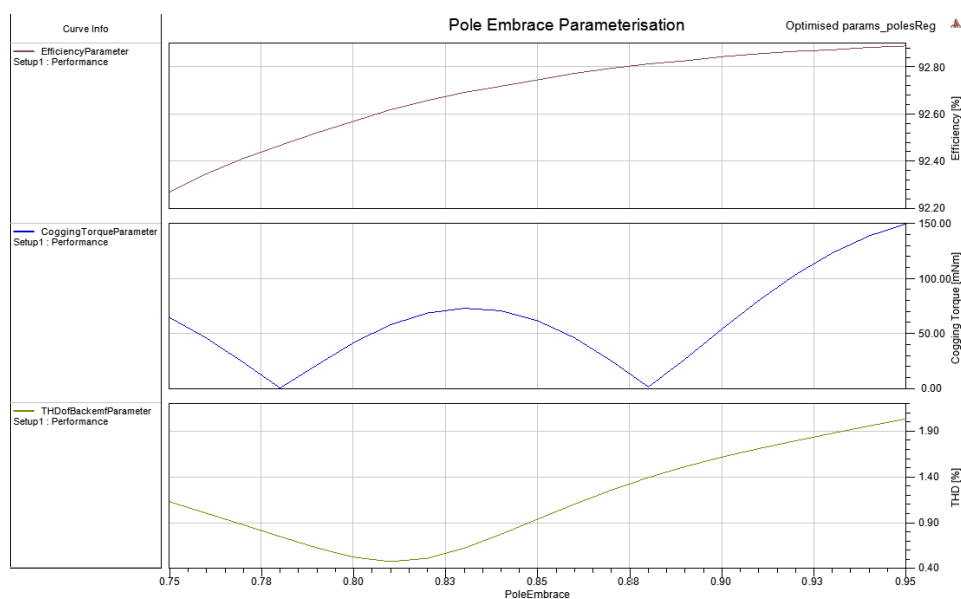


Figure 6: Pole embrace parametric analysis for 20-pole machine

3.8 Windings

The winding arrangement refers to how the copper coils are wound in the machine. There are several different methods of windings with two main categories: concentrated, and distributed. These two different winding methods are shown in Figure 7.

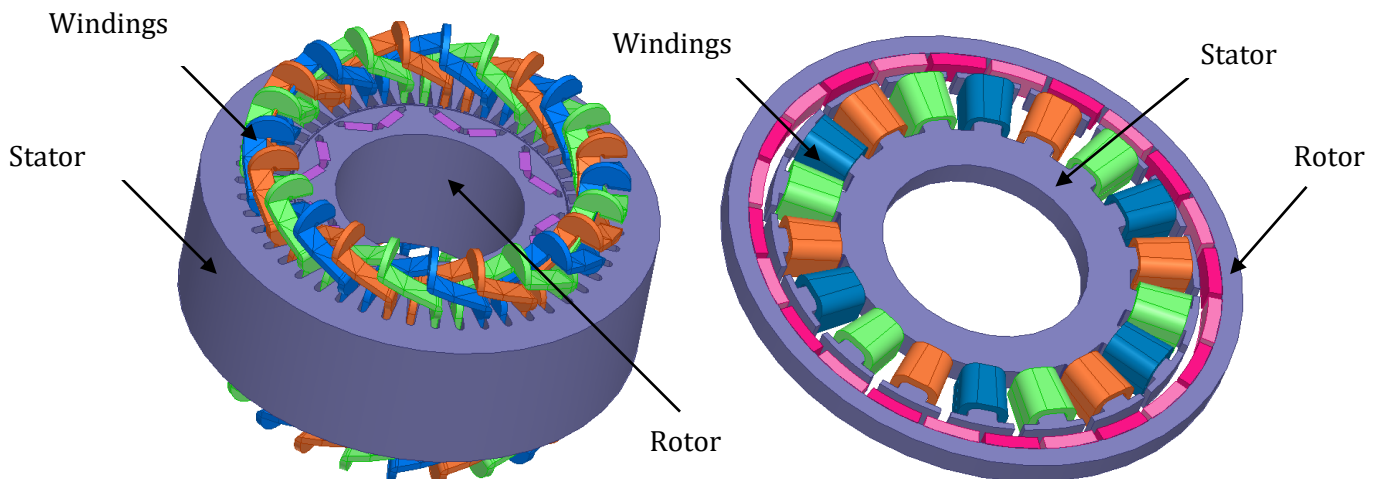


Figure 7: (left) Distributed windings (right) Double-layer concentrated windings

Concentrated windings are positioned over the stator teeth with no overlapping of coils. Distributed windings have coils that are overlapping.

Results presented in previous papers [10] show that double-layer concentrated windings tend to have lower cogging torque compared to distributed windings, and is therefore the preferred configuration in the proposed design.

3.9 Dimensions

The dimensions of the machine are designed using RMXprt with design influences from the literature. Specifically, it was found that outer-rotor configurations that feature a large number of poles have a diameter that is significantly longer than the thickness, in order to form a disc shaped generator.

The airgap is the distance between the stator and rotor where the working flux passes through. Smaller airgaps tend to increase performance, but a 1mm airgap was found to be common among machines of similar size, therefore a 1mm air gap is used for the proposed design.

3.10 Power Rating

The power rating of the device is designed for charging a domestic battery bank. With an average household battery bank capacity at approximately 7kWh, the power rating must be adequate to charge this battery bank over 24 hours. The wind rose in Figure 8 is a depiction of the wind speed, direction, and frequency recorded in Ceduna, South Australia, at 10m above ground level. The recorded wind speed is greater than 2.8 ms^{-1} for 72.1% of the time, and greater than 5.6 ms^{-1} for 38.2% of the time. If the rated wind speed of the generator is 5.6 ms^{-1} with a cut in of 2.8 ms^{-1} the capacity factor is at least 38.2% in this scenario.

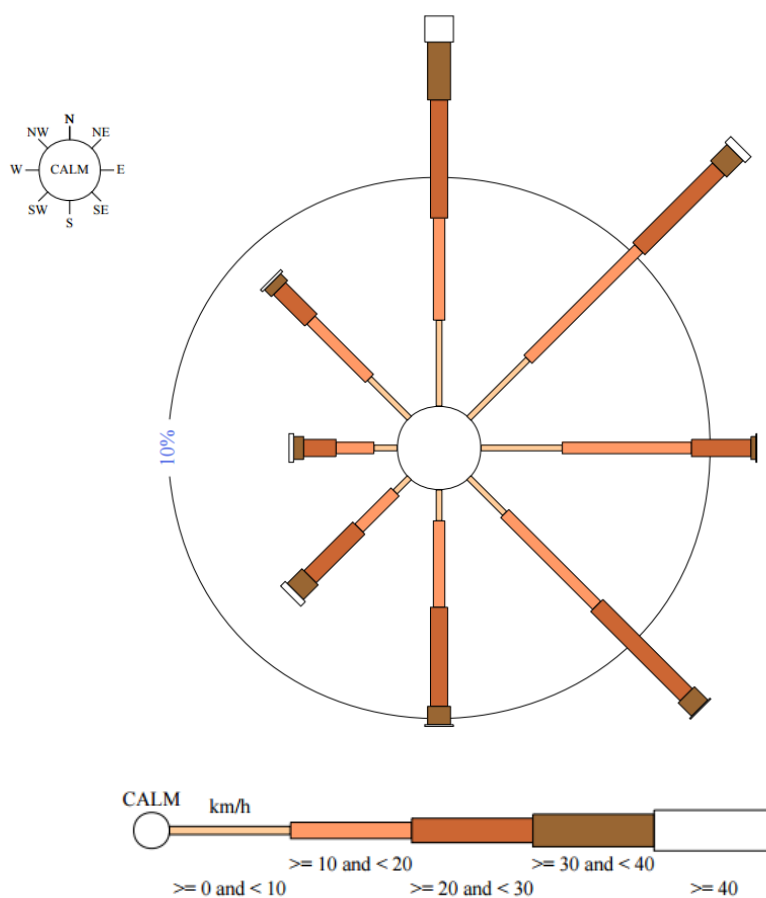


Figure 8: Wind speed rose representing average wind speed in Ceduna 10m above ground level [6]

Per day, the generator would theoretically produce energy such that:

$$\text{Energy} = \text{Capacity Factor} \times \text{Power Rating} \times 24 \text{ hours}$$

Which results in a generated energy of 9.6 kWh per day using a 1 kW generator. The overrating of the energy output provides a safety margin.

3.11 Rated Speed

The rated speed of the machine is the speed that the generator is designed to run at, and is usually the speed at which it is most efficient. Characteristics such as power factor, voltage, and current, are usually quoted at rated speed.

A direct-drive turbine has a rated speed that is very low in comparison to its geared counterparts. Where geared turbines may be rated at well over 1000 rpm, direct-drive turbines are usually rated at 150-400 rpm.

The speed rating of this machine is set at a low value, which increases mechanical safety of the setup, and can reduce iron losses by minimising the frequency of the alternating flux. The rated speed of 200 rpm is selected.

3.12 Thermal Considerations

Although the thermal design was considered conceptually, the enclosure and other aspects are not simulated during the tests. The thermal properties of the machine are not considered for testing and results.

3.13 Final Design

The final proposed designs are detailed in the following sections. The difference between the five designs is the number of poles used. The total magnet material used is constant as are all other dimensions and properties.

3.13.1 Rotor

The rotor is the rotating section of the machine and is positioned on the outside of the body for an outer-rotor configuration. The rotor is made of unlaminated electrical steel. The rotor is not laminated as the magnetic flux is not alternating inside the iron, and therefore iron losses are minimal. The dimensioned drawing of the rotor is shown in Figure 9, with the dimensions presented in Table 1.

Table 1: Dimension and property values for the proposed rotor

Rotor		
Inner Diameter	230	mm
Outer Diameter	264	mm
Rotor Steel Density	7872	kg/m ³
Length	50	mm
Airgap Length	1	mm

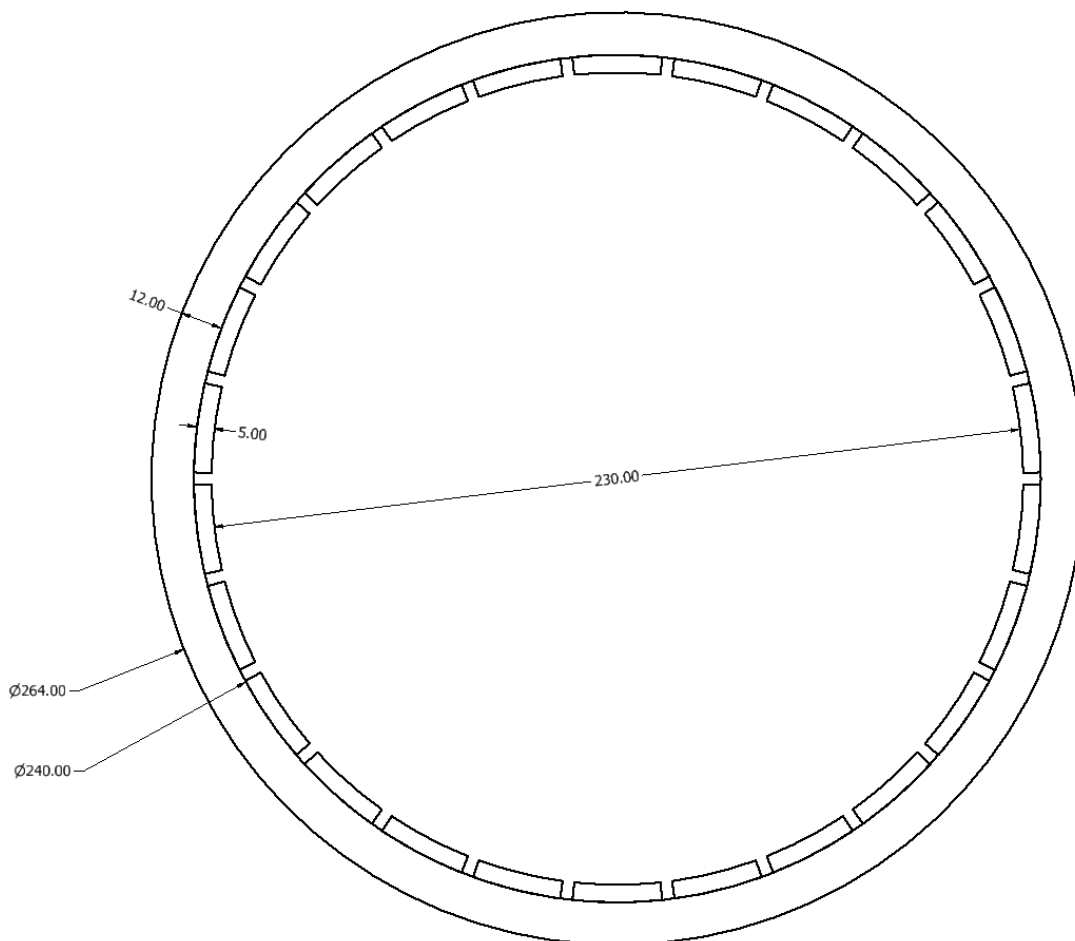


Figure 9: Dimensioned drawing of the rotor (not to scale)

3.13.2 Stator

The stator is the housing for the copper windings, and is made of laminated electrical steel. The inner diameter is relatively short, and can potentially be enlarged if the slot fill factor is increased. The stacking factor is the ratio of the steel laminate to the bonding material. The stator is slightly skewed, as this is found to reduce cogging torque with negligible adverse effects. The 2D simulation also uses the skew as a parameter. The stator properties are summarised in Table 2 with dimension drawing in Figure 10.

Table 2: Stator dimensions and properties

Stator		
Outer Diameter	228	mm
Inner Diameter	60	mm
Stator Steel Density	7872	kg/m ³
Stacking Factor	0.94	-
Length	50	mm
Skew	1.6	degrees

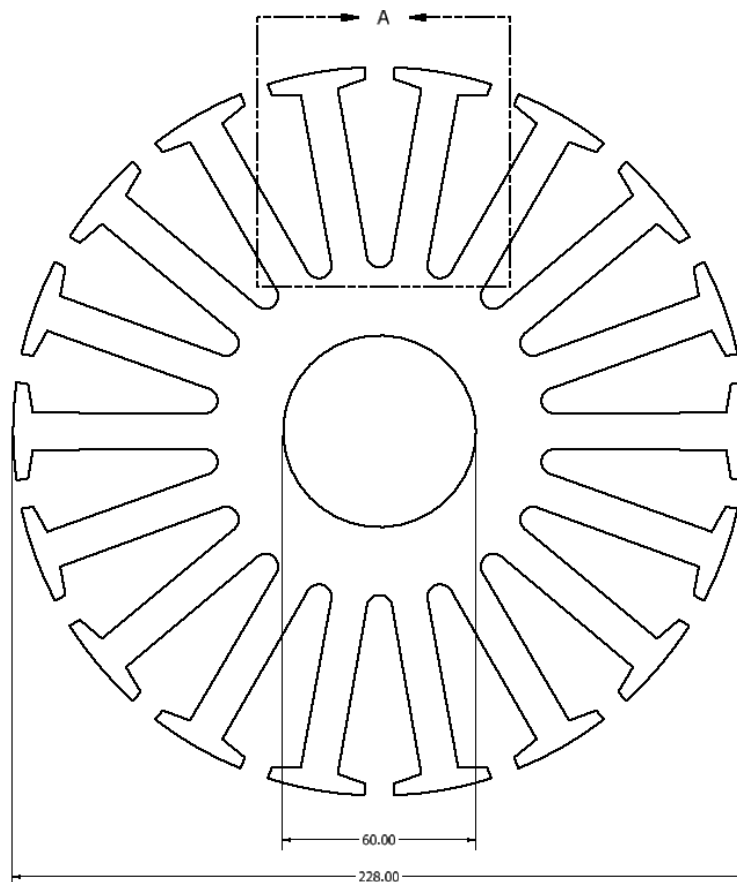


Figure 10: Dimensioned drawing of the stator and stator slot (not to scale)

3.13.3 Stator Slot

The stator slots in Figure 11 are the openings where the windings are situated. They are designed to have maximum space for the windings while leaving an opening for easier access. The teeth have a uniform cross section along the body. The detailed slot dimensions are presented in Figure 13, with the dimensions collated in Table 3.

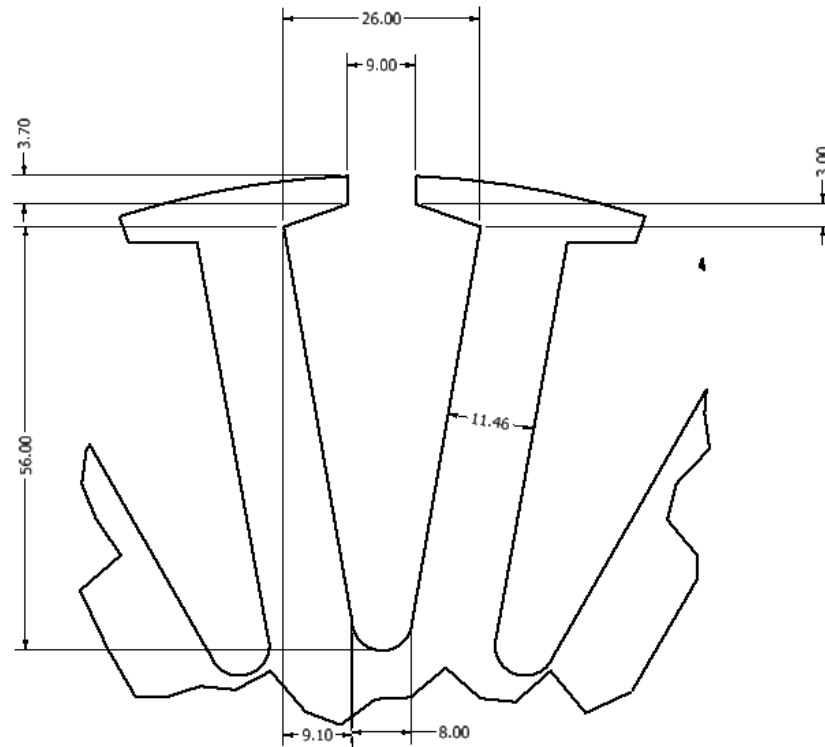


Figure 11: Stator slot detail view (not to scale)

Table 3: Slot dimensions for the design

Slot Dimensions		
Hs0	3.7	mm
Hs1	3	mm
Hs2	52	mm
Bs0	9	mm
Bs1	26	mm
Bs2	8	mm
Slot Area	9.68	cm ²
Number of Slots	18	-
Tooth Width	11.46	mm
Slot Fill Factor	54.7	%

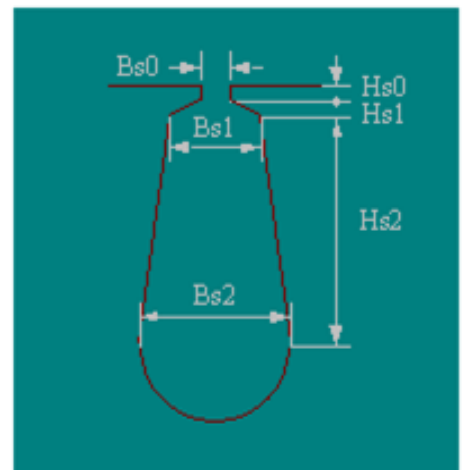


Figure 13: Detailed slot dimensions

3.13.4 Core Steel

The rotor and stator are constructed from core steel that is derived from two library materials: *steel_1010*, and *M19-24G*. *steel_1010* models the electrical steel conductivity, and provides the BH curve shown in Figure 14. Saturation of the steel occurs at approximately 1.9T.

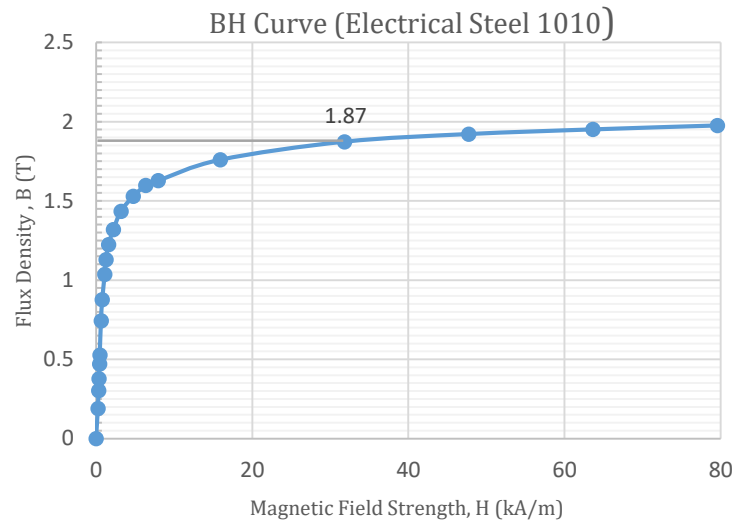


Figure 14: BH Curve of *steel_1010*

M19-24G is used for the loss coefficients to simulate iron loss in the material. Using these properties together formed an electrical steel material that closely modelled the real-world core material M19 non-oriented core steel. M19 is a common material for rotating machine cores. The modelled material has an iron loss of ≈ 3.03 W/kg for 1.5T at 50Hz using a 0.47mm lamination. M19 is a grade of steel which is slightly more expensive than higher loss core materials, but is commonly used in rotating machine cores. The rotor and stator use the same material, however, the stator is laminated with a lamination factor of 0.94. The steel properties are given in Table 4.

Table 4: Core steel properties including loss coefficients

Core Steel Properties		
Conductivity	2,000,000	Siemens/m
Density	7650	kg/m ³
Kh	68.66	-
Kc	0.1817	-

The values Kh and Kc are loss coefficients and are used in the simulation to model the electrical losses due to hysteresis and eddy currents respectively. Kh and Kc are both unitless values derived by ANSYS from the BH curve.

3.13.5 Winding

The wire diameter is relatively thick (2.174 mm). Thicker wire increases efficiency in high current applications, such as battery charging. The number of turns in a winding is 56, which is calculated to result in a phase voltage of approximately 48VRMS at 200 rpm. The windings are double-layer concentrated type. The wire and winding properties are given in Table 5.

The copper material is the basic ANSYS library default: *copper*. The characteristics of this material reflects standard magnet wire used in rotating machines. The wire is simulated as a solid, circular cross-section, insulated copper conductor.

Table 5: Wire dimensions and winding properties

Winding Properties		
Wire Diameter	2.174	mm
Winding Turns	56	-
Wires per Conductor	1	-
Wire Cross Section	3.71	mm ²
Slot Fill Factor	54.7	%
Phase Inductance	0.20453	mH
Phase Resistance	0.281562	Ω
Copper Properties		
Conductivity	58,000,000	Siemens/m
Density	8933	kg/m ³

3.13.6 Permanent Magnets

The selected magnets are sintered Neodymium-Iron-Boron (NdFeB). These offer high remanent flux density for relatively low cost. They are the preferred magnet type for this type of electrical machine. The magnet properties are given in Table 6.

The magnet material properties are derived from the ANSYS library material *NdFe35*. This corresponds to an N35 grade neodymium magnet that is commonly found in permanent magnet machines. The N35 grade is not the strongest type, and common grades extend up to N50, with N52 being the highest grade commercially available. The number of the grade is representative of the strength of the magnet, and corresponds to the materials maximum energy product.

The material *NdFe35* is used as it has favourable magnetic characteristics, and is commonly available.

Table 6: Properties of the magnets used in the design

Magnet Properties		
Magnet Thickness	5	mm
Pole Embrace	0.88	-
Magnet Type	NdFeB (Sintered)	-
Magnet Density	7400	kg/m ³
Remanent Flux Density	1.23	Tesla
Relative Permeability	1.09978	
Resistivity	1.6×10^{-6}	Ωm
Coercivity	-890,000	kA/m

3.13.7 Material Consumption

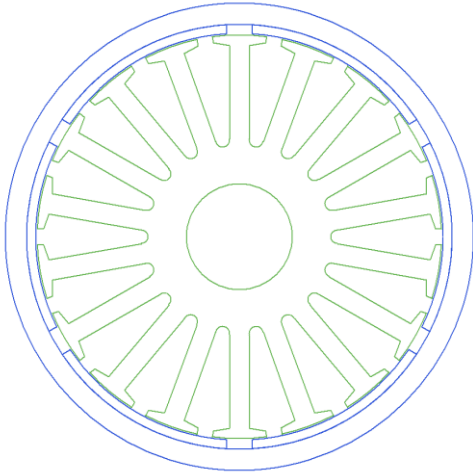
The material consumption of the machine is relatively high for the power rating of 1 kW. The large amount of iron used is to prevent saturation for the lower pole configurations, which have higher flux densities. As the machines with more poles require less iron to support the flux, they can be redesigned to be much lighter. However, to control the number of variables in the experiment, the stator design is constant throughout the different machines. The material consumption for the machines is given in Table 7.

Table 7: Material consumption of the proposed machine

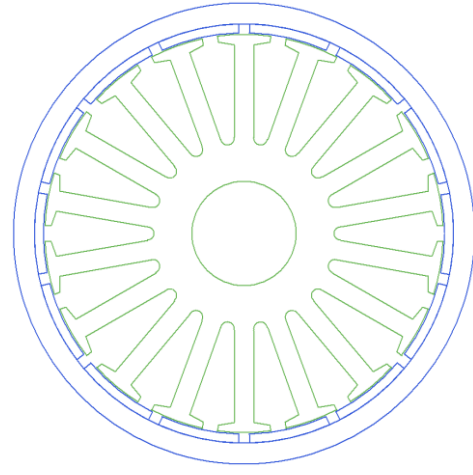
Rotor		
Rotor Volume	850.11	cm ³
Rotor Weight	6.69	kg
Stator		
Stator Volume	1028.90	cm ³
Stator Weight	8.10	kg
Slot Fill Factor	54.7	%
Wire		
Length	123.89	m
Copper Volume	459.89	cm ³
Copper Weight	4.11	kg
Magnet		
Magnet Volume	139.1726	cm ³
Magnet Weight	1.05	kg
Total	19.95	kg

3.13.8 Pole-Slot Combinations

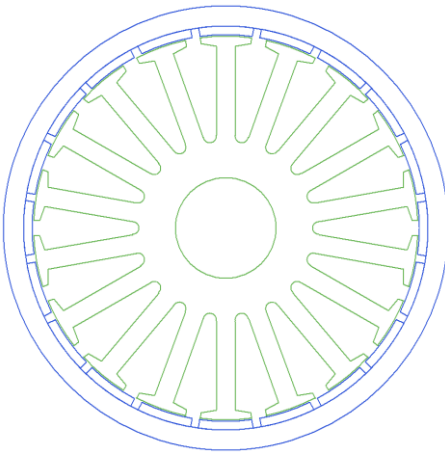
The proposed designs are presented in Figure 15. The designs only differ in the number of poles used. All other characteristics, including total magnet mass, is identical.



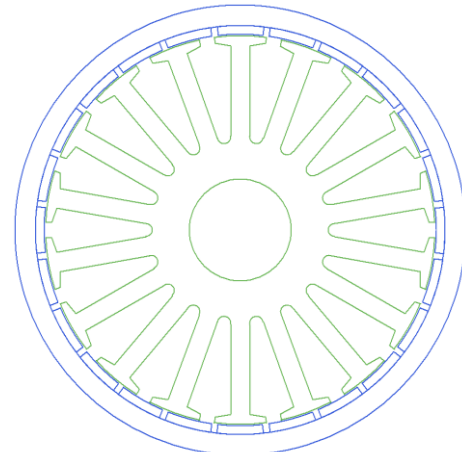
18 Slot 6 Pole Machine ($q = 1.0$)



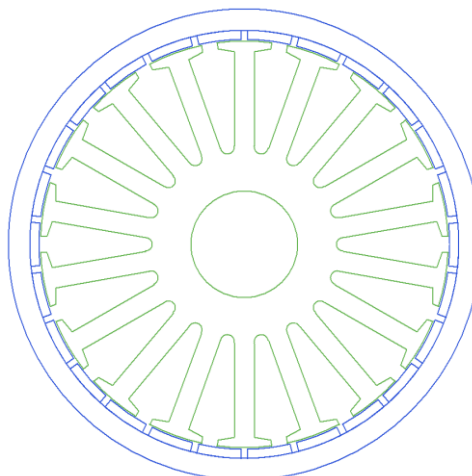
18 Slot 14 Pole Machine ($q = 0.43$)



18 Slot 20 Pole Machine ($q = 0.3$)



18 Slot 24 Pole Machine ($q = 0.25$)

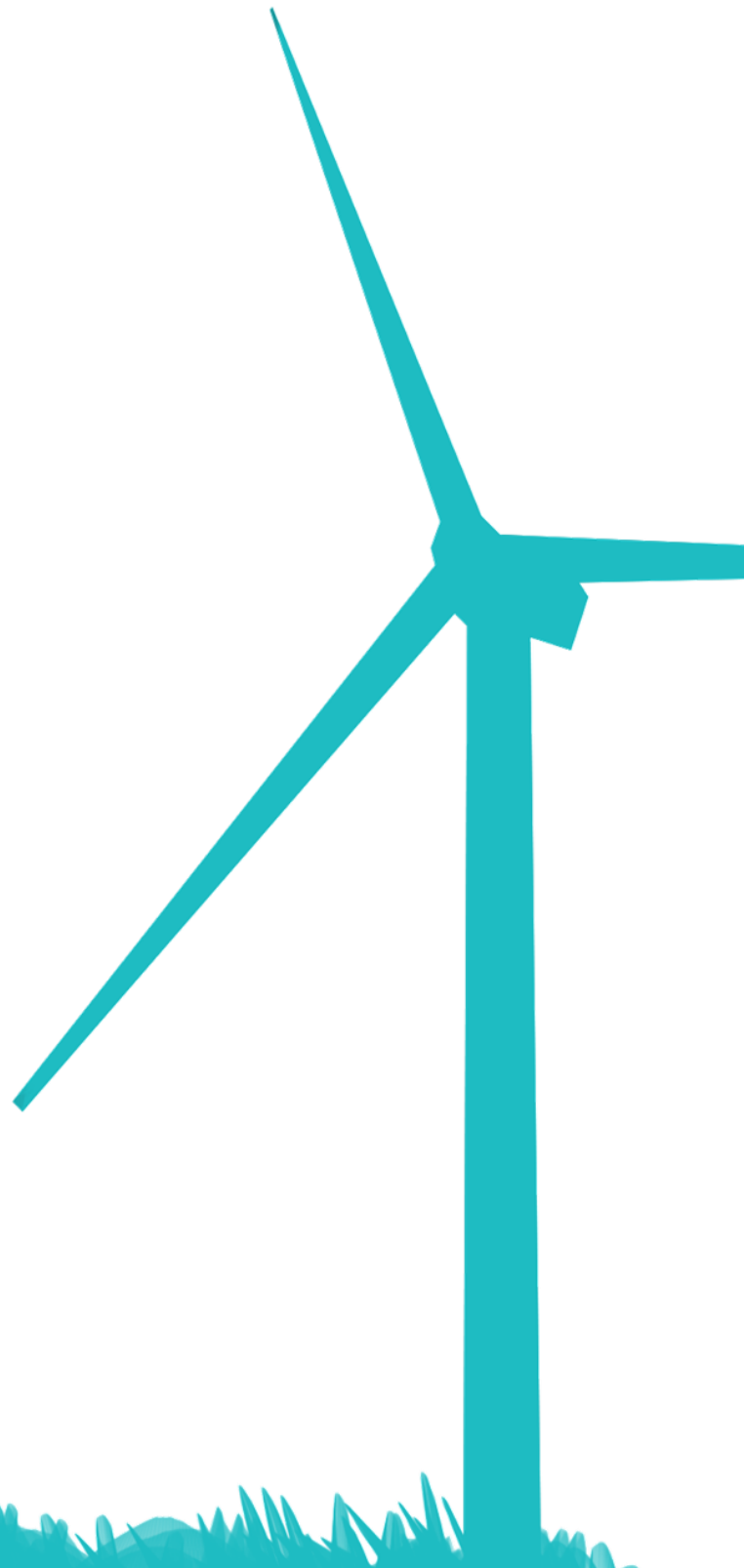


18 Slot 26 Pole Machine ($q = 0.23$)

Figure 15: Final proposed machines for testing

Chapter 4

Testing and Results



4.1 System Analysis Methods

4.1.1 Maxwell RMXprt

ANSYS Maxwell RMXprt is an algorithmic simulation program that uses input dimension values to apply classical analytical motor theory and equivalent magnetic circuit analysis to calculate machine performance in several categories. The results can be simulated in a very short period of time, enabling the systematic testing of many different parameters. However, the results from this type of simulation are not completely reliable as they are designed to provide quick results that are not comprehensive. Therefore, FEA is still performed to provide a comprehensive and more reliable system simulation.

This software is typically used to support initial sizing decisions, as well as selecting initial values for a number of different parameters using the Optimetrics parametric design tool. While the software calculates outputs using equivalent magnetic circuit analysis, it will also display a diagram of the machine, as shown in Figure 16 below.

In this project ANSYS RMXprt is used for the initial sizing of the motor, as well as performing initial optimisation with parametric optimisation.

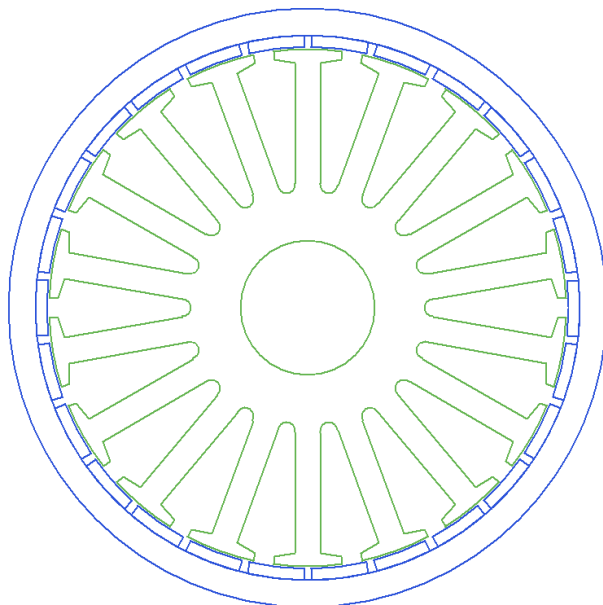


Figure 16: RMXprt generator diagram after parameter specification

4.1.2 Maxwell 2D/3D FEA

Maxwell 2D and 3D are finite element analysis software packages used to simulate magnetostatic, and transient electrical operation of a rotating machine. Maxwell 2D uses a 2D cross-sectional model, and has slightly reduced accuracy compared to Maxwell 3D. Effects occurring in the Z-axis are ignored in 2D simulation. Maxwell 3D uses a 3D model which takes into account fringing effects and 3D geometries, however, the simulation time is substantially increased due to the large increase in simulation elements. The differences in the models can be seen in Figure 17.

Finite element analysis works by breaking the machine model into 2D or 3D elements using a meshing process. A finer mesh using a higher number of elements is more accurate. The 2D mesh used is presented in Appendix H. For each of the elements, magnetic and electrical field modelling equations are applied. The results of each element are then systematically recombined in order to simulate the total system response. For transient analysis this process is repeated while the machine is rotating, using the results of the previous iterations. The length of the time interval may greatly impact accuracy in transient simulations.

Maxwell 2D/3D is used to simulate the open circuit operation of the generator. Additionally, the models are used in a cosimulation to determine the operation using a number of different loads.

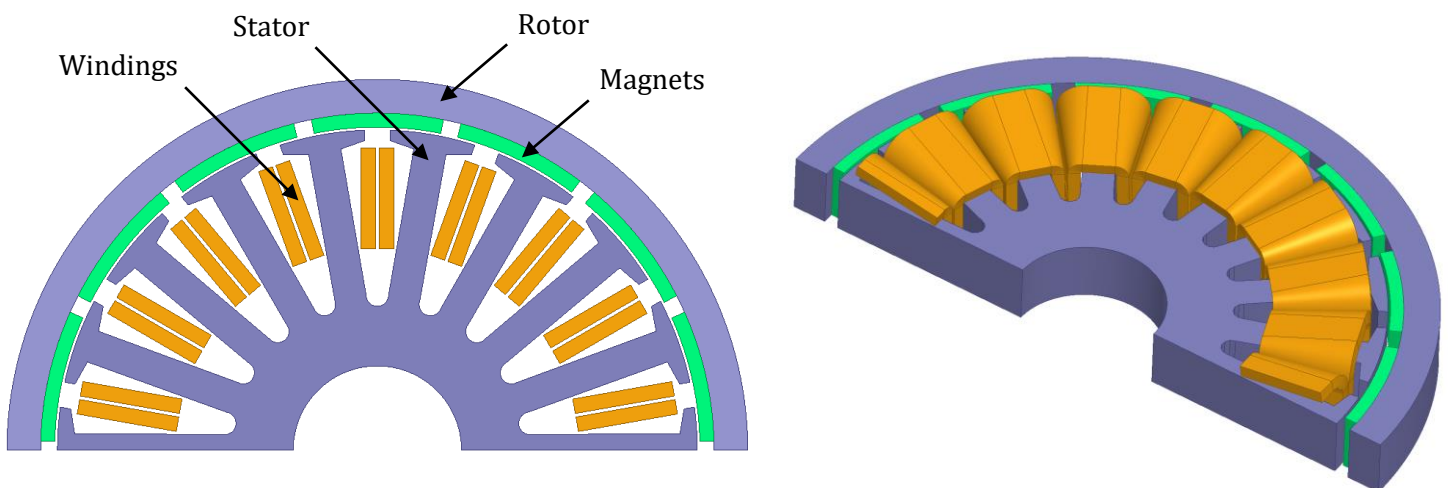


Figure 17: (left) Maxwell 2D model (right) Maxwell 3D Model

4.1.3 Simplorer Systems Modelling

ANSYS Simplorer is a systems modelling software package that can be used to simulate a number of basic electrical, fluid, thermal, and mechanical systems. Simplorer can be used in a cosimulation with Maxwell in order to test the generators' responses to different electrical systems and mechanical inputs. The cosimulation uses mechanical input from Simplorer to apply a torque signal to the generator in Maxwell, the generator is simulated and returns an electrical signal to Simplorer, which is applied to the modelled electrical load. The basic cosimulation block diagram is presented in Figure 18. An example setup in Simplorer is shown in Figure 19.

Simplorer is used to simulate the generator in loaded conditions in different electrical configurations. Circuits that include three-phase loads and three-phase rectifiers are used. The loads are purely resistive or battery loads. No capacitive or inductive loads are used as the designed purpose of the generator does not include usage with inductive or capacitive loads. Testing for inductive and capacitive loads is deemed unnecessary.

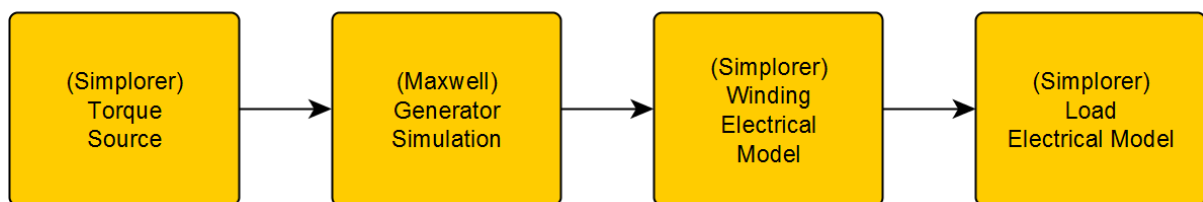


Figure 18: Simplified block diagram of cosimulation process

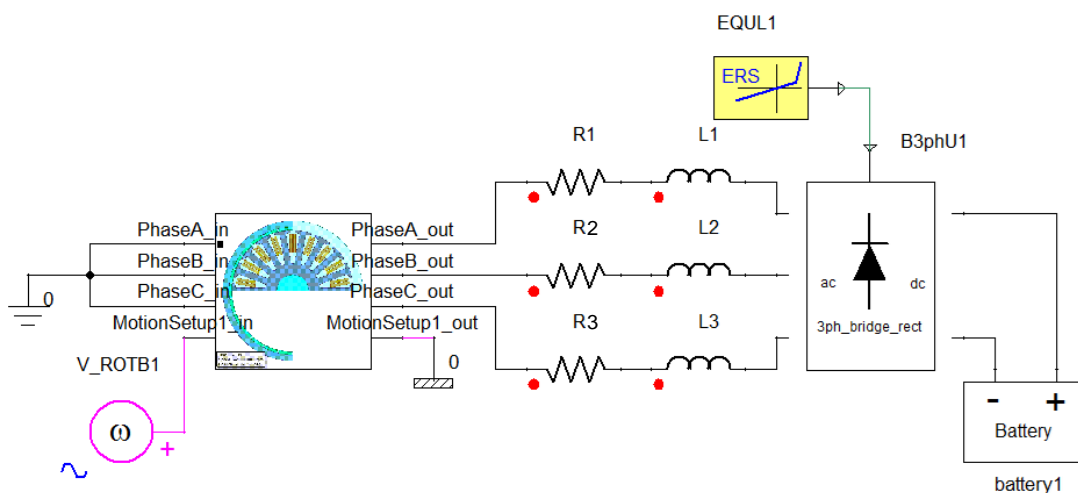


Figure 19: Maxwell/Simplorer Cosimulation with rectifier and battery load

4.2 Magnetic Analysis

The first stage of analysis is the magnetic analysis of the machine in ANSYS Maxwell. The magnetic analysis is used to obtain an understanding of the magnetic circuit in the machine. This highlights areas where the core may be saturating, and can be used to improve the magnetic paths of the design. As the process is repeated for all machines, it gives an insight to the magnetic behaviour of the designs as the number of poles increases.

The magnetic analysis is tested under no-load, and full-load conditions. No load conditions will ensure there is no magnetic flux created by current in the windings. The machine terminals are left as an open-circuit to ensure that there is no current flowing through the windings. There is still an EMF generated at the terminals. The full-load conditions use a 4Ω , three-phase resistive load and show the effects of winding current on the flux density of the machine.

The magnetic fields are presented using two different representations. The first representation overlays the calculated field property over the machine geometry at a particular instance in time. This gives an overview of how the magnetic circuit is flowing through the entire machine at a particular point in time.

The second method presents a field property, such as flux density, along a line through the machine geometry. This gives an insight to the field property in a more focused approach. This method is used to present the air-gap flux density through 180 mechanical degrees of the machine when the machine is stationary. This shows how the air-gap flux density is spread while the machine is stationary.

The flux density is also presented at different points as the machine is rotated 90 mechanical degrees. This presents how the flux density changes as the machine is rotating. This is used to show the stator tooth flux density (flux linkage), and the air-gap flux density at the stator tooth tops as the machine is rotating.

4.2.1 Magnetic Flux Density

The magnetic flux density plot is used to determine the maximum flux density at any point in the structure, and to find areas where magnetic saturation of the core material is occurring. Magnetic saturation of the core occurs when the magnetic flux generated through the application of an external magnetic field experiences severely diminishing returns. This induces significantly greater losses compared to unsaturated operation. The BH curve presented earlier in Figure 14, shows saturation occurs once the flux density exceeds $\approx 1.8\text{T}$.

The full-load and no-load flux density is presented in Figure 20. This shows that as the number of poles increase in the machine, the overall flux density is decreased in the stator teeth body and the rotor. The reduction in flux density is indicated by the changing of red areas to green areas.

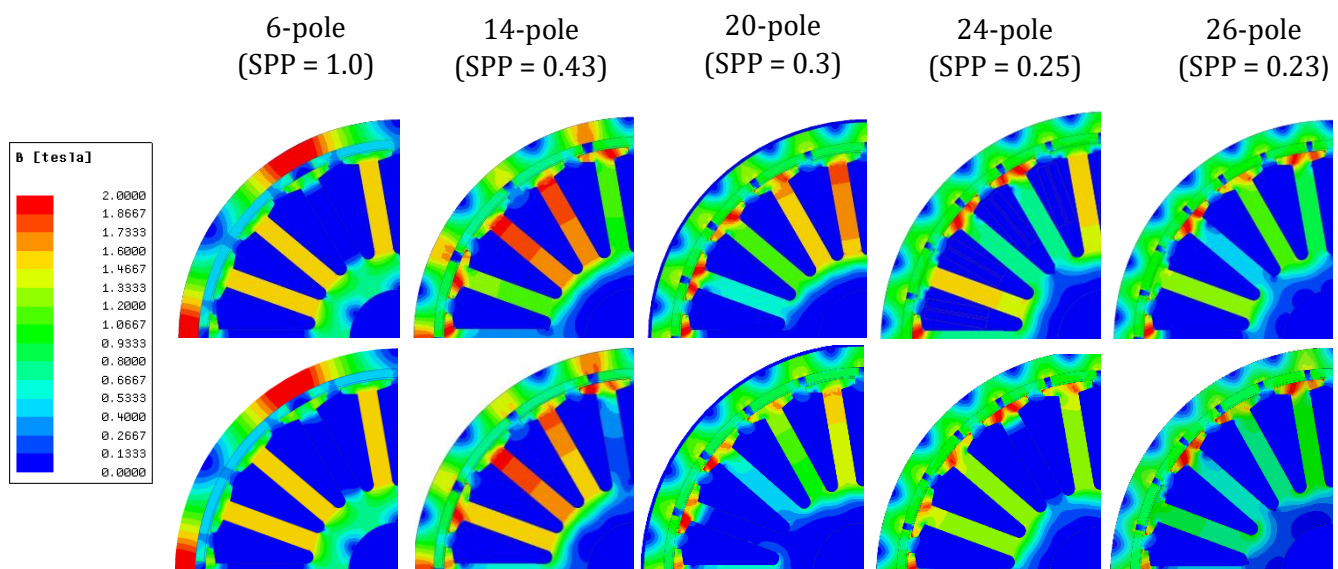


Figure 20: (Top) No-load flux density plots (bottom) full-load flux density plots for the five different machines

The 6-pole machine is shown to have high saturation in the rotor, with no saturation in the stator. The magnets in this machine are so large that they cover two slot pitches, so flux is being supported by two stator teeth. This can be seen to significantly reduce flux density in the stator. The 14-pole machine has magnets that only cover one slot pitch, and this can be seen to cause saturation in the stator teeth.

The no-load and full-load plots differ very slightly in the phase of the flux density. This is almost indiscernible in these plots and is discussed further in the flux linkage plots presented later.

Reduced flux density can be a beneficial aspect, as the generator will require less stator iron to support the flux without reaching saturation. However, lower overall flux density also reduces the flux linkage and induced EMF.

4.2.2 Magnetic Field Flux Line Representation

The magnetic flux line representation is a plot of the magnetic circuit, with segmented areas based on the magnitude of magnetic flux contained. It is a simple way of representing the magnetic circuit through the machine. The plots use a red shaded area to indicate the flux is travelling in an anti-clockwise direction, and blue shaded areas to represent flux travelling in a clockwise direction.

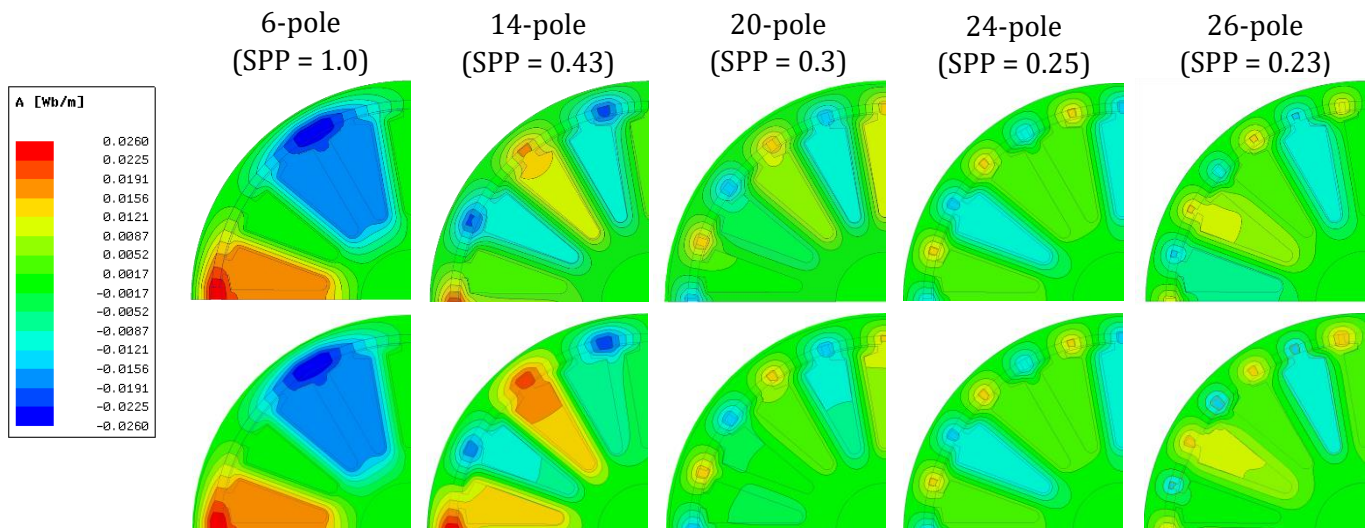


Figure 21: Flux line plots for the five machines (full figures in Appendix C)

The full-load and no-load plots again only differ slightly. The difference is attributed to a phase shift.

The flux line overlays in Figure 21 show similar results to the flux density plots, with reduced flux density shown by the reduced colour intensity. Adjacent magnets can be seen to use stator teeth tops to carry significant amounts of flux, as shown in Figure 22. As the number of poles increases, the number of these junctions increase, leading to an overall decrease in flux density in the main stator body.

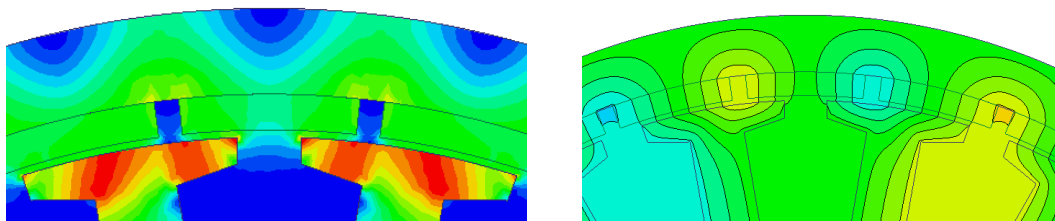


Figure 22: Magnified view of magnet junctions

4.2.3 Magnetic Flux Linkage

The flux linkage indicates how much flux is passing (being linked) through the coils. The induced EMF is proportional to the derivative of the flux linkage, and is given by:

$$e = N \frac{d\phi}{dt}$$

Where e is the induced EMF, N is the number of turns in the coil, and ϕ is the flux linkage. The ideal shape of the flux linkage is sinusoidal such that the induced EMF is also sinusoidal, as shown in Figure 23.

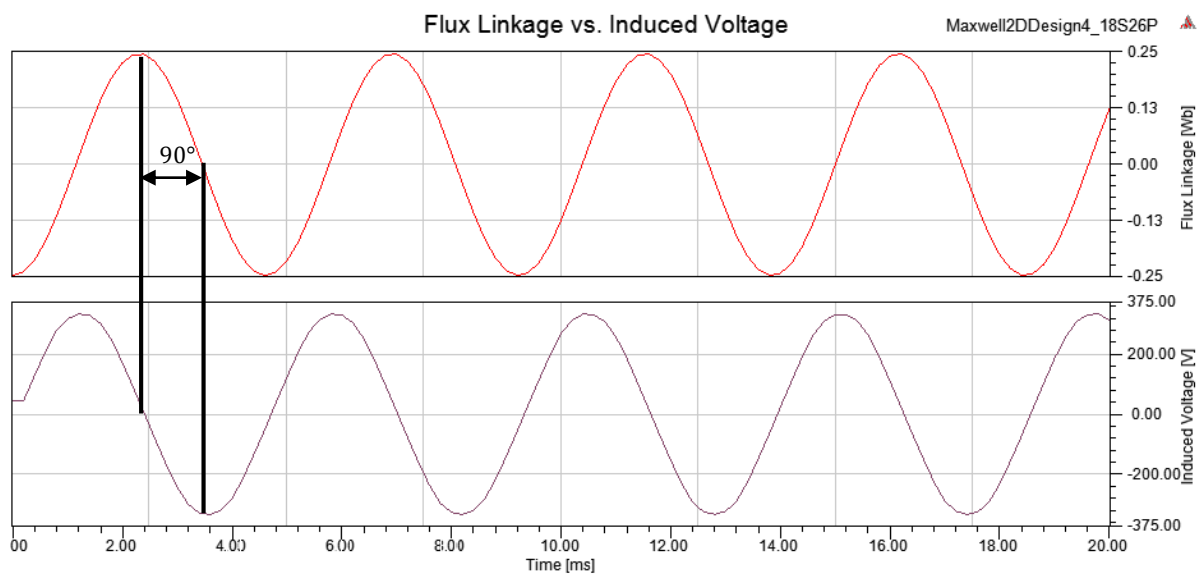


Figure 23: Relationship between sinusoidal flux linkage and induced voltage

The flux linkage has a direct effect on the THD of the back-EMF. Harmonics that are present in the flux linkage affect harmonic content in the induced EMF. As the total harmonic distortion of the EMF should be minimised, it is desirable to have a flux linkage with the lowest harmonic content possible. Harmonics in the flux linkage may be generated as a result of saturation of the core. When saturation occurs, the flux linkage waveform will exhibit clipping, as the core cannot support more flux. Clipping in the time domain will introduce odd-order harmonics in the frequency domain. The harmonic distortion is discussed in more detail later in this chapter.

The plots for the no-load flux linkage of the machines are shown in Figure 24 for 360 electrical degrees. The different colours represent different phases in a three-phase arrangement.

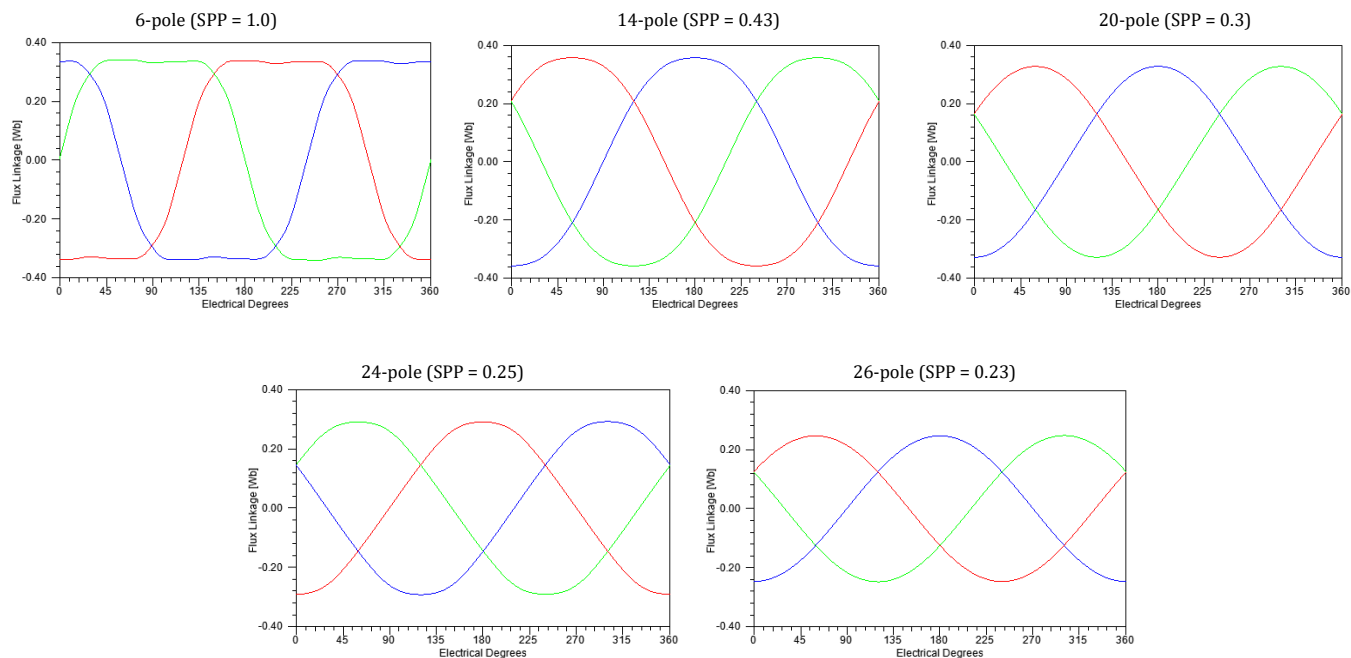


Figure 24: No-load flux linkage plots for the five machines

The flux linkage waveforms of the machines are mostly sinusoidal. The 6-pole machine has a non-sinusoidal waveform that may be a result of saturation or magnet size. As the magnet is larger than two slot pitches, the flux waveform is expected to be elongated.

As the number of poles increases, the frequency and the magnitude of the waveforms change. The frequency increases linearly with the number of poles, and the magnitude is seen to decrease.

The increase in alternating flux frequency will result in an increase of the core losses in the machine. The decreased magnitude of the flux linkage is expected from the flux density plots presented previously. As the flux density in the stator teeth body decreased with an increased number of poles it is expected that the flux linkage would also decrease.

The changes in flux linkage have a direct effect on the induced EMF. The increased frequency and decreased magnitude of the linkage is directly proportional to an increase in frequency and reduction in magnitude of the induced EMF.

The plots of the full-load flux linkage are presented in Figure 25.

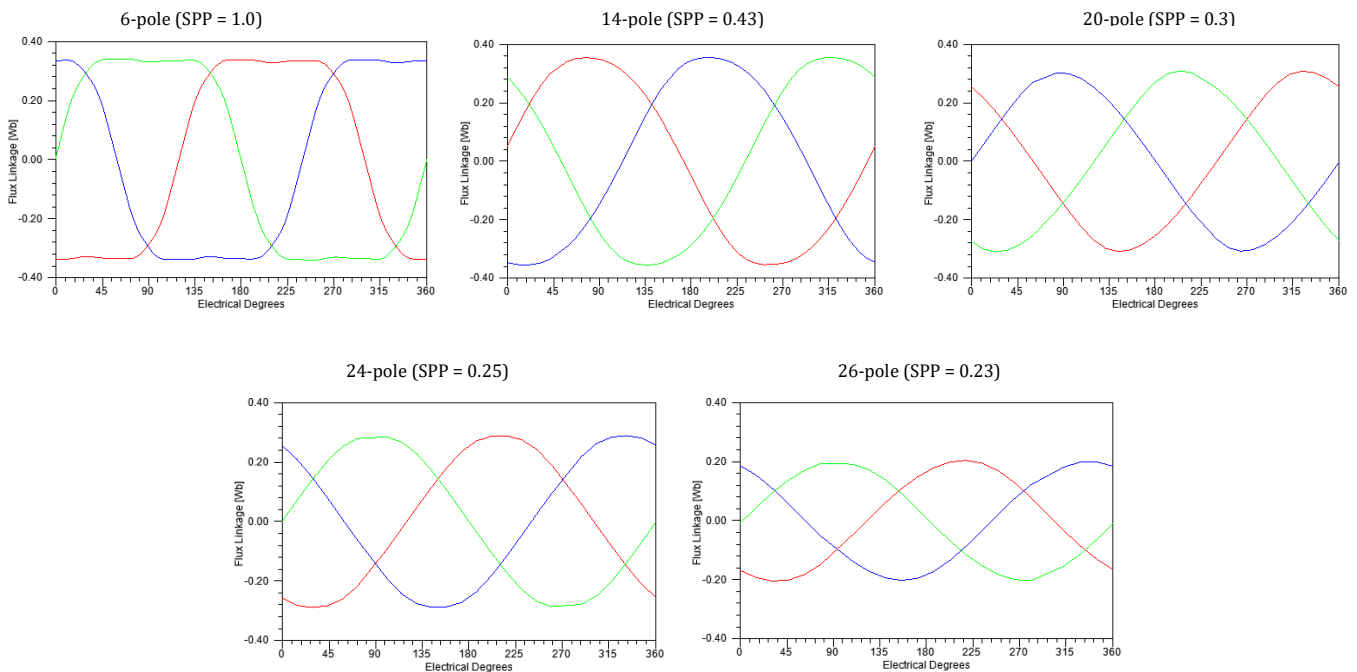


Figure 25: Full-load flux linkage plots for the 5 different machines

The full-load flux linkage is similar to the no-load flux linkage, and maintains the same frequency. However, there are several slight differences in waveform shape and amplitude. The reduction in magnitude is most noticeable for the 26-pole machine, indicating poor voltage regulation at full-load. The shapes of the waveforms are slightly distorted compared to the no-load counterparts. In particular, the 14-pole machine has noticeably different no-load and full-load waveform shape. This indicates a higher level of THD under full-load conditions.

Previously it was noted that the flux density plots showed signs of a slight phase shift. Figure 26 shows the comparison between the flux linkage of one phase for full-load and no-load operation. A significant phase shift of approximately 53.7° electrical is measured. This is most likely due to the effect of the modelled winding inductance.

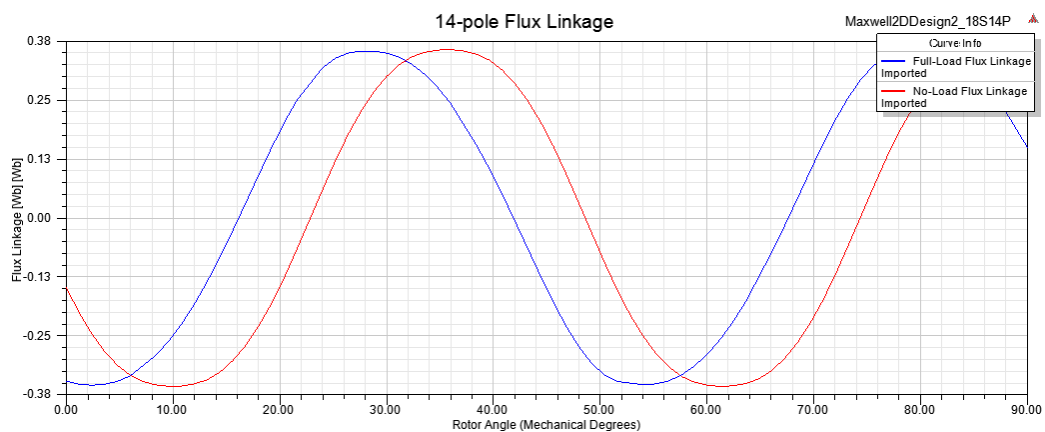


Figure 26: Comparison of flux linkage of one phase for full-load (blue) and no-load (red) operation

4.2.4 Air Gap Flux Density

The air gap flux density is the measure of the flux density in the air gap of the machine. This is measured to determine if a suitable amount of flux is crossing the airgap, and whether modifications to the airgap length should be made. The airgap flux density also gives an idea of how the flux is travelling through the air gap.

The static airgap flux density is measured while the machine is not moving. The graphs in Figure 27 show the magnitude of the airgap flux density along 180° of the circumference inside the airgap. These plots are used to verify the simulation as a trough in the plot corresponds to a stator slot, or a gap between adjacent magnets. The correspondence between the stator slot and the troughs are shown in the bottom plot of Figure 27.

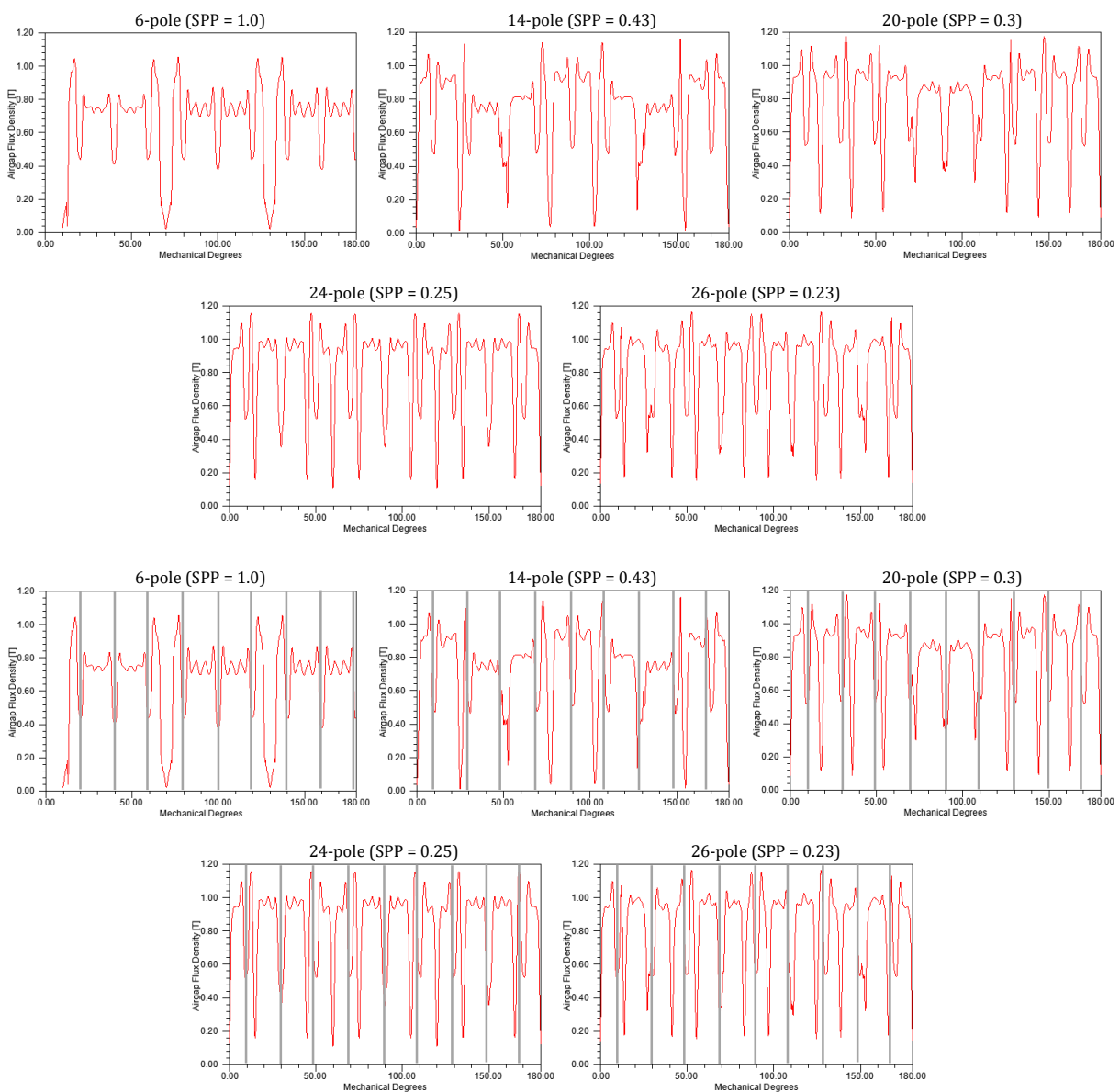


Figure 27: (Top) Airgap flux density (bottom) Airgap flux density showing stator slot positions

The average and maximum airgap flux densities are provided in Figure 28.

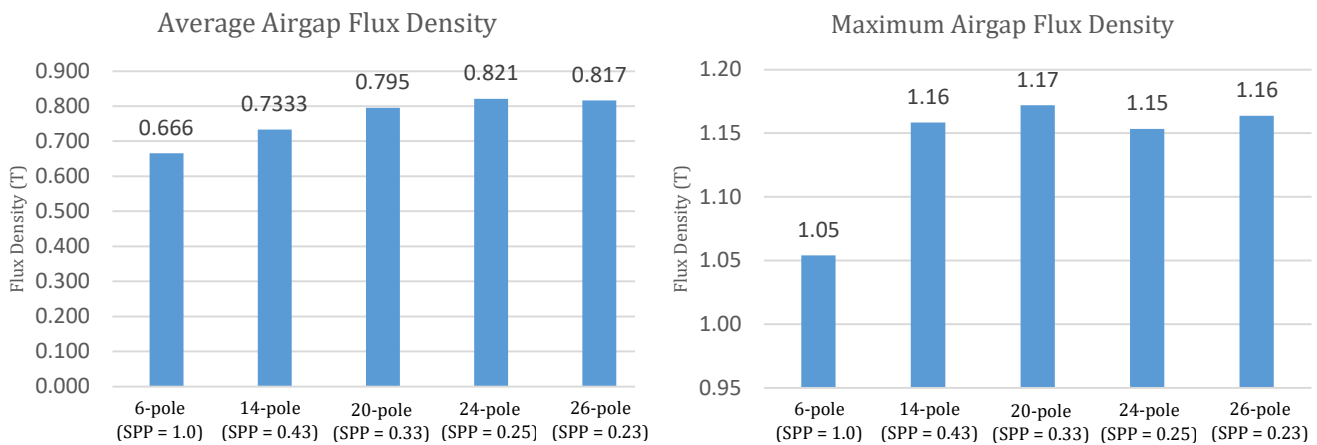


Figure 28: (left) Average airgap flux density (right) Maximum airgap flux density

The average airgap flux density is seen to increase with the number of poles, although the maximum airgap flux density is similar for all machines except the 6-pole machine. It is important to note that this is the average at this particular time step, and is not representative of all positions of the machine.

To obtain the average airgap flux density across all positions of the machine, the airgap flux density is measured over the stator tooth as shown in Figure 29. The length of the arc is one stator slot pitch, or 30° mechanical. Measurements are taken as the rotor performs a mechanical rotation of 90°.

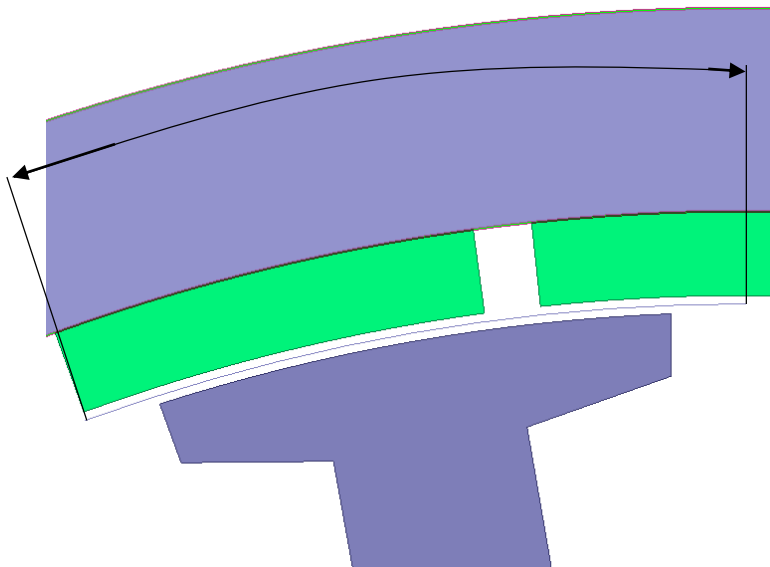


Figure 29: Arc of the magnetic flux density measurements for a rotating stator

Figure 30 shows the measurements of the airgap flux density of the machines for a 90° mechanical rotation. As the number of poles increase it is seen that the waveform converges to a square wave. Transient edges at the changing point of the flux are seen to decrease in magnitude, and the 26-pole machine has an almost perfect flat topped waveform.

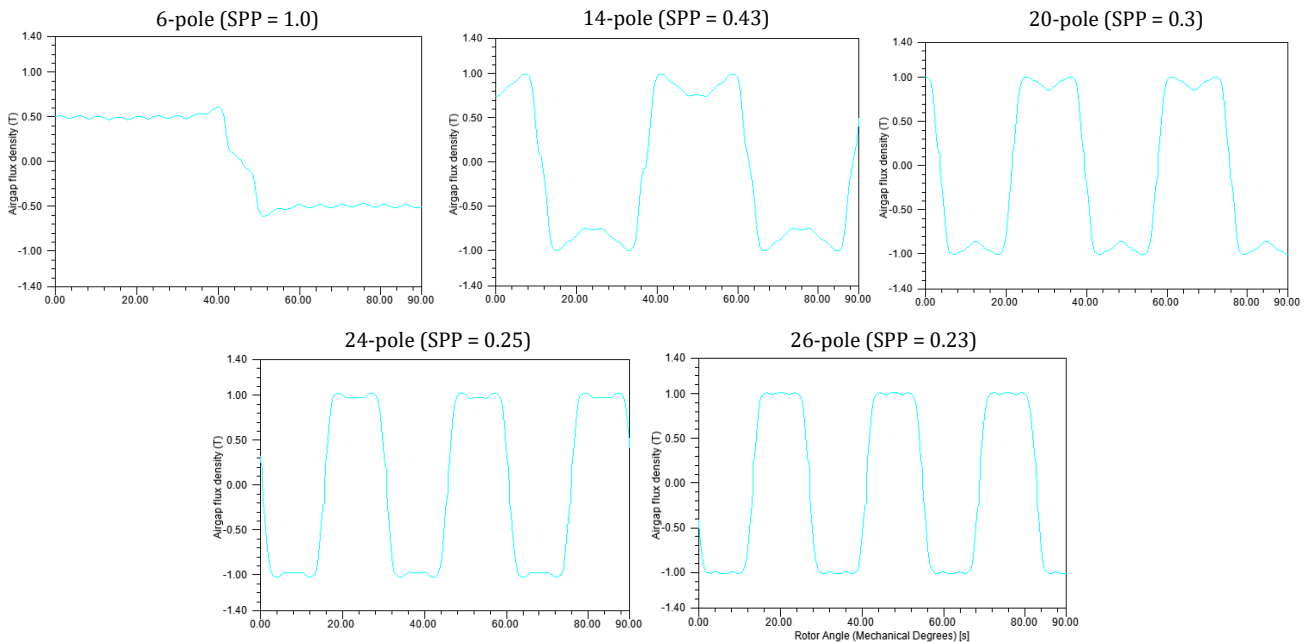


Figure 30: Measured airgap flux density for the five machines

The average flux density for these waveforms is presented in Figure 31.

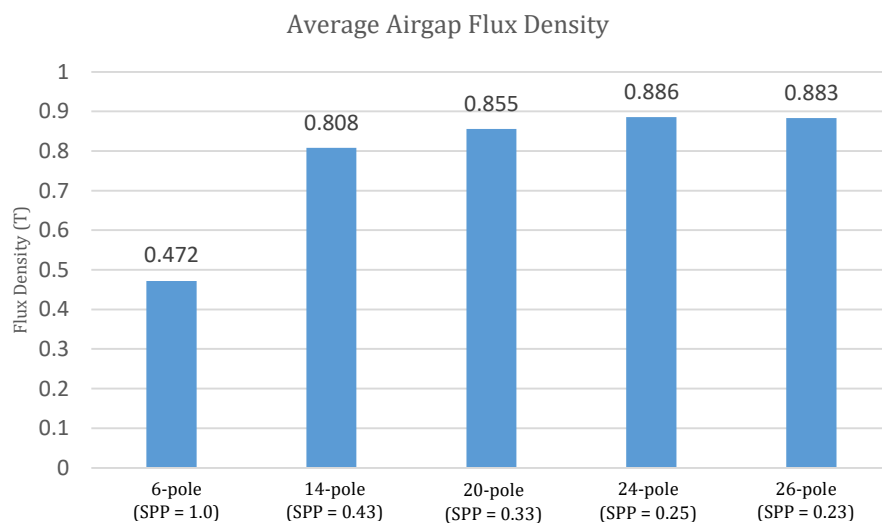


Figure 31: Average airgap flux density over a 90° mechanical rotation

The averaged results over a 90° rotation are similar to those presented in Figure 28. The main difference is the 6-pole machine has much lower airgap flux density. The airgap flux density increases as the number of poles increase. This may be caused by the increased circulating flux between adjacent magnets.

4.2.5 Summary of Magnetic Analysis Findings

In this section the magnetic analysis of the machine was performed in order to obtain an understanding of the magnetic circuit throughout the machine and the effects of the pole-slot combination on the flux density and flux linkage. A summary of the figures generated for the no-load analysis is given in Figure 32. The findings showed that:

- Increasing the number of poles increases the leakage flux between adjacent magnets which can decrease the flux linkage and flux density of the machine
- Fully-loaded circuits experience reduction of the flux linkage amplitude, and a phase shift is introduced compared to the no-load circuit

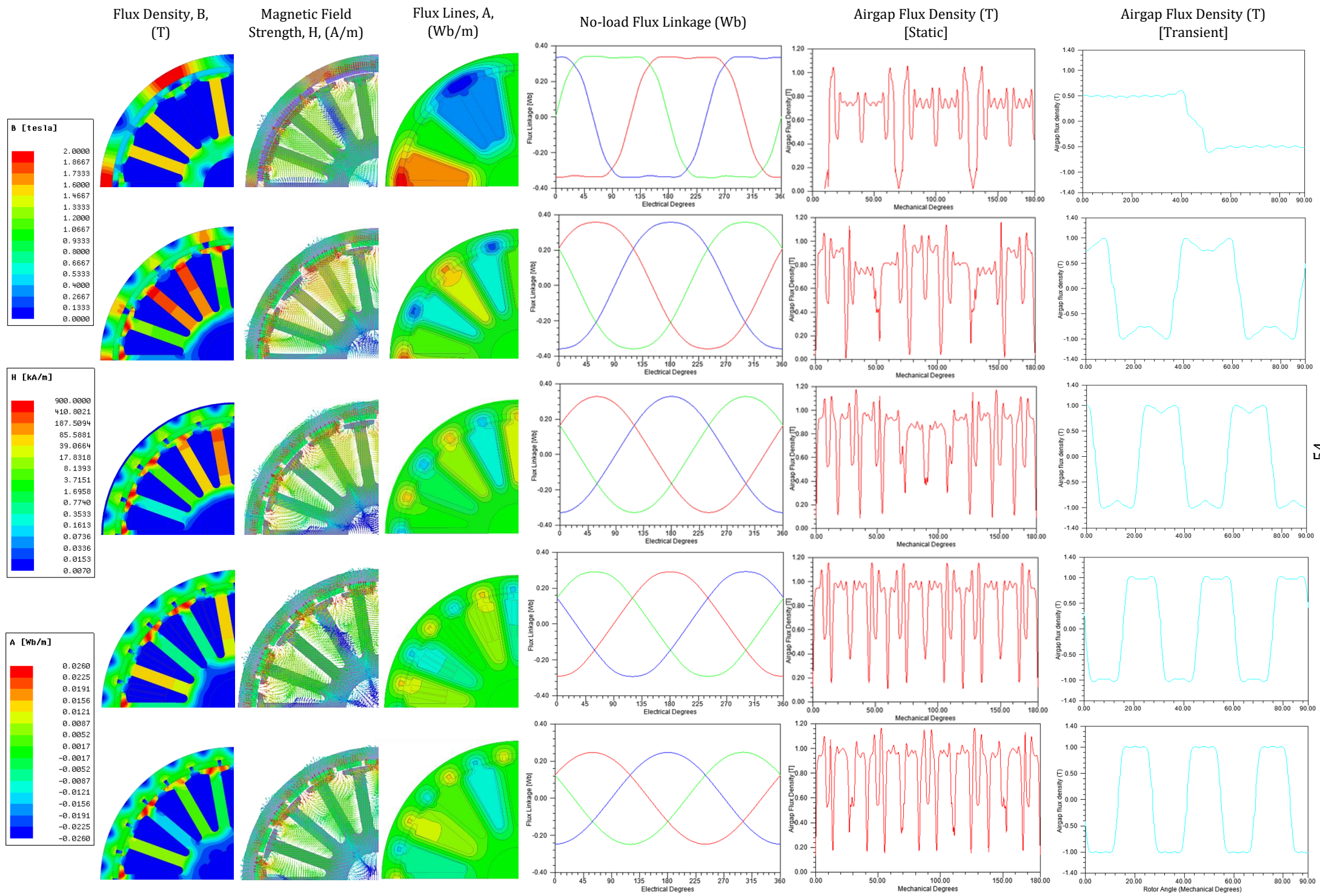


Figure 32: Summarised figures for the no-load magnetic analysis

4.3 Open Circuit Analysis

The open circuit analysis covers testing of the electrical machine when there is no electrical load on the machine. The open circuit tests are used to measure the cogging torque, the induced EMF, the total harmonic distortion, and the iron losses.

4.3.1 Cogging Torque Measurement

The cogging torque is the torque created by the interactions between the stator iron and the rotor magnets. Cogging torque creates noise, vibration, mechanical wear, and can increase the required starting wind speed of a wind turbine generator. Cogging torque is ideally minimised.

To ensure that a full torque waveform is measured, the periods of the cogging torque waveform for each machine are determined using the equation:

$$Period_{cog} = \frac{360^\circ}{LCM(N_s, 2p)}$$

Where **Period_{cog}** is the cogging torque waveform period in mechanical degrees, and **LCM(N_s, 2p)** is the Lowest Common Multiple of the number of slots and the number of poles. The results are presented in Table 8:

Table 8: Calculated periods for the cogging torque waveforms

	18S6P	18S14P	18S20P	18S24P	18S26P
LCM	18	126	180	72	234
Period_{cog} (° Mech.)	20.0°	2.86°	2.00°	5.00°	1.54°

The cogging torque is measured using a simulation run in Maxwell 2D with a simulation length of 200 ms, and a time step of 0.2 ms. These parameters result in a rotational step of 0.24°, over a total sweep of 240°. This is calculated to be a sufficiently high resolution and length to accurately capture the entire torque waveform of all the machines. The extended simulation length is necessary for measurement of other parameters such as induced EMF.

In terms of frequency, the simulation refreshes at 5 kHz. Using the Nyquist sampling theorem, a 5 kHz sampling rate will prevent aliasing of signals below 2500 Hz, and is able to accurately obtain signals below 500 Hz. The highest fundamental frequency of the cogging torque is expected to be 234 Hz and so is reproduced accurately.

The measured waveforms for the cogging torque are presented in Figure 33. The plots use different Y-axis scales in order to show the shape of the waveforms. It is seen that the 6-pole and the 24-pole machine have fewer high frequency transients, compared to the other machines. Full figures including waveform characteristics are found in Appendix D.

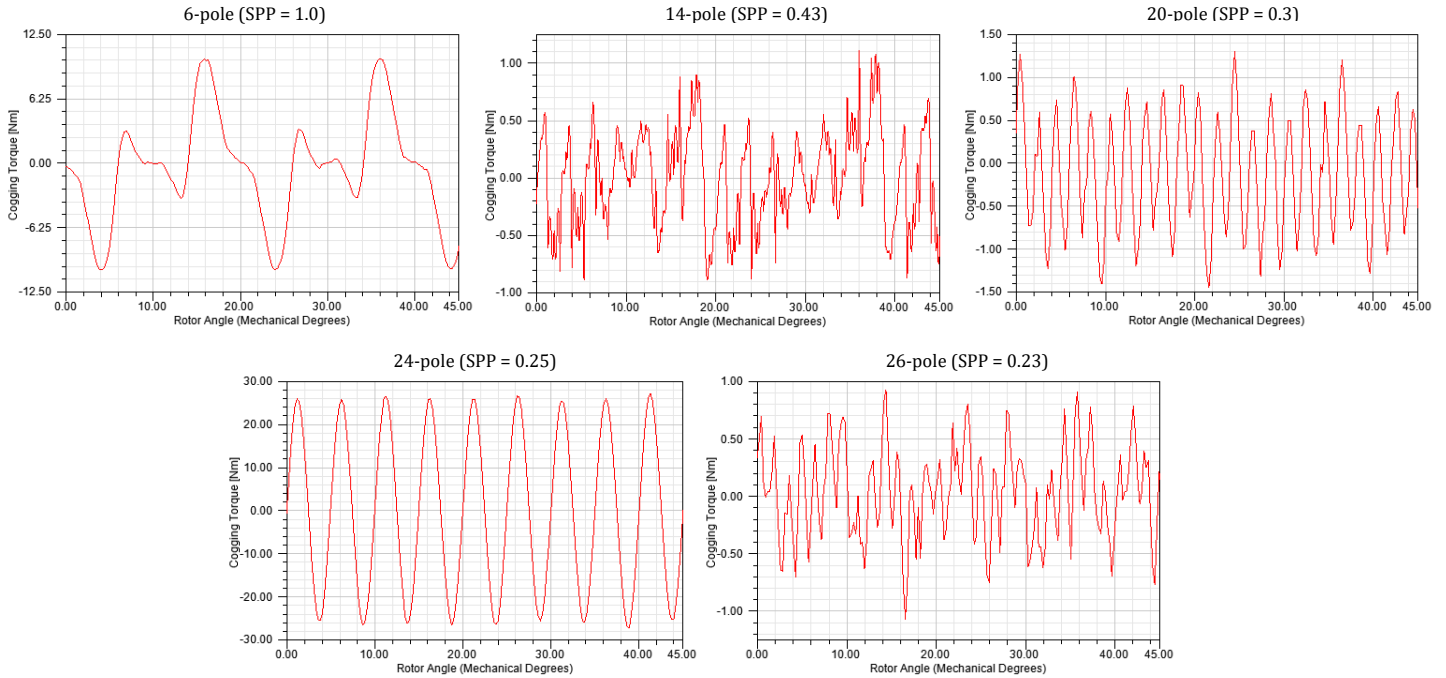


Figure 33: Cogging torque plots for the machines showing waveform shape

The measured periods and calculated periods are compared in Table 9. The results show that the theory correctly determines the cogging torque fundamental frequency. However, while some waveforms are straightforward to measure, others are less accurate estimates due to the transients present in the waveforms. The machines marked with an asterisk in Table 9 represent results that are taken as the average of multiple measurements due to the irregular nature of the waveforms.

Table 9: Calculated and measured torque waveform fundamental periods

	18S6P	18S14P*	18S20P	18S24P	18S26P*
LCM	18	126	180	72	234
Period (° Mech.)	20.00°	2.857°	2.000°	5.000°	1.538°
Period_{measured} (° Mech.)	20.08°	2.532°	1.896°	5.004°	1.524°

The Y-axis scale for the graphs in Figure 34 are then set to a uniform range to compare the differences in magnitude between the waveforms.

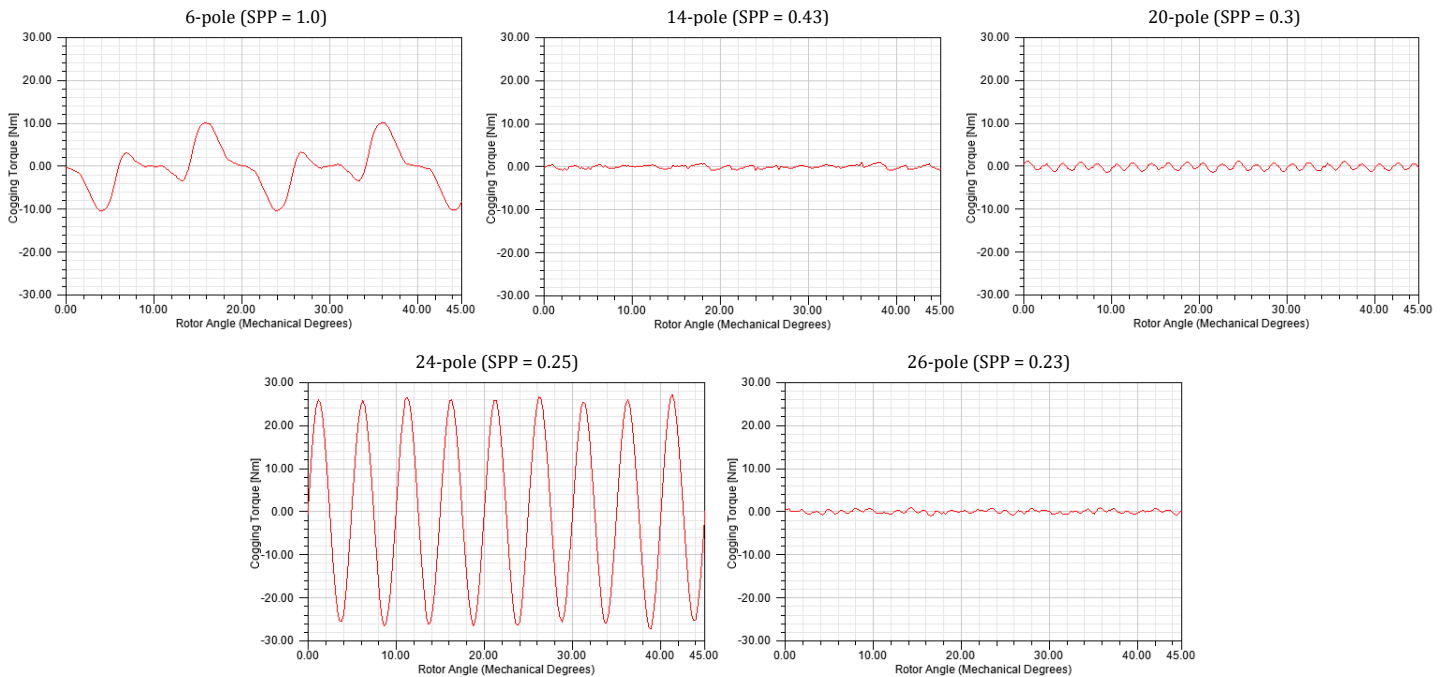


Figure 34: Cogging torque plots for the machines showing magnitude variations between machines

As the number of poles is increased, the cogging torque does not seem to follow a distinct pattern. However, the cogging torque reaches large values at certain pole-slot combinations. A summary of the cogging torque magnitudes at 200 rpm is shown in Figure 35.

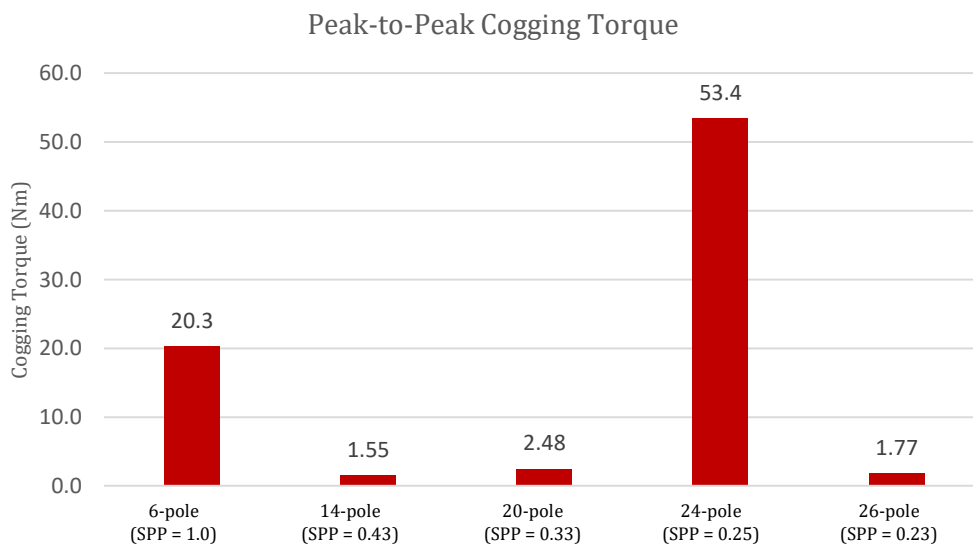


Figure 35: Summary of cogging torque values at 200 rpm

The two machines that exhibit significant cogging torque are the 6- and 24-pole machines. The other three machines all exhibit significantly lower cogging torque. The 6- and 24-pole machines are hypothesised to have greater cogging torque due to their particular pole-slot combination, rather than the number of poles. The pole-slot combination will have an effect on the overall alignment of the stator teeth and rotor magnets, and affects whether the cogging torque will constructively or destructively interfere throughout the machine.

There are various methods to estimate the magnitude of cogging torque based on the number of slots and poles. One particular method uses the fractional value of the SPP. As mentioned previously, the pole-slot combination can be expressed as the SPP using the equation:

$$q = \frac{N_s}{2p \times N_\phi}$$

Where q is the slots per pole and phase, p is the number of pole pairs ($2p$ is the number of poles), N_s is the number of slots, and N_ϕ is the number of phases. If the fractional part of this value has a unity numerator, it is an indicator that the cogging torque will be high. The values for the machines are given in Table 10.

Table 10: Slots per pole and phase for the variants

Machine	6-pole	14-pole	20-pole	24-pole	26-pole
q	$\frac{1}{1}$	$\frac{3}{7}$	$\frac{3}{10}$	$\frac{1}{4}$	$\frac{3}{13}$

The results indicate that the 6-pole and 24-pole machines will have high cogging torque. This is reflected in the measured results presented earlier. Although this has correctly identified machines with a high cogging torque, it gives no indication as to the magnitude for any of the machines, and therefore produces little information.

A second method of estimating cogging torque uses the lowest common multiple (LCM) of the number of slots and the number of poles. The cogging torque is roughly related to the inverse of the LCM of the number of slots and the number of poles [26]. The result is a series of numbers proportional to the cogging torque, rather than an actual value of torque.

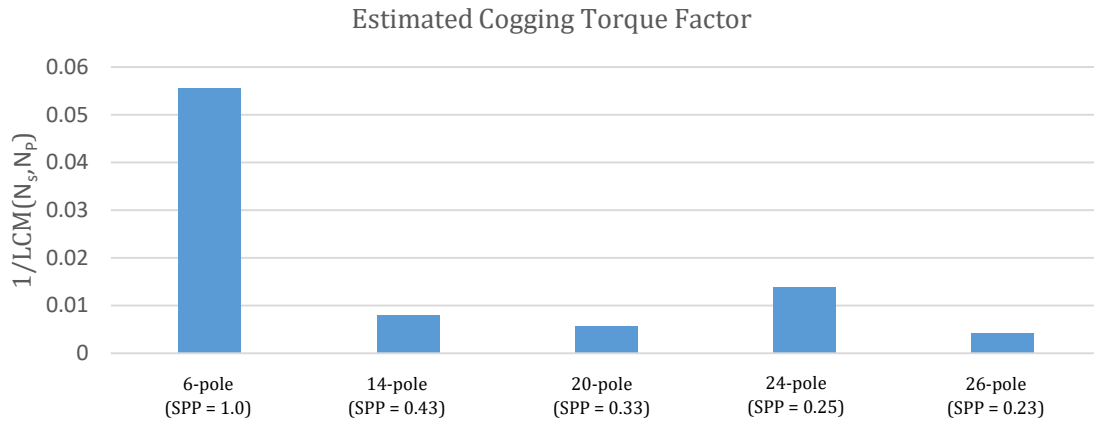


Figure 36: Inverse of the LCM of the number of poles and slots

The trends shown in Figure 36 are similar to the trends seen in the simulated cogging torque for the machines.

A third method of estimating the cogging torque introduces the factor C_T [27]:

$$C_T = \frac{N_s \times N_p}{LCM(N_s, N_p)}$$

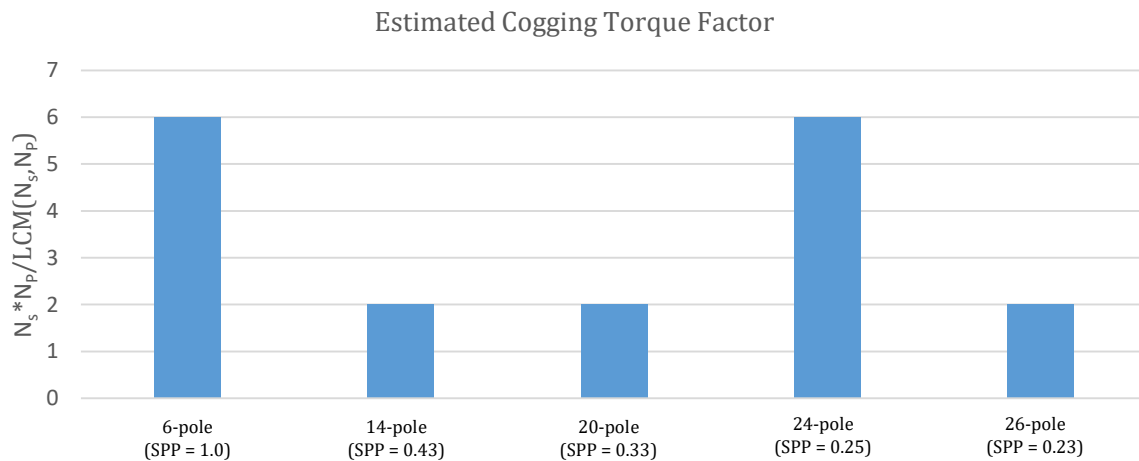


Figure 37: Estimated cogging torque using scaling factor

The factor, C_T , uses the inverse of the LCM but also includes a scaling factor derived from the number of slots and poles. The calculated values of C_T presented in Figure 37, show very similar trends compared to the observed values, with large cogging torque values expected for the 6-, and 24-pole machines. This method is shown to provide the most accurate indication of cogging torque values.

4.3.2 Induced EMF Measurement

The induced EMF waveforms are measured under open circuit conditions at rated speed. The waveforms are presented in Figure 38. The peak and RMS voltages of the EMF are measured from the waveforms, and the total harmonic distortion is also calculated. The THD at open circuit conditions determines the distortion created by the machine, rather than as a function of the load.

The simulation is performed in Maxwell 2D with a simulation length of 200ms and a time step of 0.2ms. The simulation parameters are identical to the cogging torque simulations specified previously.

To prevent aliasing, the highest measured frequency of the voltage waveform is calculated and compared to the sample rate of 5 kHz. The maximum frequency of the fundamental is calculated using the following relation:

$$f_{fund} = p \times \frac{\omega}{60}$$

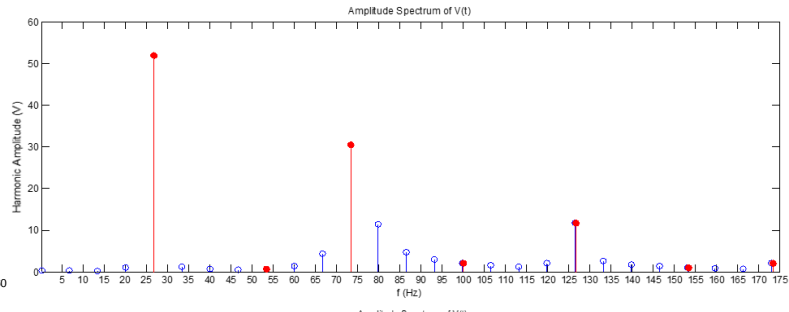
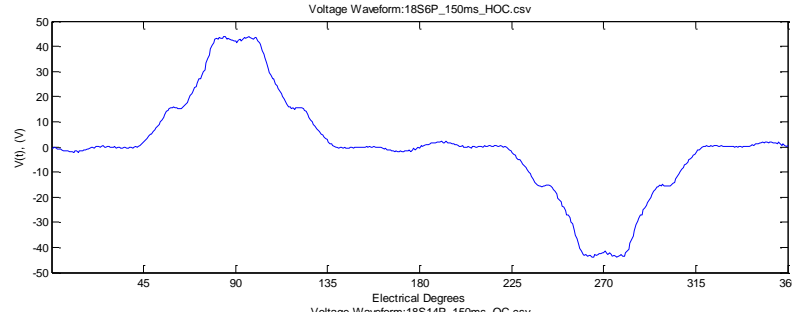
Where f_{fund} is the fundamental frequency of the EMF waveform, p is the number of pole pairs, and ω is the frequency of rotation in rpm. The 26-pole machine had the highest fundamental frequency of 43.33 Hz. The frequency components of the waveform are calculated up to the 7th harmonic. Therefore, the maximum measured frequency is 303 Hz. The sampling rate of 5 kHz is high enough to measure this accurately. The spectral plots presented later show there is still a moderate amount of quantisation error in some instances. This could be reduced by significantly increasing the sample frequency. This approach is computationally expensive, and the results would not justify the greatly increased time taken to solve the simulations.

A MATLAB script was written to calculate the THD using the Fast Fourier Transform and the property:

$$THD = \frac{\sqrt{V_2^2 + V_3^2 + V_4^2 + \dots + V_n^2}}{V_1}$$

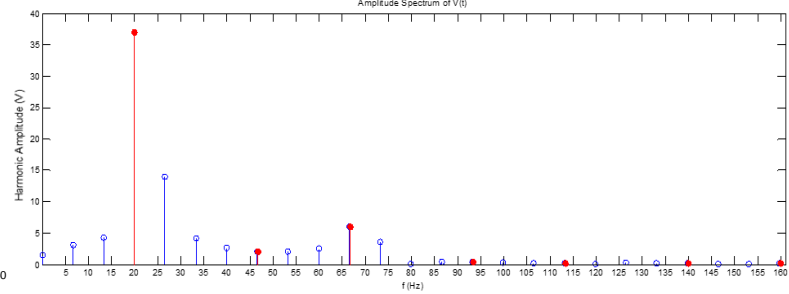
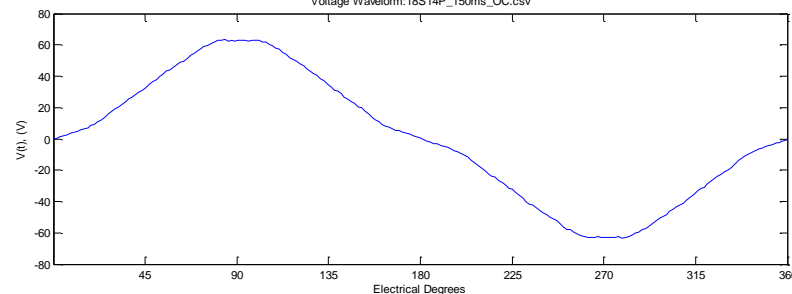
Where V_n is the RMS amplitude of the n^{th} harmonic. The MATLAB script is used to determine the THD and to provide a visual representation of the amplitudes of the harmonics, as shown in Figure 38. In the spectral graphs the harmonics are highlighted in red. A detailed description of the measurement process with measured values is available in Appendix E. It is important to note that due to the quantisation error, the magnitude of the harmonics may be scaled differently. However, this is not seen to significantly affect the distortion measurements.

18/6p
(SPP = 1.0)



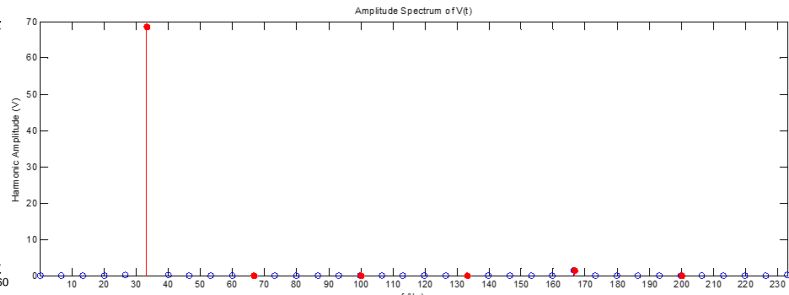
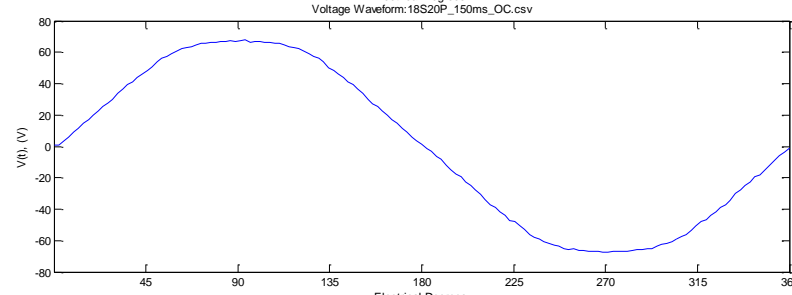
THD: 71.1%

18/14p
(SPP = 0.43)



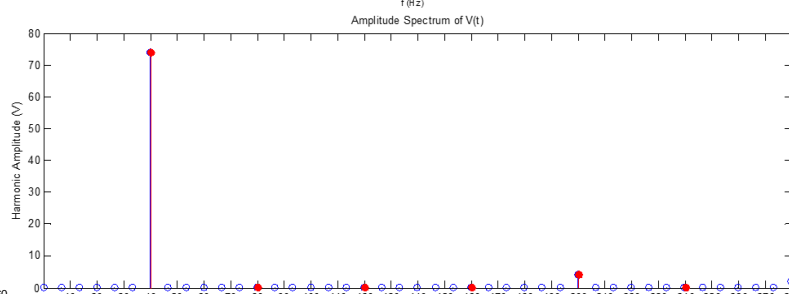
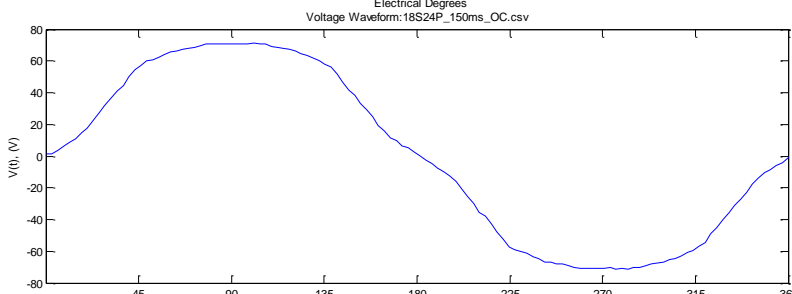
THD: 17.3%

18/20p
(SPP = 0.3)



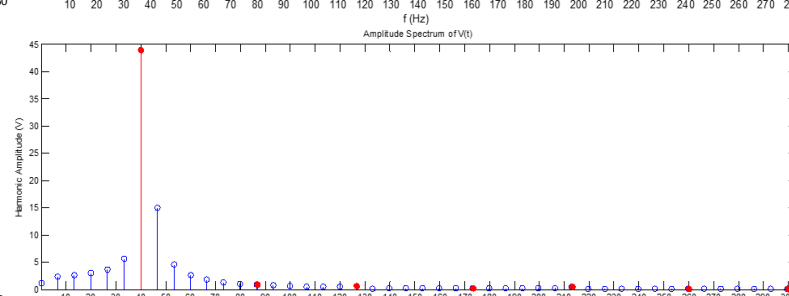
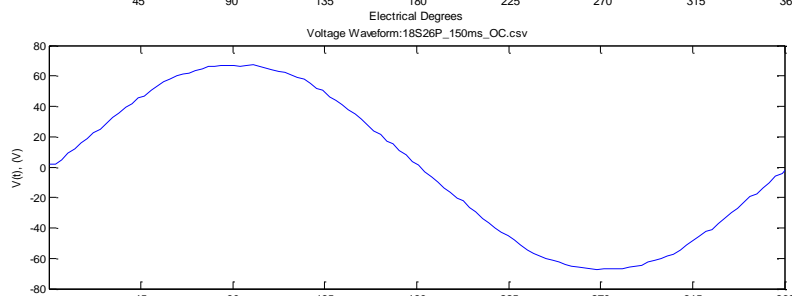
THD: 2.40%

18/24p
(SPP = 0.25)



THD: 6.37%

18/26p
(SPP = 0.23)



THD: 2.61%

Figure 38: Induced EMF waveforms and spectral representation

4.3.2.1 Total Harmonic Distortion

The THD is measured as the number of poles increased for the machine variants and is presented in Figure 39.

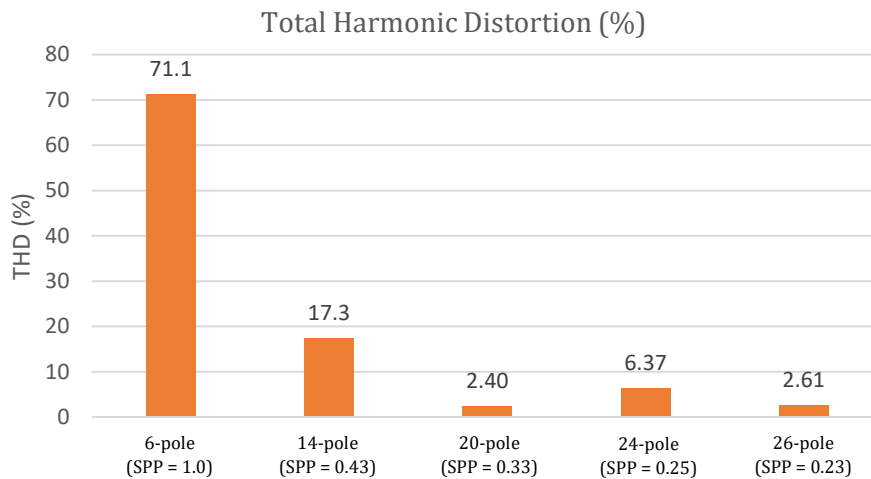


Figure 39: Summary of the THD measurements

The general trend shows that the total harmonic distortion decreases as the number of poles increases. The downward trend may be a product of the reduced saturation caused by the decrease in flux density observed previously. The THD of the 24-pole machine is slightly larger than the machines with a similar number of poles, which is unexpected.

Another measure of distortion is the harmonic factor. The harmonic factor enables the comparison of the contribution of different harmonic frequencies to the overall distortion. The harmonic factor is the ratio of the harmonic amplitude and the fundamental amplitude calculated as:

$$HF_n = \frac{V_n}{V_1}$$

Where V_1 is the voltage of the fundamental harmonic and V_n is the voltage of the n^{th} harmonic. The harmonic factors for the third, fifth, and seventh harmonic are shown in Figure 40.

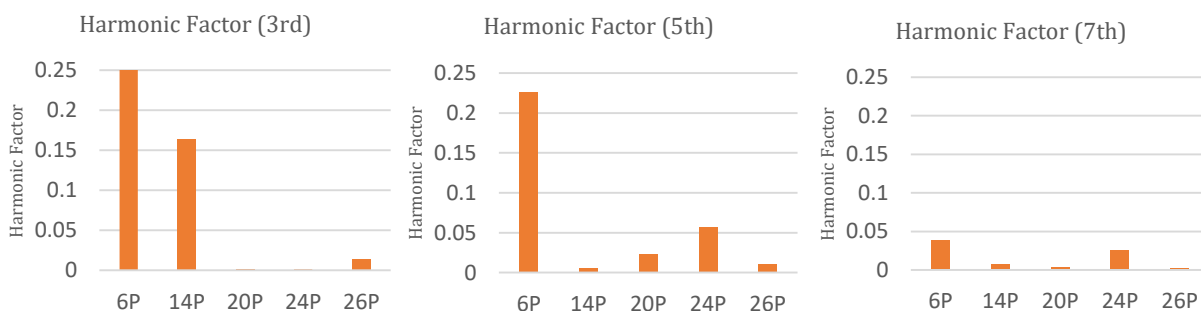


Figure 40: Harmonic factors for the third, fifth, and seventh harmonics

This shows that the third harmonic contributed the most to the 6- and 14- pole machines, whereas the fifth harmonic is more prominent in the other machines.

4.3.2.2 Induced EMF Measurements

A summary of the peak and RMS measurements for the EMF is shown in Figure 41. As the number of poles increases the voltage increases to a maximum at the 24-pole machine, and then begins to reduce. The difference in peak voltages from the 14-pole machine to the 26-pole machine is slight.

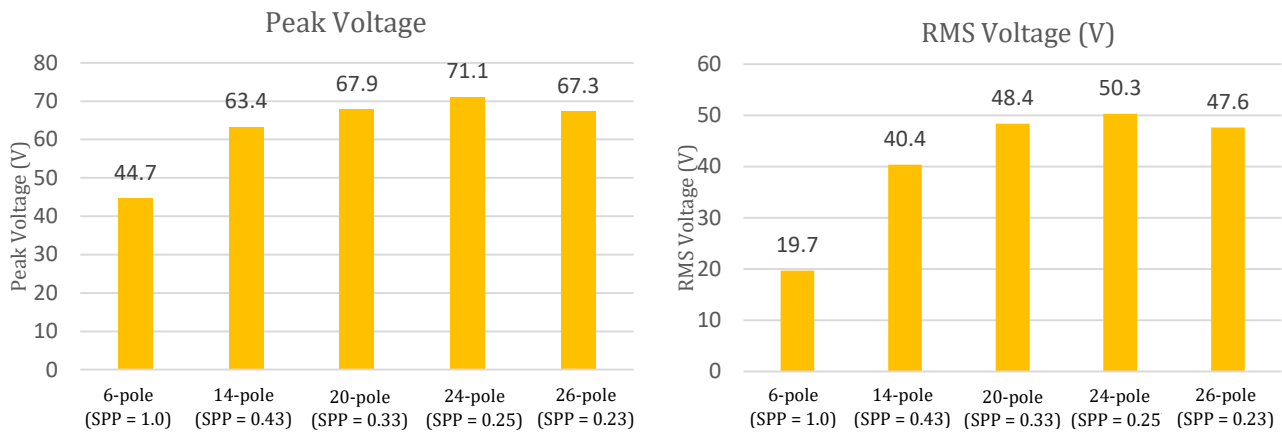


Figure 41: Summary of the peak and RMS voltages of the EMF in the open circuit tests

The RMS voltages show a similar trend as the peak voltage, however, the discrepancy between the 6- and 14- pole machines, and the other designs can be seen to increase slightly. The high distortion present in the lower pole number machines increases the crest factor of these waveforms, and so the effective RMS voltage is lower even though the peak voltage is high.

Crest factor is a measure of how extreme the peaks are in a waveform, and is calculated as the ratio of the peak and RMS values. A large crest factor indicates a high peak voltage with a low RMS value. A large crest factor is undesirable. The calculated crest factors for the open circuit tests are shown in Figure 42.

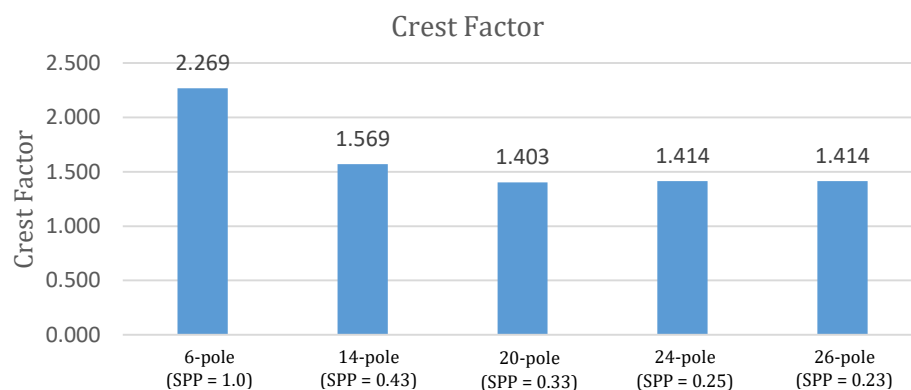


Figure 42: Calculated crest factors for the open circuit tests

The plot highlights the difference in the 6- and 14-pole machines waveforms, showing they have increased peak voltage, with lower RMS values. The crest factor plateaus as the number of poles increase. This is because the waveform becomes more sinusoidal with a greater number of poles.

4.3.3 Core Losses

The core losses of the machine are the combined losses from the hysteresis and eddy current losses. Hysteresis losses are caused by the magnetic hysteresis effect of the steel, which causes energy to be consumed as the magnetic flux changes polarity through the material. The eddy current losses are caused by the induced electrical currents in the machine iron. These induced currents dissipate energy as heat when circulating through the iron.

The core losses are measured to determine the impact of an increased number of poles. The core losses are related to the alternating flux frequency, and are expected to increase with a greater number of poles. The measured core losses are separated into eddy current loss, and hysteresis loss, and presented in Figure 43.

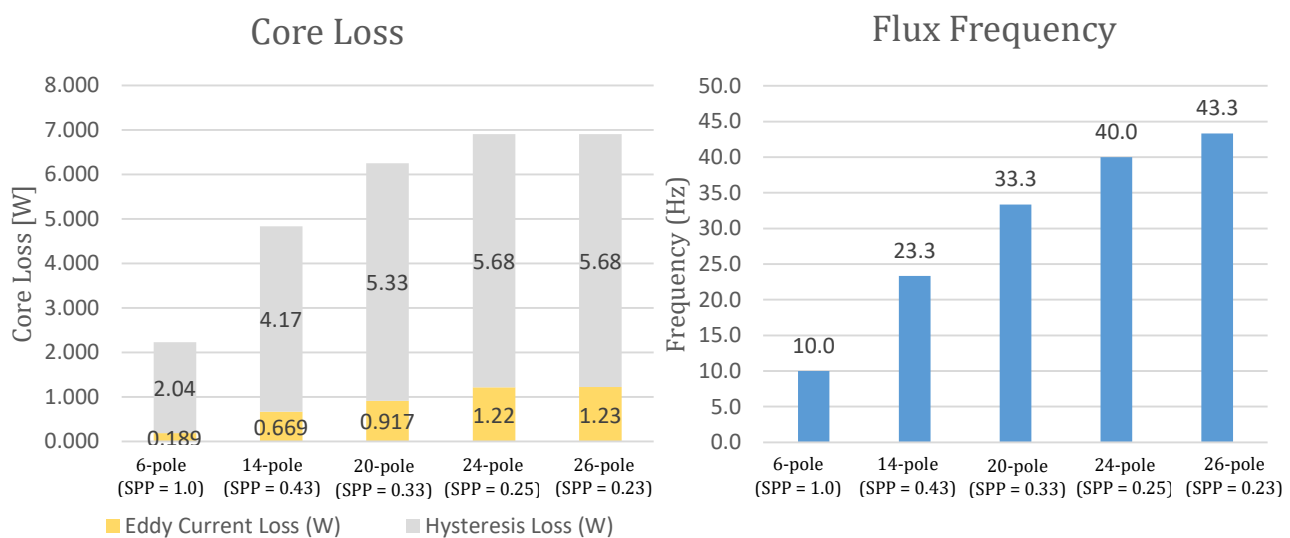


Figure 43: (left) Core losses with separated loss components (right) Alternating flux frequency

Figure 43 shows the core losses steadily rising with the increase in pole numbers. However, the loss seems to plateau towards the higher pole numbers, even as the frequency increases. This may be caused by the reduced flux density of the higher-pole systems. As the direct-drive design is rotating at such a low speed, the core losses are low, and are not expected to make a large contribution to any discrepancy of efficiency between the machines.

4.3.4 Summary of Open Circuit Analysis Findings

The open circuit tests measured the outputs of the machine under no electrical loading. The cogging torque, induced EMF, THD, and core losses are measured. The findings showed that:

- The cogging torque of the machines does not show a significant trend as the number of poles increase, but the magnitude can be approximately predicted using the combination of the pole and slot number, specifically, the lowest common multiple of the two numbers.
- The THD of the induced EMF generally decreases as the number of poles increases. The crest factor calculations indicate the waveforms tend to become more sinusoidal as the pole number increases. The EMF waveforms can be seen to become more sinusoidal.
- The core losses of the machines are low as the alternating flux frequency throughout the core steel is low. This is an advantage of direct-drive machines. The core losses increase with the number of poles.

4.4 Load Test – Three-Phase Operation

The next section of testing simulates the generators with a balanced three-phase resistive load. A three-phase resistive load would be similar to the use of a water heater or other heating element in a practical scenario. Wind turbines are commonly used to heat a tank of hot water for household use, or to heat a thermal mass for other general heating applications.

Inductive, capacitive, and combinations of these types of load are not considered. The turbine is not designed for applications which present these types of load, so the information is not considered necessary. Similarly, unbalanced loads are not considered. The basic setup block diagram is presented in Figure 44. The Simplorer setup diagram with a brief explanation of the system components can be found in Appendix J.

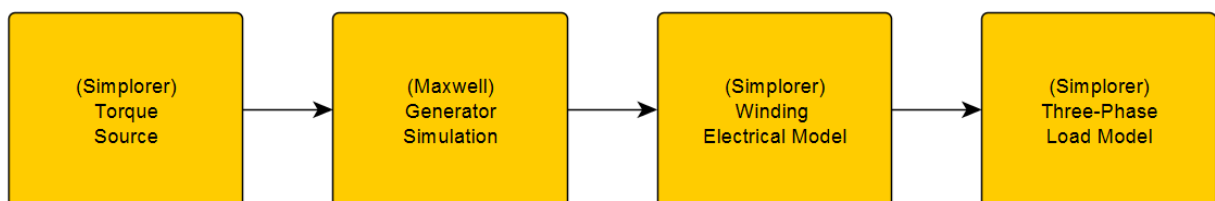


Figure 44: Simplorer simulation block diagram

4.4.1 Resistive Load

The velocity input defines the acceleration profile of the generator. If the velocity is changed from motionless to maximum speed with no time difference, the required torque is infinite. Simplorer prevents this from happening, although the simulation still requires a long time to stabilise a sudden change in velocity, resulting in high overshoot and long settling times. For this reason the ramp acceleration profile in Figure 45 is used to provide a response that reaches a steady state with minimum overshoot and a low settling time.

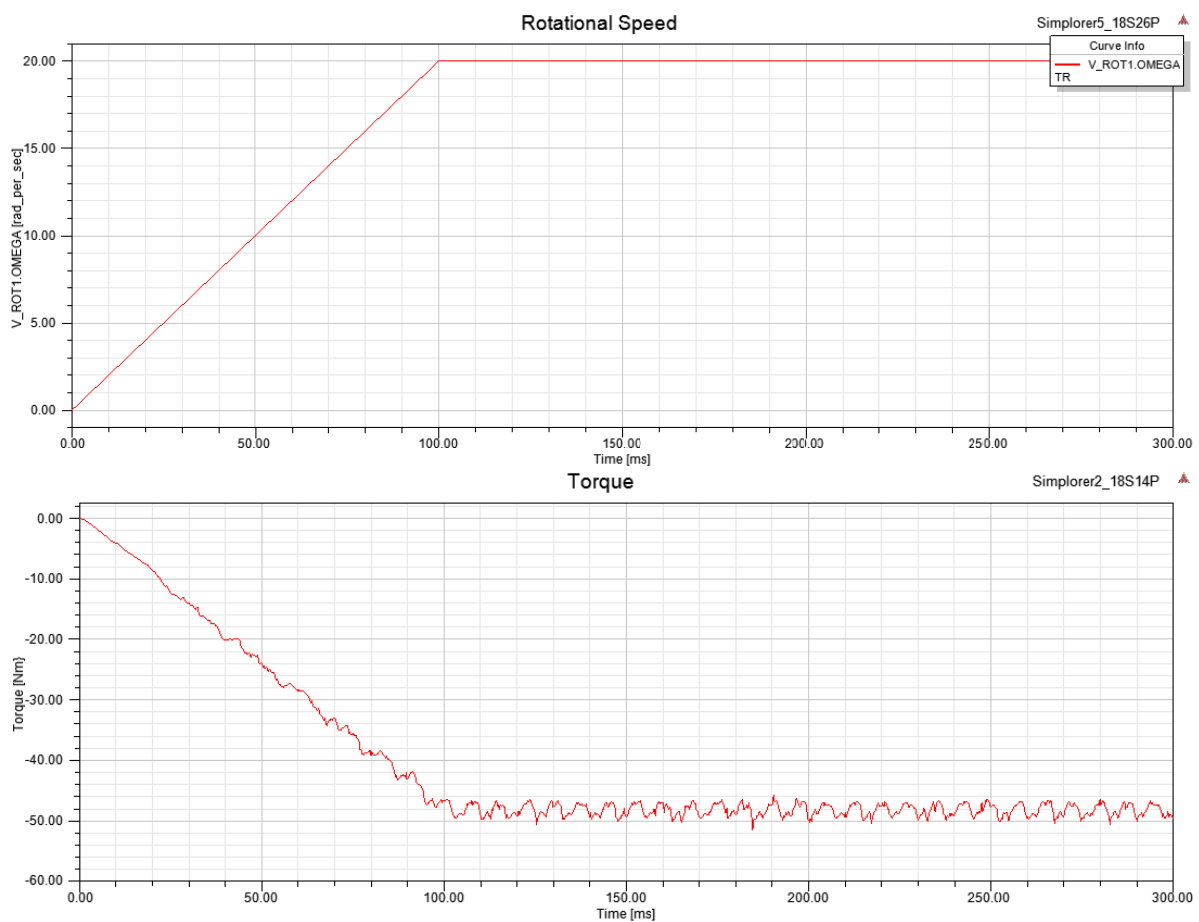


Figure 45: (top) Acceleration profile of the simulation (bottom) Torque curve generated with acceleration

The ramping time of 100ms was found to remove overshoot for all of the simulations.

The load resistance is set at 4Ω . Initial testing showed that most designs could provide 1kW at 200 rpm for this load. The 6-pole machine could not provide 1 kW as it was found to require extremely high speeds to operate effectively.

The main measurements taken are torque, load current, load voltage, electrical power, mechanical power, and efficiency. The total harmonic distortion is calculated from the load current waveforms.

4.4.1.1 Load Torque

The torque waveforms for each machine resemble the cogging torque plots presented previously. From Figure 46 it is seen that the 6- and 24-pole machines exhibit fewer transients compared to the other three machines.

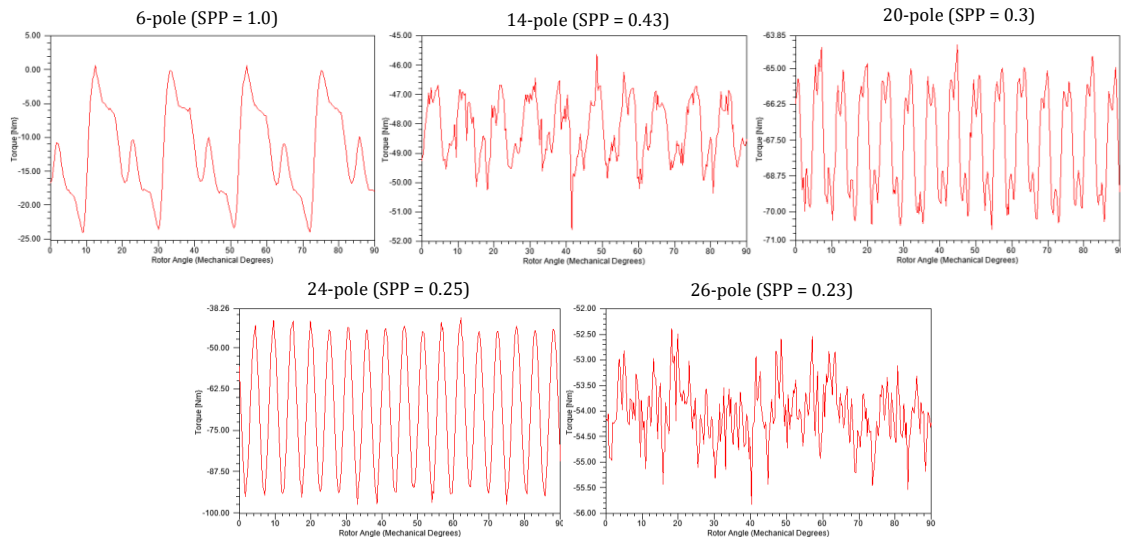


Figure 46: Torque plots for the three-phase resistive loads using individual y-axis scales

Figure 47 shows that the average torque increases to a maximum value for the 24-pole machine and then continues on a downward trend. The comparison between the torque ripple and the cogging torque shows that the 26-pole machine has the lowest value of torque ripple, and also the lowest discrepancy between torque ripple and cogging torque.

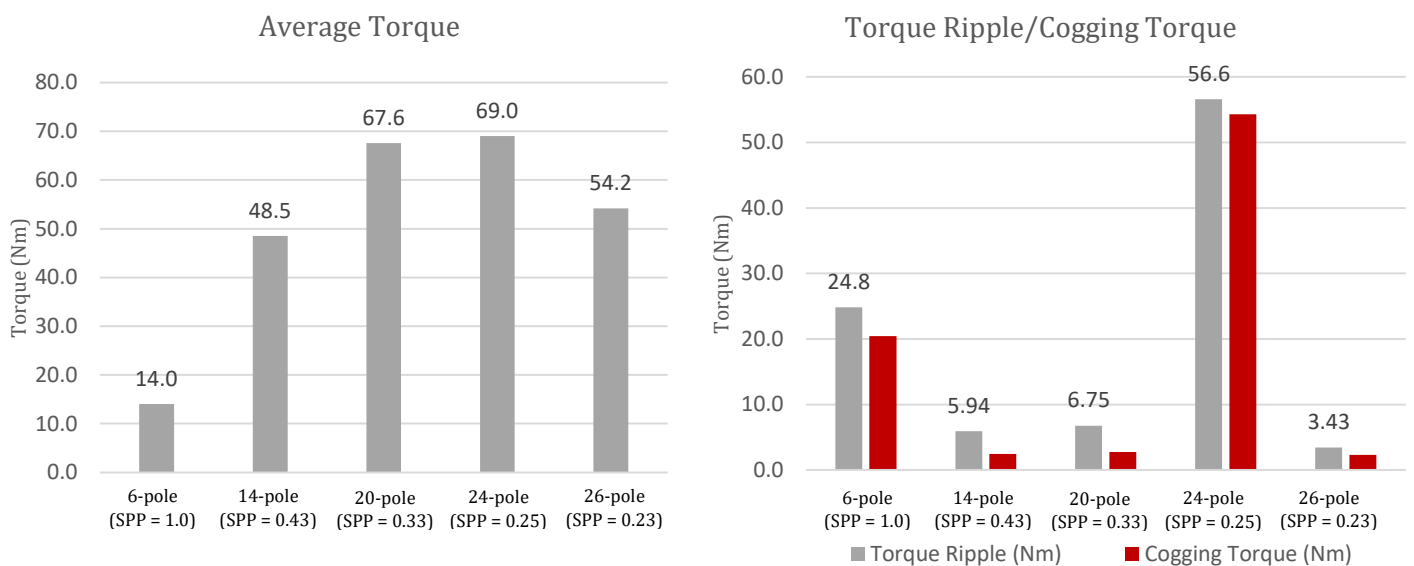


Figure 47: (left) Average torque measurements (right) Comparison between torque ripple and cogging torque

4.4.1.2 Load Voltage/Current

The load voltage and load current are measured for the three-phase resistive load. The measurements and captured waveforms are based on a single phase of the output. As the load is purely resistive, the current and voltage waveforms are identical in shape and differ only in magnitude. Therefore, only the current waveforms are presented in Figure 52.

The RMS voltage and current measurements are presented later in Figure 48. The same parabolic increasing and decreasing trend is observed.

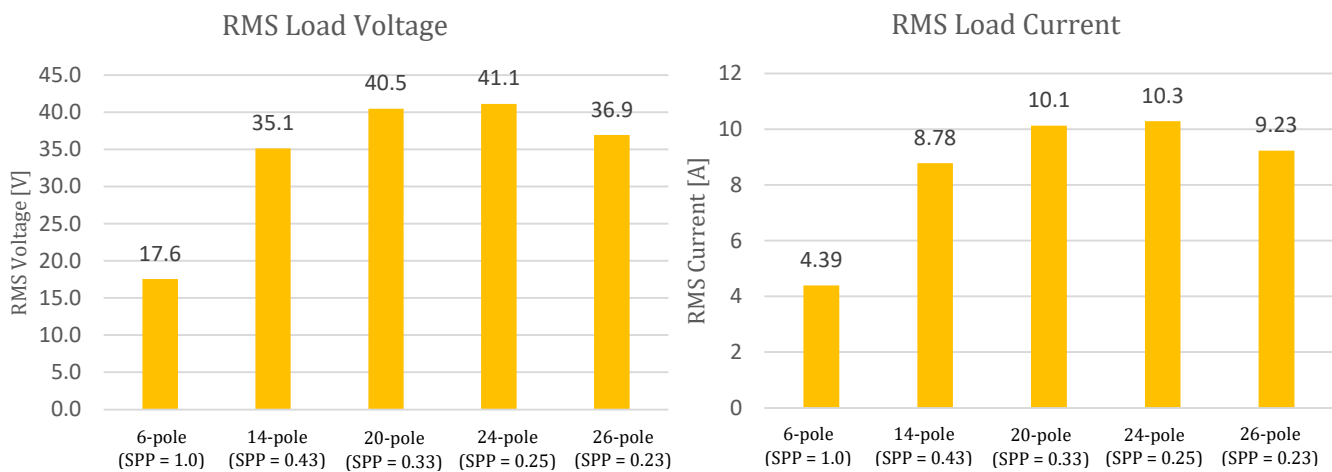


Figure 48: RMS voltage and current measurements from one phase

The crest factor is calculated and presented in Figure 49 to compare the loaded and unloaded results. The loaded crest factor behaves similarly to open circuit operation, however the 14- and 20-pole machines have slightly lower factors.

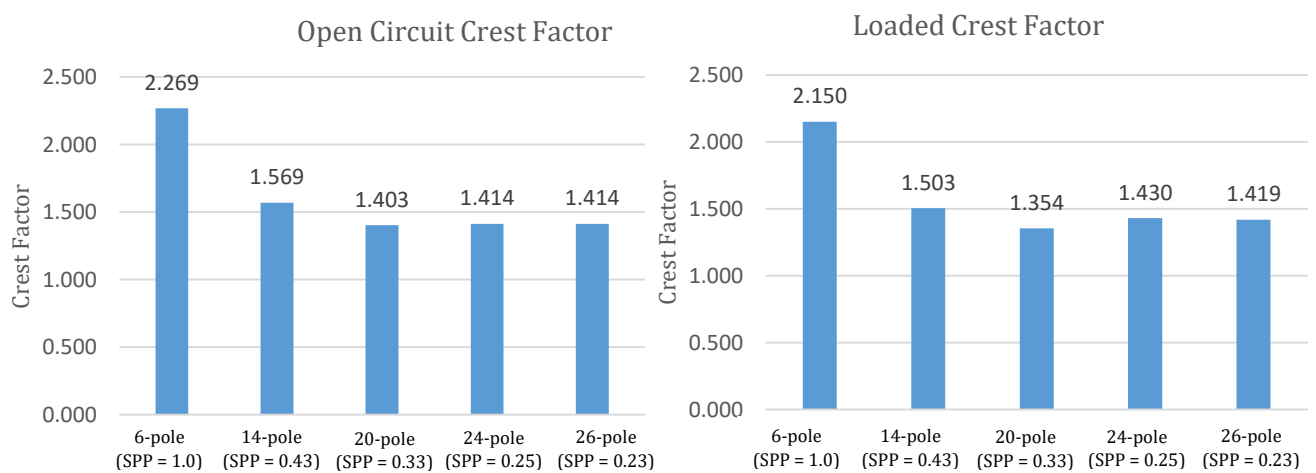


Figure 49: (left) Open circuit crest factors (right) Loaded crest factors

4.4.1.3 THD

The total harmonic distortion of the machines is calculated during the load test. The THD is calculated from one phase using the current waveform through the load. The current waveforms are presented in Figure 52. As the load is purely resistive, the load current is identical to the source current, so the result reflects the THD in the source and the load. The THD is presented in Figure 50.

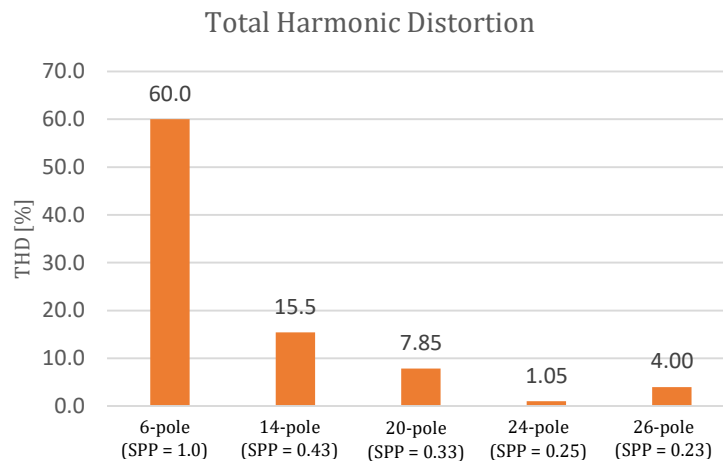


Figure 50: Summary of THD values calculated for the source current waveform

The load has a varied effect on the source THD for the different machines. The 6-, 14-, and 24-pole machines experience a reduction in THD, while the 20-, and 24-pole machines experience an increase. Most notably, the 24-pole machine exhibits a much lower THD as compared to the open circuit tests, and the current waveform is seen to be much more sinusoidal. The harmonic factors of the waveform are calculated for the 3rd, 5th, and 7th harmonics. The results are presented in Figure 51. The harmonic factors show that a majority of the distortion is as a result of the third harmonic.

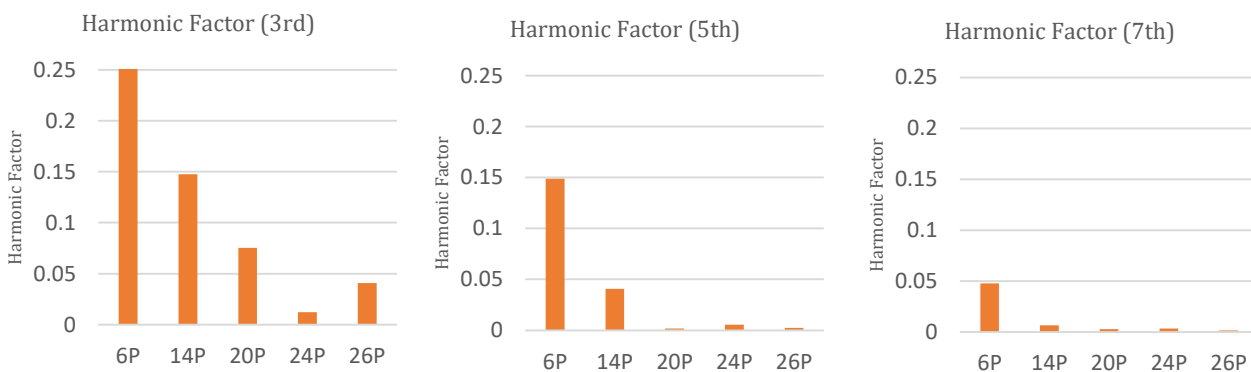
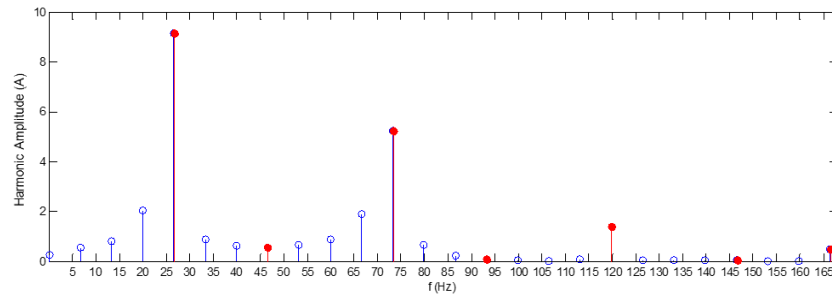
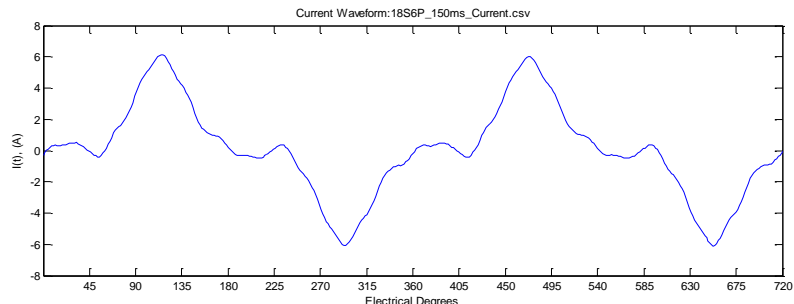


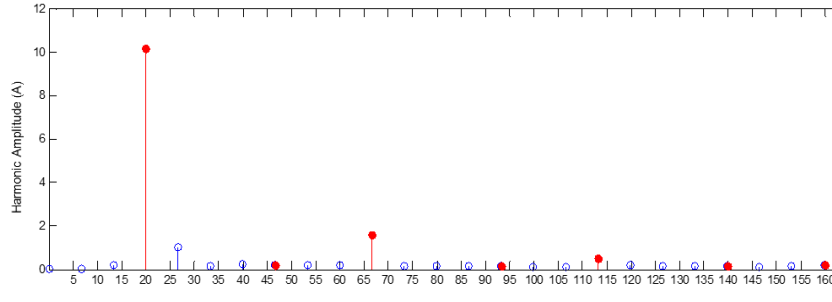
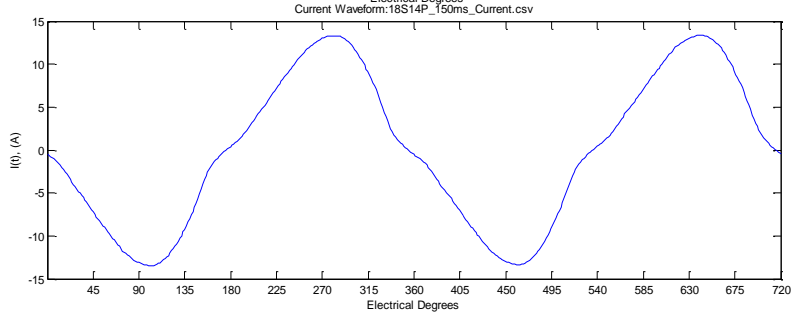
Figure 51: Harmonic factor for the 3rd, 5th, and 7th harmonics

18/6
(SPP = 1.0)



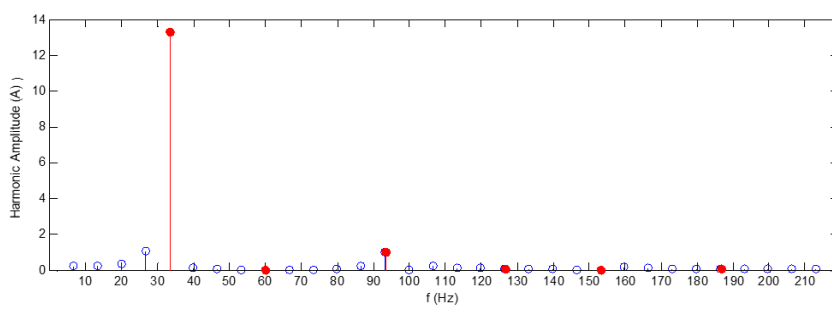
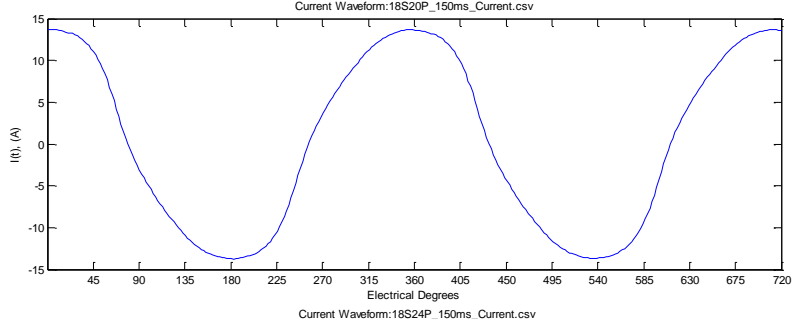
THD: 60.0%

18/14
(SPP = 0.43)



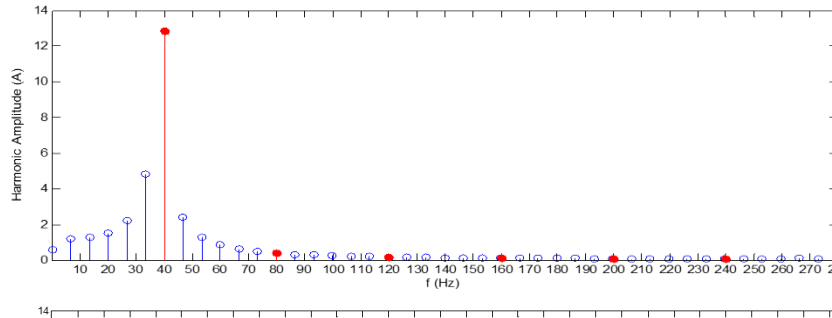
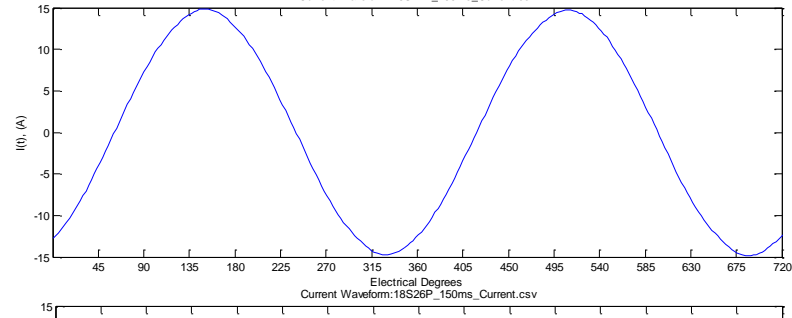
THD: 15.5%

18/20
(SPP = 0.3)



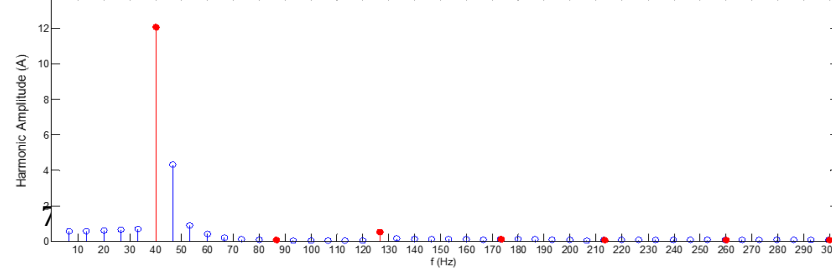
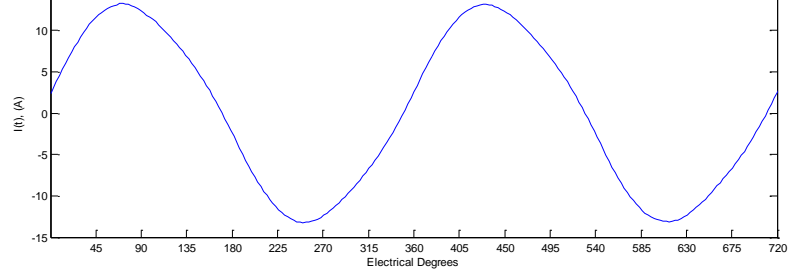
THD: 7.85%

18/24
(SPP = 0.25)



THD: 1.05%

18/26
(SPP = 0.23)



THD: 4.00%

71

Figure 52: Current waveforms and spectral plots for the purely resistive load

4.4.1.4 Electrical Load Power

The electrical power generated by each of the machines is displayed in Figure 53. The power ripple generally decreases as the number of poles increases, however, the waveforms become more irregular. The plots use uniform y-axis divisions with the exception of the 6-pole machine due to the large ripple content.

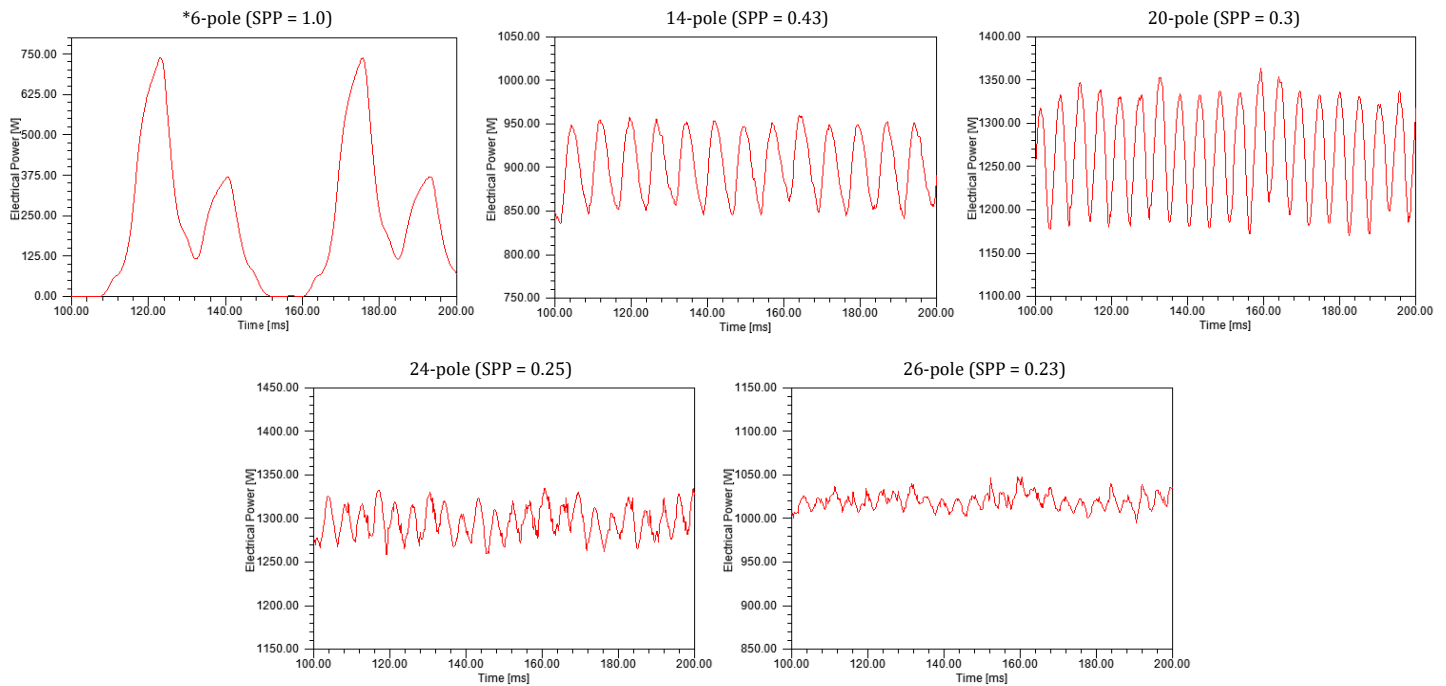


Figure 53: Measured electrical power dissipated in the load (*Note: 6-pole machine is a different scale)

Figure 54 shows the average load power, and the percentage power ripple. The percentage ripple is calculated using the peak-to-peak ripple and the average load power. The average load power rises to a peak and falls as the poles increase, and the electrical power ripple exhibits a decreasing trend as the pole number increases.

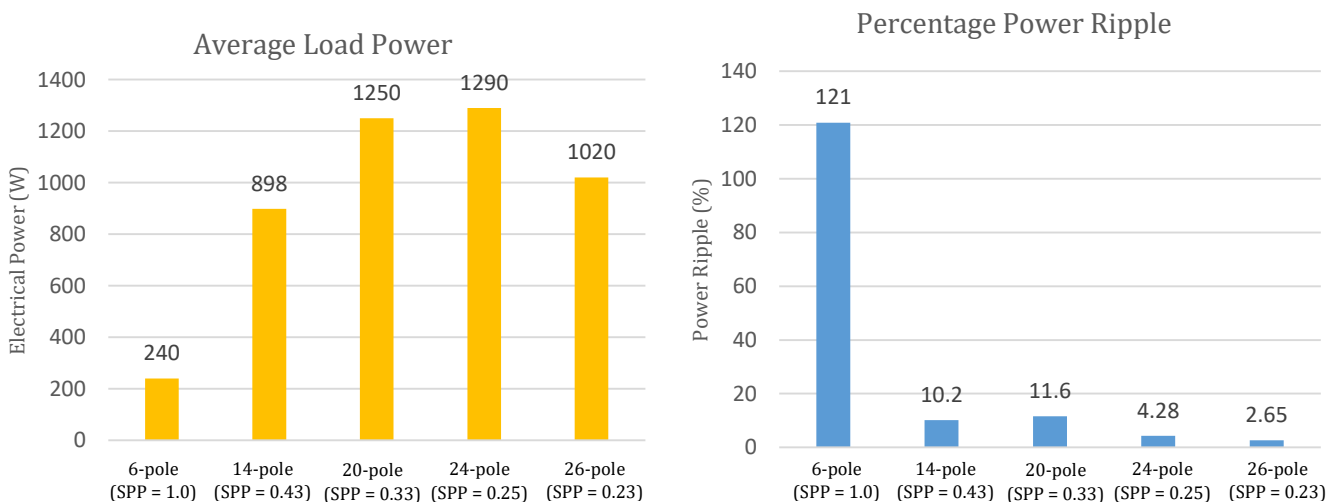


Figure 54: (left) Average load power (right) peak-to-peak ripple in the power waveform

4.4.1.5 Mechanical Power

The mechanical power supplied to the machines is presented in Figure 55. The graphs use a uniform value for the divisions. The comparison between the waveforms show that the 6- and 24-pole machines have very high ripple waveforms. This is due to the high value of torque ripple in these machines.

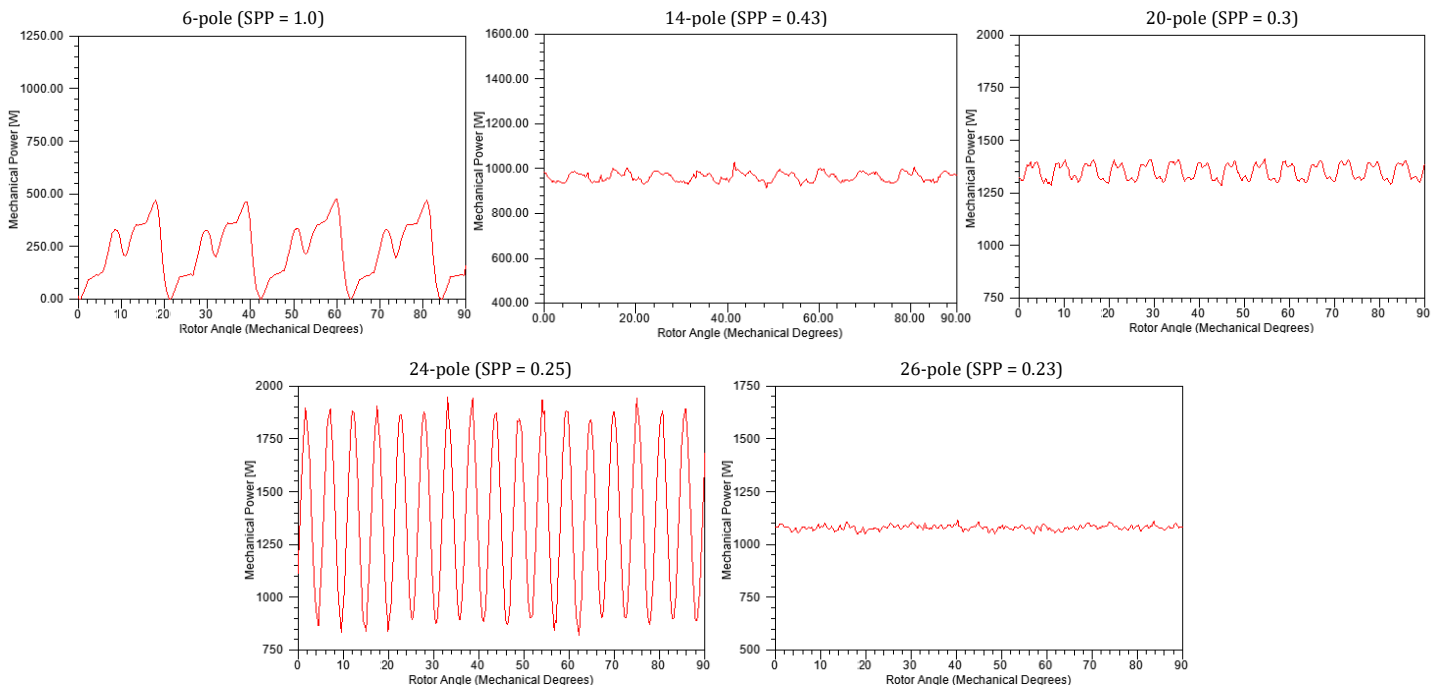


Figure 55: Measured mechanical power supplied to the machine

The average mechanical power in Figure 56 shows a similar increasing then decreasing trend observed previously. The ripple observed in the supplied mechanical power waveforms are correlated with the torque ripple values.

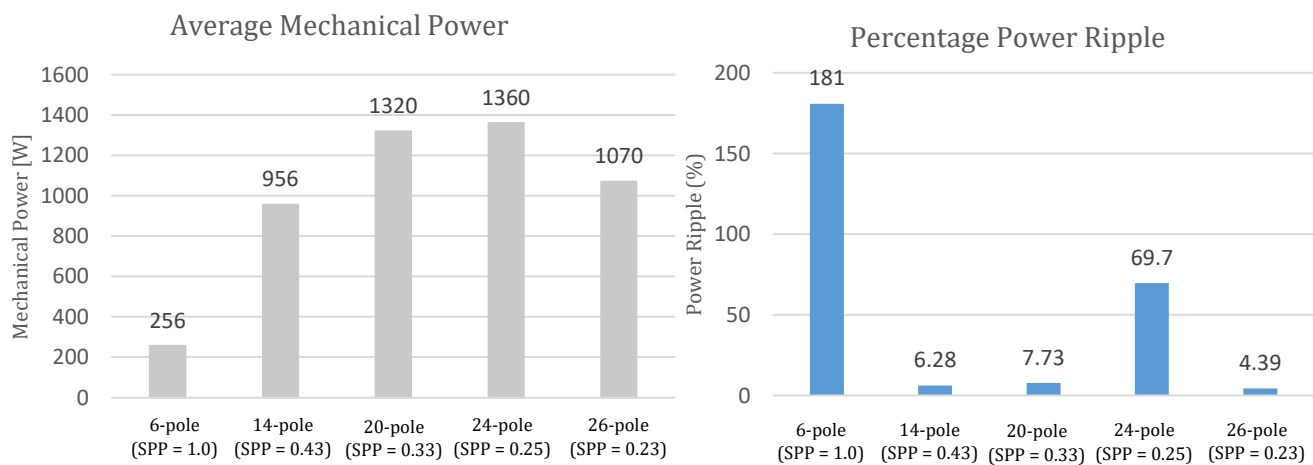


Figure 56: (left) Average mechanical power supplied (right) Percentage mechanical power ripple

4.4.1.6 Efficiency

The efficiency is calculated using the integration of the electrical power dissipated in the load and the integration of the mechanical power supplied to the machine. This results in the ratio between the total mechanical energy and the electrical energy dissipated in the load.

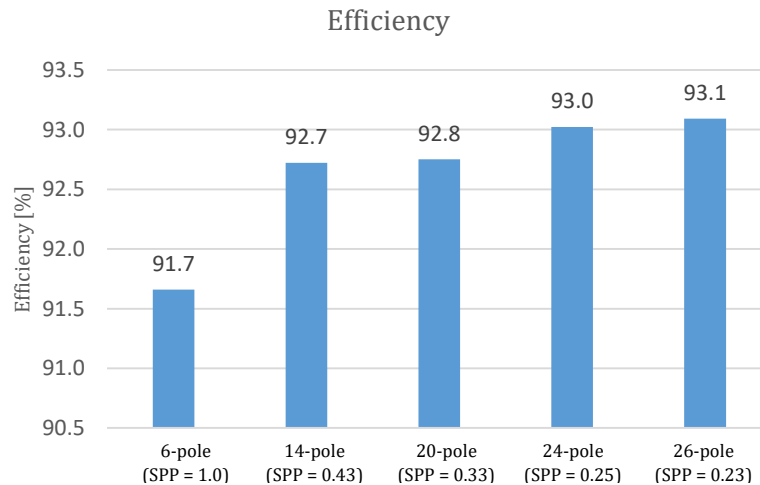


Figure 57: Calculated efficiency of the machines

Figure 57 shows that the efficiency of the machines slightly increases as the number of poles increase, despite the greater core losses.

4.4.1.7 Voltage Regulation

The voltage regulation of the machines is a measure of the difference between no-load voltage and the voltage measured over the rated load. That is, the percentage difference between the induced EMF under open circuit conditions, compared to the voltage measured under fully loaded conditions. The graph for voltage regulation is shown in Figure 58.

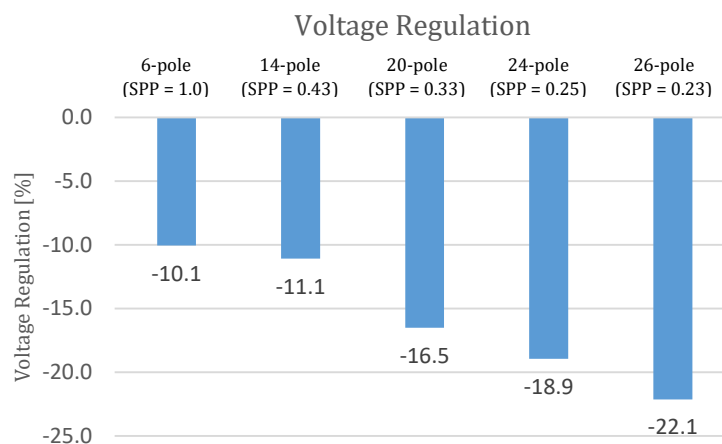


Figure 58: Voltage regulation as the load is increased

For an identical rated load of 4Ω the voltage regulation performance of the machines decreases as the number of poles increases. The lower pole machines are shown to be more effective at regulating their voltage at the rated load.

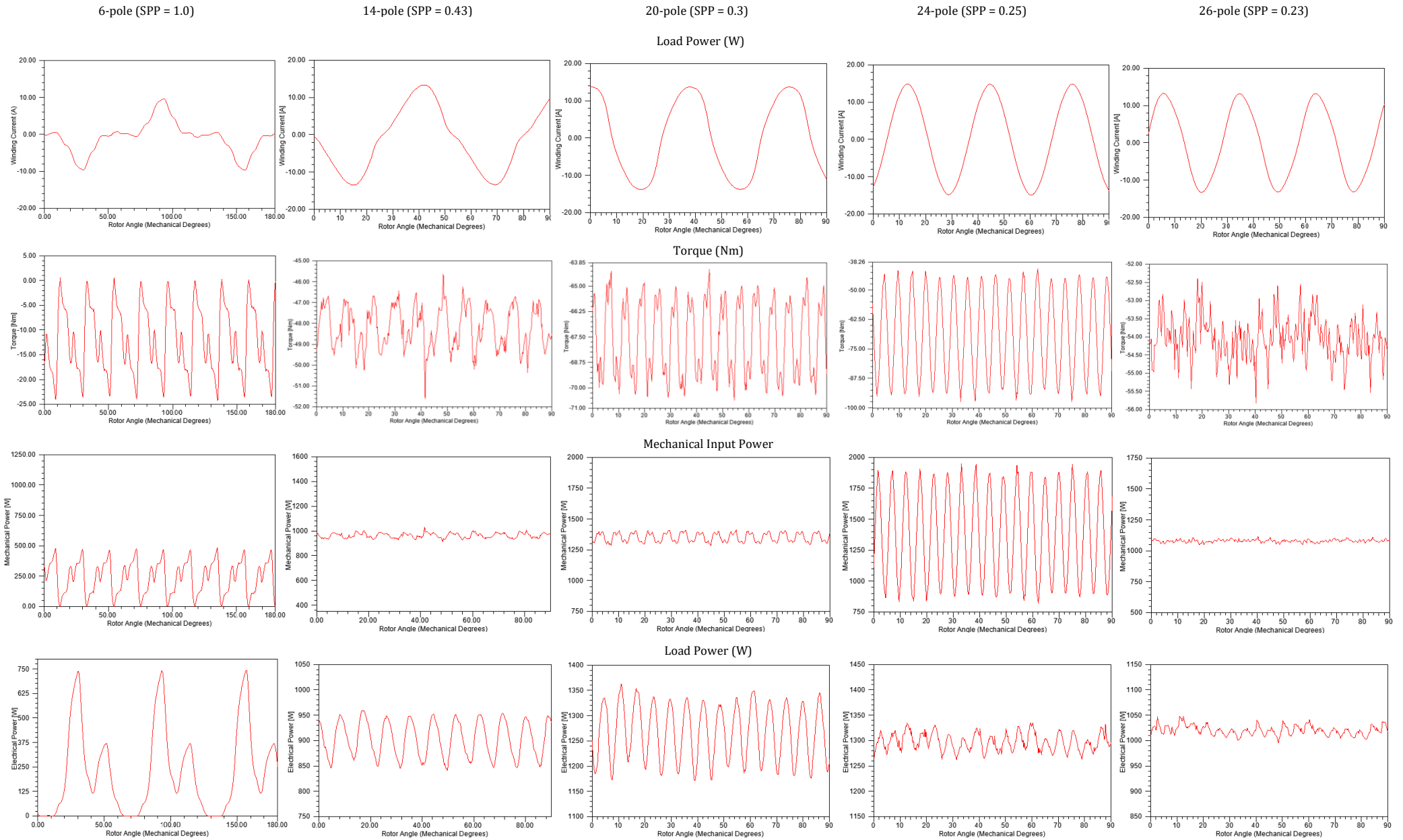


Figure 59: Summary of graphs for the three-phase load test

4.4.2 Variable Resistance Load

The next set of tests uses the same circuit setup as before. The load resistance in this setup is used as the independent variable and is swept from 0.25Ω to 15Ω in increments of 0.5Ω . The measured values of the generator are the electrical power, peak voltage, and efficiency. The results of this test are used to give a better idea as to the optimal working point of the generators with regard to electrical loading, and the effect of the number of poles on the machine outputs.

The 6-pole generator has consistently been achieving poor results indicating the design is not suitable for this working configuration and is therefore excluded from analysis. It is included in the plots for completeness.

4.4.2.1 Output RMS Voltage

The RMS voltage of the generated output waveforms is measured for the sweep of load resistances. The results are shown in Figure 60.

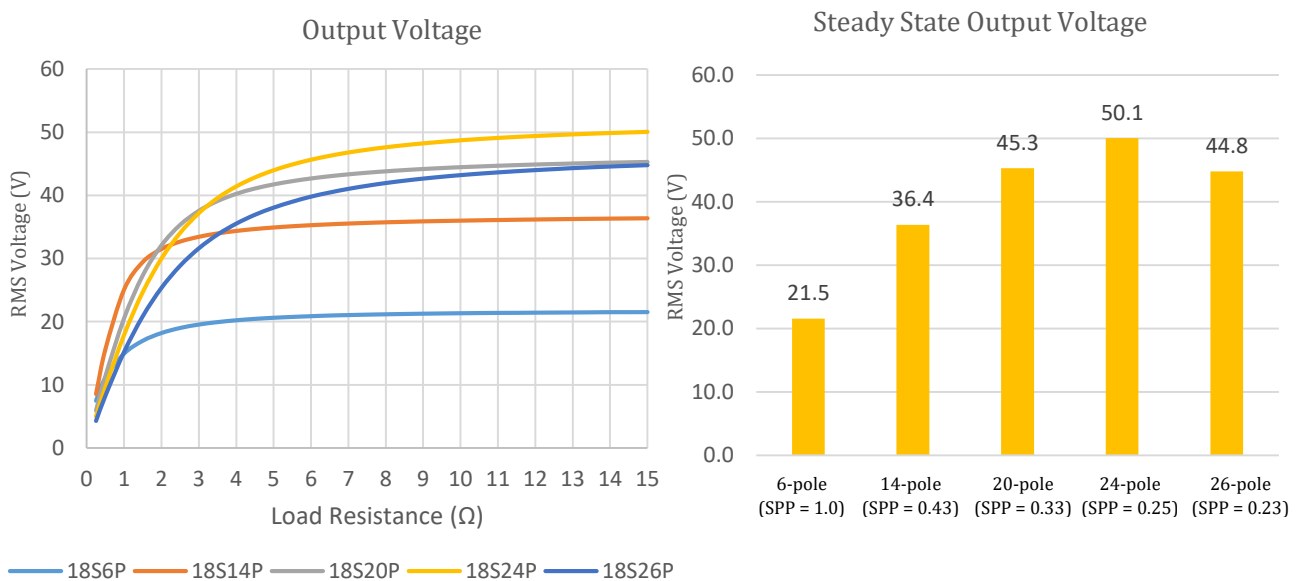


Figure 60: Plot of the RMS values of the output from the machines as the load is varied

The voltages tended to reach a steady state as the load decreased. The 14-pole machine generated the highest voltages at the highest loading, but had a very low steady state value. The 24-pole machine had lower voltages at high loading, but exhibited the highest steady-state voltage. The trends in the steady-state measurements are similar to those obtained in the open-circuit tests. It is important to note that an increasing load resistance results in a decreasing electrical load, and the highest loading point uses a load resistance of 0.25Ω .

4.4.2.2 Load Power

The load power curves in Figure 61 display the response of the generator to decreasing load.

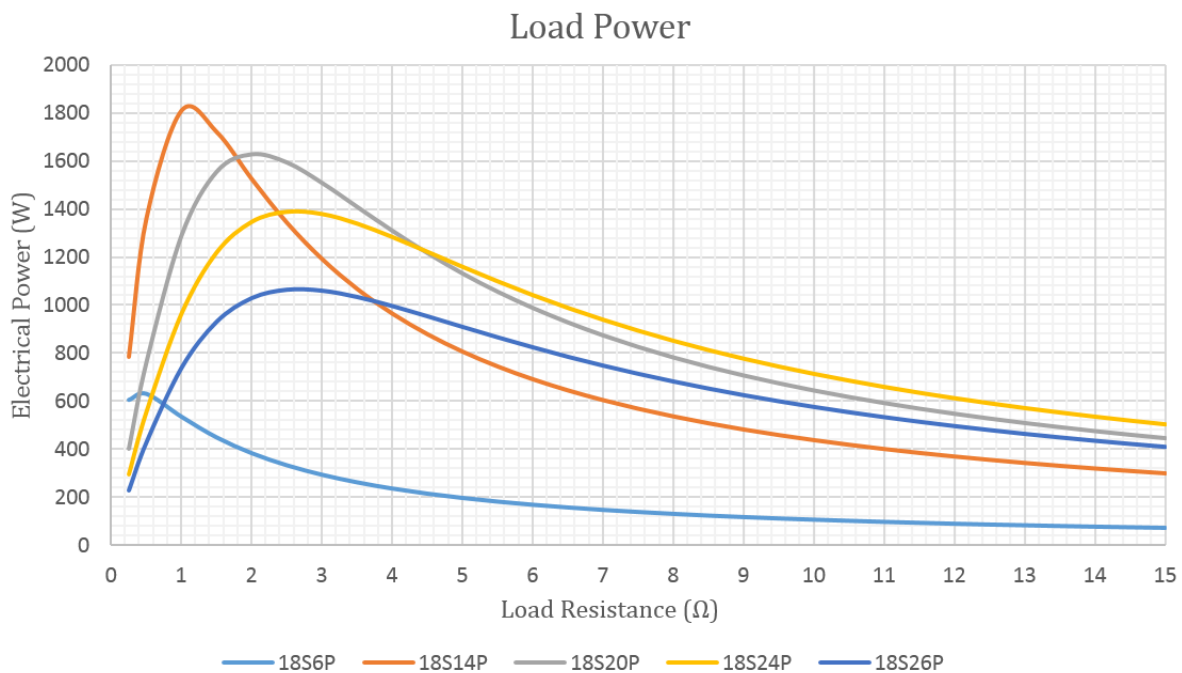


Figure 61: Load power plot for the three-phase variable load test

The maximum load power is generated by the 14-pole generator at approximately 1.8 kW, shown in Figure 62. However, as the load decreases, the power output decreases sharply. This shows that the machine has a very narrow operating point, and may not be as flexible in usage as the other generators. The 24-pole machine shows the most uniform power output as the load changes.

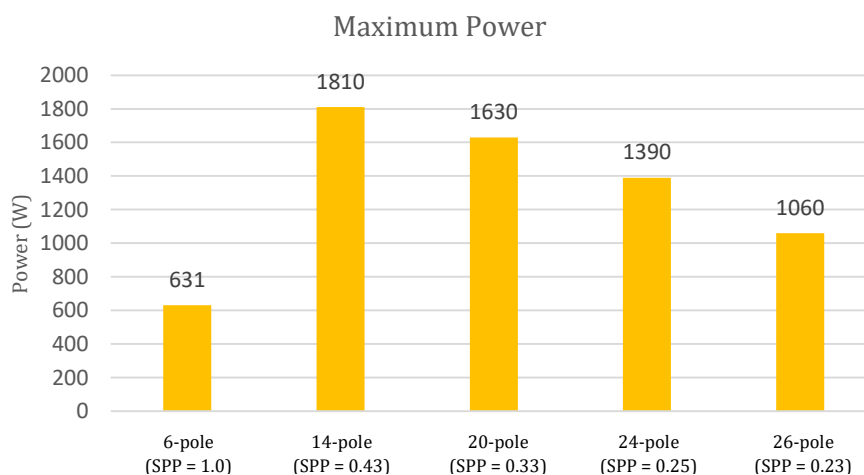


Figure 62: Maximum power outputs over the load range at rated speed

4.4.2.3 Efficiency

The efficiency curves in Figure 63 show that most of the machines experience the same changes in efficiency as the load is increased. The only irregular waveform is the 6-pole machine, which exhibits a significantly reduced efficiency. The efficiency calculation does not take into consideration windage or frictional losses, and is based on the mechanical rotational power and the electrical power dissipated in the load as measured during the simulation.

The efficiency is seen to asymptotically rise to 100%. As the load resistance is increased the electrical power output is decreased, however, the required mechanical power is also decreased. As there are no frictional losses taken into account for these measurements, the efficiency increases towards 100%. If frictional losses are taken into account the mechanical power required would tend to a constant value as the electrical load is increased, and thus the efficiency would tend to zero. This would be the case in a practical scenario. As it stands, the efficiencies close to 100% correspond to a power output of a Watt to sub-Watt value.

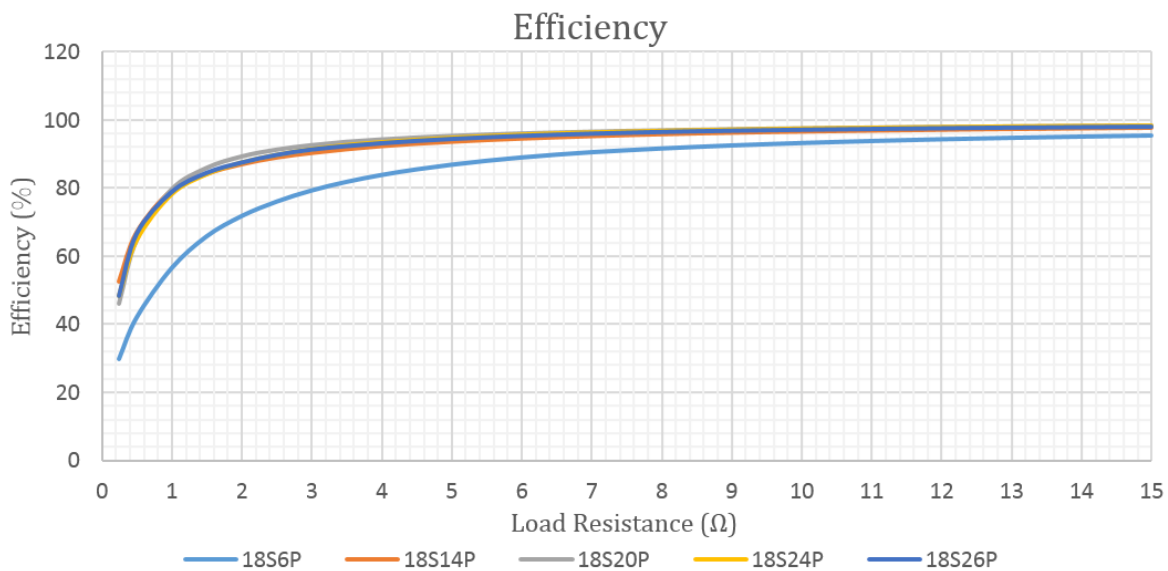


Figure 63: Efficiency curves for the machine variants using a variable resistance load

4.4.3 Variable Speed Analysis

The final set of testing for the three-phase load circuit is a variable speed test. In this configuration the circuit setup is kept the same, with the load resistance set at 4Ω . The rotational speed is swept from 20 rpm to 600 rpm with increments of 20 rpm. With a rated speed of 200 rpm, the working speed would typically be from 100 rpm to 400 rpm. The speed is varied up to 600 rpm to determine if the different machines may be working more effectively at higher speeds. Similarly to the previous tests, the analysis of the results generally exclude the 6-pole machine due to irregular simulation performance. The plots include the 6-pole machine simulations for completeness.

4.4.3.1 Torque Characteristics

The torque characteristics in Figure 64 show the results from the variable speed tests. The 14-pole machine has low torque at low-load operation, however, has the highest maximum torque. This is a similar conclusion that was drawn from the variable load tests. The maximum torque for each machine decreases as the number of poles increases.

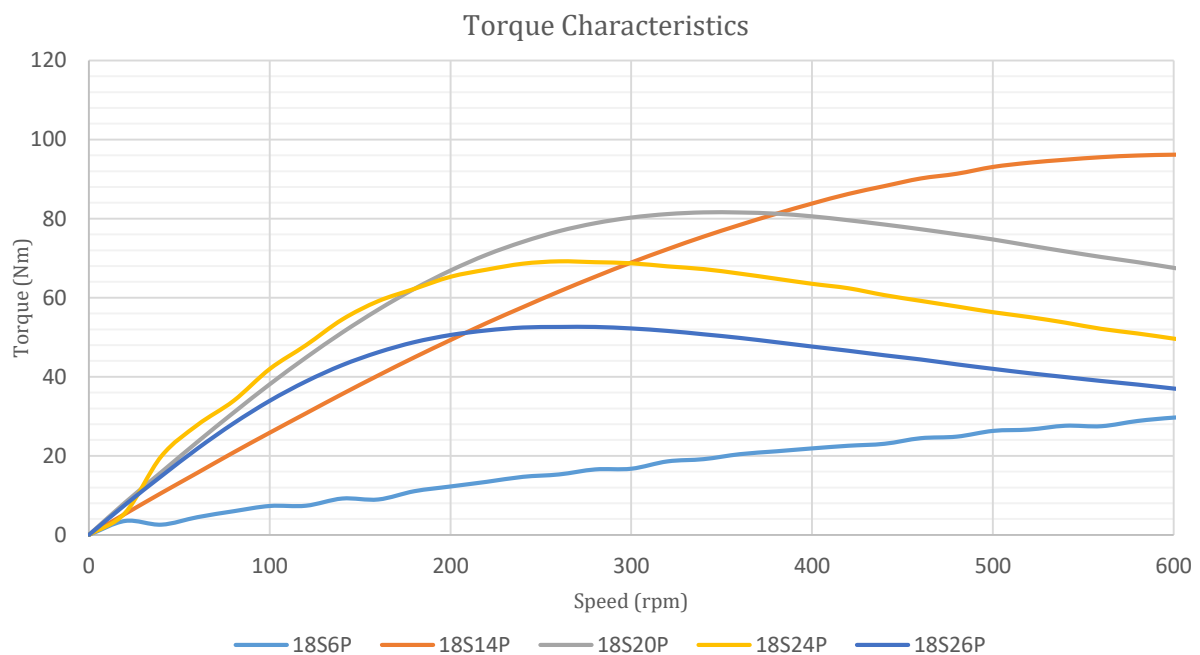


Figure 64: Torque curves for the machine variants from the variable speed test

4.4.3.2 Output RMS Voltage

The RMS voltage plot in Figure 65 shows that the induced EMF at low speeds (below 300 rpm) is of similar magnitudes across all machine designs. The difference in RMS values becomes more pronounced as the speed tends to higher values. At high speeds there is a clear trend that shows that the load voltage decreases as the number of poles increases. The graph displays considerable fluctuations as the speed increases. The cause of this is unknown, and may be due to the simulation's internal RMS calculation. The other measured curves display little or no fluctuation.

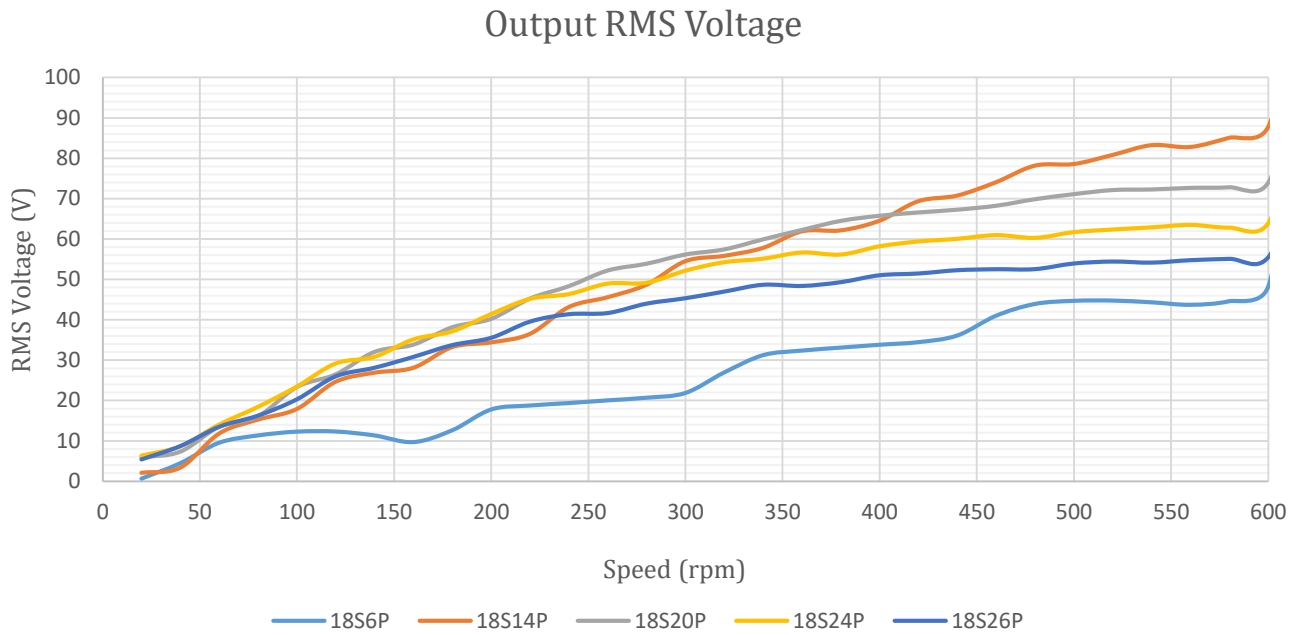


Figure 65: RMS voltage values for the machine variants from the variable speed test

The load voltage at 200 rpm and 600 rpm is shown in Figure 66. This plot shows how the load voltage across machines changes shape from the rated speed to high speeds. At higher speeds the lower pole machines are seen to work more effectively.

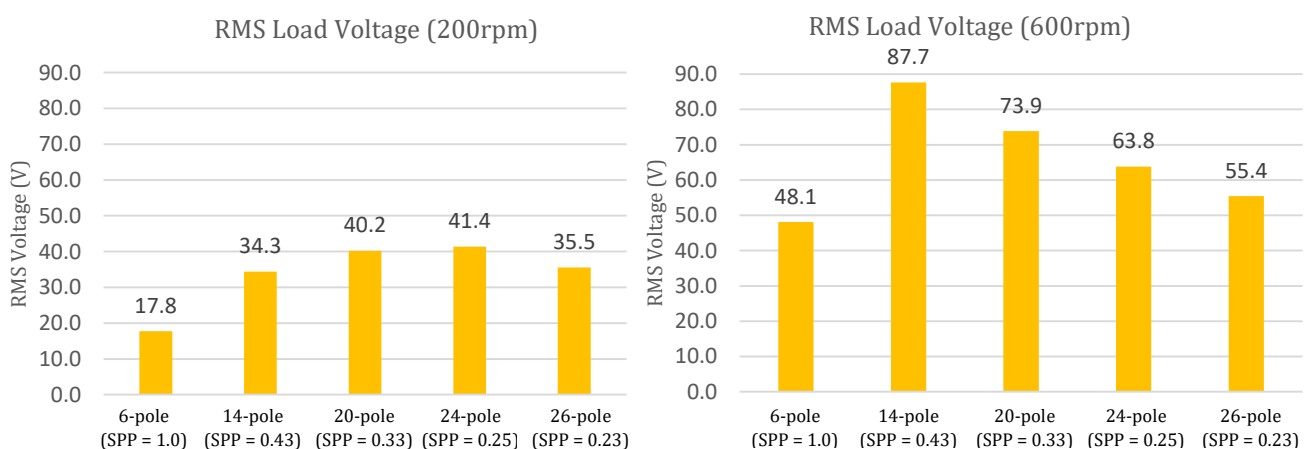


Figure 66: Measured RMS load voltage at different speeds

4.4.3.3 Load Power

The electrical power generated from the machines shown in Figure 67 followed a similar pattern to the results of the variable load tests. The 14-pole machine exhibits the highest maximum power output at the highest loading, however, it has reduced performance at lower loading. This is problematic for direct-drive generators operating from 100-400 rpm.

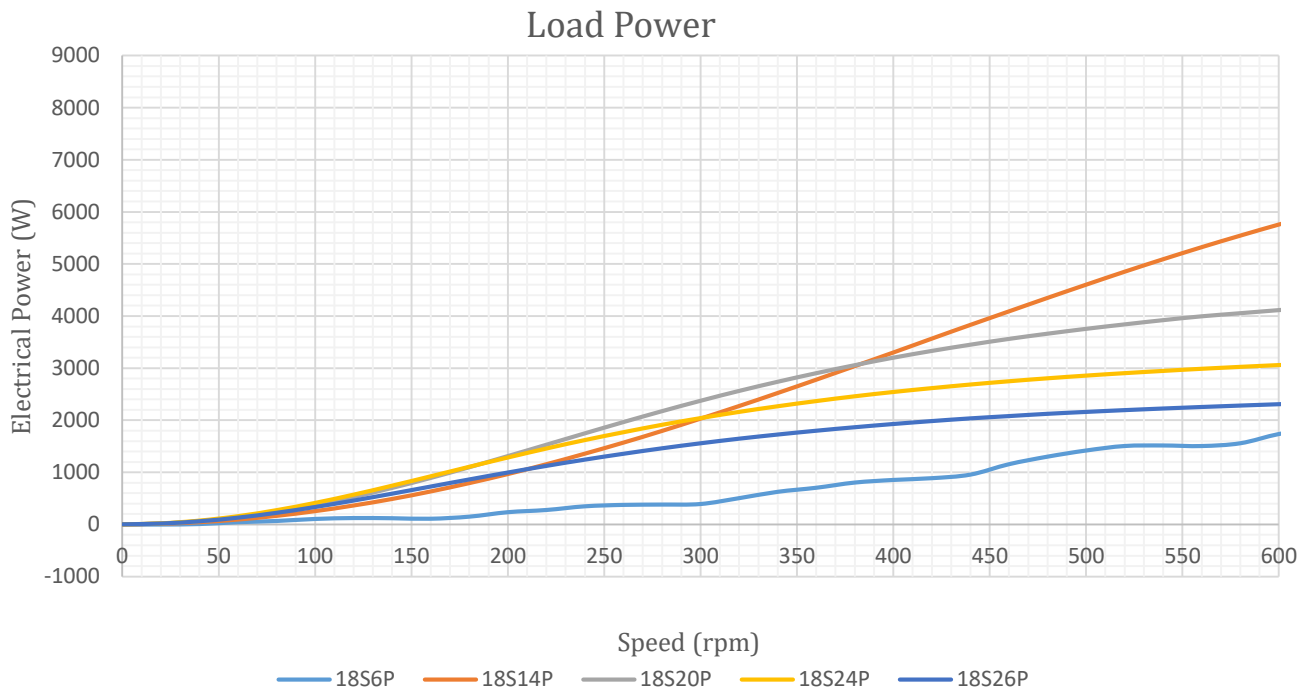


Figure 67: Electrical power measurements for the machine variants from the variable speed test

For a wind turbine that is frequently changing speeds, it is desirable to supply rated power at the lowest speed possible. The 20- and 24-pole machines supply 1kW at 170 rpm, while the 14- and 26-pole machines supply 1kW at ≈ 200 rpm. The advantage of the 14-pole machine is its high maximum output power. The differences between power output at rated speed and maximum speed shown in Figure 68 mirror the trends observed for the RMS values presented in Figure 66.

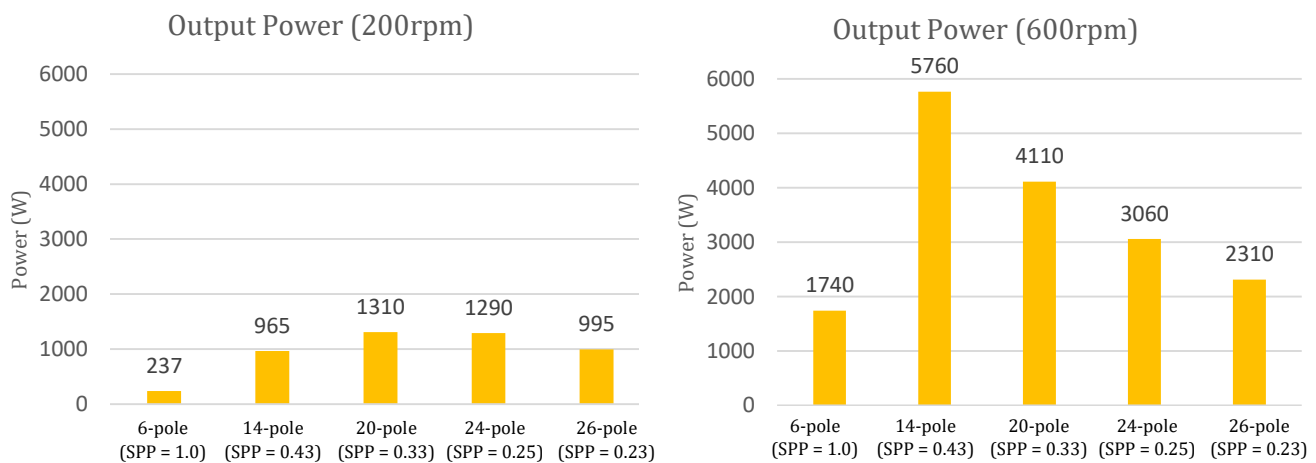


Figure 68: Output power for 200 rpm and 600 rpm

4.4.4 Summary of Three-Phase Load Analysis Findings

The proposed machine designs were simulated with a three-phase resistive load. The simulations were performed in three main sections: rated load at rated speed, rated load at variable speed, and variable load at rated speed. The findings showed that:

- The output voltage, current, and power at rated speed all exhibit the same parabolic trend with the value reaching a maximum for the 24-pole machine and slightly decreasing for the 26-pole machine.
- The lower pole machines work more effectively at higher mechanical and electrical loads, and have higher maximum outputs. However, they work significantly less effectively at low load.
- The efficiency slightly increases as the number of poles increases, despite the increased core losses.
- The voltage regulation capability of the machines decreases as the number of poles increases.
- The 6-pole machine does not work effectively for the rated speed of 200 rpm, and only begins to present marginally acceptable outputs at 600 rpm.

4.5 Load Test – DC Operation

The next type of circuit setup used is the three-phase rectifier setup. The modelled rectifier is used to convert the three-phase AC to DC voltage. The rectifier may cause irregularities by inducing stator current harmonics.

The first test uses a resistive load after the rectifier. This is to simulate a single-phase heating element, incandescent lights, or other resistive loads that may require DC input. The simplified simulation block diagram is shown in Figure 69.

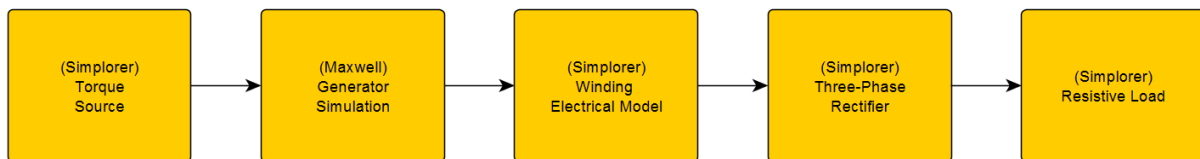


Figure 69: Simulation block diagram using a three-phase rectifier and a resistive load

The three-phase rectifier is a simple uncontrolled rectifier using 6 ideal diodes in a full-wave bridge configuration. This is used due to its simplicity and effectiveness.

The 6-pole machine did not work effectively for the loading conditions and is generally excluded from analysis, however, the graphs include the output for completeness.

4.5.1 Resistive Load

4.5.1.1 Load Torque

The torque waveforms for each machine are presented in Figure 70. Most of the waveforms exhibit reduced transients as compared to the three-phase operation. However, it is important to note that the ripple torque has increased.

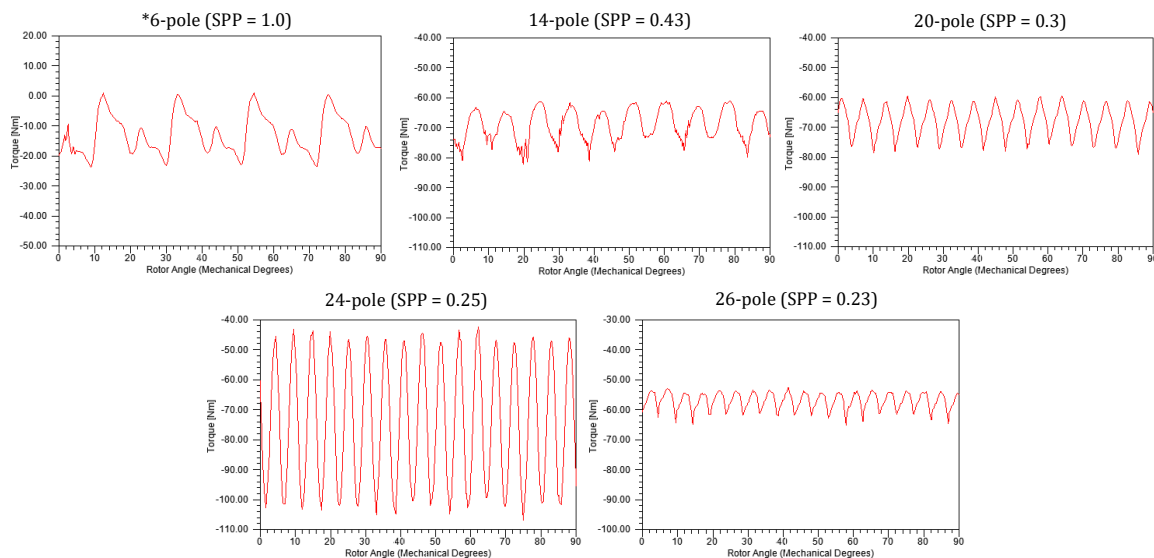


Figure 70: Torque plots for the three-phase resistive loads using individual y-axis scales

Figure 71 shows that the average torque is similar across the machines. The comparison between the torque ripple and the cogging torque shows that the torque ripple is now primarily a factor of the rectifier load for the 14-, 20-, and 26-pole machines, while the 6- and 24-pole machines have very small increases in torque ripple due to the loading.

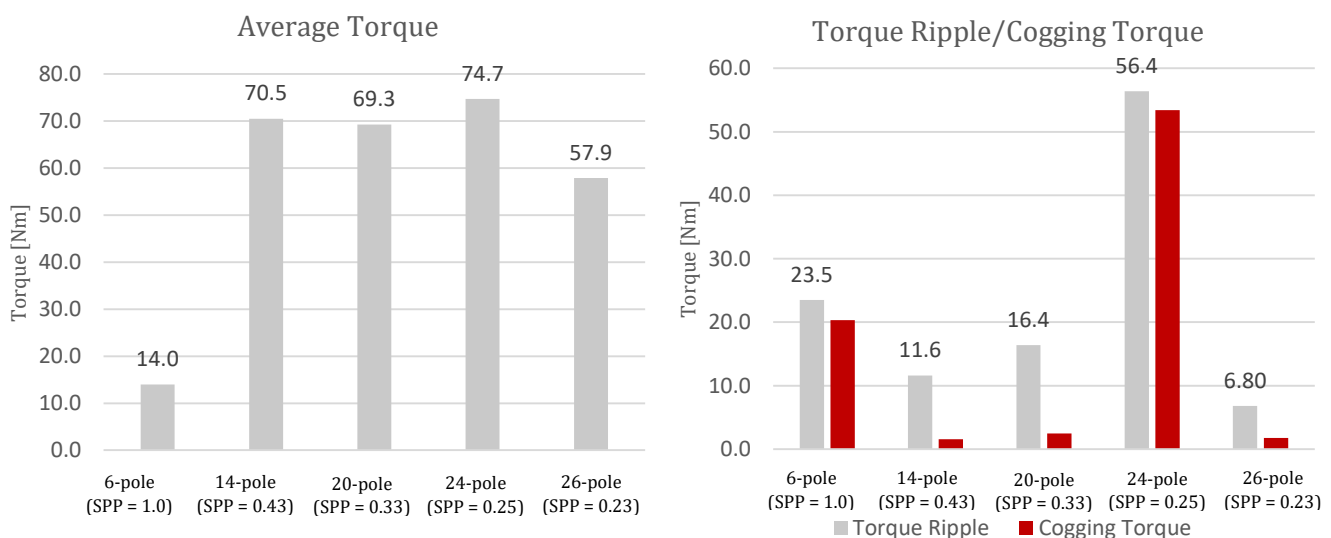


Figure 71: (left) Average torque measurements (right) Comparison between torque ripple and cogging torque

4.5.1.2 Load Current/Voltage

The load current and voltage are measured after the rectification process. No distortion measurements are taken over the output. The load is purely resistive, therefore the current waveform is a scaled version of the voltage waveform. Due to this, only the load current waveform is presented.

The average DC rectified load voltage and current values are recorded and presented in Figure 72. Excluding the 6-pole machine, the voltages and currents are similar in magnitude across the machines.

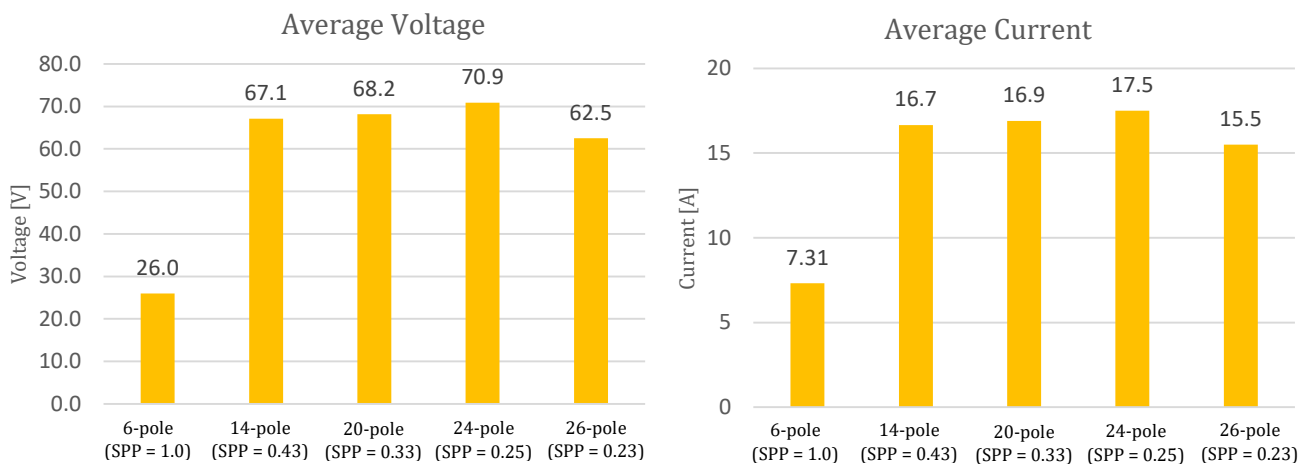


Figure 72: Average voltage and current measurements from the load

Figure 73 shows that the output ripple for both the voltage and current. As the load is purely resistive, the percentage ripple is identical for voltage and current waveforms. With the exception of the 6-pole machine, the output ripple is fairly constant across the machines.

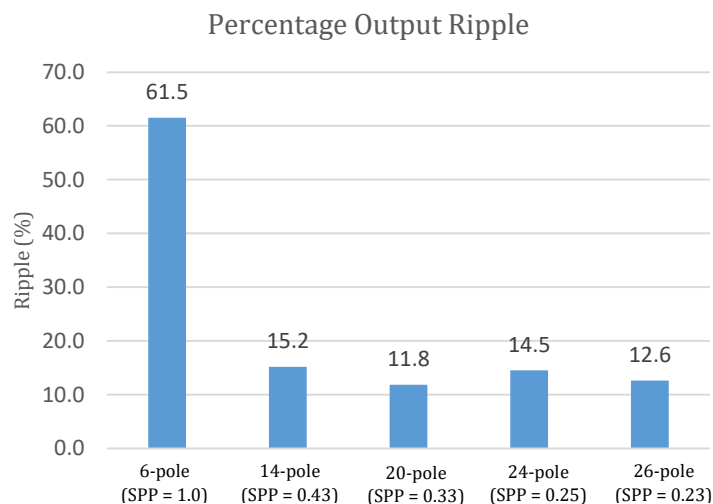


Figure 73: Calculated percentage output ripple

4.5.1.3 Source Current THD

The source current is measured from the generator terminals. As the output is now rectified, the THD measurements are taken from the current waveforms at the source side, while the voltage and current measurements are taken over the load. The measured THD is presented in Figure 74.

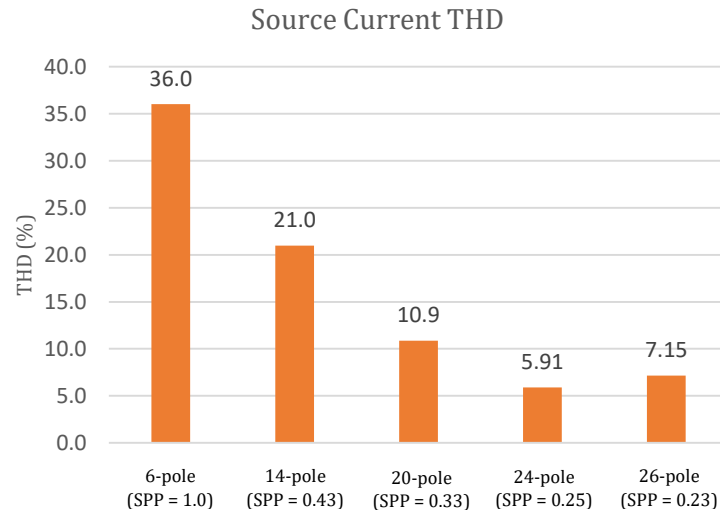


Figure 74: Summary of THD values calculated for the source current waveform

In general, the rectifier increases the THD of source current compared to open circuit, and three-phase load conditions. The notable exception is the 6-pole machine, which experiences a significant reduction in THD. The harmonic factors of the first three odd harmonics are shown in Figure 75. It can be seen that the rectifier effectively suppresses the third harmonics, while increasing the contribution of the fifth harmonic. This explains why the 6-pole machine experiences an overall reduction in THD, as previously it is seen that the third harmonic is the largest contributor to distortion.

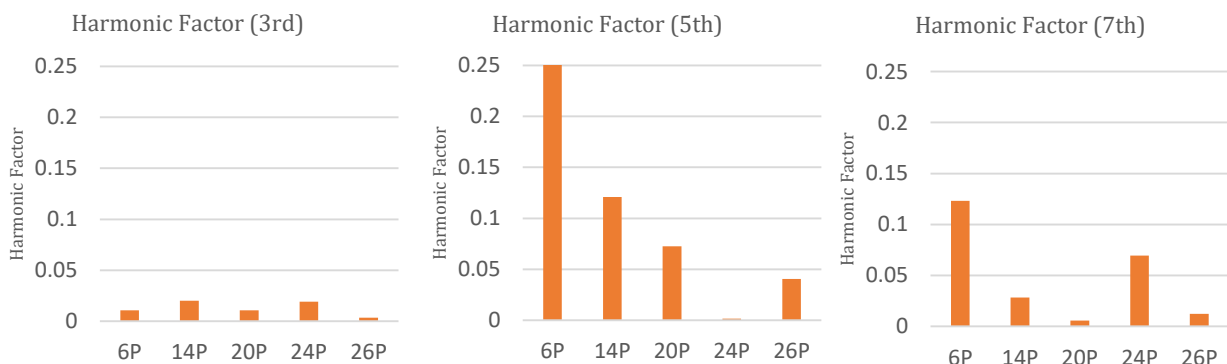
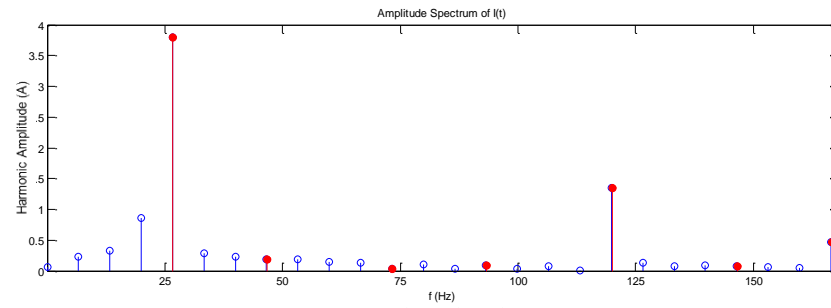
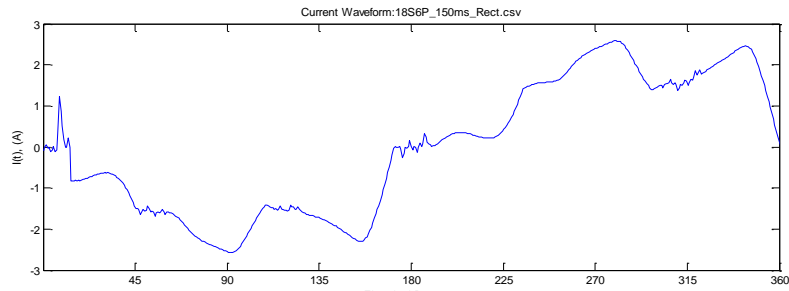


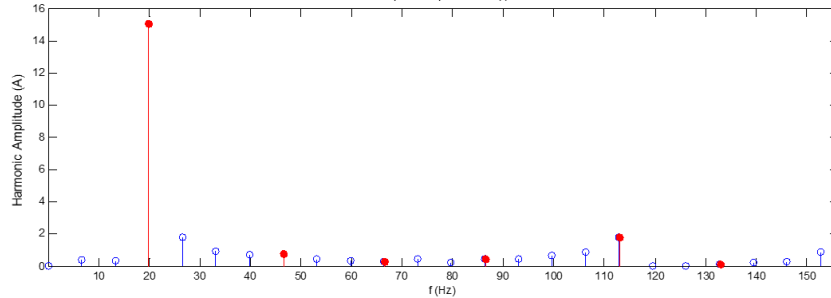
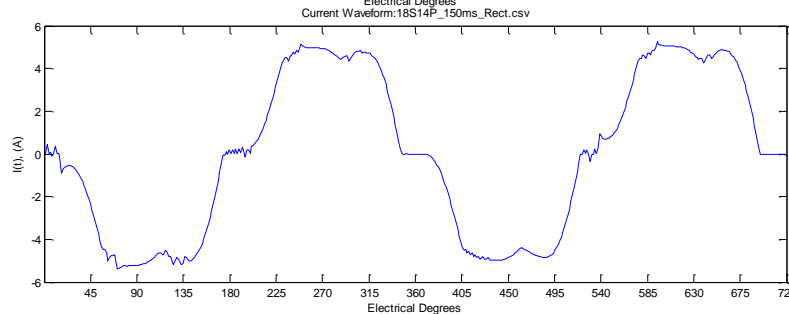
Figure 75: Harmonic factor for the 3rd, 5th, and 7th harmonics

18/6
(SPP = 1.0)



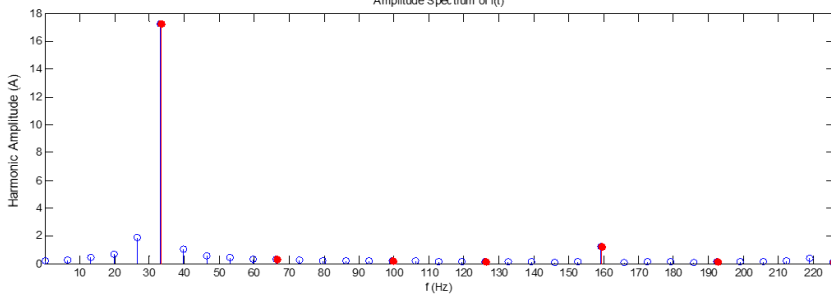
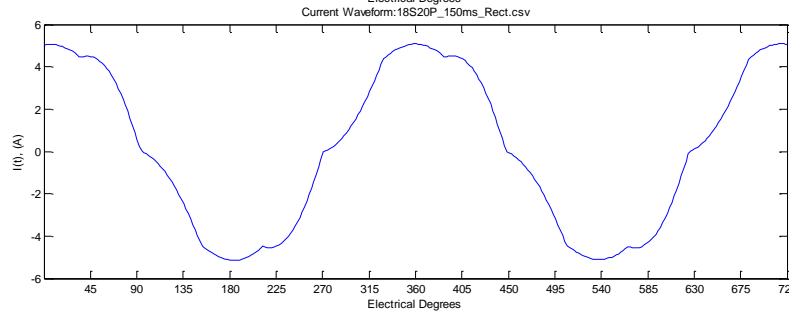
THD: 36.0%

18/14
(SPP = 0.43)



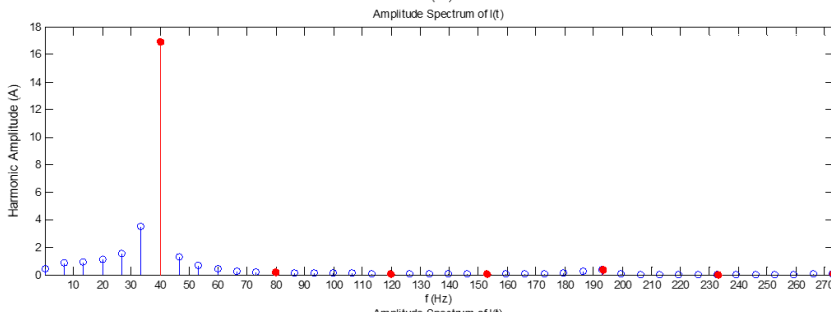
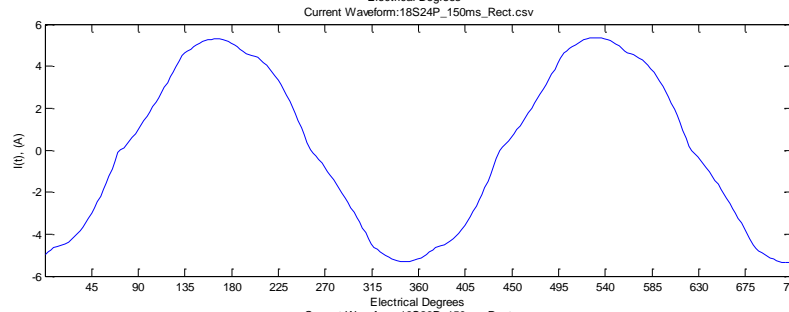
THD: 21.0%

18/20
(SPP = 0.3)



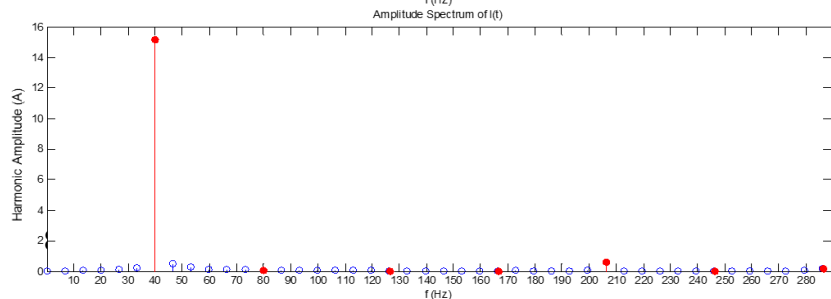
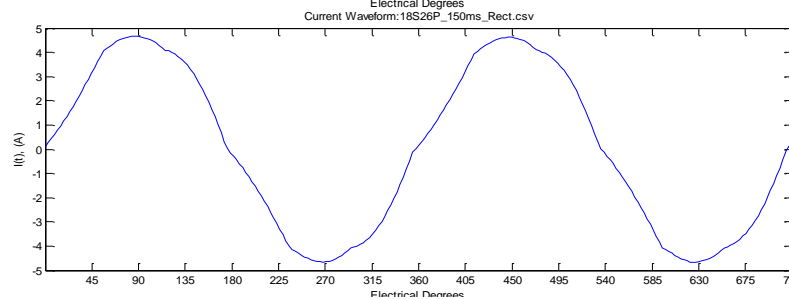
THD: 10.9%

18/24
(SPP = 0.25)



THD: 5.91%

18/26
(SPP = 0.23)



THD: 7.15%

Figure 76: Current waveforms and spectral plots for the rectifier load

4.5.1.4 Electrical Load Power

The electrical power dissipated by the load is displayed in Figure 77. The magnitude of ripple of each of the waveforms is much more uniform than for previous tests. The waveforms show an increase in frequency due to the rectifier, and except for the 14-pole machine, the waveform shape appears more regular with reduced transient behaviour.

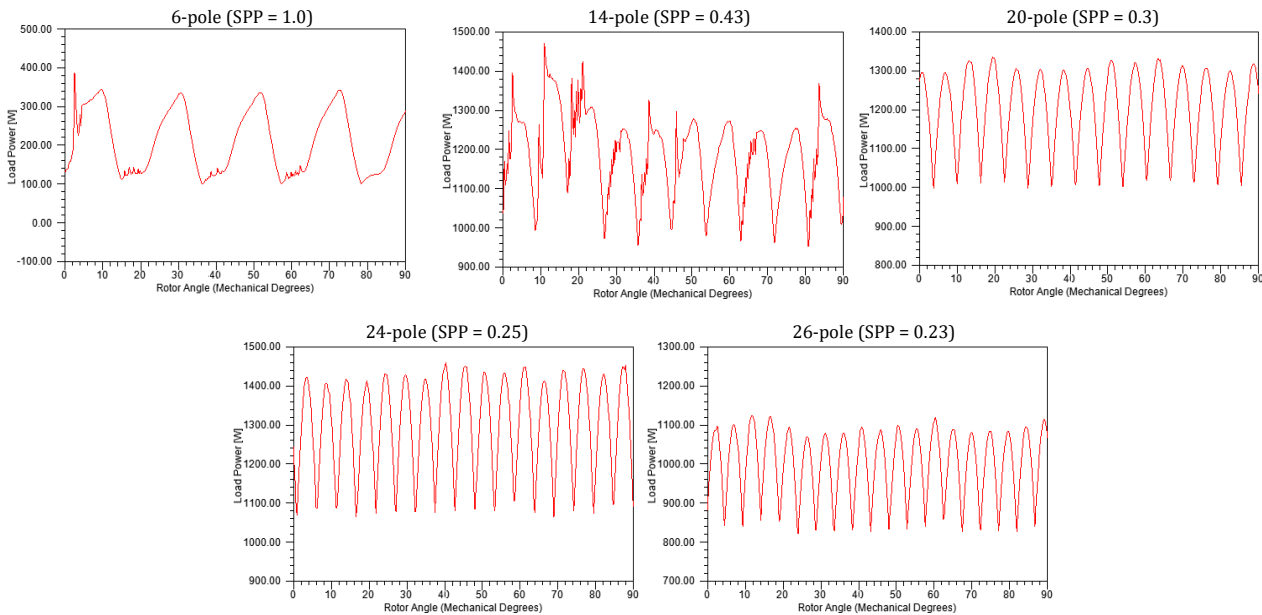


Figure 77: Measured electrical power dissipated in the load

Figure 78 shows the average load power and the percentage ripple of the measured power waveform. They show that the average load power rises to a peak and falls as the poles increase. The electrical power ripple exhibits a slight increasing trend as the pole number increases.

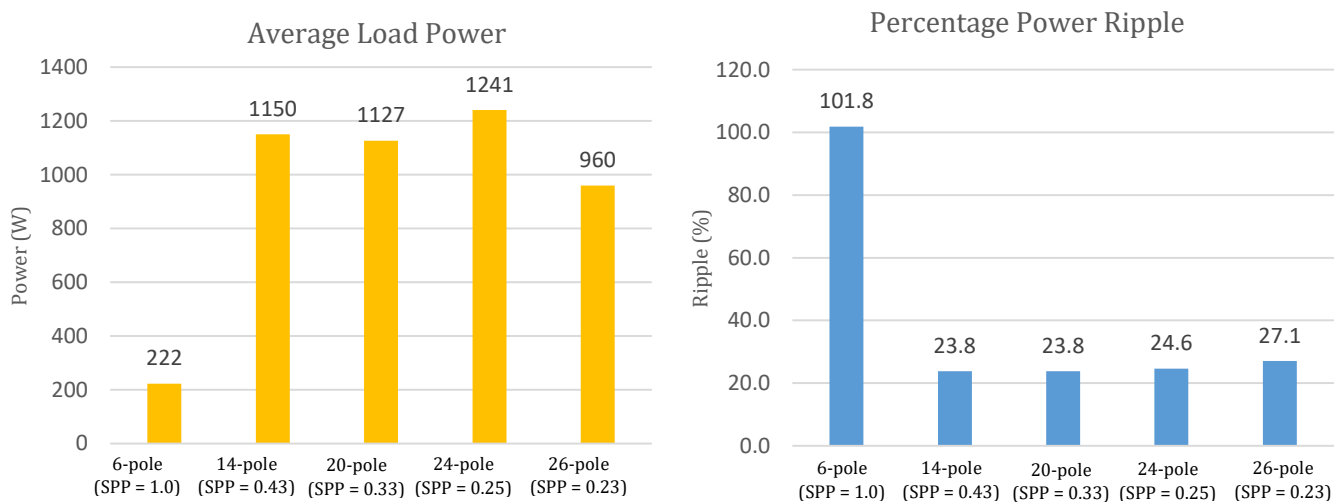


Figure 78: (left) Average load power (right) Percentage ripple in the power waveform

4.5.1.5 Mechanical Power

The mechanical power supplied to the machines is presented in Figure 79. The comparison between the waveforms show that the 24-pole machine has the highest ripple waveform. This is due to the high value of cogging torque. The 26-pole exhibits the lowest torque ripple.

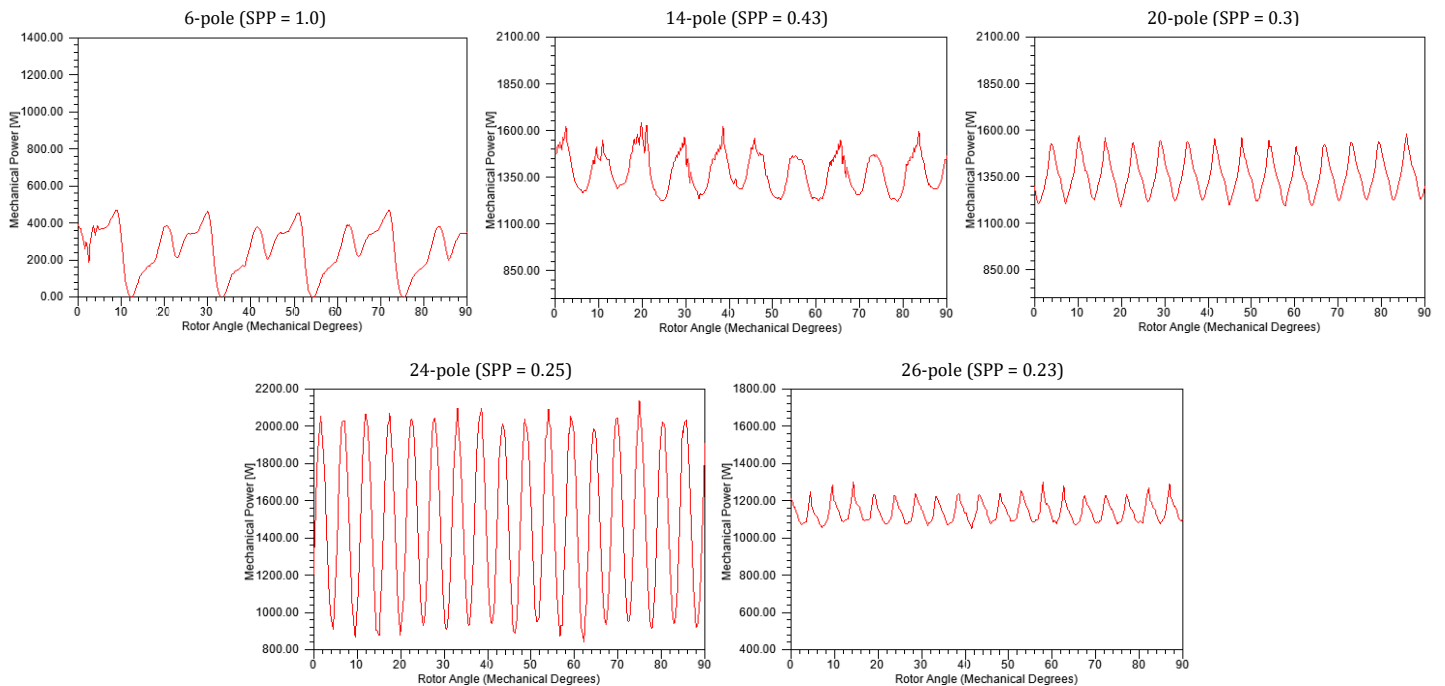


Figure 79: Measured mechanical power supplied to the machine

The average mechanical power in Figure 80 shows a similar increasing then decreasing trend observed previously. The ripple observed in the supplied mechanical power waveforms follows identical trends to the torque ripple waveforms presented earlier.

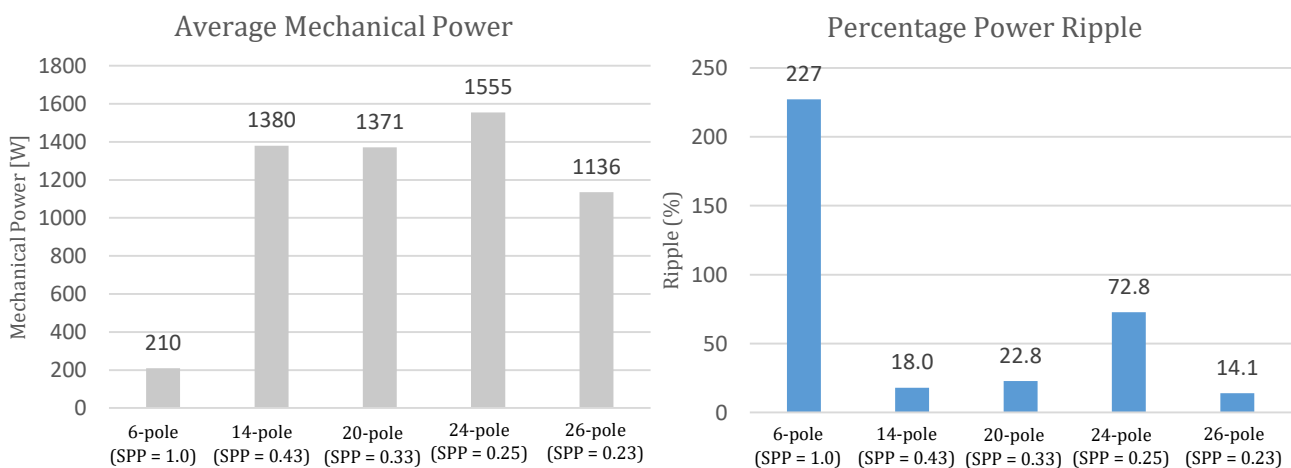


Figure 80: (left) Average mechanical power supplied (right) Percentage mechanical power ripple

4.5.1.6 Efficiency

The efficiency is calculated using the integration of the electrical power dissipated in the load and the integration of the mechanical power supplied to the machine.

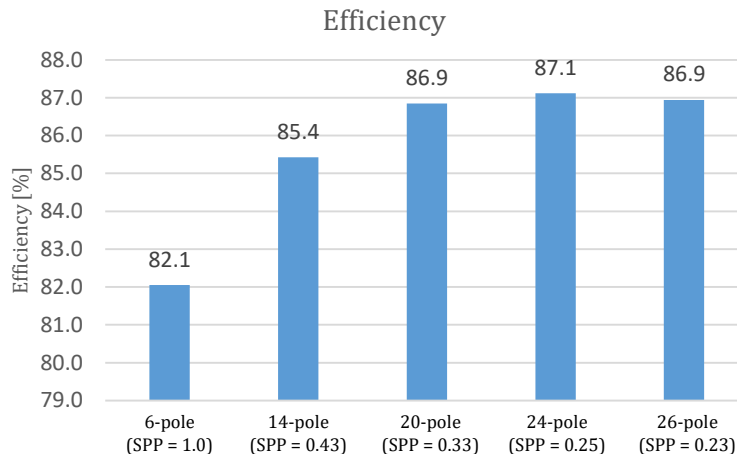


Figure 81: Calculated efficiency of the machines

Figure 81 shows that the efficiency of the machines increases as the pole number increases, but reaches a maximum efficiency for the 24-pole machine. The difference in efficiencies for the 20-, 24-, and 26-pole machines is minimal. The efficiency when using a rectifier is shown to be significantly lower than when presenting a three-phase load.

4.5.1.7 Voltage Regulation

The voltage regulation compares the full-load voltage and the no-load voltage. Figure 82 below shows the reduction in voltage caused by the addition of the rated load.

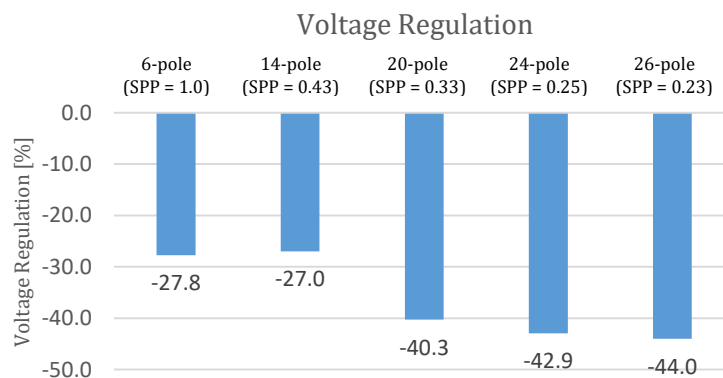


Figure 82: Voltage regulation as the load is increased

It can be seen that for a load of 4Ω the voltage regulation performance of the machines decreases as the number of poles increases. The lower pole machines are more effective at regulating their voltage at the rated load. The 6- and 14-pole machines have significantly lower voltage reduction as compared to the other machines. The 20-, 24-, and 26-pole only have a slight discrepancy between each other for loaded voltage reduction.

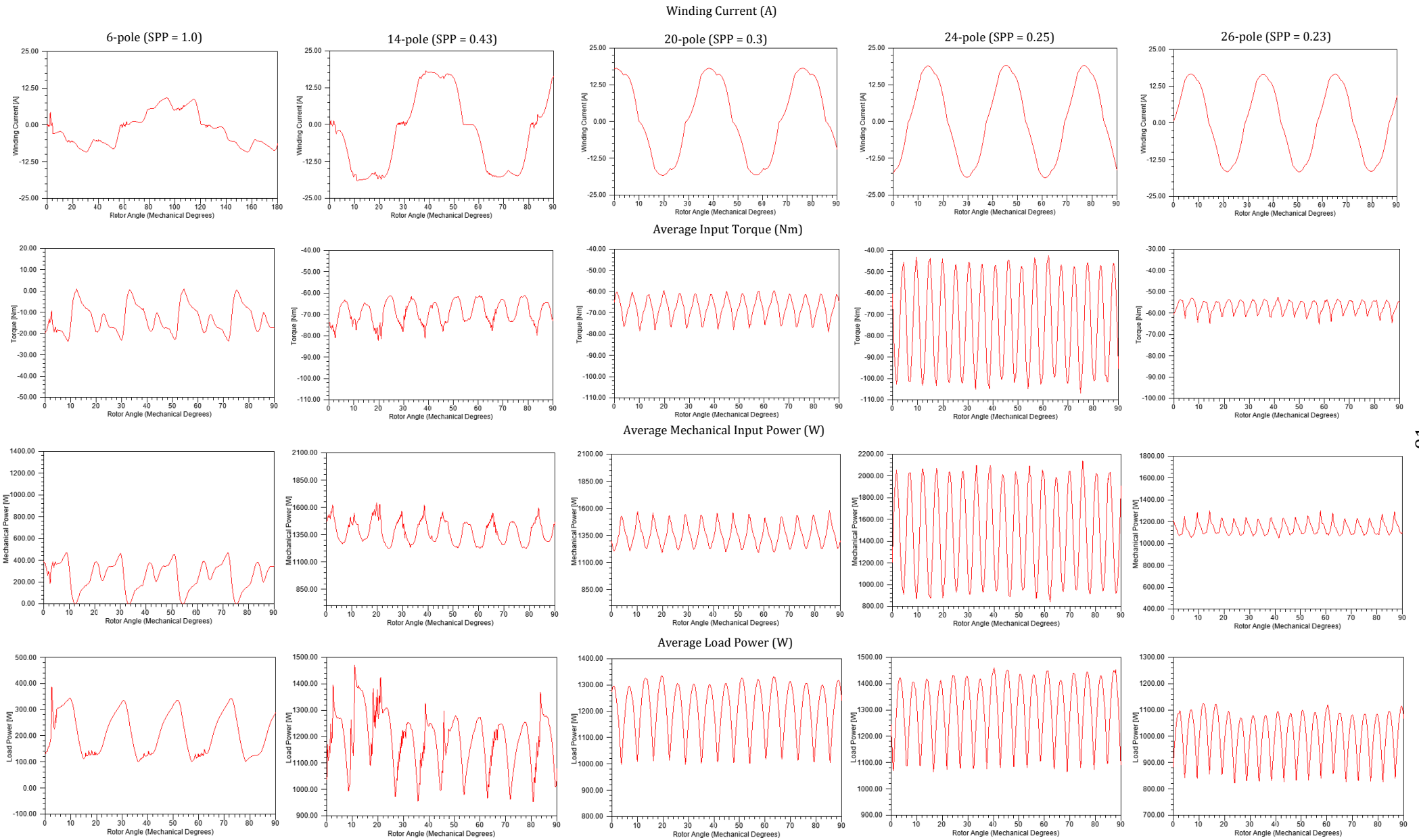


Figure 83: Summary of graphs presented for the rectifier resistive load tests

4.5.2 Variable Resistance Load

The simulation setup is then modified to make a sweep of the load resistance. Similar to the three-phase test, the resistance is changed from 0.25Ω to 15Ω with increments of 0.5Ω . This is to determine the electrical loading point at which the machines operated most effectively.

4.5.2.1 Average Voltage

The inclusion of the rectifier in the system produced some noise in the measured outputs. However, it can be seen that the rectifier does not majorly impact the average output voltage. The trends that are observed for a three-phase load can also be seen when using a rectifier.

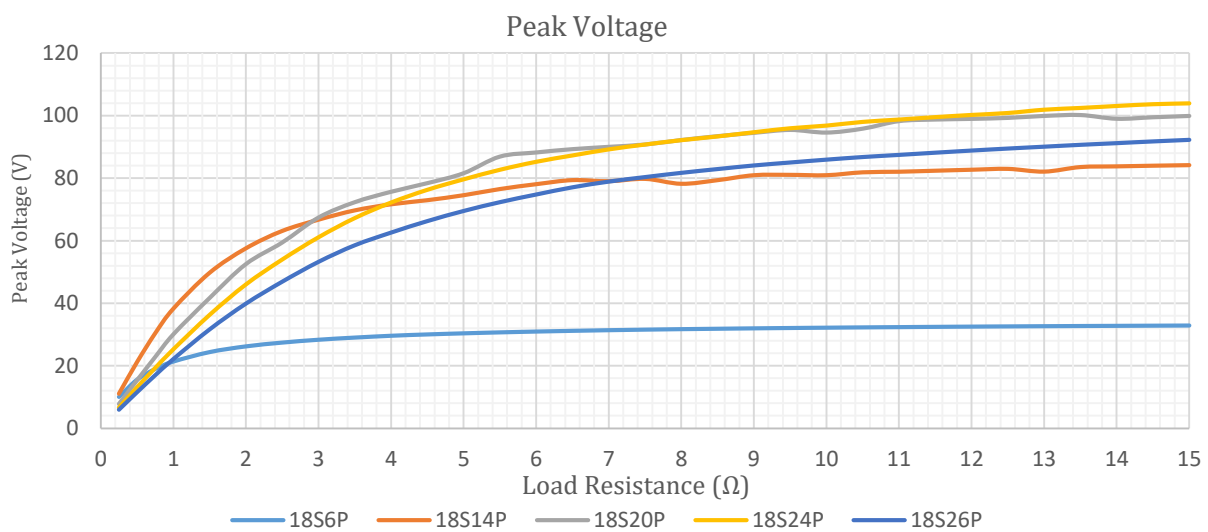


Figure 84: Peak voltage of the machine variants for a variable resistance

The steady state output voltages in Figure 85 exhibit a similar shape as the steady state voltages for the three-phase variable load test.

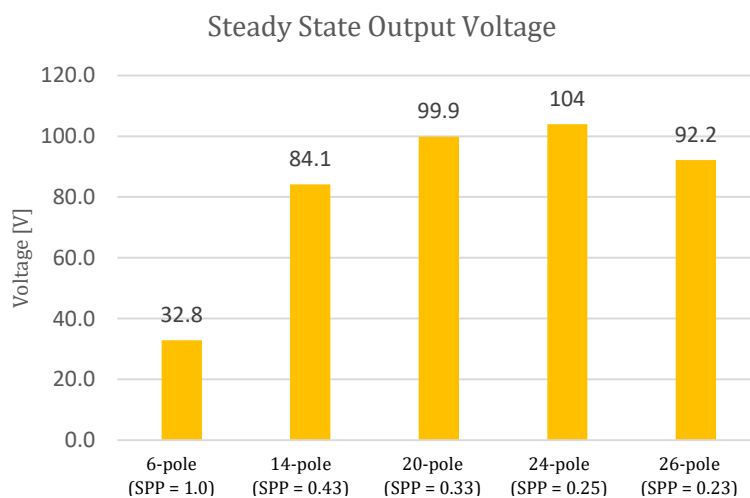


Figure 85: Steady state output voltage of the rectifier

4.5.2.2 Load Power

The load power plots are shown in Figure 86. These can be seen to be highly similar to the previously measured three-phase system. This indicates that the addition of the rectifier has a minor impact on the characteristics of the output. The 14-pole machine has the highest power capability, as shown in Figure 87.

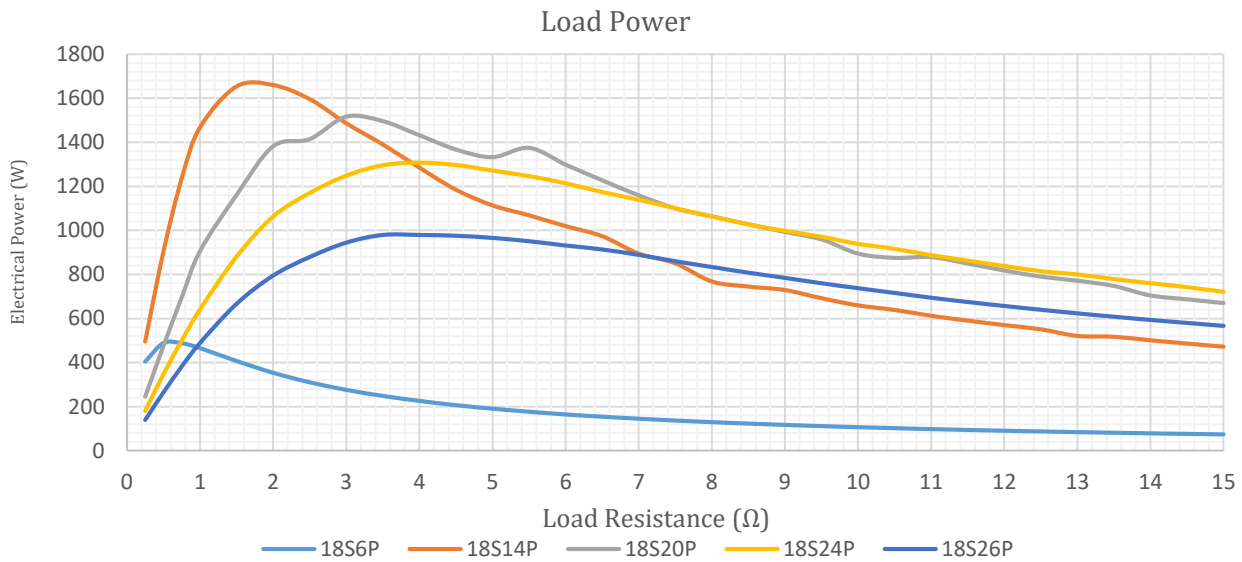


Figure 86: Load power of the machine variants for a variable resistance

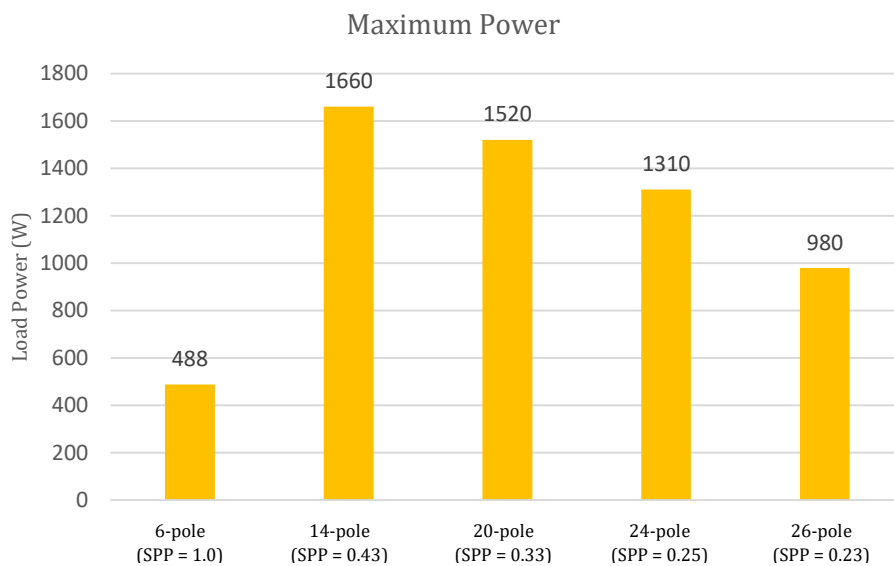


Figure 87: Maximum power delivered to the load at rated speed

4.5.2.3 Efficiency

The efficiency plot shown in Figure 88 is also very similar to the previously measured values for a three-phase load. The main difference is the 6-pole machine, which now exhibits comparable efficiency compared to the other machines.

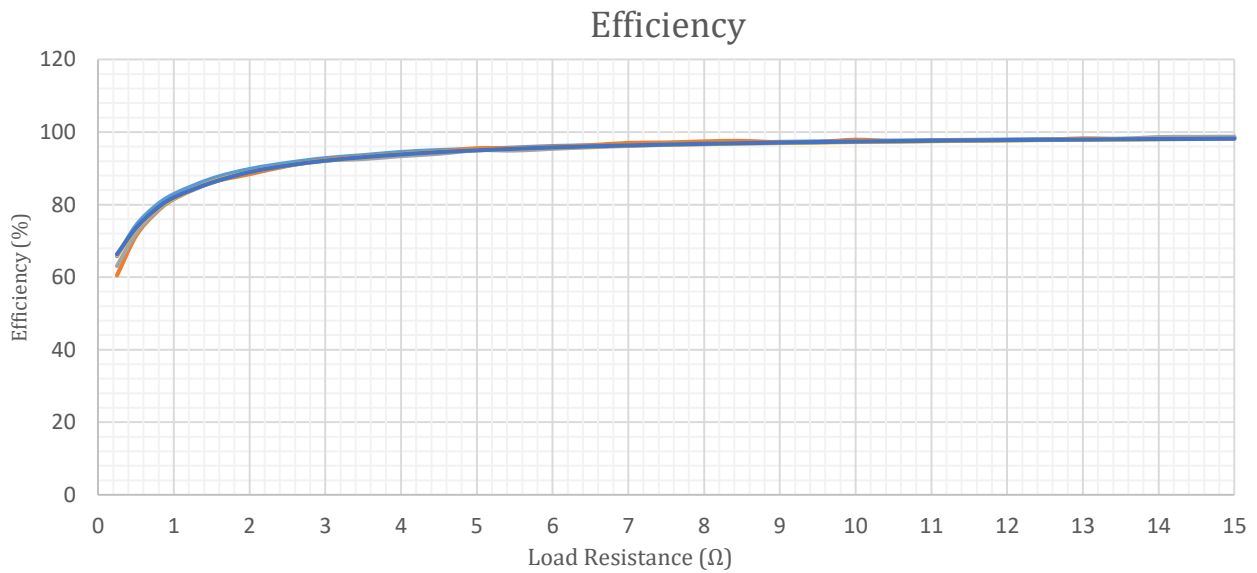


Figure 88: Efficiency of the machine variants for a variable resistance

4.5.3 Variable Speed Analysis

The circuit setup is then modified to sweep the speed from 20 rpm to 600 rpm with 20 rpm increments. The load resistance is set at 4Ω .

4.5.3.1 Average Voltage

Figure 89 shows the average voltage measured over the speed range has similar trends to the three-phase load. As the number of poles decreases, the steady state voltage also decreases. At low speeds, the generated voltages are approximately the same, but as the speed increases, the output voltages become separated by larger margins.

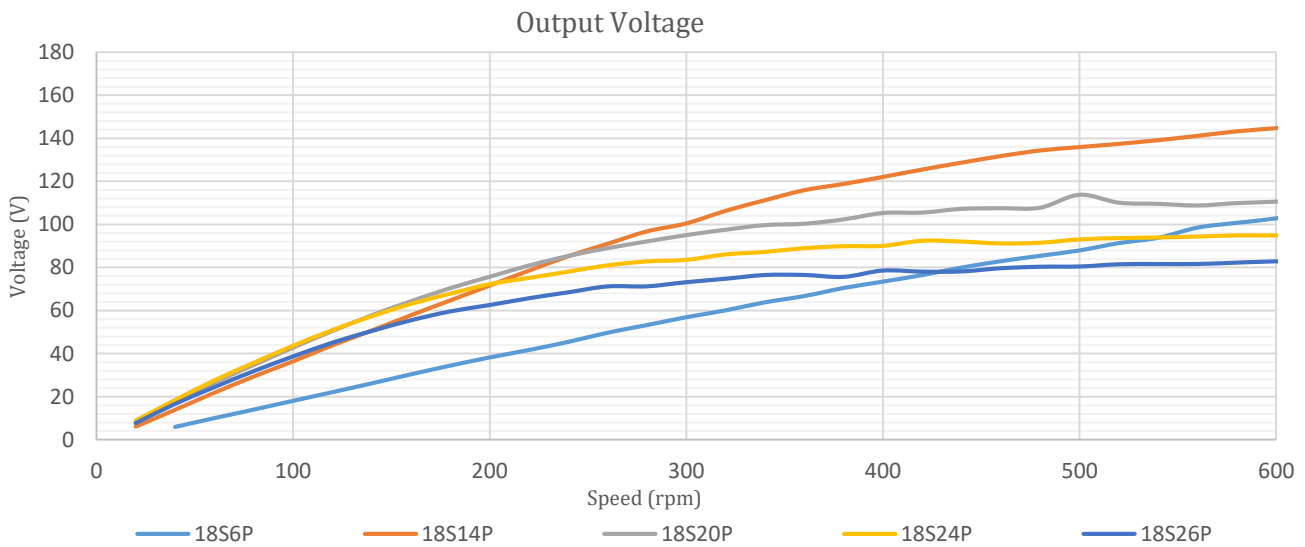


Figure 89: Plot of the average voltage over the speed range

Figure 90 shows the difference in relative output voltages at rated speed and at maximum speed. The 14-pole machine has a disadvantage at lower speeds, but has significantly higher output at 600 rpm.

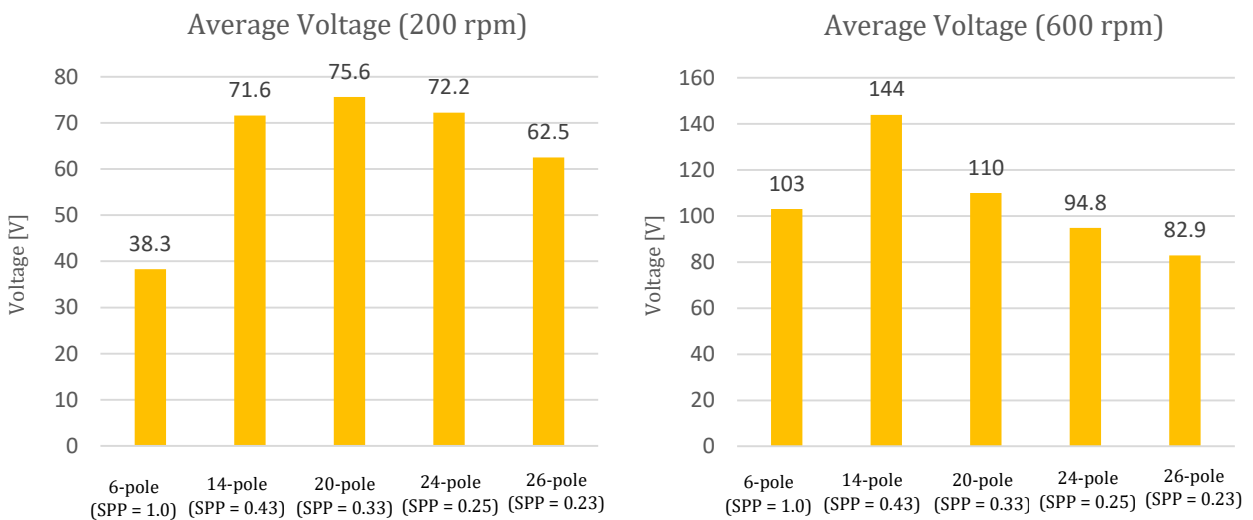


Figure 90: Average load voltage at rated speed and at 600 rpm

4.5.3.2 Load Power

The load power measured over the speed range is presented in Figure 91. The curves are shown to be almost identical in shape as the three-phase resistive load variable speed tests. Again it can be seen that the 14-pole generator has the highest maximum power, but performs poorly at lower speeds.

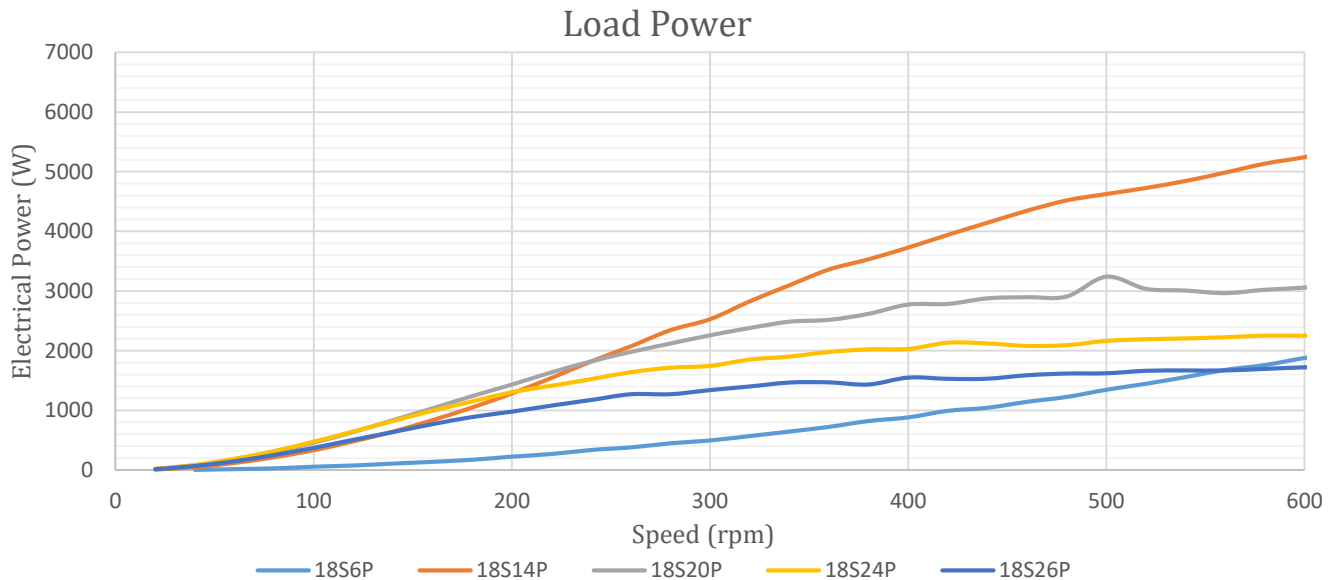


Figure 91: Plot of the load power generated by the machine variants for the variable load tests

Similarly to the output voltage, Figure 92 shows that the 14-pole machine underperforms at low speeds, but has a significant advantage at higher speeds.

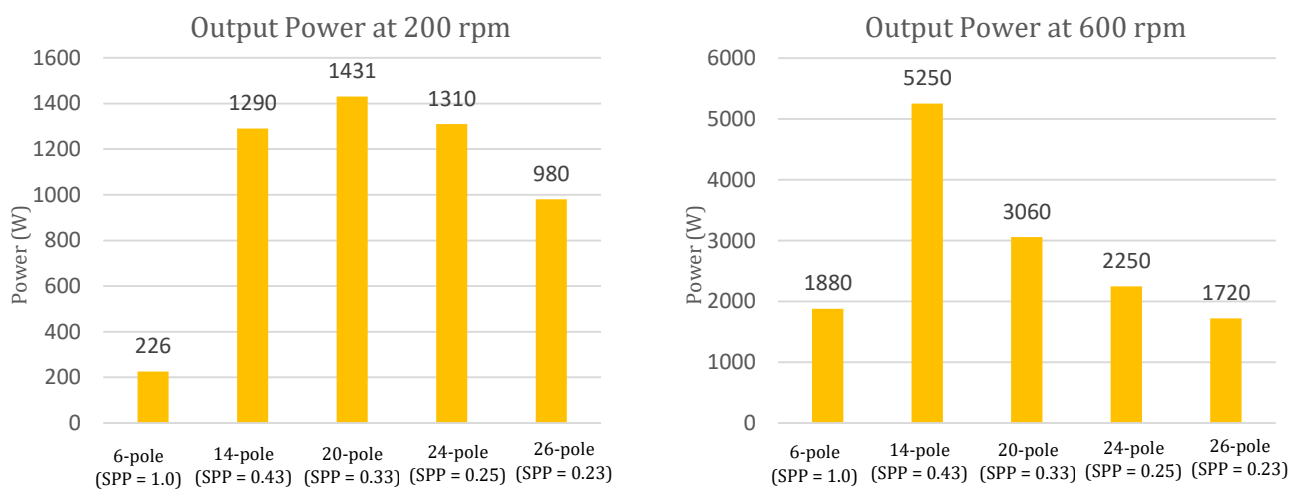


Figure 92: Output power at rated speed and at maximum operating speed

4.5.4 Summary of DC Analysis Findings

In this section the machine designs were simulated in a circuit including a three-phase rectifier and a resistive load. The simulations were performed in three main sections: rated load at rated speed, rated load at variable speed, and variable load at rated speed. The general findings showed that:

- The inclusion of the rectifier only minimally changes the output characteristics. The most significant difference is the reduction in efficiency.
- The rectifier slightly increases the THD of the source current. This is to be expected from the nature of the rectifier.

4.6 Load Test – Battery Charging Configuration

The next stage in the analysis uses a battery as a load. This is a typical setup that the generator would be used in. The Simplorer setup features a three-phase rectifier and a battery load. The simplified block diagram of the system is shown in Figure 93. In a practical application, this setup would be similar to systems used to rectify the current to charge a battery. A more realistic scenario would also include a form of charge controller, to monitor the battery charging regime, and to disconnect the load when the battery is fully charged. As stated earlier, complex power conversion and control modules are not in the scope of this project, and therefore are not included in the analysis.

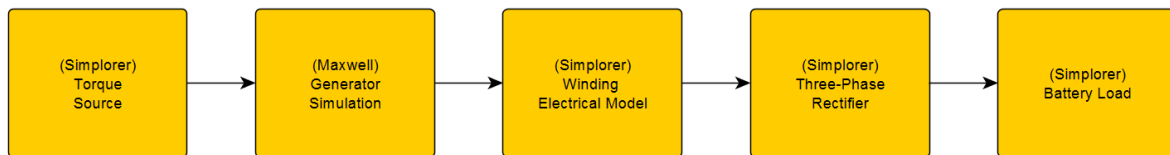


Figure 93: Simplorer cosimulation setup with a battery load.

4.6.1 Setup Notes

The diode characteristic equation models an ideal diode. There is no voltage drop present across the diodes, and the diodes are instantly switched on and off. The resistors and inductors used to model the windings are still included in the system.

The battery used is a simplified 6-cell, 12V battery, with a terminal voltage of 12.8V. Batteries such as sealed lead acid (SLA) batteries commonly have a terminal voltage that can vary up to 0.4V per cell between its charged and discharged states i.e. 12.0V-14.4V. The power delivered to the battery is dependent on its state of charge, and will tend to decrease as the battery charges due to the increase in terminal voltage. The terminal voltages used in the simulation are representative of discharged batteries. Slightly lower power delivery would be expected for batteries with a higher state of charge.

The battery voltage is set at four different values for the tests. The different battery voltages represent four commonly used battery voltages. That is, 12V, 24V, 36V, and 48V. The voltages quoted are not exact terminal voltages and are used for naming purposes only. The terminal voltages used are 12.8V, 25.6V, 38.4V, and 51.2V. The aim of these tests is to determine the type of battery that would work most effectively with the machine.

4.6.2 Preliminary Simulations

Preliminary simulations are performed for the rated speed of 200 rpm. These simulations are used to determine the voltage of the battery that the generators can use most effectively.

4.6.2.1 Electrical Power

The electrical power generated by the machines is presented in Figure 94. It is seen to increase linearly as the battery voltage increased. The main exception is the 6-pole machine that exhibited decreased power output. The output voltage of the 6-pole machine at 200 rpm is not high enough to surpass the battery voltage and therefore cannot supply current. The battery will only charge if the generated voltage is greater than the terminal voltage, so the 6-pole generator could only deliver minimal power reducing to zero power as the terminal voltage increased.

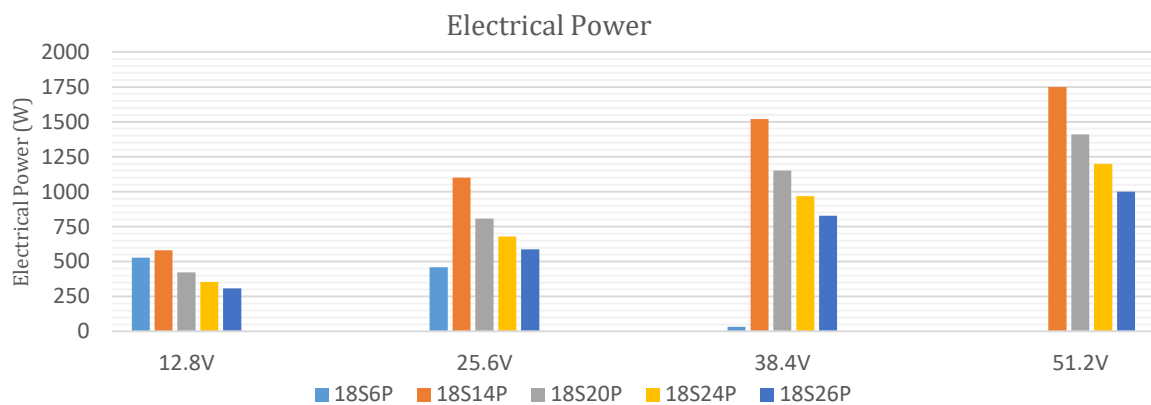


Figure 94: Electrical power delivered to the load

The rating of the battery used in this setup is proposed to be 7 kWh. Using this rating, the total charge time of the battery is calculated for all the different combinations of machine and battery voltage. The results are presented in Figure 95. Logically, as the power delivered increases, the charging time is decreased. The 6-pole machine does not reach charging voltage for the 36V and 48V battery and is not included in Figure 95.

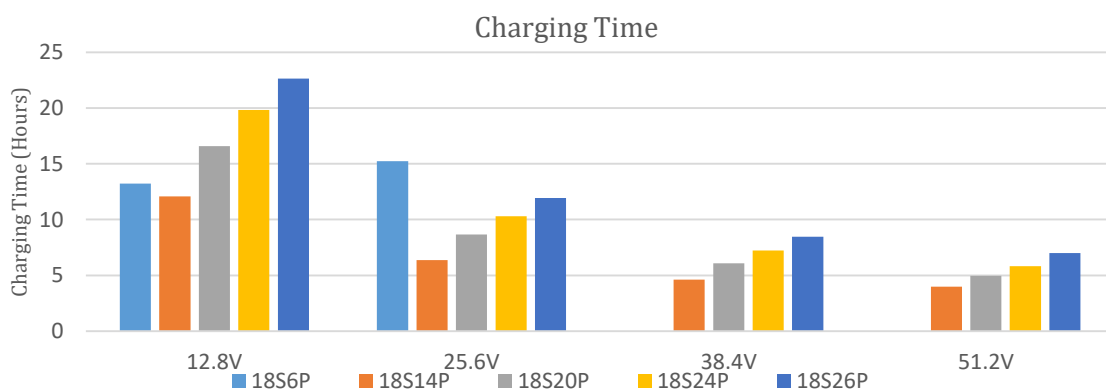


Figure 95: Charging time at rated speed

4.6.2.2 Efficiency

The efficiency of the machines in Figure 96 can be seen to have a positive trend as the number of machine poles increase, as well as the battery voltage increasing. The results for the 6-pole machine at 36V, and 48V are not shown, as explained previously.

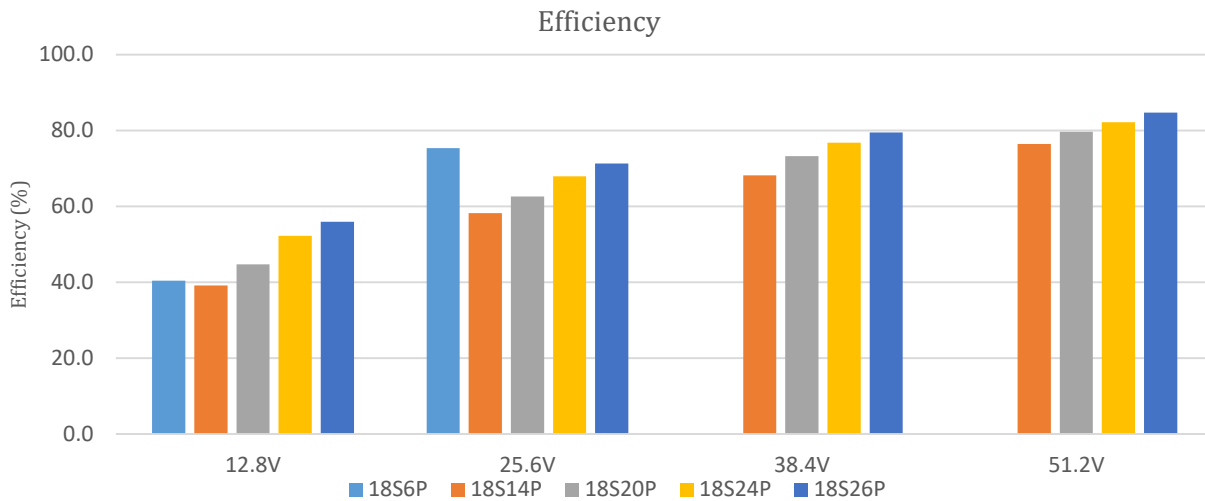


Figure 96: Efficiency of the machines for the four different battery voltages

4.6.2.3 Total Harmonic Distortion

The THD in Figure 97 does not show a clear pattern, with THD increasing in some combinations, while decreasing in others. The THD of the 6-pole machine is clipped in the graph below due to its magnitude.

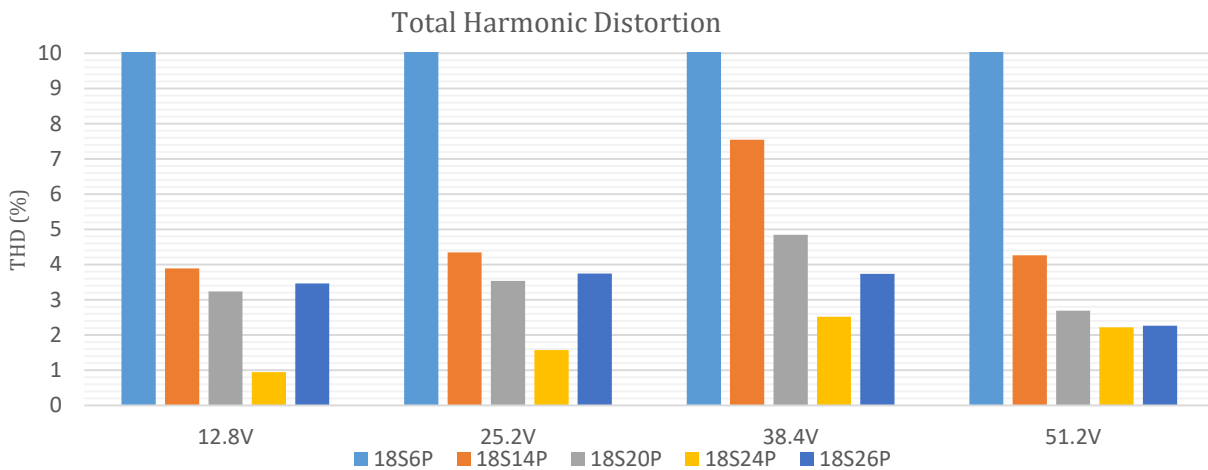


Figure 97: THD of the machines for the four different battery voltages

4.6.2.4 Preliminary Results

The results indicate that the 48V battery setup uses the generators in the most effective manner. The 48V battery configuration has the greatest power delivered, the lowest charging times, the greatest efficiency, and the THD is comparable to the other battery voltages. The 48V battery is selected as the rated battery load.

4.6.3 48V Battery Configuration

A more detailed analysis is undertaken using the 48V battery with the rectifier circuit setup. Previously, variable speed tests were performed, however, this is too computationally expensive to run for all load types, and the results are expected to be similar across the different loads. For these reasons variable speed tests are not performed for the battery load. For this analysis the 6-pole machine is not considered as there is no power transfer at rated speed due to the low output voltage.

4.6.3.1 Load Torque

The torque waveforms for each machine are shown in Figure 98. None of the waveforms exhibit transient behaviour.

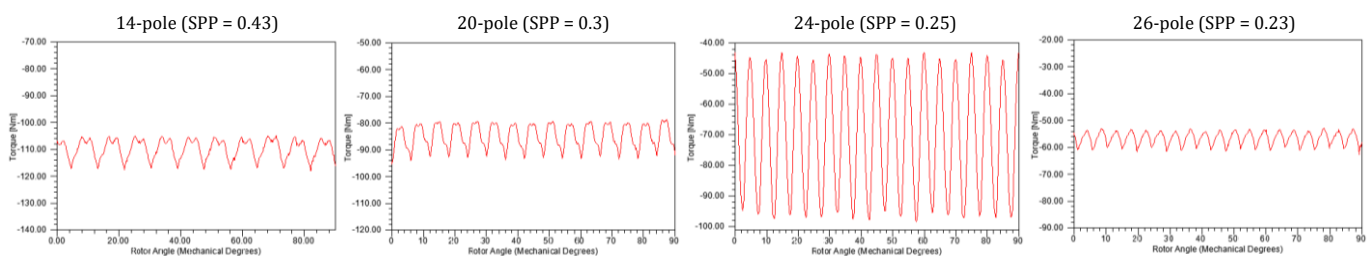


Figure 98: Torque plots for the rectified 48V battery load using identical y-axis scales

Figure 99 shows that the average torque reduces significantly as the number of poles increases. The comparison between the torque ripple and the cogging torque shows that the torque ripple is now primarily caused by the load for the 14-, 20-, and 26-pole machines, while the 24-pole machine is mostly comprised of the cogging torque.

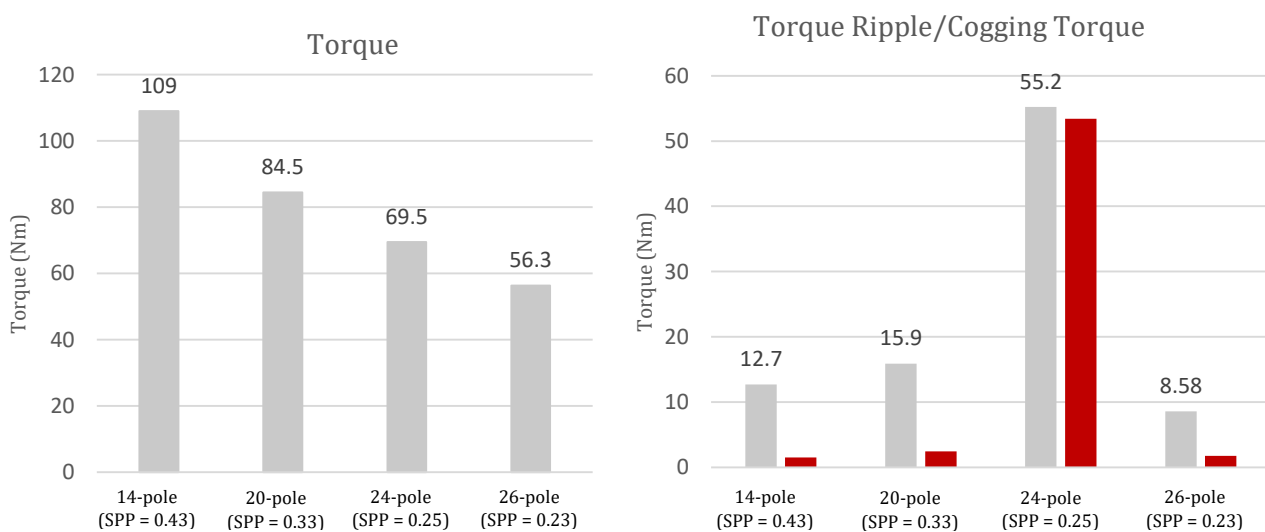


Figure 99: (left) Average torque measurements (right) Comparison between torque ripple and cogging torque

4.6.3.2 Load Current/Voltage

The load current is measured through the load. As the load is a battery, the output voltage is clamped at the terminal voltage and so is not considered.

The average DC rectified current values are recorded and presented in Figure 100. The average current is seen to decrease as the number of poles increases.

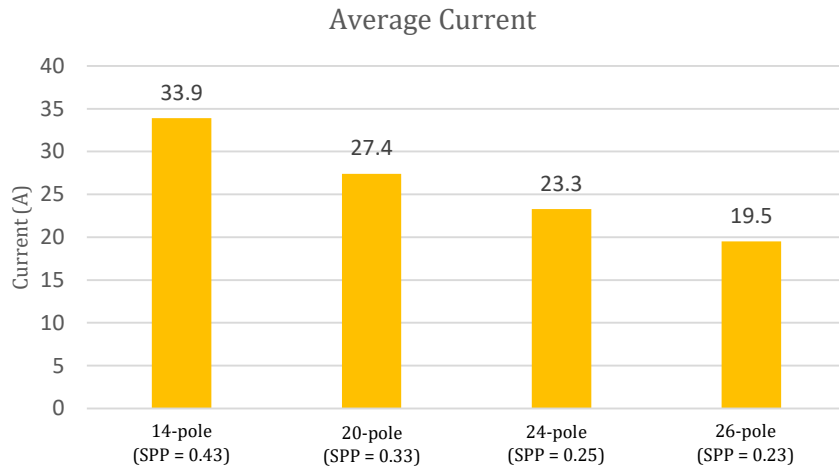


Figure 100: Average current measurements through the load

The ripple percentage in Figure 101 is based on the peak-to-peak current ripple and the average current value. The ripple is very similar across the machines and the values all fall between 14%-16%. Reduced ripple is advantageous to minimise the size and cost of power filters.

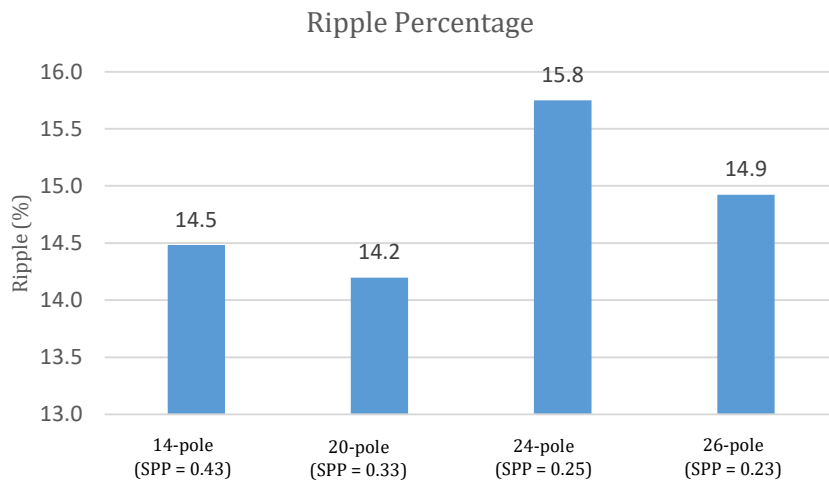


Figure 101: Calculated percentage output ripple

4.6.3.3 Source Current THD

As the output is now rectified, the THD measurements are taken from the current waveforms at the source side, while the voltage and current measurements are taken over the load. The current waveforms are presented in Figure 104 overleaf, and the summarised results for the THD are presented in Figure 102.

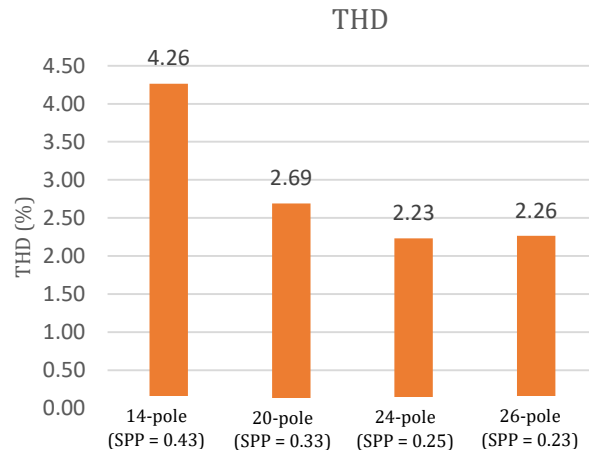


Figure 102: Summary of THD values calculated for the source current waveform

The THD values show a downward trend as the number of poles increased. The overall magnitude is lower than with other load types, and the discrepancy between the machines is also very small. The harmonic factors for the 3rd, 5th, and 7th harmonics are calculated and presented in Figure 103. Similarly to the other rectifier circuit, the third harmonics are suppressed. The other harmonics are also reduced, but to a lesser degree. The overall THD is shown to be the lowest of all the load tests.

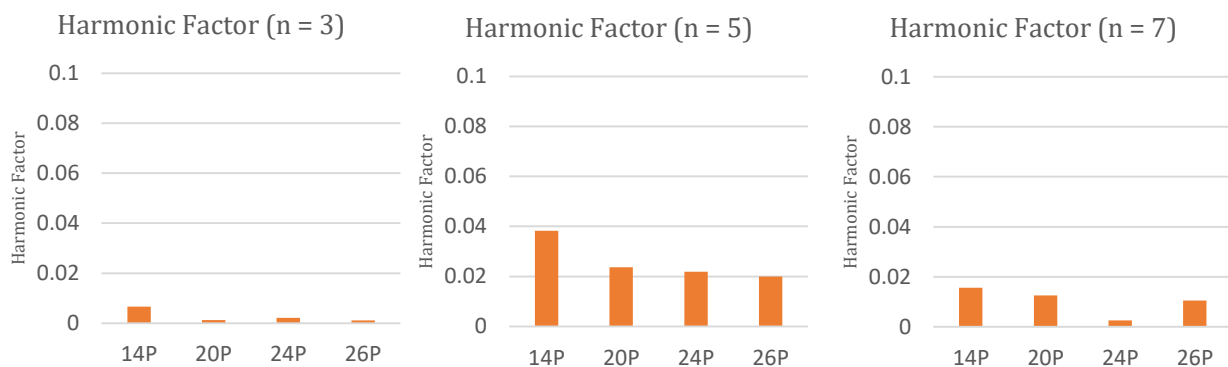
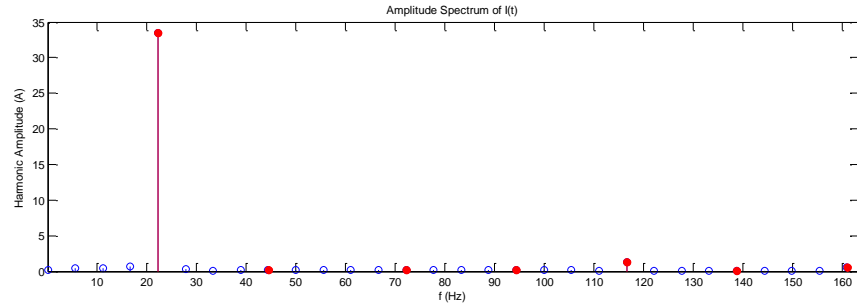
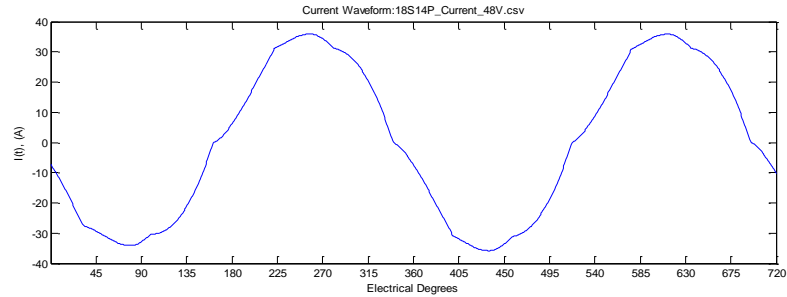


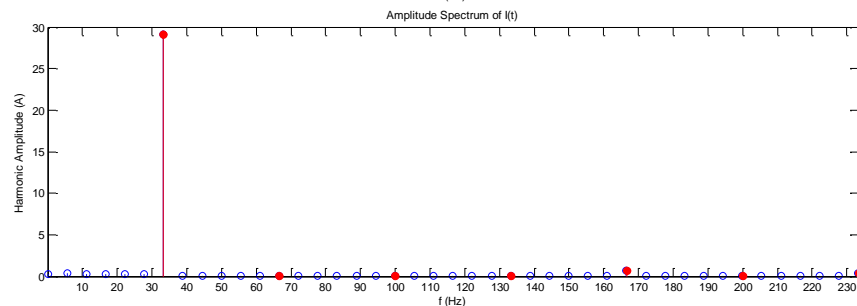
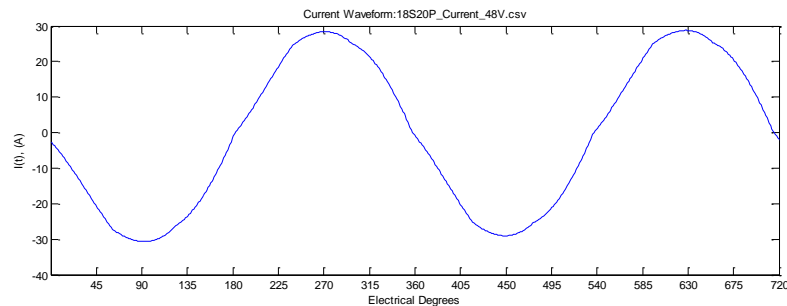
Figure 103: Harmonic factors for the 3rd, 5th, and 7th harmonics

18/14
(SPP = 0.43)



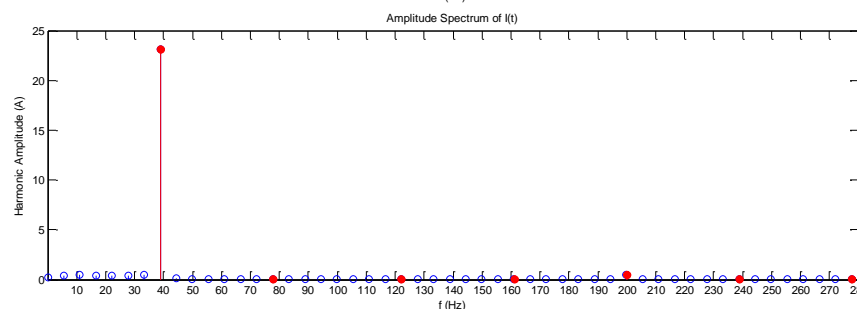
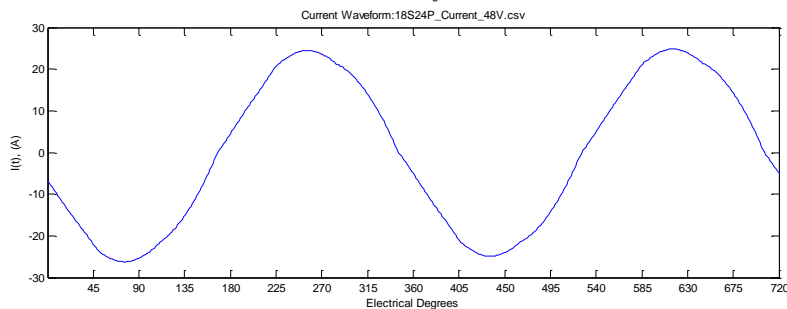
THD: 4.26%

18/20
(SPP = 0.3)



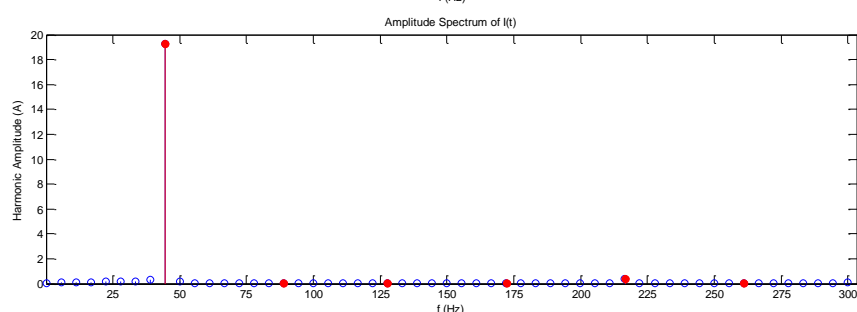
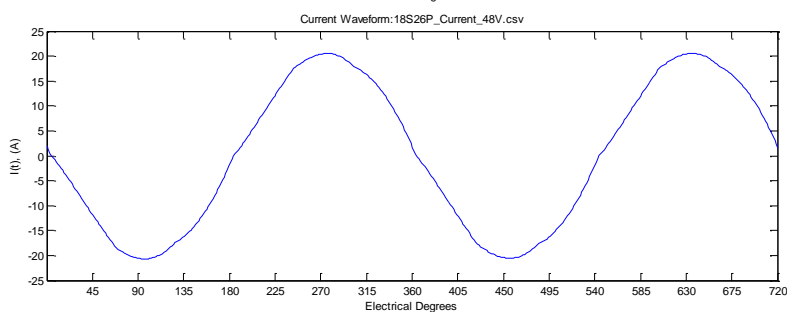
THD: 2.69%

18/24
(SPP = 0.25)



THD: 2.23%

18/26
(SPP = 0.23)



THD: 2.26%

Figure 104: Current waveforms and spectral plots for the rectifier load

4.6.3.4 Electrical Load Power

The electrical power generated by each of the machines is displayed in Figure 105. The waveforms display the most similar ripple out of all the load tests thus far.

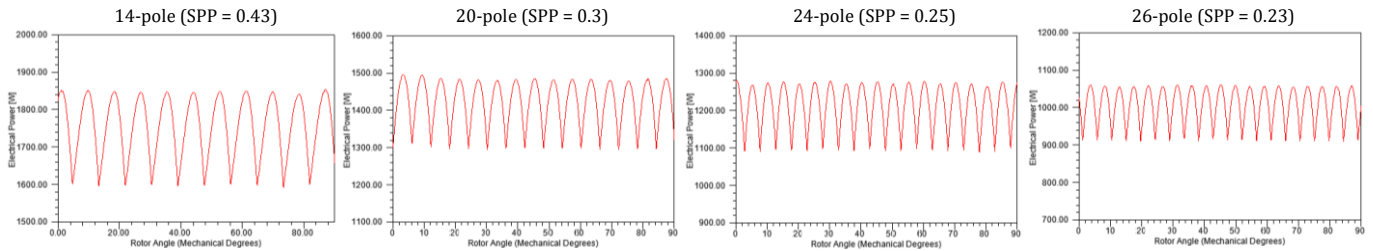


Figure 105: Measured electrical power dissipated in the load

Figure 106 shows the average load power and the percentage ripple of the measured power waveform. This shows that the average load power steadily decreases as the poles increase. The electrical power ripple is identical to the current ripple presented previously. This is due to the clamped output voltage.

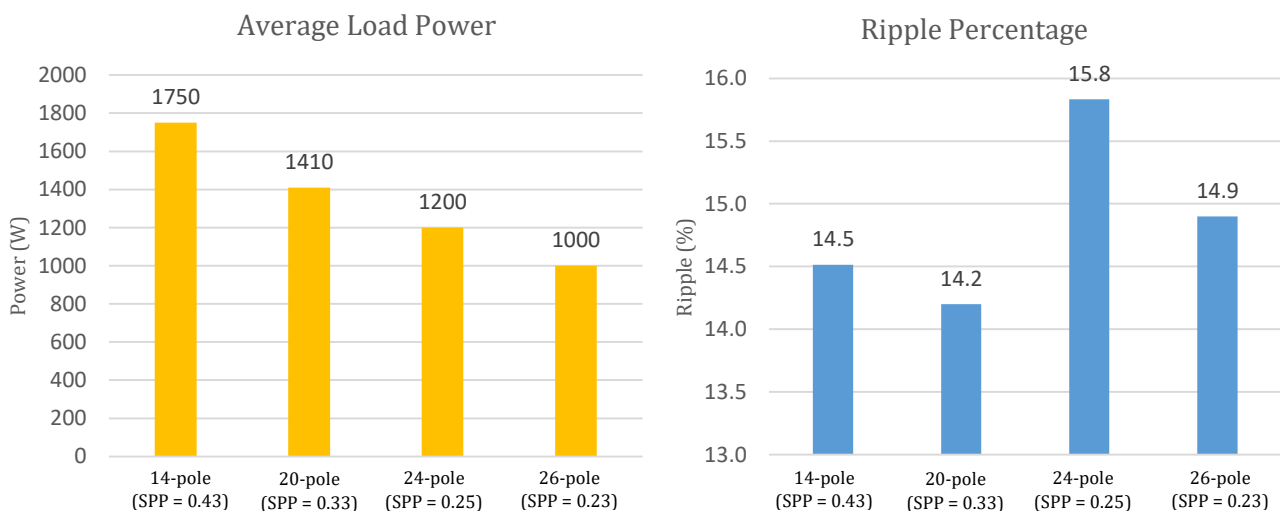


Figure 106: (left) Average load power (right) Percentage ripple in the power waveform

4.6.3.5 Mechanical Power

The mechanical power supplied to the machines is presented in Figure 107. The graphs use a uniform value for the divisions. The comparison between the waveforms show that the 24-pole machine has the highest ripple waveform. This is again due to the high value of torque ripple.

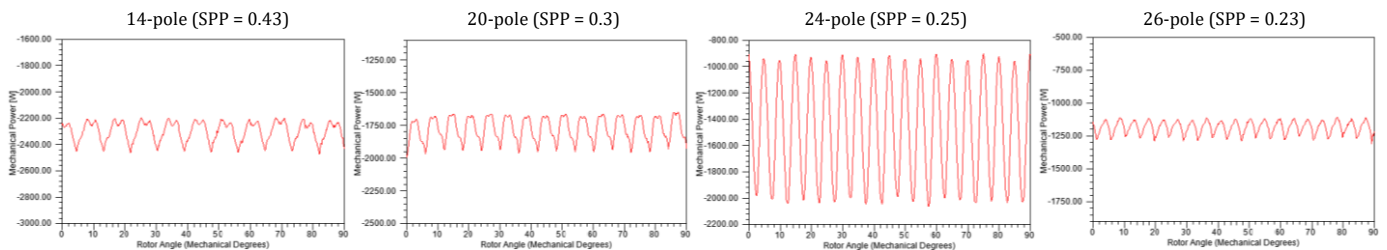


Figure 107: Measured mechanical power supplied to the machine

The average mechanical power and the percentage ripple of the mechanical power waveform are presented in Figure 108. The average mechanical power decreases steadily as the number of poles increases. The ripple observed rises to a peak for the 24-pole machine and then reduces.

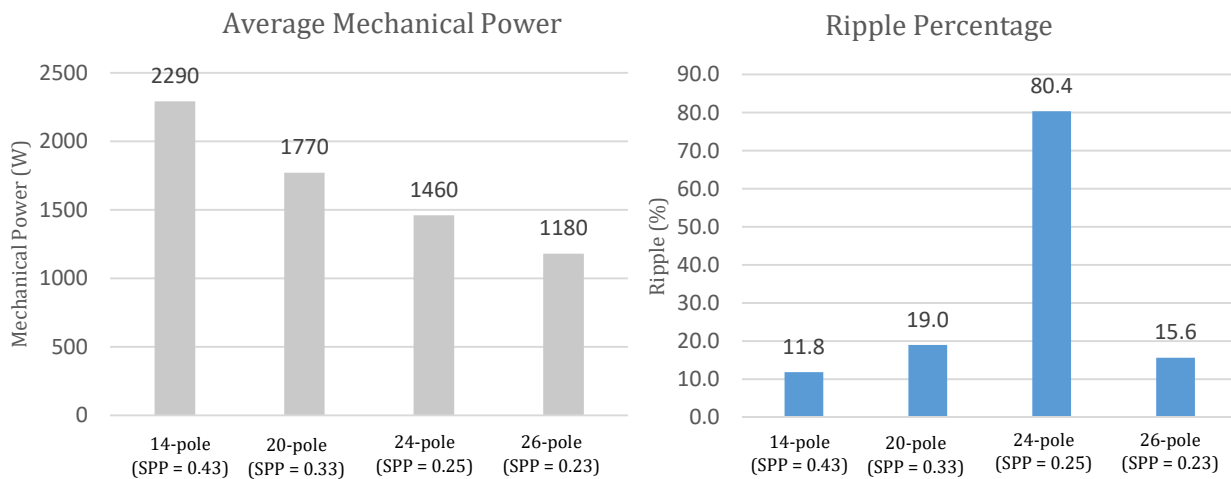


Figure 108: (left) Average mechanical power supplied (right) Percentage mechanical power ripple

4.6.3.6 Efficiency

The efficiency is calculated using the integration of the electrical power dissipated in the load and the integration of the mechanical power supplied to the machine. It does not take into account mechanical losses such as windage or friction, and the copper losses do not take into account the effect of different end-winding lengths for the machines.

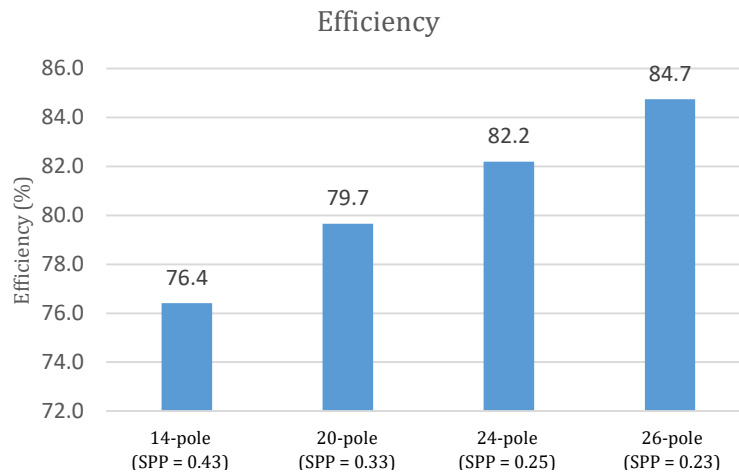


Figure 109: Calculated efficiency of the machines

Figure 109 shows that the efficiency of the machines increases as the pole number increases, with a significant discrepancy between the lowest and highest efficiency values. This change in efficiency is due to the copper losses. As the output voltage is constant, any increases in power delivered is a result of increased current and therefore increased copper losses. As the lower-pole machines generate higher power, they will incur greater copper losses. Therefore, in this case the efficiency graph does not accurately represent the comparative performance of the machines as it is highly dependent on power output. That is, the 26-pole would have similarly reduced efficiency if it supplied increased power and current.

4.6.4 Summary of Battery Load Analysis Findings

In this section the proposed designs were simulated in a battery charging configuration using a 48V battery. The findings showed that:

- As the battery voltage is increased, the power delivered to the battery is also increased
- As the pole number of the machine increases the power delivered to the battery is also increased
- The THD of the source current is generally very low

4.7 Design Summary and Evaluation

Several rounds of testing have been performed on the generator designs. The final section of this chapter presents a scoring chart that attempts to provide a ranking of each design's performance. Each design is assigned a score from 1 to 5 based on the performance in the applicable category. These scores simply give an indication of the performance of the generator designs with respect to each other and are not a definitive evaluation. A summary of each design will provide comments on the performance to complement the scoring. The scoring chart is provided overleaf.

	6-pole	14-pole	20-pole	24-pole	26-pole
Magnetic Characteristics					
Core Saturation	2	2	3	4	5
Sinusoidal No-Load Flux Linkage	1	3	4	4	4
Average Airgap Flux Density	1	3	4	5	5
Open-Circuit Operation					
Cogging Torque	2	5	5	1	5
THD	1	2	5	3	5
Induced EMF	1	3	5	5	5
Crest Factor	1	3	5	5	5
Core Losses	5	3	2	1	1
Three-Phase Operation					
Torque Ripple	3	5	5	1	5
Load Current	1	4	5	5	5
THD	1	2	3	5	4
Load Power	1	3	5	5	4
Efficiency	3	4	4	5	5
Voltage Regulation	5	5	3	2	1
Variable Load Operation					
Steady State Voltage	2	3	4	5	4
Maximum Power	1	5	5	4	3
Efficiency	1	4	4	4	4
Variable Speed Operation					
Maximum Power	1	5	4	3	2
DC Operation					
Torque Ripple	3	3	3	1	5
Load Current	1	5	5	5	5
THD	1	2	3	4	4
Load Power	1	5	5	5	5
Efficiency	1	4	5	5	5
Voltage Regulation	4	4	2	2	2
Variable Load Operation					
Steady State Voltage	1	3	4	4	3
Maximum Power	1	4	4	3	2
Efficiency	5	5	5	5	5
Variable Speed Operation					
Maximum Power	2	5	3	3	2
48V Battery Operation					
Torque Ripple	-	4	4	1	5
Load Current	-	5	3	2	1
THD	-	3	5	5	5
Load Power	-	5	3	2	1
Efficiency	-	2	3	4	5
Total Scores					
Total / 165	53	123	132	118	127
Total / 100%	37.9	74.5	80.0	71.5	77.0

6-pole Machine

The 6-pole machine scored 37.9% in the evaluation and was ranked 5th of the 5 designs. This design was repeatedly shown to operate poorly at the rated speed and is unsuitable for a direct-drive applications because of this. The main shortcomings of this design were the high cogging torque, high total harmonic distortion, and low output voltage.

14-pole Machine

The 14-pole machine scored 74.5% in the evaluation and was ranked 3rd of the 5 designs. This design was seen to work much more effectively at higher loads, and higher speeds. This machine may have applications in a higher-speed application. The main shortcomings of this design were high THD, and reduced power output at low speeds.

20-pole Machine

The 20-pole machine scored 80.0% in the evaluation and was ranked 1st of the 5 designs. This design worked effectively through different loading ranges and offered low cogging torque and low THD while still maintaining high power output. This machine performs highly across the whole series of tests. However, this machine does not exhibit the best characteristics in any aspect. It is ranked the highest due to its consistency across the tests.

24-pole Machine

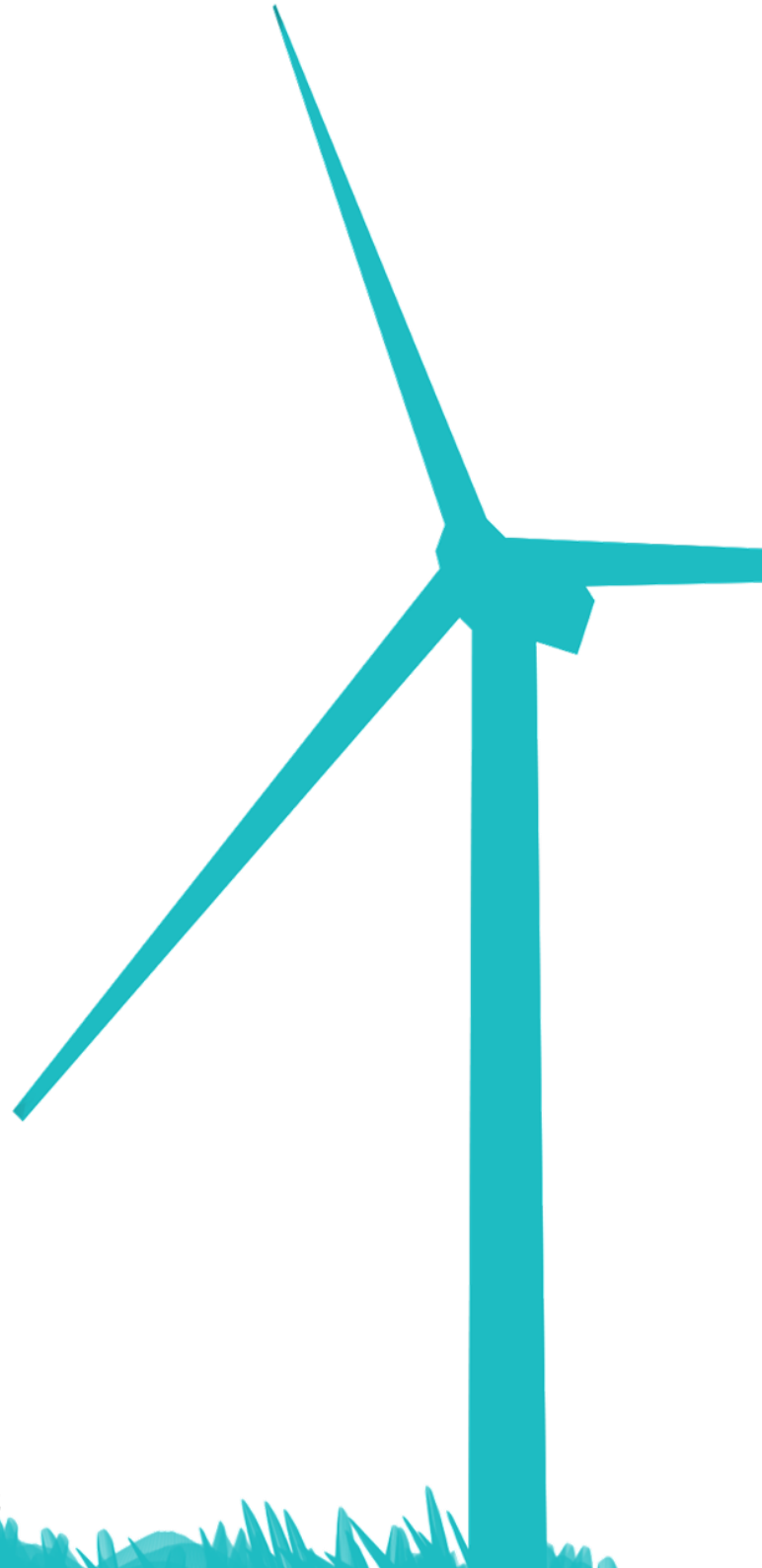
The 24-pole machine scored 71.5% in the evaluation and was ranked 4th of the 5 designs. This design offered high output power and the lowest THD of the machines. However, this design is unusable in its current form due to the excessive amount of cogging torque. The torque ripple observed in each of the tests is severe enough to prevent the machine operating. The design would only be feasible if shaped magnets or stator skewing were used to significantly reduce the cogging torque.

26-pole Machine

The 26-pole machine scored 77.0% in the evaluation and was ranked 2nd of the 5 designs. This design offered low THD, the highest efficiency, and the lowest cogging/ripple torque out of the proposed designs. The main shortcoming of this machine was the low power output. If the power density of the machine is not highly important in an application, this is the best performing machine design.

Chapter 5

Prototyping



5.1 Introduction

Prototyping one of the proposed designs is a desirable project objective. Prototyping can be used to validate simulations, and to test the design in practical applications. Unfortunately, due to budget constraints, it was not possible to build the proposed design. This chapter presents an alternative generator design in lieu of the proposed design presented in the main body of the thesis. This chapter is intended to be a standalone chapter as it does not directly relate to the findings presented in the main text. The process of creating the alternate design is presented in this chapter, with simulations, analysis, and preliminary experimental measurements. The chapter concludes with further direction for this project, and how the alternate generator design may be used to validate the effects of the pole-slot combination that were presented in the main body of the thesis.

5.2 Alternative Build Design

As a prototype of the proposed design could not be realised, an alternative build is proposed. The idea of the alternative is to source and modify a motor with similar characteristics. The motor would be converted into a generator and used to test different combinations of SPP, and the measured values compared against theoretical simulated results. The simplified flow of operations is shown below:

1. Identify suitable motor for conversion
2. Convert motor into generator
3. Model generator in Maxwell/Simplorer and perform preliminary simulations
4. Design and build test rig
5. Test generator and compare with expected results
6. Build new rotor with modified SPP and repeat step 5

Although these are the desired objectives, time, budget, and system constraints prevented the work from being fully realised.

5.2.1 Identification of Suitable Motor

Although small generators are available on the market, they are typically quite expensive. Additionally, generators of any wattage are rarely discarded except for cases where the machine has developed a fault. Conversely, electric motors can be found in almost every whitegoods appliance, and are often discarded in working condition. The main motors used in these appliances are induction motors, and permanent magnet motors are rarely used.

5.2.1.1 Induction Motors

Induction machines are highly efficient, and use field coils to create the magnetic field required for operation. This is the first problem, as this entails coils in the stator and the rotor. This type of motor can be roughly converted to a Permanent Magnet Generator (PMG) by removing windings in either the stator or the rotor, and replacing them with magnets. However, the resultant generator would be significantly different from the studied topology as induction machines usually contain distributed windings, have fewer slots, are inner-rotor, and have a markedly different diameter to length ratio compared to the proposed design.

5.2.1.2 Permanent Magnet Motors

A less common type of machine used in appliances is a permanent magnet motor. These would be ideal for conversion. It was found that Fisher and Paykel are one of the few manufacturers that use permanent magnet motors in their washing machines. The series of washing machines that utilise this motor is called the Fisher and Paykel SmartDrive series.

5.2.1.3 Fisher and Paykel SmartDrive

The F&P SmartDrive is a unique motor among whitegoods. It utilises an outer-rotor, direct-drive, permanent magnet motor that is electronically commutated. This type of machine is very similar to the proposed design.

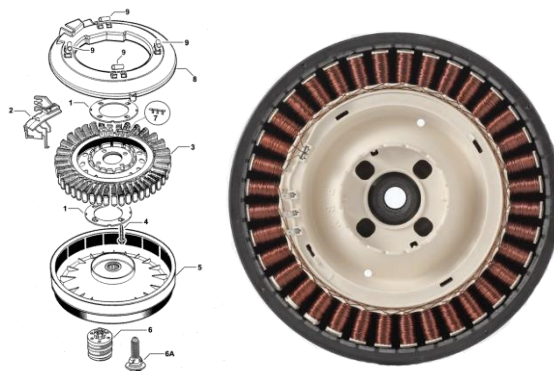


Figure 110: (left) Blown-up diagram of the SmartDrive (right) front view of the SmartDrive [28]

The SmartDrive comes in several different models and sizes. The different sizes are simply scaled versions used for differently sized washing machines. Different models, however, can differ significantly in design. Following is a list of the different models that could be identified:

(1990-1992)

- **100 Series (NIB):** 42-Slots, 56-Poles, 1.00mm Copper Wire, NdFeB Magnets

(1992-2004)

- **100 Series (Fe):** 42-Slots, 56-Poles, 1.00mm Copper Wire, Ferrite Magnets
- **80 Series:** 42-Slots, 56-Poles, 0.80mm Copper Wire, Ferrite Magnets
- **60 Series:** 42-Slots, 56-Poles, 0.60mm Copper Wire, Ferrite Magnets

(2004-Current)

- **M Series (Al):** 36-Slots, 48-Poles, 0.60mm Aluminium Wire, Ferrite Magnets
- **M Series (Cu):** 36-Slots, 48-Poles, 0.60mm Copper Wire, Ferrite Magnets

The motor that most closely approximated the proposed design is the SmartDrive. No other motors were found to be suitable to a similar degree. The most suitable of the SmartDrive models is the 100 Series (NIB). This motor used NdFeB magnets, as well as much thicker wire. However, this is a more uncommon motor due to its age.

The sourced motor is an 80 Series SmartDrive salvaged from a broken 5.5kg washing machine. The motor is rated at 165W. The much lower phase resistance of a 100 Series ($\approx 1\Omega$) compared to the 80 Series ($\approx 6\Omega$) is desirable, however, due to its rarity, the 100 Series could not be sourced.

5.2.2 Motor Modelling

The next stage of the process is the modelling of the Fisher and Paykel motor. Similarly to the proposed design, this is performed in ANSYS Maxwell 2D/3D, RMXprt, and Simplorer.

5.2.2.1 2D/3D Modelling

The design is modelled to give an idea of the machine performance when working as a generator. Once the motor was sourced, the dimensions were measured and a 2D model and a 3D model were created. There are difficulties measuring dimensions due to the plasticised nature of some parts of the motor. The Fisher and Paykel uses a mostly plastic stator and rotor that encases the core. Due to this, some of the dimensions are estimated using the measured thickness of the plastic.



Figure 111: Picture showing the plastic coating of the stator, with exposed iron at the tips [28]

The other problem with modelling the system is the strength and orientation of the ceramic magnets in the rotor. The magnets are arranged in ceramic blocks that contain four poles per block. The orientation of the magnets is also slightly skewed, to reduce cogging torque. These attributes could not be measured accurately, and the datasheet did not make the information available. The magnets are modelled simply as standard grade C5 ceramic magnets, with no skew. Although this is not expected to give accurate simulation results, it helped give a ballpark figure as to the back-EMF, and other machine parameters.

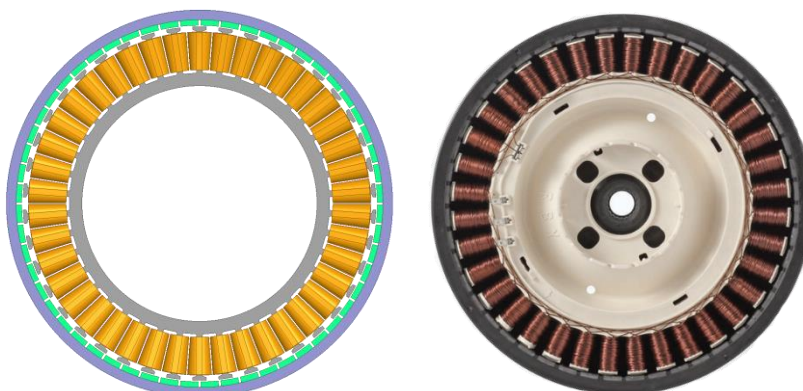


Figure 112: (left) 3D motor model (right) SmartDrive motor [28]

5.2.2.2 Open Circuit Simulation

The 2D modelled design is tested under open circuit conditions. This is to determine the open circuit voltage that could be expected at the rated speed of 200 rpm.

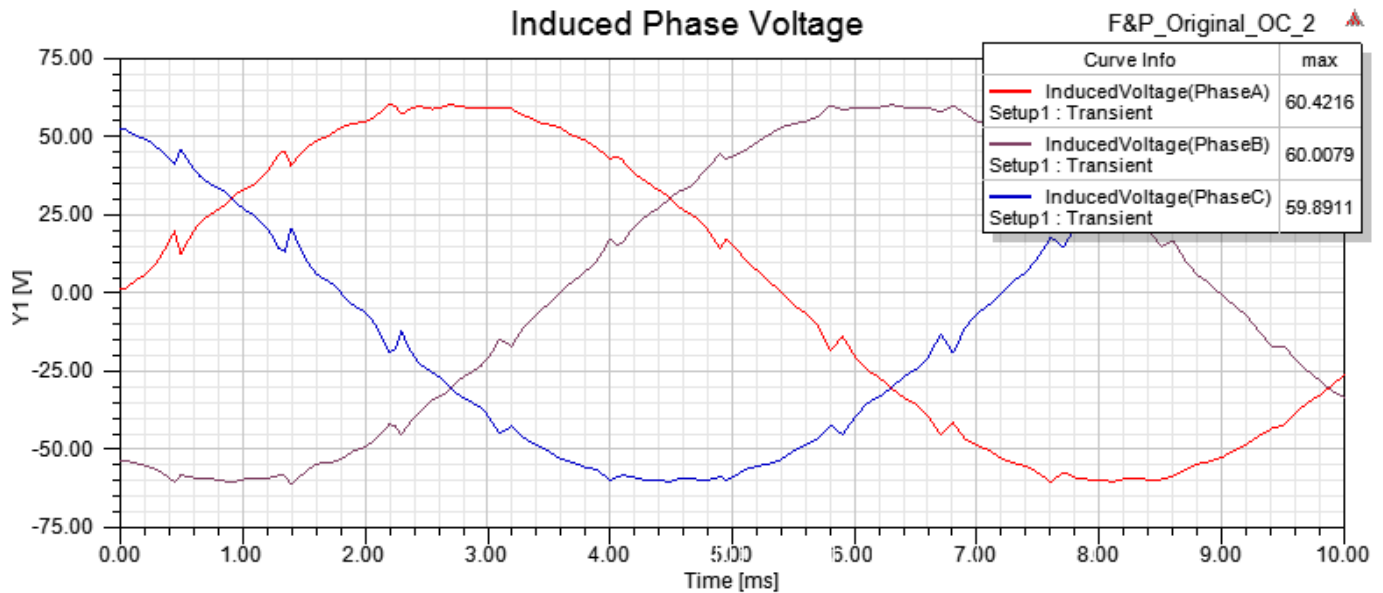


Figure 113: Induced phase voltage simulated under open circuit conditions

Figure 113 shows the induced phase voltage is approximately 60V peak at 200 rpm. The voltage was found to get as high as 170V peak at 1000 rpm. The cogging torque is measured and found to have a low peak-to-peak value of approximately 1.4 Nm.

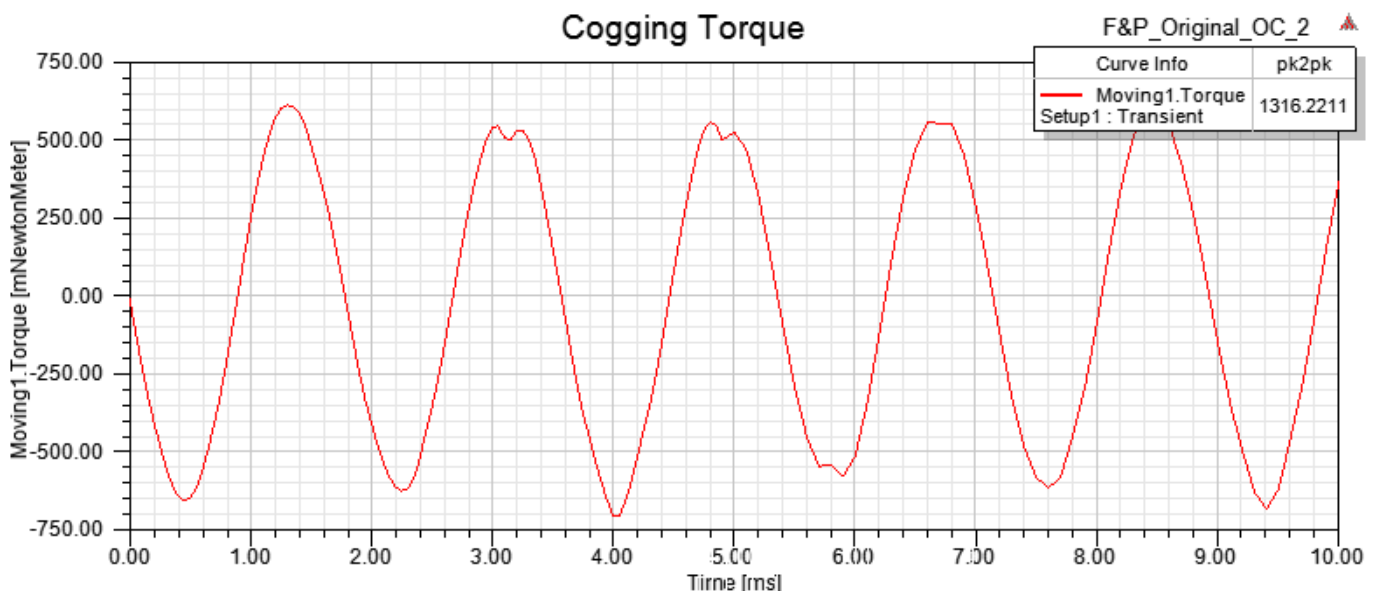


Figure 114: Simulated cogging torque of the SmartDrive in mNm

5.2.3 Motor Conversion

The next stage is to determine how to convert the motor into a generator. As noted previously, it is difficult to convert an induction machine, or other motor that uses field coils. However, the SmartDrive is a permanent magnet motor, and therefore should require much less reworking. The main process for conversion consists of two main stages: rewiring of the coils, and replacing the rotor magnets.

5.2.3.1 Rewiring Coils

The process of rewiring coils is necessary due to the high voltages of the machine in regular operation. The machine uses three-phases, and therefore has three groups of 14 coils. These coils are wired in series, such that the phase voltage generated is the addition of all the induced coil voltages. This also causes the phase resistance to be significant. The 80 series motor has a phase resistance of 6.1Ω .

The high voltage generated by the motor is problematic as it is potentially dangerous. As this generator would likely be used for charging a 12V, or 24V battery, the voltage is unnecessarily high. The high phase resistance poses a problem as this will induce very large copper losses, especially for high current applications such as battery charging.

To reduce the voltage and the phase resistance, the coils of a single phase are to be reconnected into two parallel groups of 7. As there are 14 coils, there are a very limited number of possible combinations that can be used. The available combinations are:

- 1 Group x 14 Coils Per Phase
- 2 Groups x 7 Coils Per Phase
- 7 Groups x 2 Coils Per Phase
- 14 Groups x 1 Coil Per phase

It was found that the initial winding pattern was not suitable. 7 parallel groups would not be able to produce a high enough voltage to charge batteries at direct-drive speed, which also rules out using all 14 coils in parallel. The remaining option is the coil arrangement that used 2 parallel groups of 7 coils per phase. This configuration would halve the phase voltage, while increasing current and reducing phase resistance.

5.2.3.2 Replacing Magnets

The motor is rated at 165W, and uses weak ceramic magnets in the rotor. To generate 1kW of power it would require more powerful magnets. However, the stock ceramic magnets were not replaced due to a combination of budget and system constraints.

The main reasons that powerful NdFeB magnets were not used are high expected levels of copper losses and core saturation. The magnet wire is only 0.80mm in diameter, and after rewiring has a phase resistance of 1.6Ω. This resistance would incur heavy losses in the system, which would be dissipated as heat. NdFeB magnets are highly sensitive to heat, and would likely be demagnetised quickly. The saturation of the core also prevents the use of NdFeB magnets. The amount of steel used in the motor is very small, which is suitable for supporting the flux of the weak magnets. However, introducing significantly stronger magnets would push almost all the iron into saturation, resulting in high output THD and greater core losses. Again, this would be dissipated in heat and could potentially burn the generator out.

The solution to the increased copper losses is to individually rewind the entire stator with thicker wire in order to reduce the resistance and increase the current carrying capability of the wire. This is a tedious, time-consuming, and difficult process, and may not be able to be realised due to the limited stator slot area. The rewiring is not carried out for these reasons.

The saturation of the core can be reduced by using slightly weaker magnets, that is, weaker grades of NdFeB.



Figure 115: Regrouped stator with rotor and shaft attached

5.2.4 Test Rig Design

The next section of the prototyping process is the testing rig. The rig should enable testing up to 300 rpm, to measure voltage, current, and power output of the machine.

The ideal design for the testing rig would use a speed controlled DC machine directly coupled to the SmartDrive shaft. This would allow the input power and output power to be measured at precisely controlled speeds. Again, due to budget constraints, this was not realised.

5.2.4.1 Mechanical Design

The actual testing rig was designed and built using available parts in order to create a rudimentary testing setup. The setup is shown below.

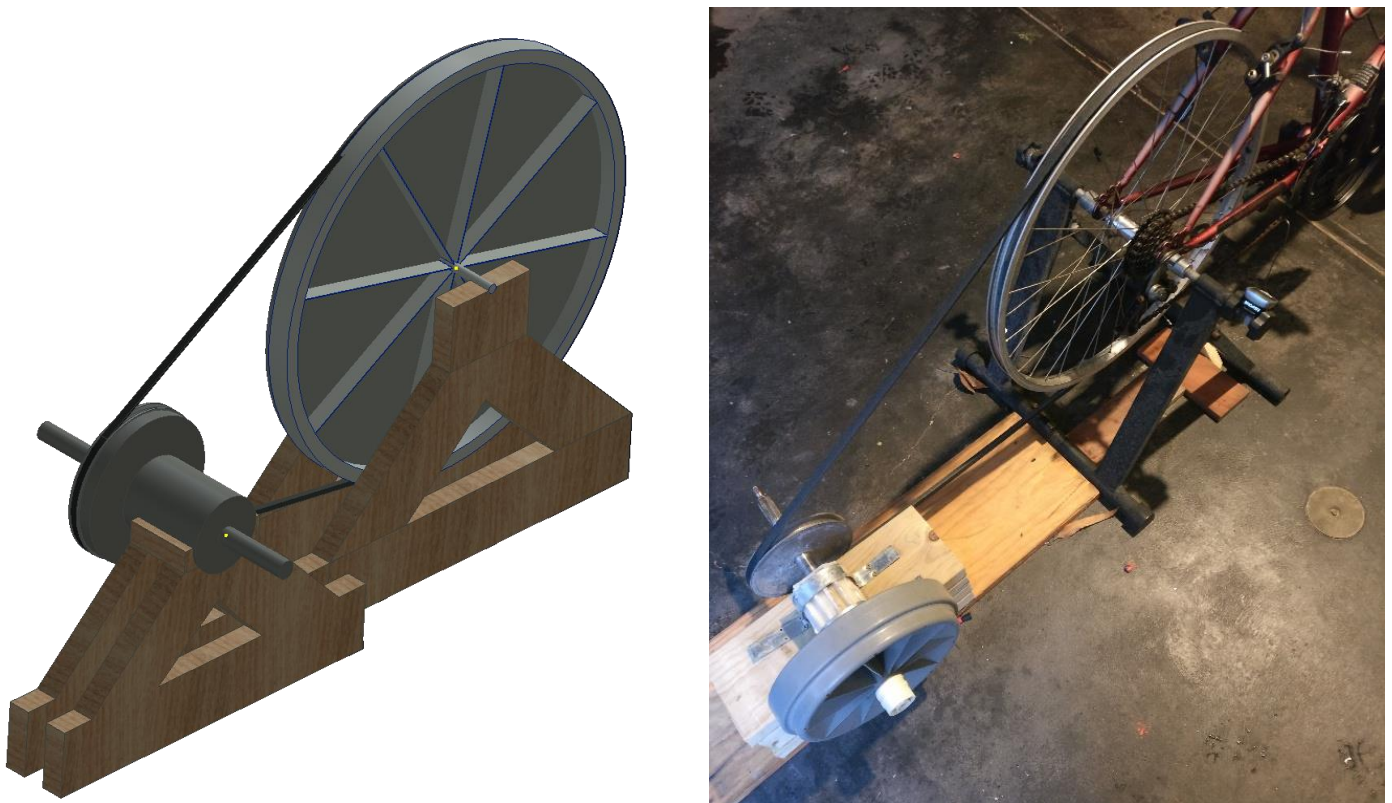


Figure 116: (left) 3D mock-up of testing rig (right) implemented build

The testing rig used a bicycle wheel to supply the mechanical power to the shaft of the generator. The bicycle wheel can be consistently rotated between 10 rpm to 100 rpm. The bicycle is an ideal candidate as it includes a gearing system to increase speed, and also features a tachometer. A pulley is placed on the SmartDrive shaft, and a V-belt is used to couple the bicycle and the generator. The main drawback to the system is that there is no method of measuring input mechanical power. Adding a heavy flywheel would maintain speed with a greater consistency at high electrical loading.

5.2.4.2 Speed Measurement

Speed measurements are an essential part of the testing procedure. The bicycle wheel uses a hall-effect sensor tachometer. This could be used in combination with the known ratio of wheel and pulley diameters to determine the speed of the generator.

However, measuring the speed had several shortcomings which reduced the reliability of the readings. The first is that the minimum speed measured is 2.0 km/h. The second is that the sensor refreshed every revolution, which ultimately is a low refresh rate, especially for lower speeds. The resolution of the sensor is 0.2 km/h, which corresponded to ≈ 6.4 rpm. To increase the precision of the results, the readings are taken as the average over multiple tests.



Figure 117: Tachometer in the setup used for speed measurement

5.2.4.3 Electrical Measurements

The electrical measurements of the prototype include the terminal voltage, the load voltage, and the load current. The first test is in open circuit operation, to measure the open circuit voltage. This is performed using a multimeter between two phase terminals.

The second test measures load voltage, load current, and power through two different types of loads, similar to the setups used for the simulations.

Incandescent Load

The first load is six 12V, 20W incandescent bulbs. These are wired with two bulbs in series per phase. These are used as the initial test loads as they have a resistance value that increases as the temperature increases. This helps prevent the load from drawing too much power. No measurements are recorded for this load.



Figure 118: Three-phase incandescent bulb load

Three-Phase Resistive Load

The three-phase resistive load is a combination of 24 5W, 47 Ω resistors. Each phase has a group of 8 resistors wired in parallel, such that the resistance is $\approx 6\Omega$ and has a power rating of 40W.

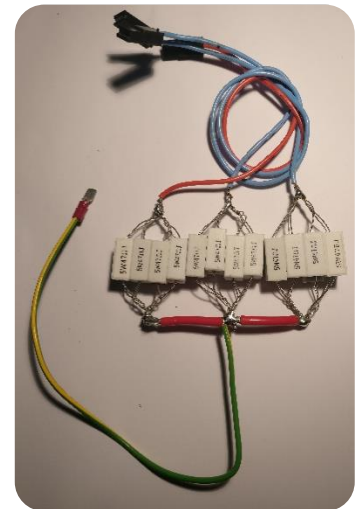


Figure 119: Three-phase resistive load

Rectifier and Resistive Load

The rectifier is built using the same circuit setup as in the simulations: a full-wave bridge rectifier using 6 diodes. The diodes had a low current rating and so each diode is replaced by a combination of two parallel diodes. The resistive load used is the three-phase resistive load, although using rearranged connections to present a 3 Ω load rated at 80W.

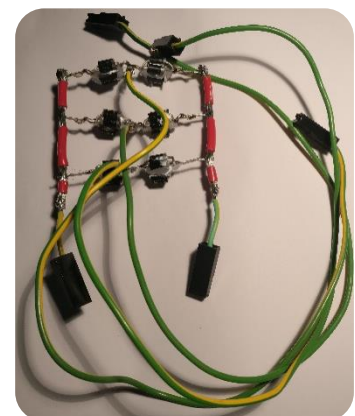


Figure 120: Three-phase bridge rectifier

5.2.5 Generator Testing and Results

The generator tests extended from 80 rpm to 300 rpm, with increments of 20 rpm. 80 rpm is the lowest speed measured by the tachometer. The three tests are:

- Open Circuit
- Three-Phase Resistive Load
- Rectifier and Resistive Load

It was desirable to test the generator with a battery, however, there were none available, and it was too expensive to purchase one.

5.2.5.1 Open Circuit Test Results

The open circuit test results showed that the simulation gave results that are significantly higher than obtained in the tests. This is most likely due to the difference in magnet strength in the real and simulated machines. The SmartDrive was also recovered from an old, broken washing machine, and demagnetisation may have occurred through the life of the product.

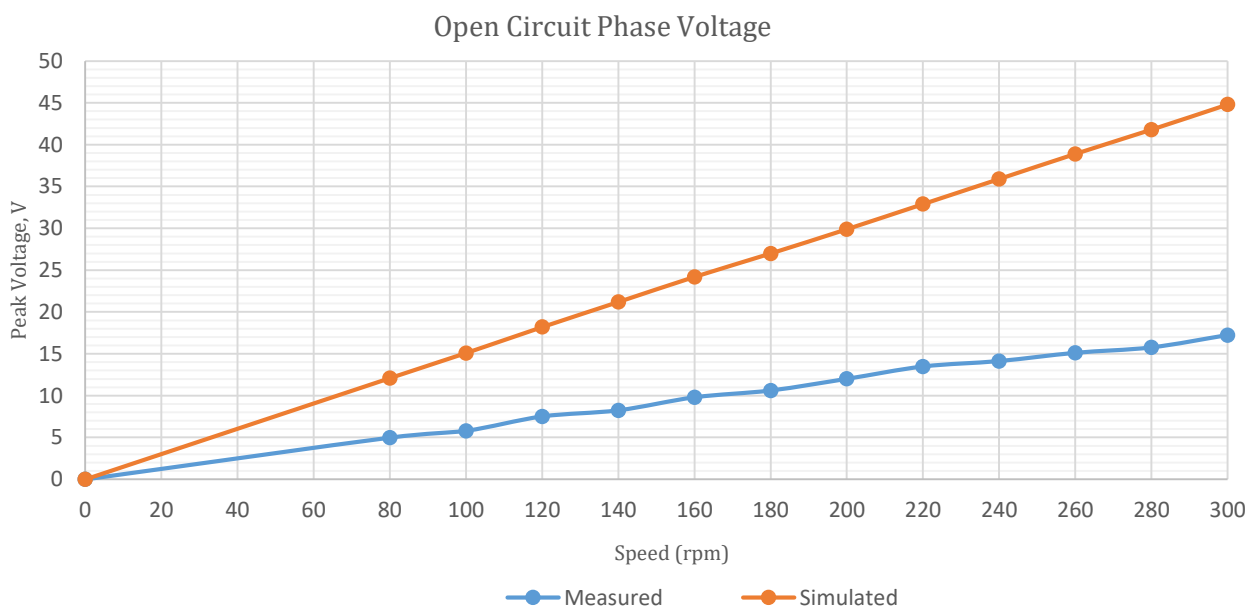


Figure 121: Plots of the phase voltage as obtained by measurements and simulation

Although the voltage is lower than expected, it can still generate 12VAC at 200 rpm. If this is used with a rectifier, the DC voltage will increase to approximately 20 VDC. This is still a very useful voltage level for battery charging capabilities.

5.2.5.2 Three-Phase Resistive Load Results

The three-phase resistive load is the next test. The three main measurements are the load voltage, load current and load power.

5.2.5.2.1 Load Voltage

The RMS voltage over a single phase load is measured and is presented in Figure 122. The voltage shows a linear increase as expected. The voltage curve will eventually reach an asymptote, but as the speed range measured is small, the voltage curve is still linear in this region.

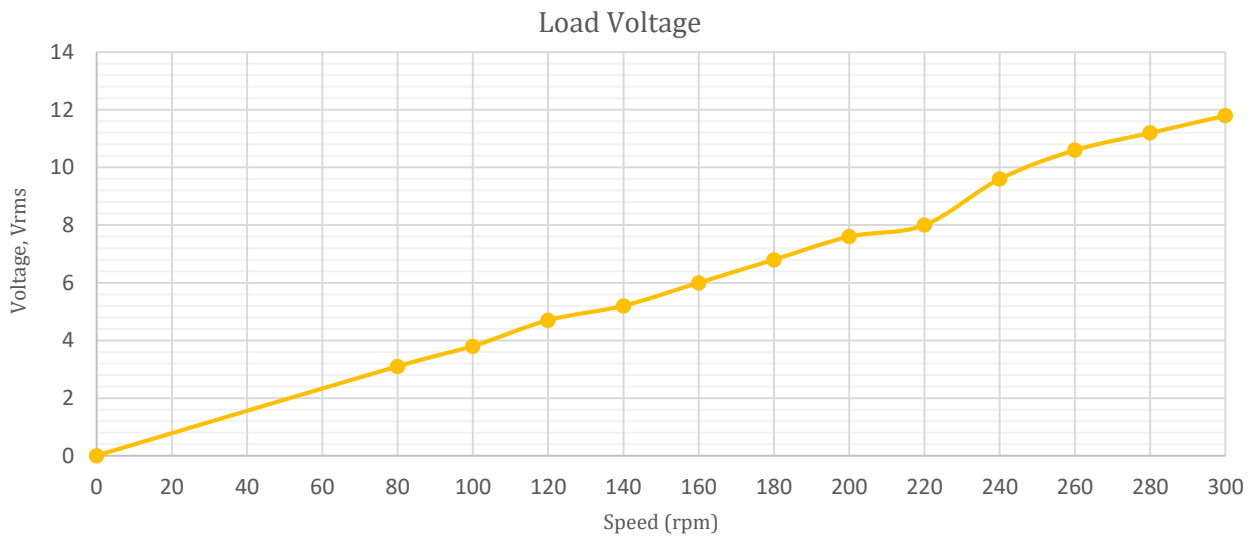


Figure 122: Measured single phase load voltage from the three-phase load

5.2.5.2.2 Load Current

The load current through a single phase is shown in Figure 123. The curve is also linear in this

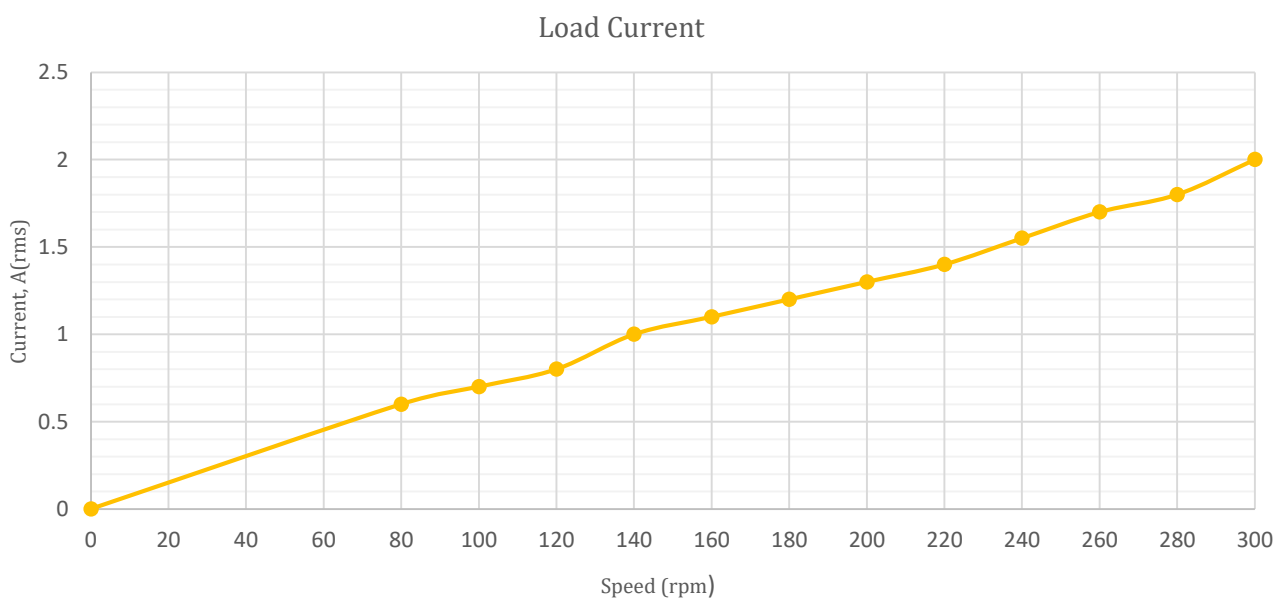


Figure 123: Measure load current from a single phase in the three phase load

5.2.5.2.3 Load Power

The load power is calculated as the product of the RMS load current and RMS load voltage and multiplied by the three phases.



Figure 124: Load power calculated for the three-phase resistive test

The load power reaches 70W in total. This is very far from 1kW, however, this amount of power is a respectable amount given it is using weak ferrite magnets, and a small 165W motor.

5.2.5.3 Rectifier and Resistive Load Test Results

The rectifier is attached to the three phase terminals to convert the three-phase AC into a single DC output. This is attached to the resistive load that is reconfigured into 16 parallel 5W 47 Ω resistors. This presented a 3 Ω load rated at 80W. This is necessary as the power is expected to be greatly in excess of the previous power rating of 40W.

5.2.5.3.1 Load Voltage

The load voltage shown in Figure 125 initially increases linearly, but begins tapering off at higher speeds. This indicates that it is reaching the maximum voltage for this load. The rectified voltage is 14V at 200 rpm, which is ideal for charging a 12V battery.

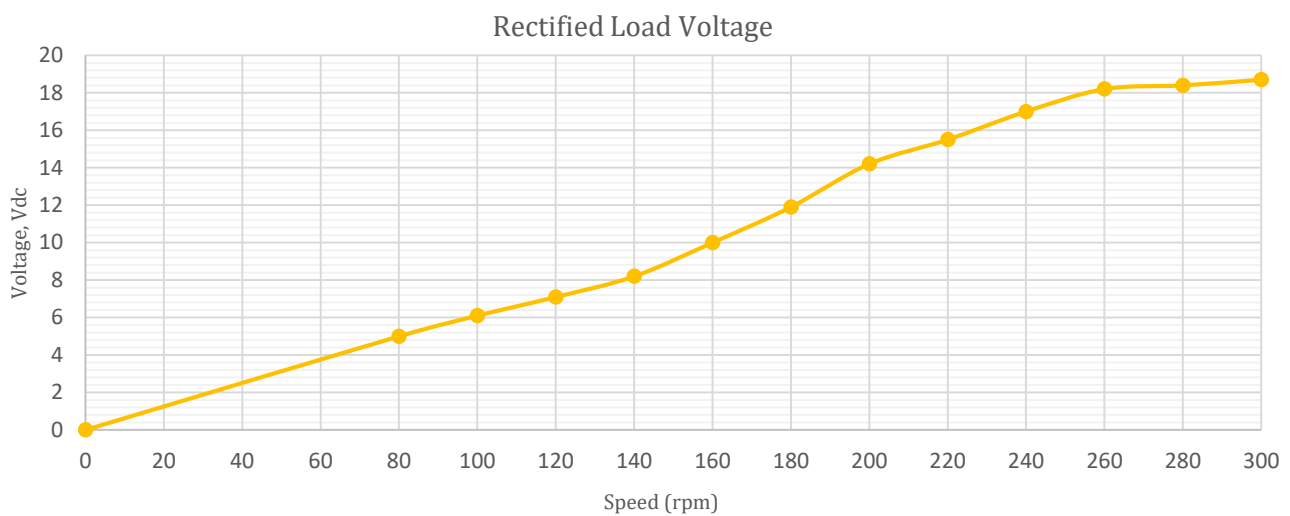


Figure 125: Measured voltage over 3 Ω load with rectified output

5.2.5.3.2 Load Current

The load current in Figure 126 follows a linear pattern, and steadily increases to a maximum of 6.5A. This is a high current output, also suitable for charging a battery.



Figure 126: Measured current over 3 Ω load with rectified output

5.2.5.3.3 Load Power

The load power of the load increased quadratically for the first section up to ≈ 200 rpm, and then increased linearly. At 200 rpm it produces 65W, and at 300 rpm produces 120W. For a 165W motor with the weak ceramic magnets, this is an acceptable power level. Replacing the magnets with NdFeB magnets could reasonably be expected to increase the power output by at least five times.

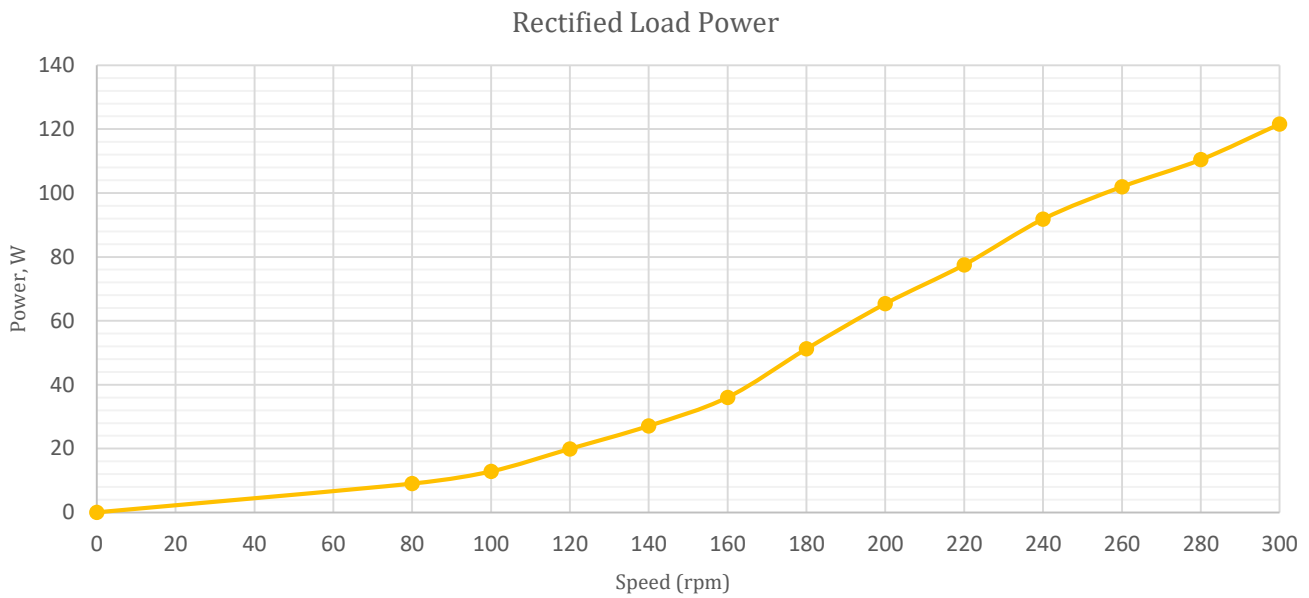


Figure 127: Calculated power over 3Ω load with rectified output

5.3 Further Conversion

The next step in the prototyping process would be to replace the magnets in the rotor with significantly stronger NdFeB magnets. The machine would be tested at low speeds to verify the thermal aspects of the design, as the NdFeB magnets can be permanently damaged by heat. Only if absolutely necessary, the windings from the stator would be rewound with lower gauge wire to reduce copper losses and prevent the generator from burning out.

At least two different SPP values would be chosen when replacing the magnets. The results from these generators would be compared to simulated results to verify the simulation data. The simulation results are presented in the following sections.

5.3.1 Pole-Slot Combination of Prototype

One of the main objectives of the prototyping process is to verify the results obtained in simulation for the proposed PMG design. Therefore, the SPP of the prototype must be chosen such that it is possible to measure and compare significant results from the prototype and simulation. A wide range of SPP values are chosen in order to determine suitable candidates. The combinations chosen are as follows:

Table 11: Proposed pole-slot combination for the prototype machine

Poles	14	32	46	48	56	60	72
SPP (42-Slots)	1.00	0.44	0.30	0.29	0.25	0.23	0.19

Significant SPP values such as 1 and 0.25 are chosen to verify previous findings, while others are selected based on performance parameters developed using RMXprt.

5.4 NdFeB Prototype Preliminary Simulations

The various machines are simulated in Maxwell 2D and Simplorer. The machines are simulated to choose two variants to be implemented as prototypes. As the previous simulations of the SmartDrive are inaccurate due to incomplete data concerning the magnets, replacing the magnets should result in a much more reliable simulation. It is important to note that some graphs are used to compare relative values and as such do not have the exact results labelled.

5.4.1 Open Circuit Tests

5.4.1.1 Peak Voltage

The peak voltage displays a parabolic trend as seen previously. As the number of poles increase, the voltage increases to a maximum, and then begins to reduce.

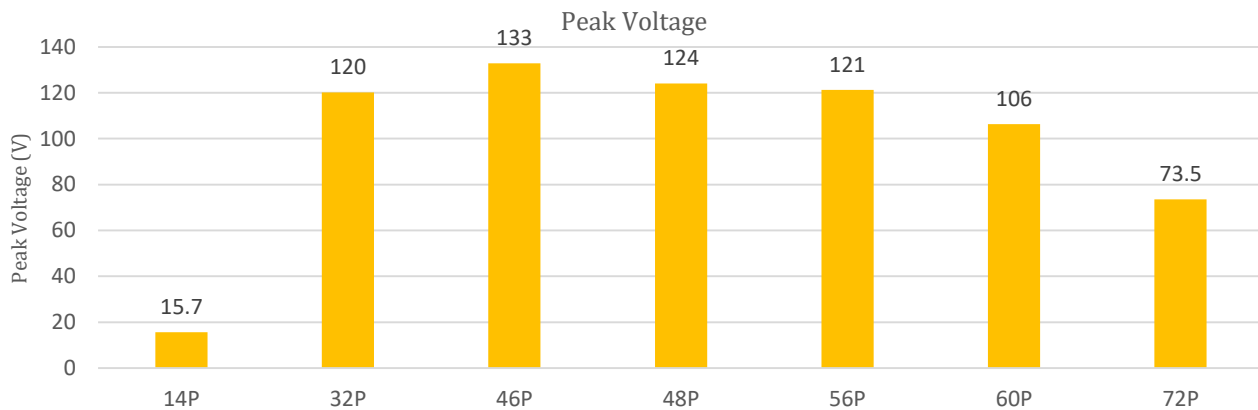


Figure 128: Peak voltage measured in open circuit tests for the F&P NdFeB generator variants

5.4.1.2 Cogging Torque

The cogging torque shows a decreasing trend as the number of poles increase. There are two very large values at 14-poles and 56-poles. The SPP values of these two machines are $\frac{1}{4}$ and 1, and are the only SPP values with a unity numerator. As noted previously, this is an indicator of high

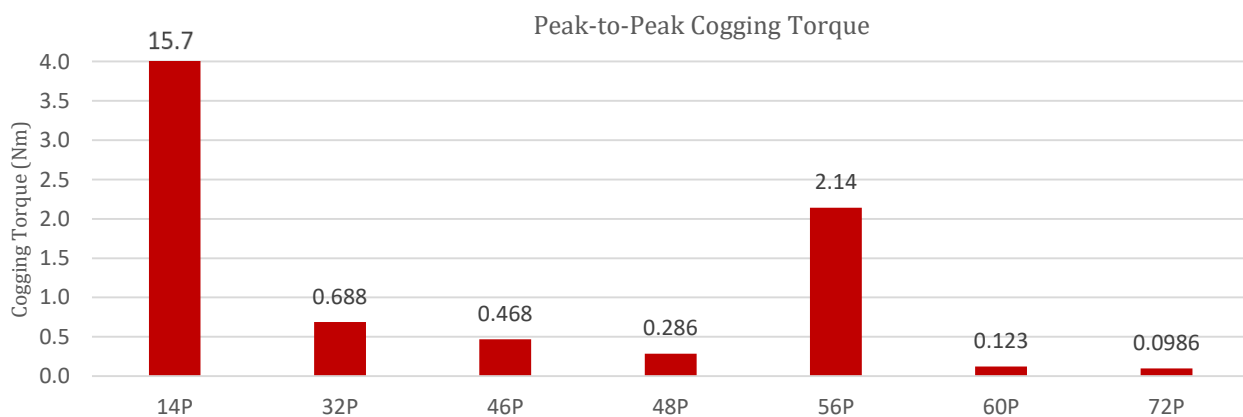


Figure 129: Cogging torque measured in open circuit tests for the F&P NdFeB generator variants

5.4.2 Battery Tests

The second test used Simplorer to model a three-phase rectifier and a battery load. The battery voltage is varied from 12V to 48V, similar to previous tests.

5.4.2.1 Electrical Power

The electrical power of the machines is seen to experience a considerable increase in power as the NdFeB magnets are added. The power can be seen to decrease as the number of poles increase, but the overall power increases as the battery voltage increases.

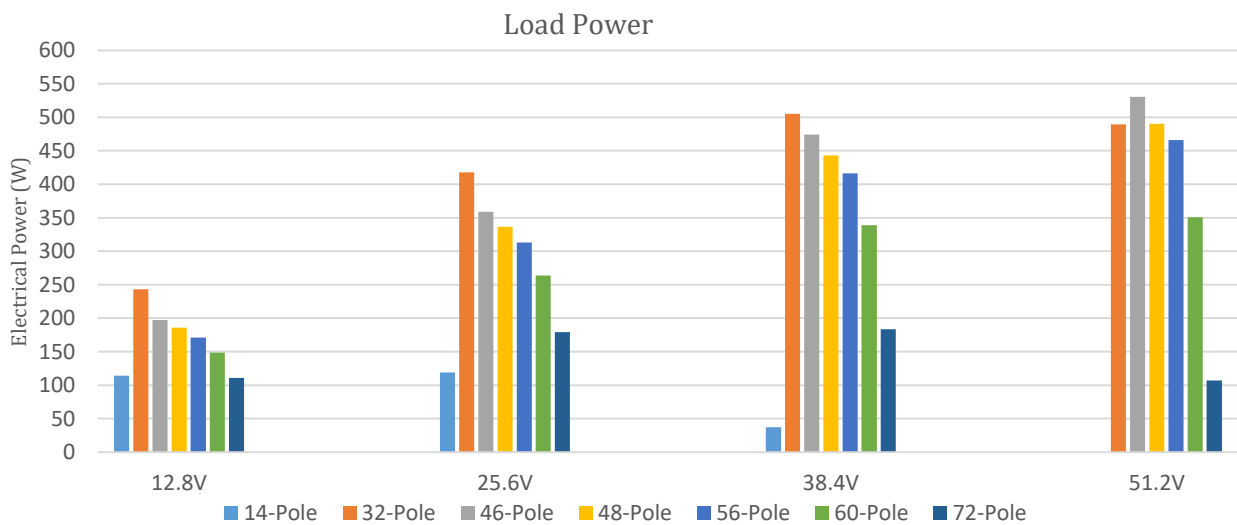


Figure 130: Load power simulated for the variants of the NdFeB SmartDrive

5.4.2.2 Torque

The torque requirements of the generator follow the same trends as seen in the load power.

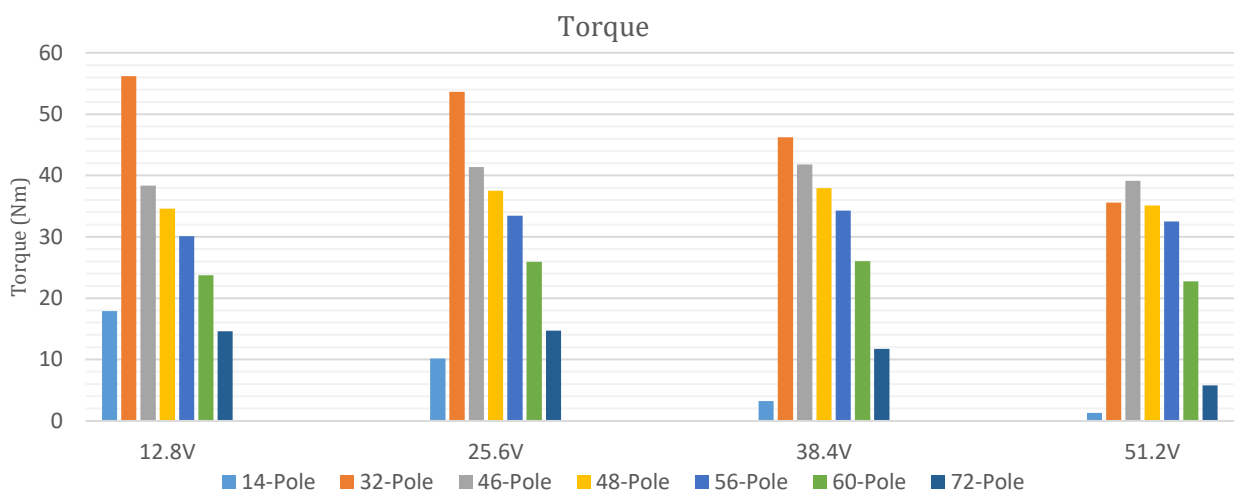


Figure 131: Torque simulated for the variants of the NdFeB SmartDrive

5.4.2.3 Efficiency

The efficiency of the machines can be seen to increase as the number of poles increases. The efficiency of the machines also increases as the battery voltage increases. This is expected, as the current draw should decrease.

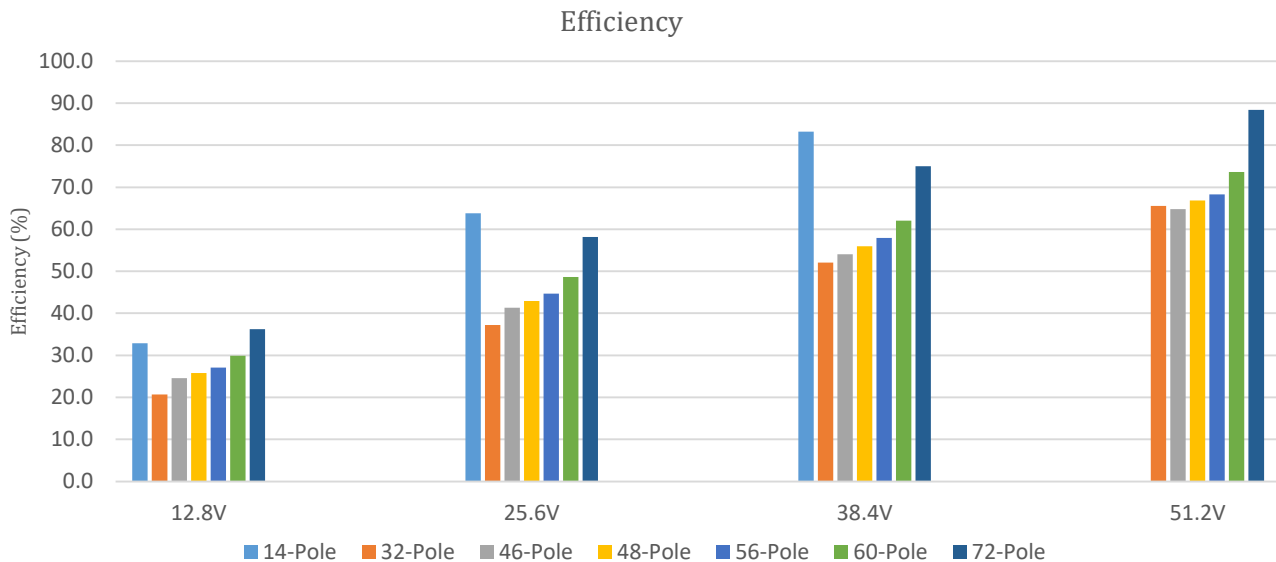


Figure 132: Efficiency simulated for the variants of the NdFeB SmartDrive

The efficiencies of the 14-pole and the 72-pole machines are deemed as outliers. This is mainly because their efficiencies tend to be much higher as their power output is essentially zero.

The overall efficiencies are very low in comparison to the 18-slot generator proposed in this thesis. This is mainly due to the high phase resistance of the windings in the SmartDrive. The SmartDrive motor is designed to be operated from a 240V source, and as such, can operate with low current draw, and high efficiency with a high phase resistance. However, when the voltage output is clamped to a much lower battery voltage, the current increases, which incurs much greater copper losses. These results illustrate the need for rewinding the stator with larger diameter wire to lower phase resistance.

5.4.2.4 Total Harmonic Distortion

The total harmonic distortion as the battery voltage increases is shown in Figure 133. It should be noted that the THD values of the 14-pole generator have been clipped. The THD is seen to generally increase as the battery voltage increases.

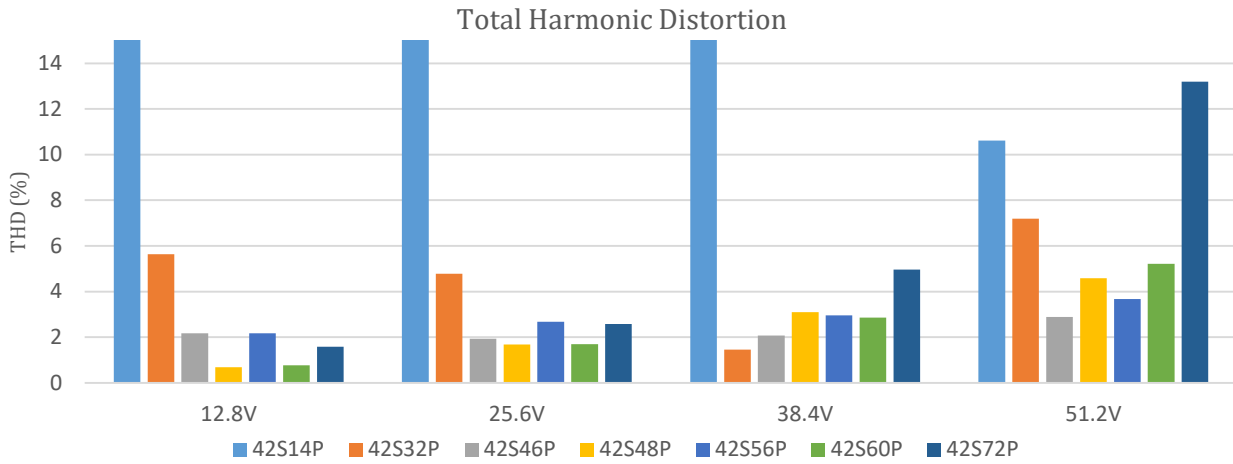


Figure 133: Total harmonic distortion for the F&P generator with various battery voltages

To illustrate how the THD is increasing, the source current waveforms and their respective amplitude spectrums are shown in Figure 134. These show that as the battery voltage increases the source current becomes less sinusoidal due to the increasing contribution of the fifth harmonic.

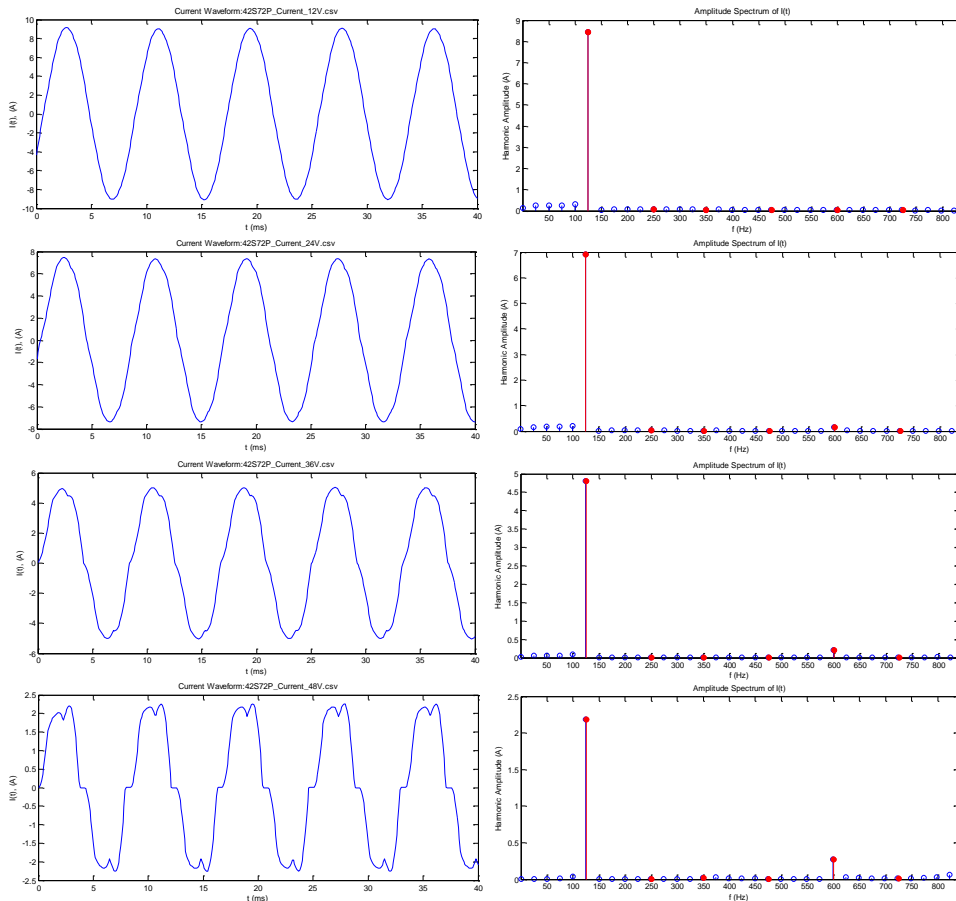


Figure 134: Winding current waveform and spectral plot for increasing battery voltage

5.4.3 Summary of NdFeB Conversion Analysis

The main purpose of these simulations is to determine which set of two pole-slot combinations would yield the most usable experimental results. Using the results from the simulations, the 48-pole and the 56-pole generators are chosen. These designs are shown to have satisfactory outputs and use a similar SPP to the design proposed in the main body of the thesis.

If the SmartDrive was converted using NdFeB magnets, the 48-, and 56-pole designs could be used to experimentally validate the findings presented in the main body of the thesis.

Chapter 6

Conclusions and Future Direction



6.1 Conclusion

This thesis evaluates the performance of a number of direct-drive surface permanent magnet machine variants with different combinations of slots and poles. A surface permanent magnet machine was designed for a direct-drive wind turbine application. Five variations of the machine were created by varying the number of poles in the design. The machines were studied in detail using finite element analysis. The study investigated the flux density, back-EMF, cogging torque, ripple torque, power delivered, total harmonic distortion, current output and power losses of the machine under open circuit, and loaded conditions. The simulation results were presented to provide useful insights on the effect of the pole and slot combination on the performance of the surface PM machine.

6.2 Key Findings

The measured effects of the pole-slot combination on the output characteristics of an outer-rotor surface permanent magnet generator are presented in the following sections.

Magnetic Flux

The magnetostatic simulation of the proposed machines showed that the flux density and flux linkage generally decreased as the number of poles increased due to the circulating flux between adjacent magnets through the stator teeth tops. Under full-load, the flux linkage experienced greater reduction as the number of poles increased, showing higher pole machines to have poor voltage regulation.

Open Circuit Operation

During open circuit operation it is found that the cogging torque is not highly correlated with an increasing number of poles, but instead by the particular pole-slot combination. Three different techniques are used to estimate the cogging torque and each achieved satisfactory results.

Three-Phase Operation

The proposed generators are simulated with resistive three-phase loads. At direct-drive speeds the designs experienced a parabolic trend in voltage, current, and power, reaching a maximum for the 24-pole machine. The THD is seen to decrease as the number of poles increases.

Rectifier Operation

A rectifier was used to convert the three-phase AC to DC. A resistive load was used to test the system. The results showed that the rectifier does not significantly affect the operation of the system. The rectifier was seen to slightly increase the THD of the source current.

Variable Load Tests

The variable load tests covered a range of resistance values for the resistive loads. The main outcomes showed that the lower-pole machines worked more effectively at high electrical loads, but much less effectively at low-loads, indicating reduced flexibility of operating conditions.

Variable Speed Tests

The variable speed tests covered a range of speeds for the resistive load configuration. Similarly to the variable load tests, the lower pole machines worked more effectively at higher mechanical loads. At direct-drive speeds of 200 rpm low-pole machines produced less output power compared to the other machines.

Battery Tests

The battery tests used a basic battery charging circuit configuration. It is found that the efficiency and delivered power significantly increased as the battery voltage increases. When the battery voltage is constant at 48V, the power delivered to the battery reduces as the number of poles increases.

Optimum Design

The most consistent performing design was found to be the 20-pole machine. This design worked effectively across the whole range of loadings, and exhibited satisfactory results for the measured outputs. The other highly performing design was the 26-pole design. This design has disadvantages regarding the voltage regulation and maximum power output, but offers the highest efficiency, lowest cogging torque, flexibility over a wide range of speeds and electrical loads, low total harmonic distortion, and low core saturation.

6.3 Further Direction

Optimisation of Other Parameters

This paper discussed the design and research into the optimisation of the pole slot combination, and presented the best performing designs out of the proposed machines. Further work may now be performed by optimising other characteristics such as the magnet shape, and winding properties.

Further Testing of the Machine

The tests provided in the main body of the thesis were not comprehensive. As such, more testing may be performed on the design, such as the machines' response to inductive and capacitive loads.

Prototyping of the Proposed Design

As the proposed design was not prototyped, the prototype and testing rig can be built for experimental validation of the simulation results.

Analysis into Salvaged Motor/Generator Turbine

The Fisher and Paykel washing machine motor was converted into a direct-drive generator. This topic could be further investigated to determine the feasibility of full-scale conversion of the motor, including magnet replacement and rewinding. This could provide a cheap way of producing wind turbine generators from salvaged motors.

Design of the Turbine Assembly and Electrical System

Other parts of the wind turbine system may also be developed such as the blade assembly, tower, and power electronics for battery charging.

References

- [1] 'Global Statistics', Global Wind Energy Council, accessed 5/10/2016,
< <http://www.gwec.net/global-figures/graphs/>>
- [2] 'About Land-Based Wind', International Energy Agency, accessed 5/10/2016,
< <http://www.iea.org/topics/renewables/subtopics/wind/>>
- [3] 'Getting Started', The Back Shed, accessed 5/10/2016,
< <http://www.thebackshed.com/Windmill/articles/GettingStarted.asp>>
- [4] 'Wind Energy', Geoscience Australia, Australian Government, accessed 5/10/2016,
< <http://www.ga.gov.au/scientific-topics/energy/resources/other-renewable-energy-resources/wind-energy#heading-2>>
- [5] 'Renewable Energy Resource Maps', Renewables SA, accessed 26/07/2016,
<<http://www.renewablesa.sa.gov.au/investor-information/resources>>
- [6] 'Wind Speed and Direction Rose', Bureau of Meteorology, Australian Government, accessed 5/10/2016,
< http://www.bom.gov.au/cgi-bin/climate/cgi_bin_scripts/windrose_selector.cgi?period=Annual&type=9&location=18012>
- [7] Dorell, D. G., 'A Review of the Design Issues and Techniques for Radial-Flux Brushless Surface and Internal Rare-Earth Permanent-Magnet Motors', *IEEE Transactions on Industrial Electronics*, Vol. 58, No. 9, pp. 3741-3757, Sep. 2011
- [8] Pyrhönen, J. Jokinen, T., Valeria, H., 2014, *Design of Rotating Electrical Machines*, John Wiley & Sons, Ltd., West Sussex, United Kingdom
- [9] Ferreira, B., van der Merwe, W., 2014, *The Principles of Electronic and Electromechanical power conversion*, John Wiley & Sons, Ltd., Hoboken, New Jersey
- [10] Rekioua, D., 2014, 'Wind Power Electric Systems', Springer-Verlag, London
- [11] Anaya-Lara, O., Jenkins, N., Ekanayake, J., Cartwright, P., Hughes, M., 2009, 'Wind Energy Generation – Modelling and Control', John Wiley & Sons, Ltd., West Sussex, United Kingdom
- [12] Choi, J-Y., Jang, S-M., Song, B-M., 'Design of a Direct-Coupled Radial-Flux Permanent Magnet Generator for Wind Turbines', *IEEE PES General Meeting, July 2010*, pp. 1-6

- [13] Lepa, E., Kilk, A., 'Analysis and Prototyping of a Low-Speed Small Scale Permanent Magnet Generator for Wind Power Applications', *2012 Electric Power Quality and Supply Reliability*, June 2012, pp.1-6
- [14] Kilk, A. & Kudrjavitsev, O., 'Study and Verification of a Slow Speed PM Generator with Outer Rotor for Small Scale Wind Turbines', *2012 Electric Power Quality and Supply Reliability*, pp. 1-6, June 2012
- [15] Gandzha, S.A., Sogrin, A.I., Kiessh, I.E., 'The Comparative Analysis of Permanent Magnet Electric Machines with Integer and Fractional Number of Slots per Pole and Phase', *Procedia Engineering*, 2015, Vol. 129, pp. 408-414
- [16] Tang, C., Soong, W. L., Liew, G.S., Ertugrul, N., "Effect of Pole and Slot Number Changes on the Performance of a surface PM Machine", *2012 XXth International Conference on Electrical Machines*, pp.220-227, March 2012
- [17] Rucker, J., 2005, 'Design and Analysis of a Permanent Magnet Generator for Naval Applications', *MSc. Electrical Engineering and Computer Science Thesis Report*, Massachusetts, MIT
- [18] Sun, T., Kim, J-M., Lee, G-H., Hong, J-P., Choi, M-R., 'Effect of Pole and Slot Combination on Noise and Vibration in Permanent Magnet Synchronous Motor', *IEEE Transactions on Magnetics*, Vol. 47, No. 5, pp. 1038-1041, May 2011
- [19] Zhang, Y., Wang, F., "Choice of Pole-Slot Number Combination for PM Generator Direct-Driven by Wind Turbine", *2008 Joint International Conference on Power System Technology*, pp. 1-4, Oct 2008
- [20] Liu, T., Huang, S., Deng, Q., Pu, Q., Huang, K., "Effect of the Number of Slots per Pole on Performance of Permanent Magnet Generator Direct-Driven by Wind Turbine", *2011 International Conference on Electrical Machines and Systems*, pp. 1-4, August 2011
- [21] Hannon B., Sergeant, P., Dupré, L., "2D Analytical Torque Study of Slotted High-Speed PMSMs Considering Pole Pairs, Slots per Pole per Phase and Coil Throw", *2014 International Conference on Electrical Machines (ICEM)*, pp. 2524-2530, 2 September 2014
- [22] Choi, J-Y., Park, Y-S., Jang, S-M., 'Experimental Verification and Electromagnetic Analysis for Performance of Interior PM Motor According to Slot/Pole Number Combination', *IEEE Transactions on Magnetics*, Vol. 48, No. 2, pp. 987-990, February 2012
- [23] Makolo, P., 2013, 'Wind Generator Co-Simulation with Fault Case Analysis'. MSc. Thesis Report, Chalmers University of Technology, Göteborg, Sweden
- [24] Dubois, M., 2004, 'Optimized Permanent Magnet Generator Topologies for Direct-Drive Wind Turbines', Les Imprimeries ABS Inc., Lévis, Canada

- [25] Parvianen, A., Niemelä, M., Pyrhönen, J., 'Performance comparison between low-speed axial-flux and radial-flux permanent-magnet machines including mechanical constraints', *IEEE International Conference on Electric Machines and Drives*, 2005, pp.1695-1702
- [26] Qui-ling Deng, A., Shoudao Hong, B., Feng Xiao C., 'Influence of Design Parameters on Cogging Torque in Directly Driven Permanent Magnet Synchronous Wind Generators', *IEEE International Conference on Electric Machines and Systems*, 2009
- [27] Zhu, Z. Q., Howe, D., 'Influence of Design Parameters on Cogging Torque in Permanent Magnet Machines', *IEEE Transactions on Energy Conversion*, Vol. 14, No. 4, pp 407-412, December 2000
- [28] 'SmartDrive Brochure', Fisher & Paykel, accessed 7/07/2016,
<http://www.directdrivemotors.com/common/pdf/4876_NZ_Motors_BRO_HR.pdf>

Bibliography

Bang, D-J., 2010, 'Design of Transverse Flux Permanent Magnet Machines for Large Direct-drive Wind Turbines', Ridderprint B.V., Ridderkerk, The Netherlands

Chen, J., Nayar, C., Xu, L., 'Design and Finite-Element Analysis of an Outer-Rotor Permanent-Magnet Generator for Directly Coupled Wind Turbines', IEEE Transactions on Magnetics, Vol. 36, No. 5, pp. 3802-3809, September 2000

Lampola, P., 2000, 'Directly Driven, Low-Speed Permanent-Magnet Generators for Wind Power Application', Published by the Finnish Academies of Technology, Espoo

Strous, T.D., 2010, 'Design of a permanent magnet radial flux concentrated coil generator for a range extender application', MSc. Thesis Report, Delft University of Technology, Delft, The Netherlands

Sitapati, K. and Krishnan, R., 'Performance Comparisons of Radial and Axial Field, Permanent-Magnet, Brushless Machines', IEEE Transactions on Industry Applications, Vol. 37, No. 5, pp. 1219-1226, September/October 2001

Tarimer, I., Ocak, C., 'Performance Comparison of Internal and External Rotor Structured Wind Generators Mounted from Same Permanent Magnets on Same Geometry', Electronics and Electrical Engineering, No. 4(92), 2009

Appendices

Appendix A: Flux Density Contour Plots

Appendix B: Magnetic Field Strength Vector Plots

Appendix C: No-Load Flux Line Plots

Appendix D: Cogging Torque Plots

Appendix E: Total Harmonic Distortion Calculations

Appendix F: Three-Phase Resistive Load Test

Appendix G: Rectified Output Load Resistive Test

Appendix H: Maxwell 2D Meshing Result

Appendix J: Simplerer Circuit Diagrams

Appendix A: Flux Density Contour Plots

6-Pole Machine

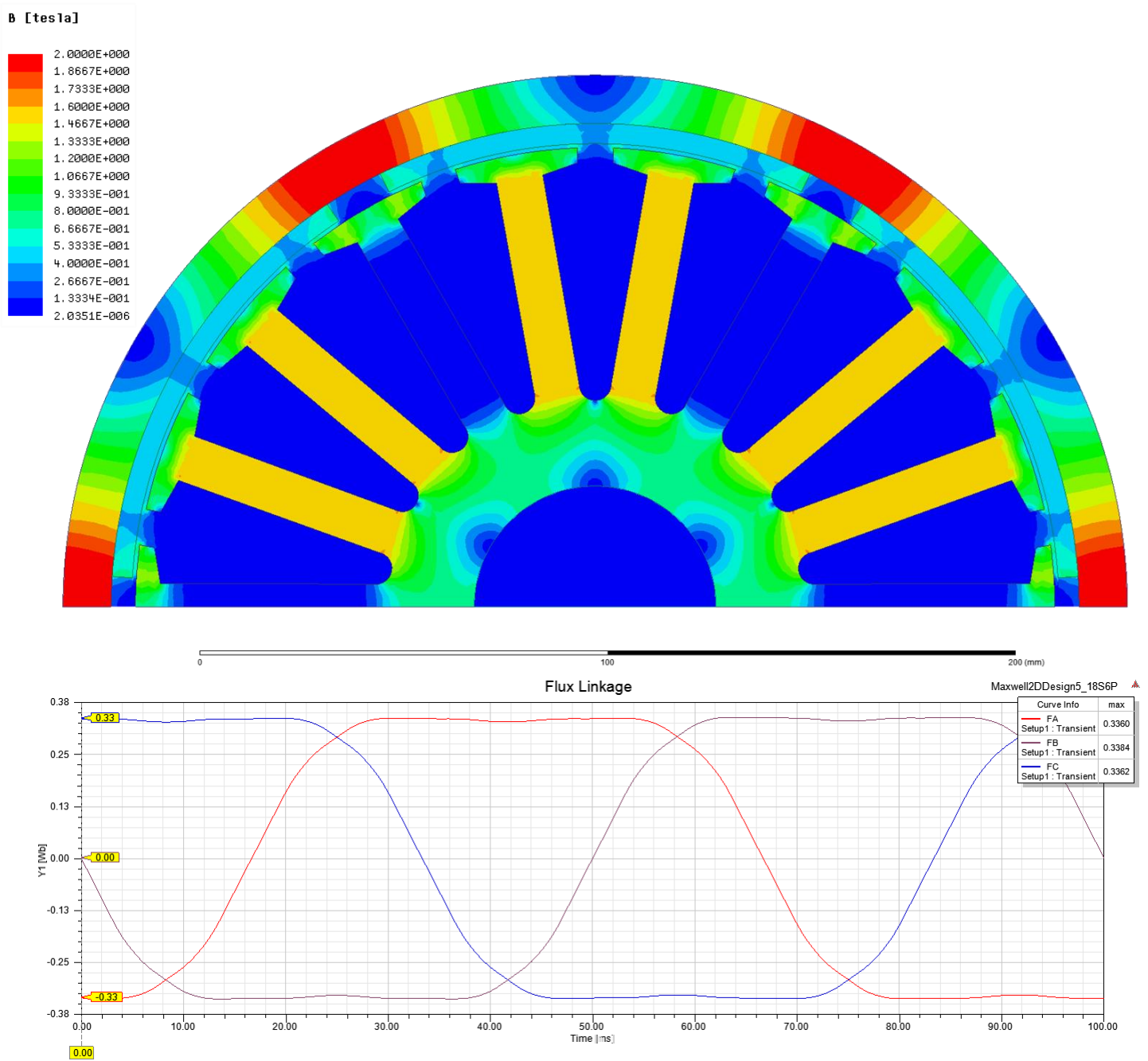


Figure 135: Flux density contour plot with corresponding flux linkage plot for a 6-pole machine

The 6-pole machine can be seen to have heavy saturation in the rotor steel, but no saturation in the stator. Due to the large width and coverage of the magnets, multiple teeth are used to support the flux, reducing the flux density in each tooth. However, this property also causes distortion as the flux linkage becomes a square wave.

14-Pole Machine

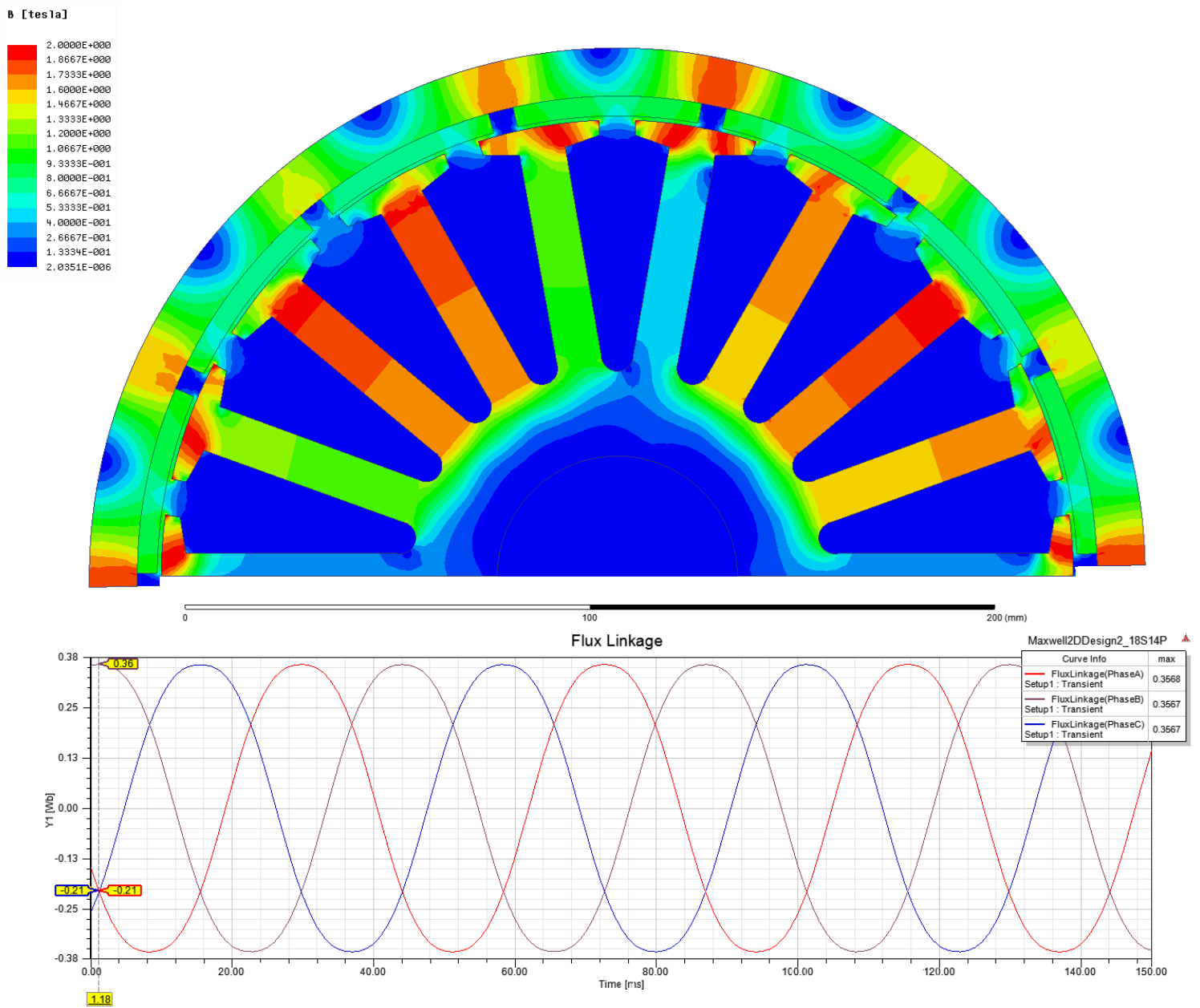


Figure 136: Flux density contour plot with corresponding flux linkage plot for a 14-pole machine

The 14-pole machine can be seen to experience greater amounts of saturation in the stator, and reduced saturation in the rotor as compared to the 6-pole machine. The magnets cover less circumference, and so the flux paths are now reduced to a single stator tooth, which greatly increases flux density. The rotor experiences less saturation as the increased number of poles more evenly spreads the concentration of flux. Despite the increase of saturation the flux linkage has low distortion.

20-Pole Machine

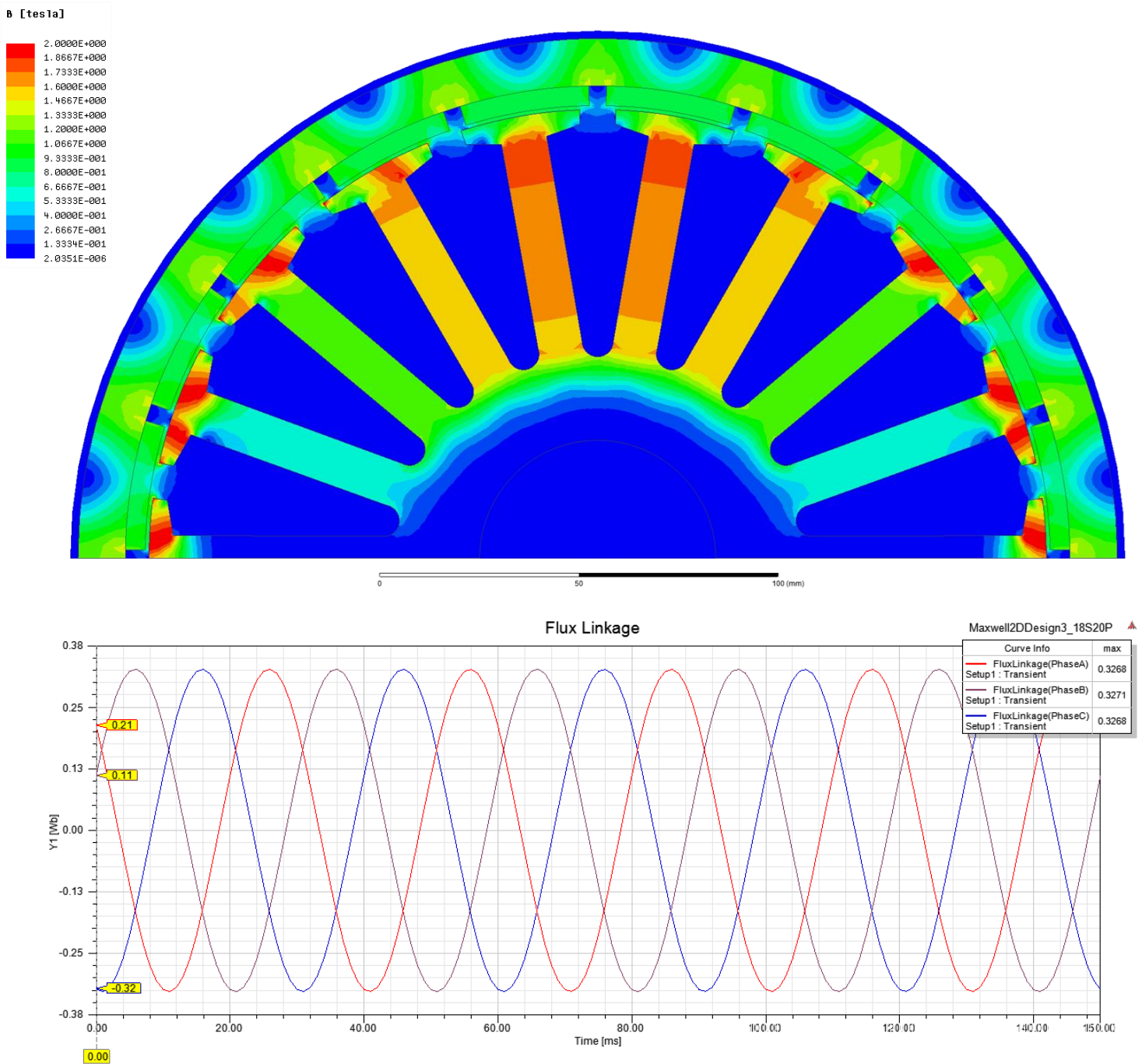


Figure 137: Flux density contour plot with corresponding flux linkage plot for a 20-pole machine

The 20-pole machine experiences low levels of saturation, with no saturation occurring in the rotor. The flux linkage is highly sinusoidal, but is slightly lower in magnitude compared to the 14-pole machine.

24-Pole Machine

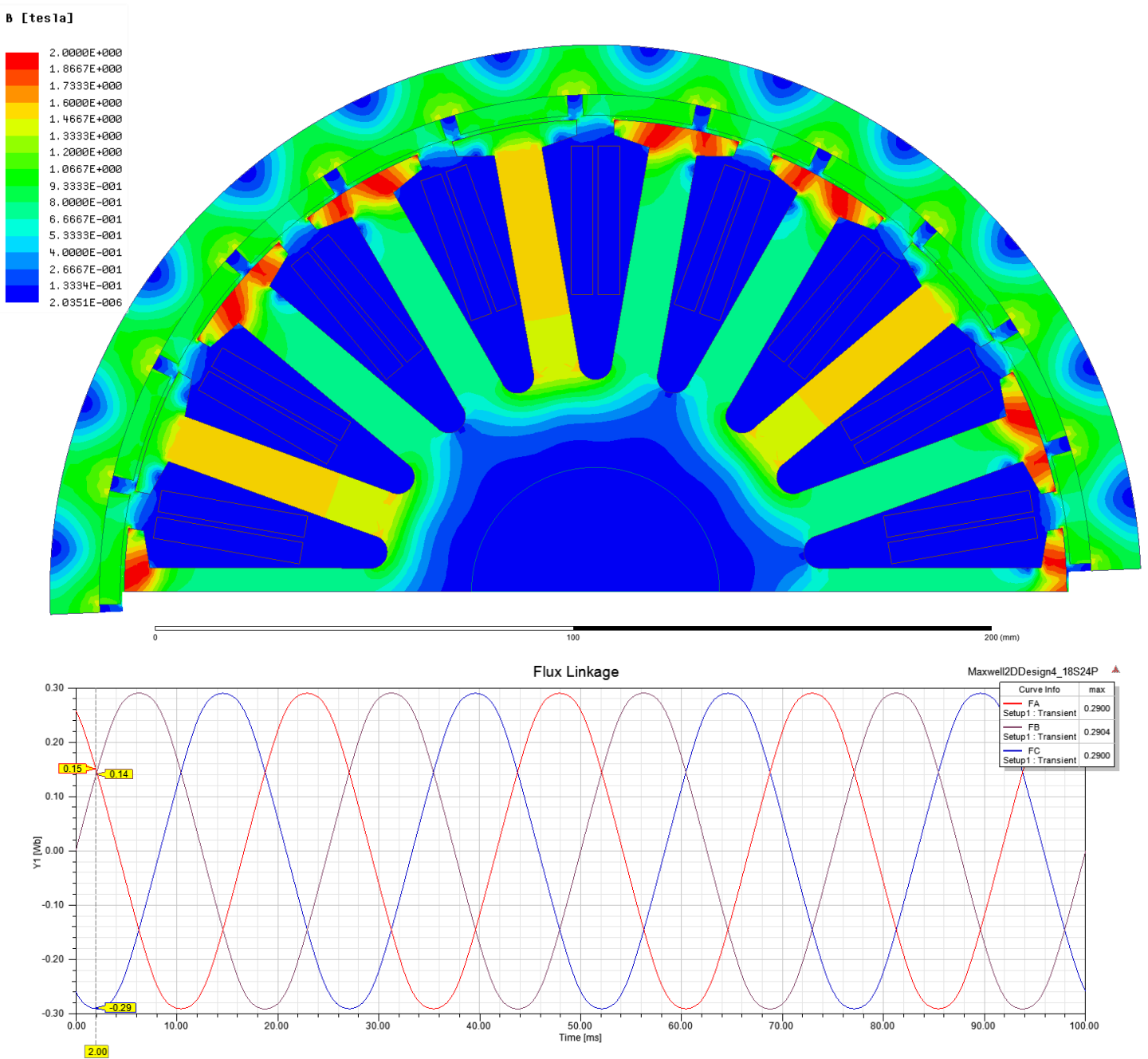


Figure 138: Flux density contour plot with corresponding flux linkage plot for a 24-pole machine

The 24-pole machine only exhibits saturation in the teeth tips. This amount of saturation is typically unavoidable. The flux linkage is highly sinusoidal.

26-Pole Machine

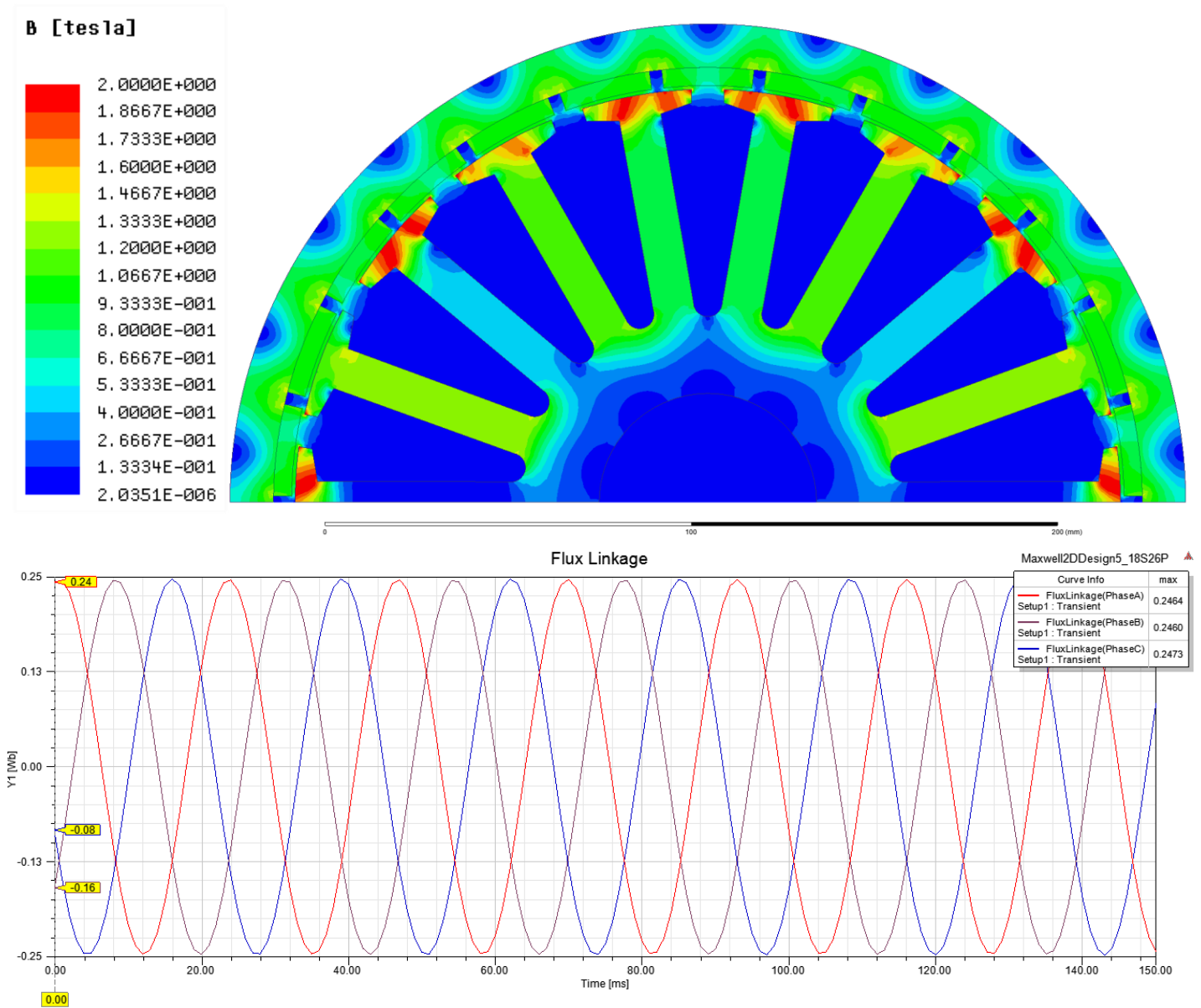


Figure 139: Flux density contour plot with corresponding flux linkage plot for a 26-pole machine

The 26-pole machine exhibits similar properties to the 24-pole machine. The slight difference is in the magnitude of the flux linkage, which is slightly smaller.

Appendix B: Magnetic Field Strength Vector Plots

The magnetic field strength inside the machine can be related to the flux density by the relationship:

$$\mathbf{B} = \mu\mathbf{H}$$

Where \mathbf{B} is the flux density, μ is the relative permeability of the medium, and \mathbf{H} is the magnetic field strength. The magnetic field strength can be represented as a vector, describing the direction and magnitude of the magnetic field at any point. The following plots show these vectors using a uniform spacing on the cross section of the machine. The vector representation is useful for determining the flow of the magnetic flux throughout the machine. However, it is important to note that the magnetic field strength can be large in air gaps, whereas the corresponding flux would be very low. This is because the permeability of air is several orders of magnitude lower than that of iron.

6-Pole Machine

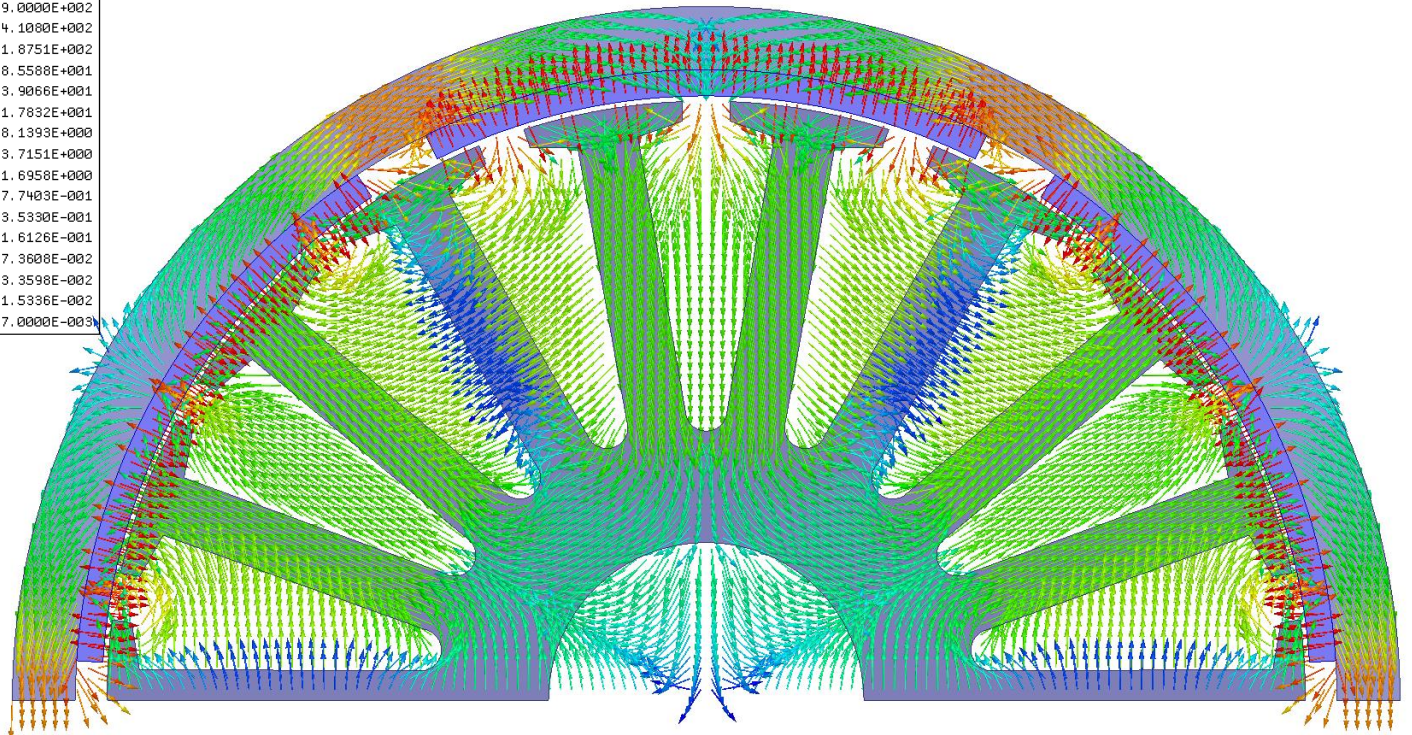
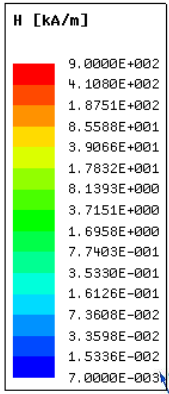


Figure 140: Vector representation of the magnetic field strength inside the 6-pole machine

14-Pole Machine

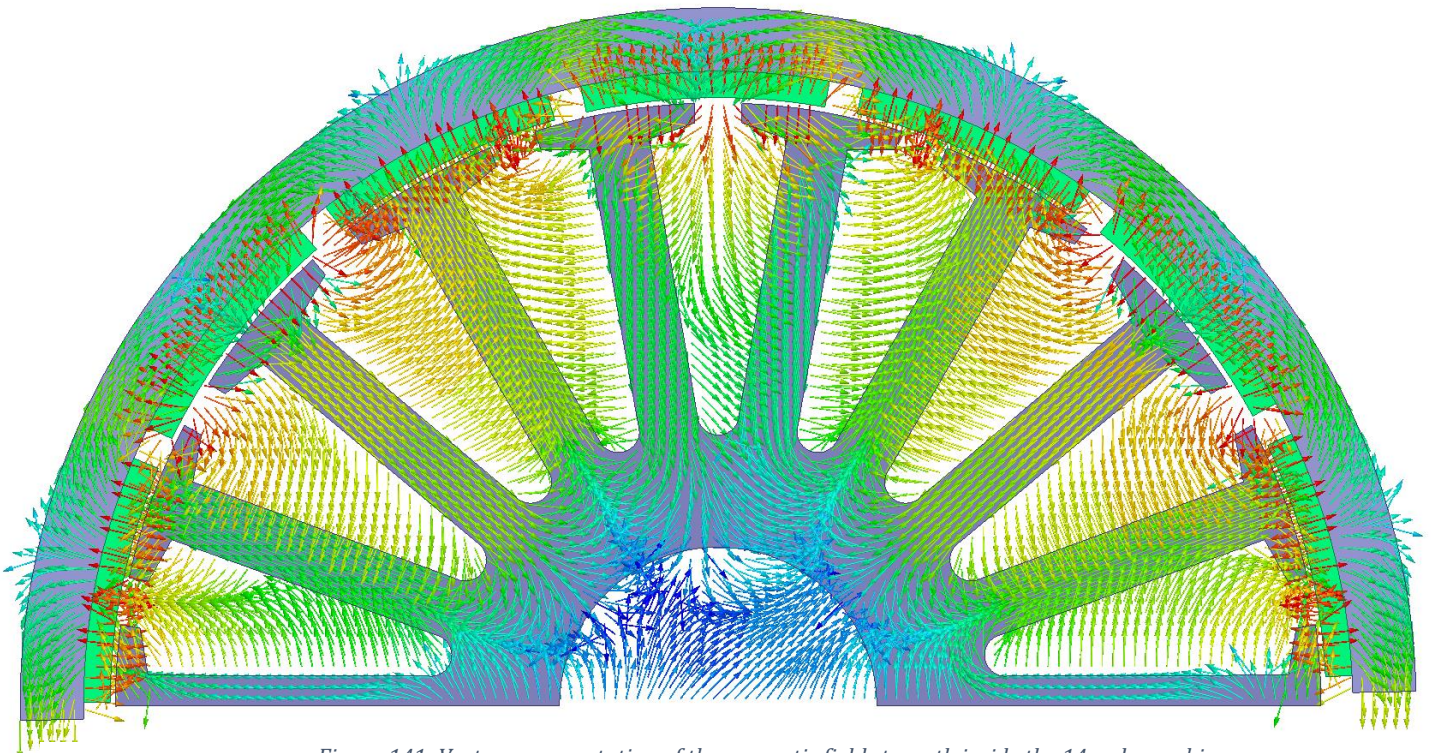
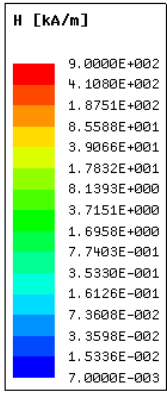


Figure 141: Vector representation of the magnetic field strength inside the 14-pole machine



20-Pole Machine

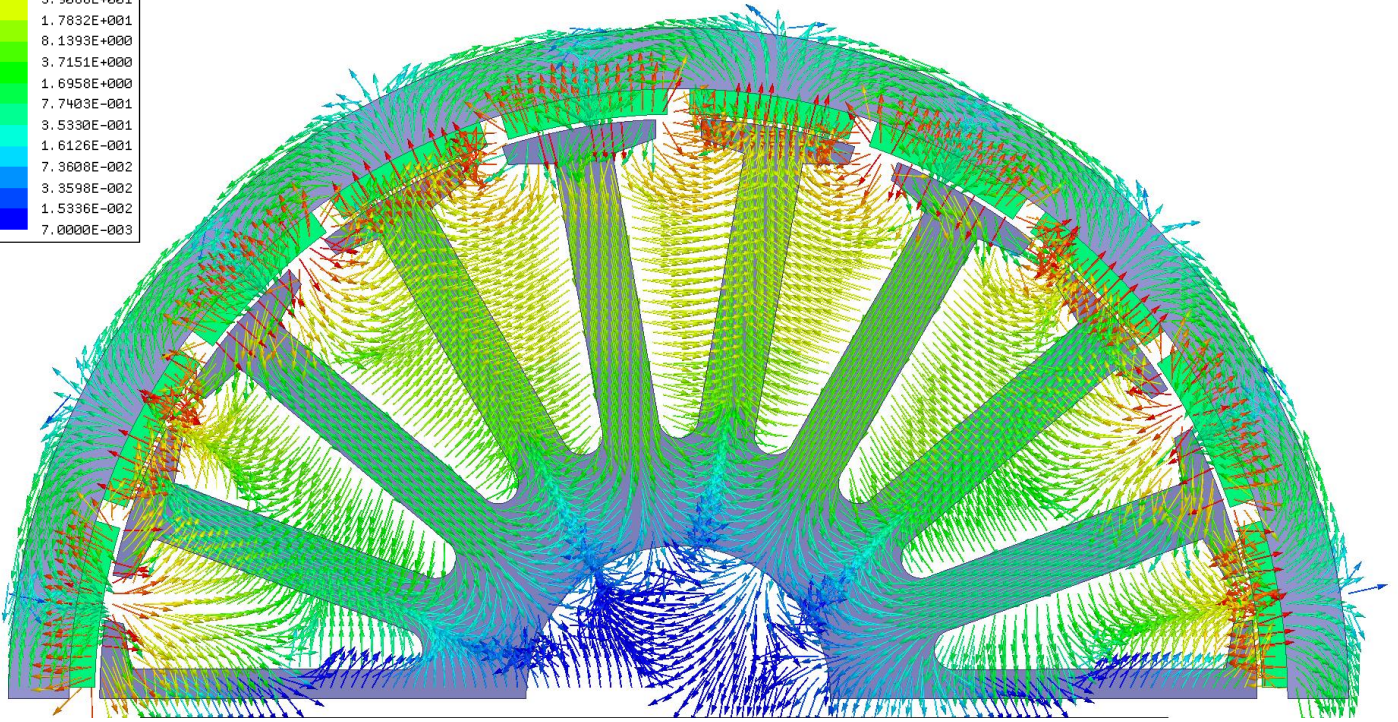


Figure 142: Vector representation of the magnetic field strength inside the 20-pole machine

24-Pole Machine

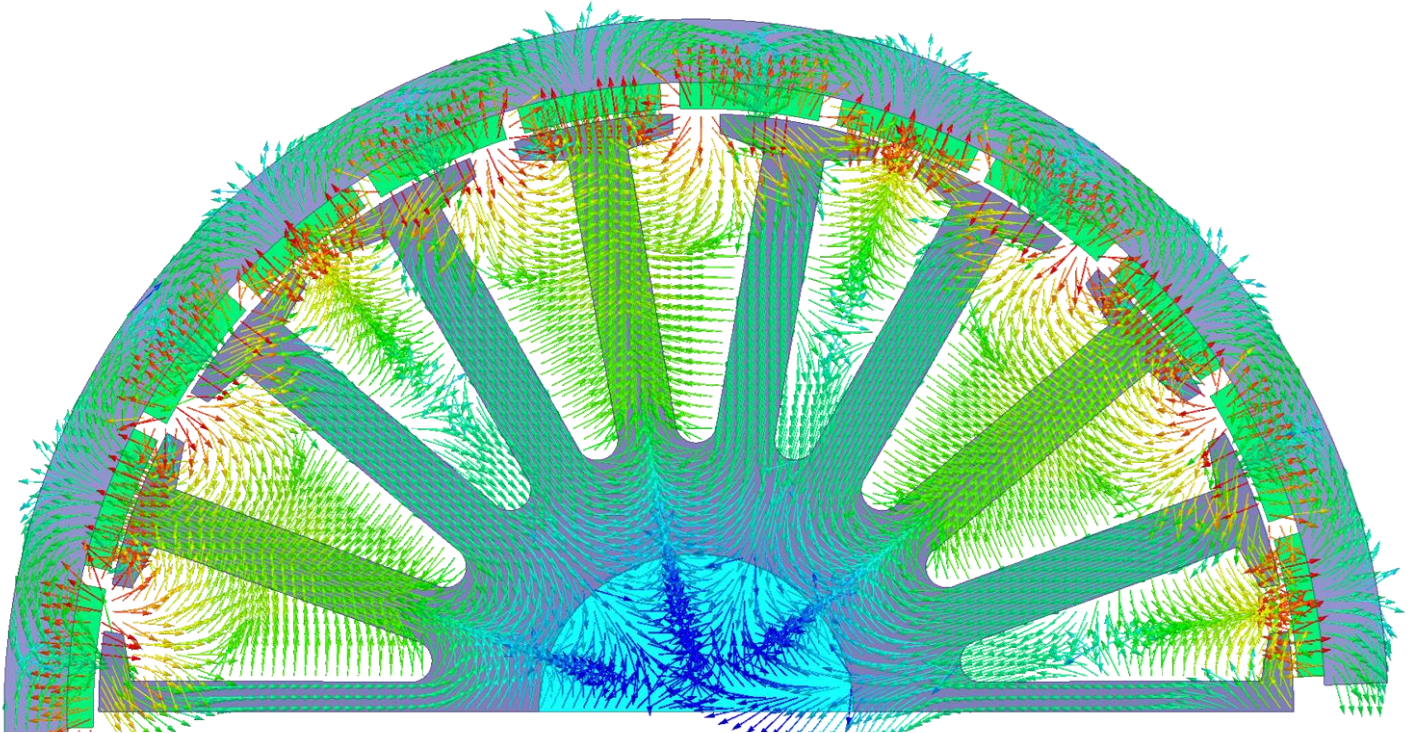
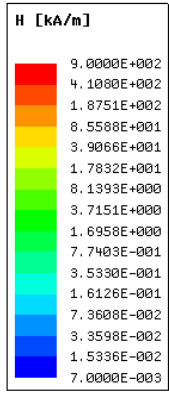


Figure 143: Vector representation of the magnetic field strength inside the 24-pole machine



26-Pole Machine

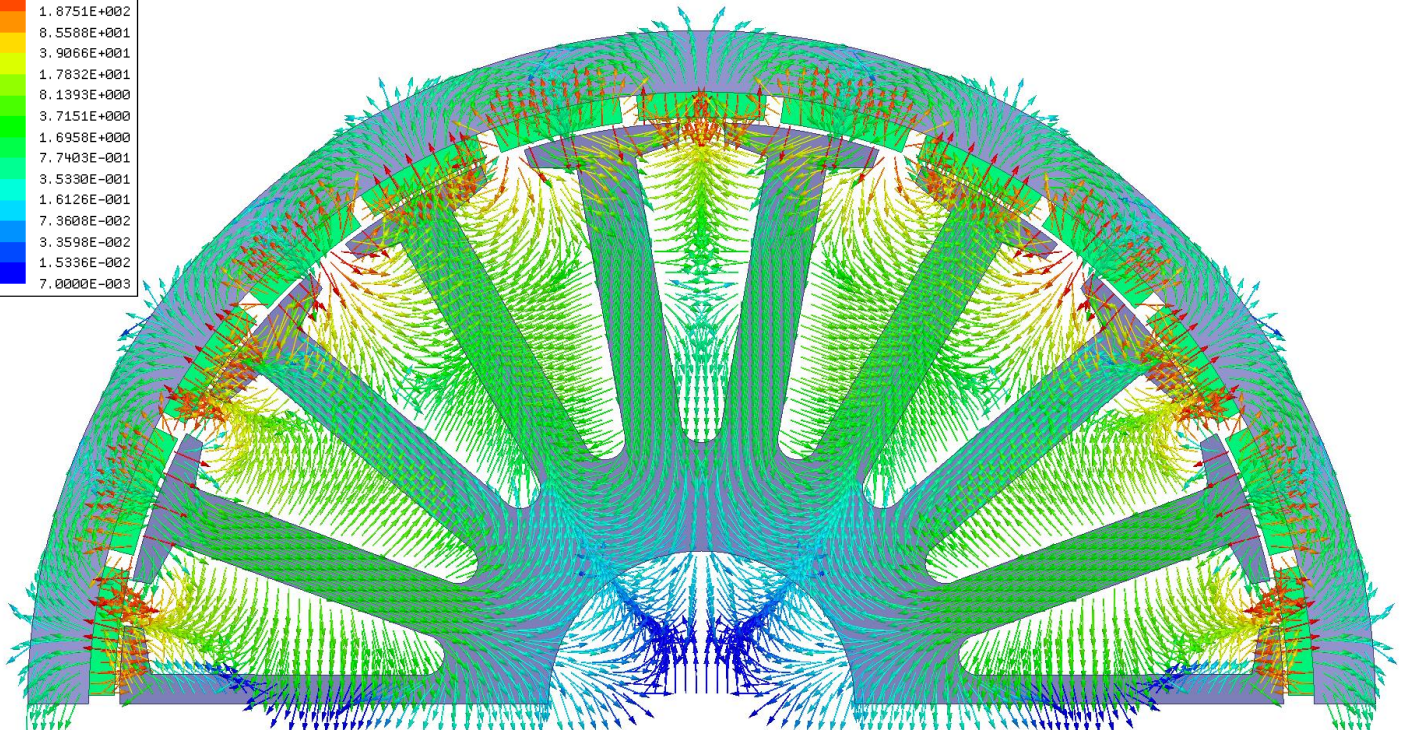


Figure 144: Vector representation of the magnetic field strength inside the 26-pole machine

Appendix C: No-Load Flux Line Plots

6-Pole Machine

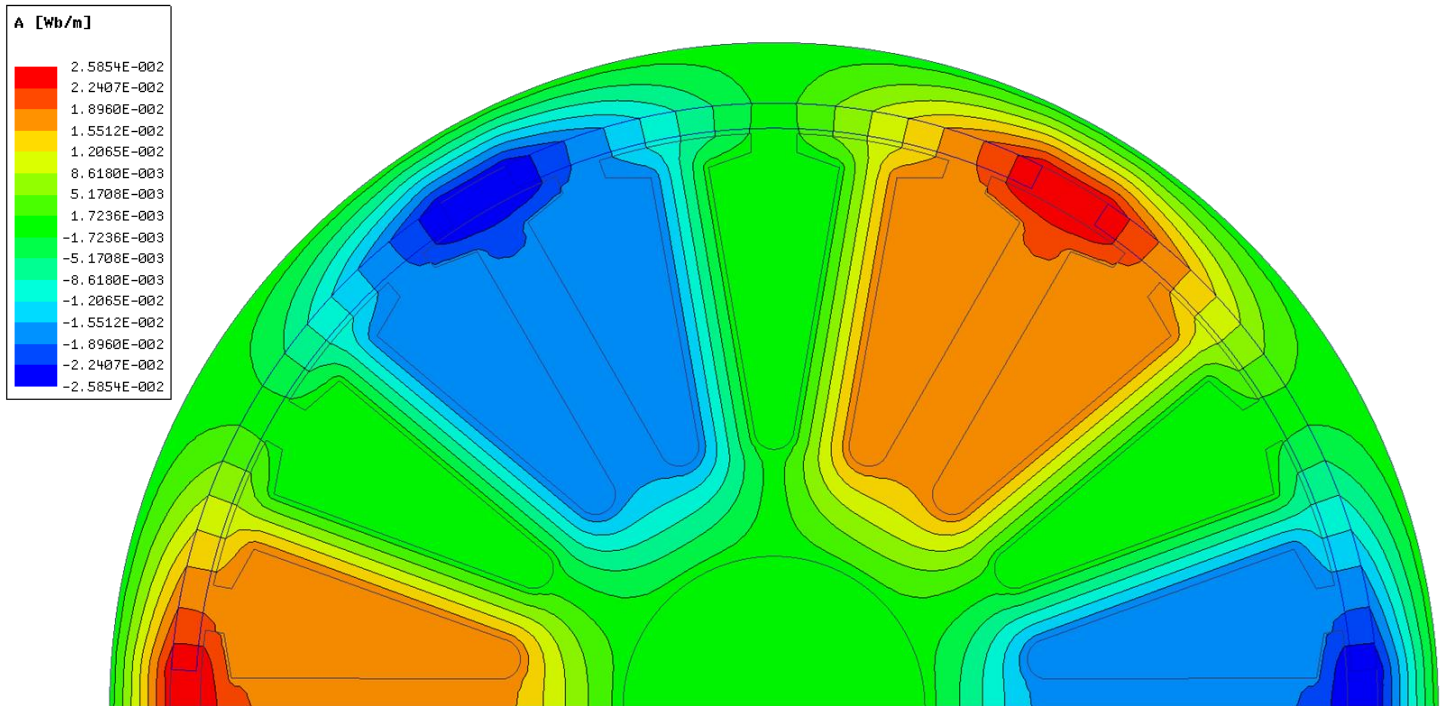


Figure 145: Flux line representation for a 6-pole machine

14-Pole Machine

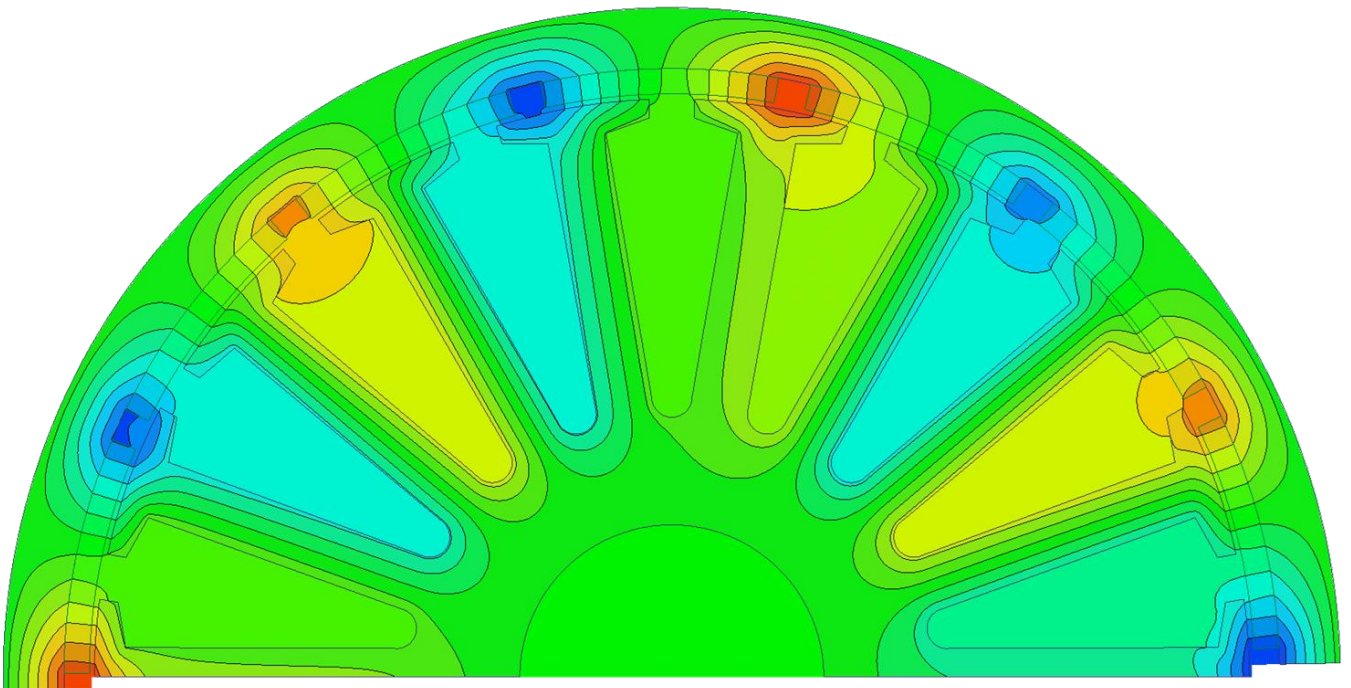


Figure 146: Flux line representation for a 14-pole machine

20-Pole Machine

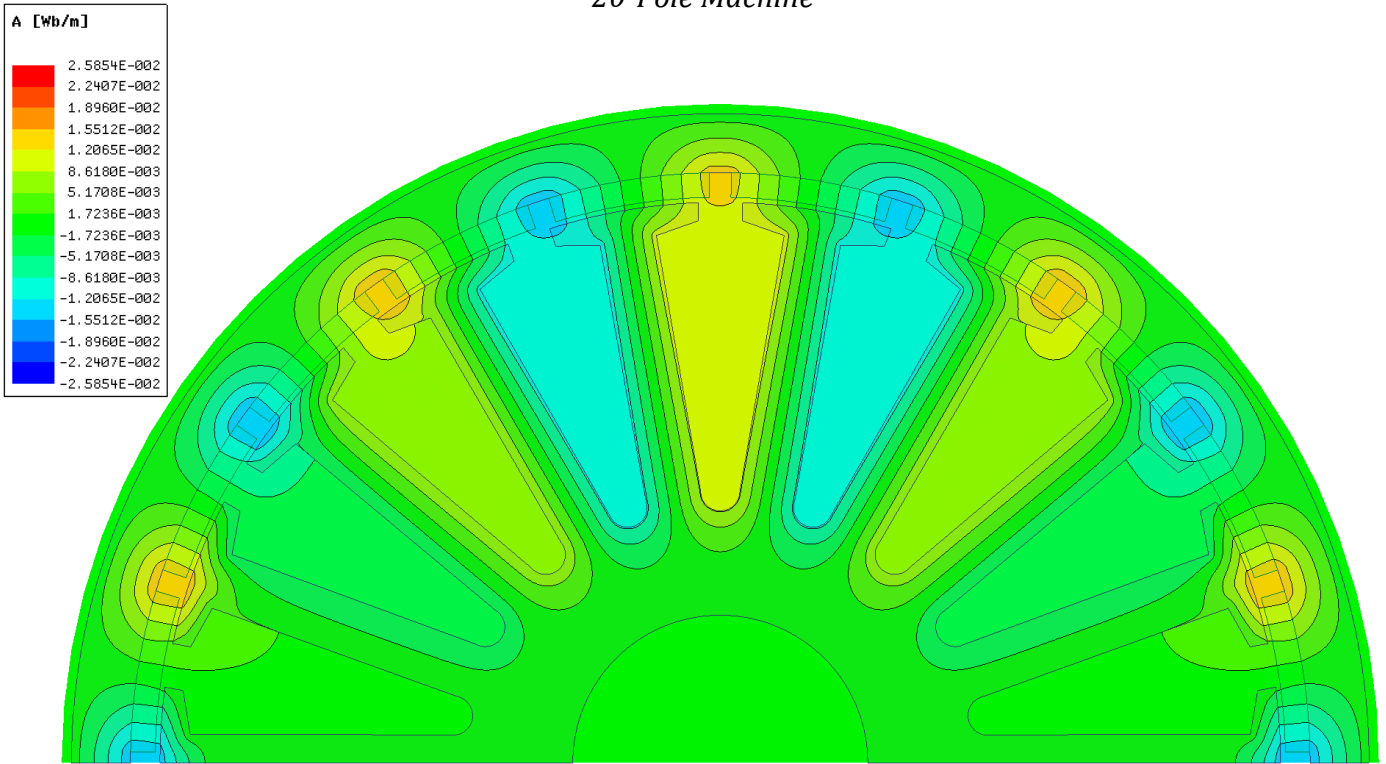


Figure 147: Flux line representation for a 20-pole machine

24-Pole Machine

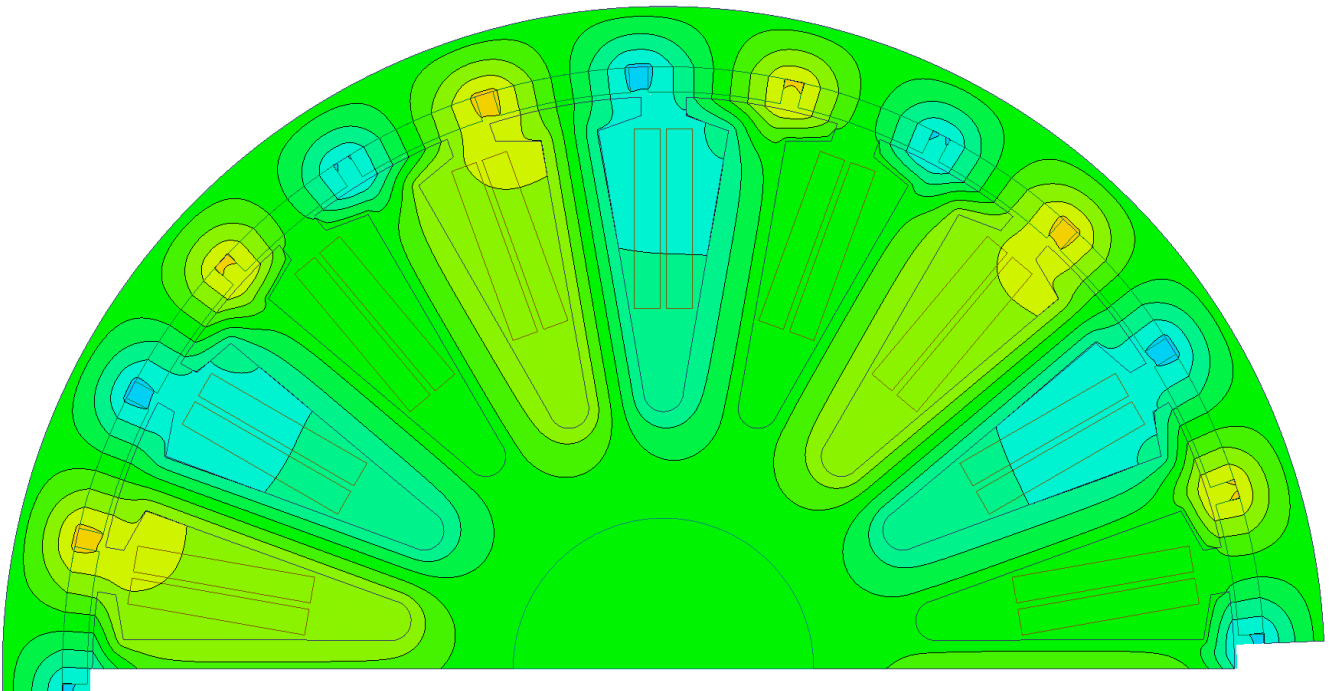


Figure 148: Flux line representation for a 24-pole machine

26-Pole Machine

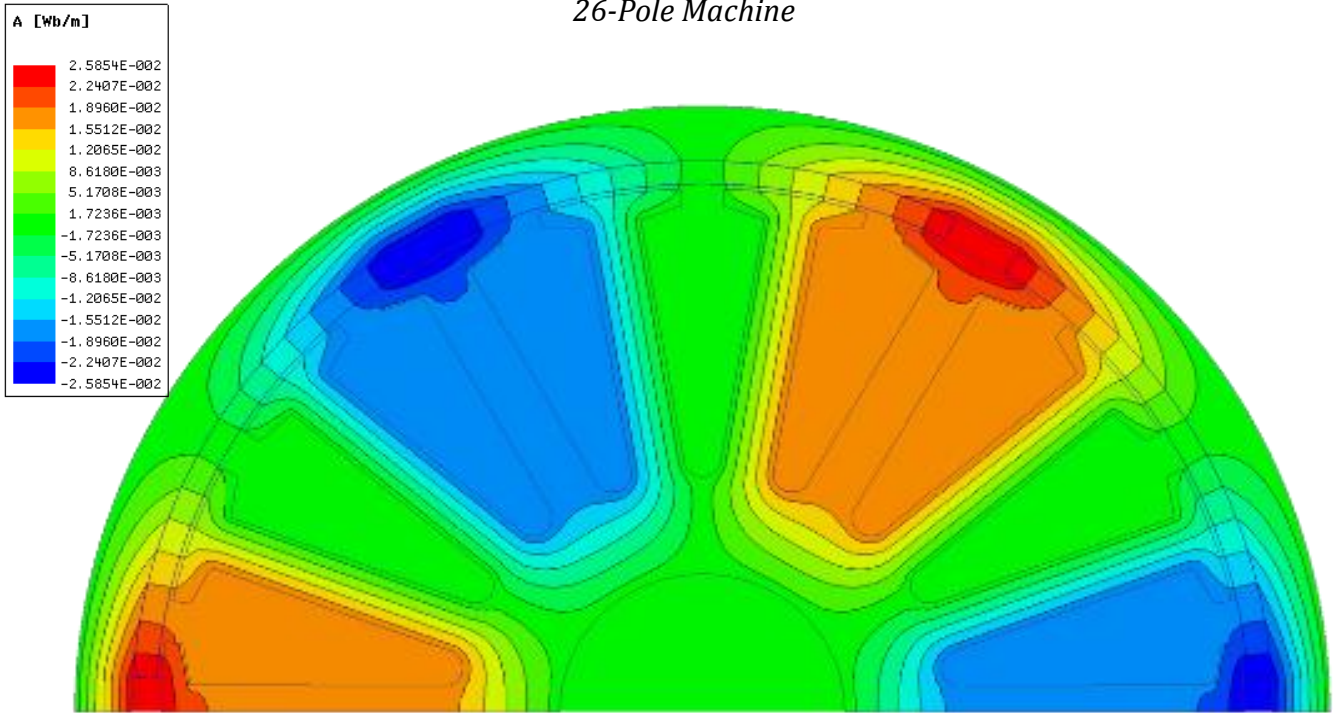
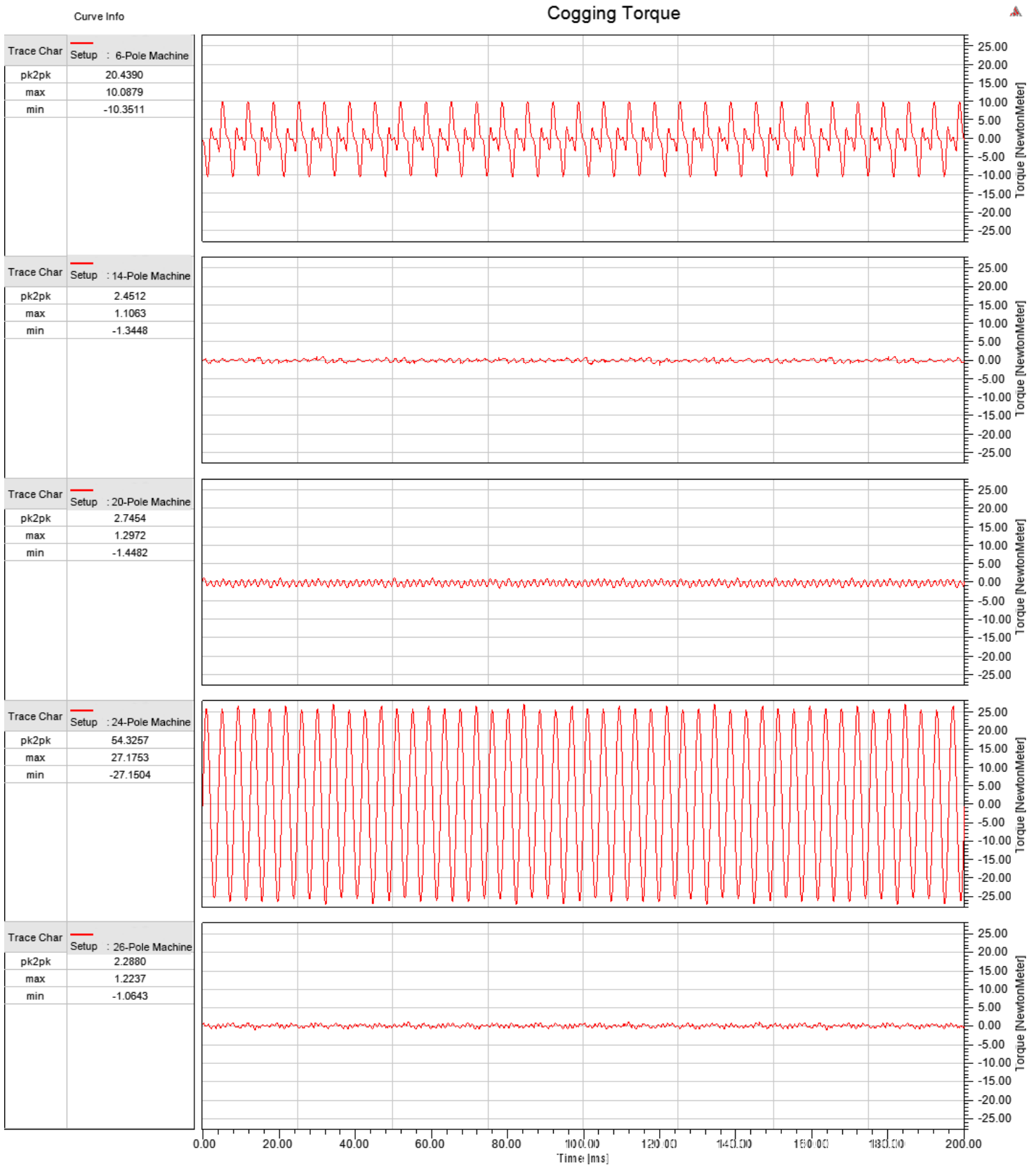


Figure 149: Flux line representation for a 26-pole machine

Appendix D: Cogging Torque Plots

*The plots of the cogging torque shown below uses a uniform Y-axis scale to display the differences in magnitude of the cogging torque for the different machines.



*The plots of the cogging torque shown below uses individual Y-axis scales to display the differences in shape of the cogging torque waveforms for the different machines.

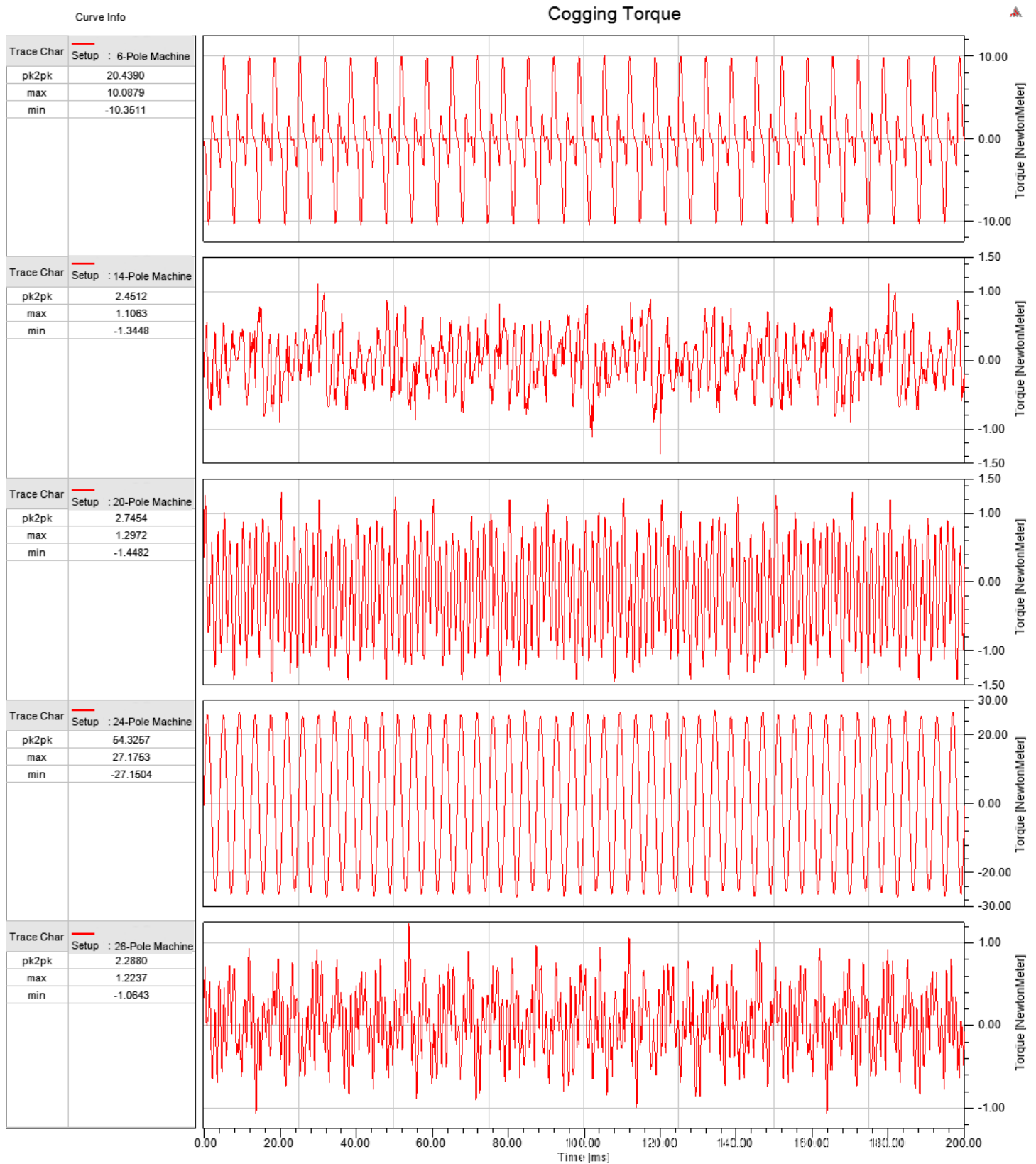


Figure 150: Stacked plot of the cogging torque waveforms for the five machine variants using individual scales

Appendix E: Total Harmonic Distortion Calculations

The THD was calculated in two different ways. The first was the built in function analysis tools in ANSYS, which specified the fundamental magnitude, and the distortion at a specified frequency.

The 6-pole machine was analysed in 2 iterations. As the voltage frequency is so low at 200 rpm, the THD could not be measured accurately. Therefore, a sweep at 200 rpm, and 500 rpm was performed. The 200 rpm sweep provided measurements for magnitude of generated voltage, while the 500 rpm sweep provided measurements for THD. This was found to be valid as the increase in speed does not generally affect the shape of the voltage waveform in open circuit operation. In this mode, the rotational speed simply affects the magnitude and the frequency of the waveform, rather than the shape.

6-Pole Machine (200 rpm)

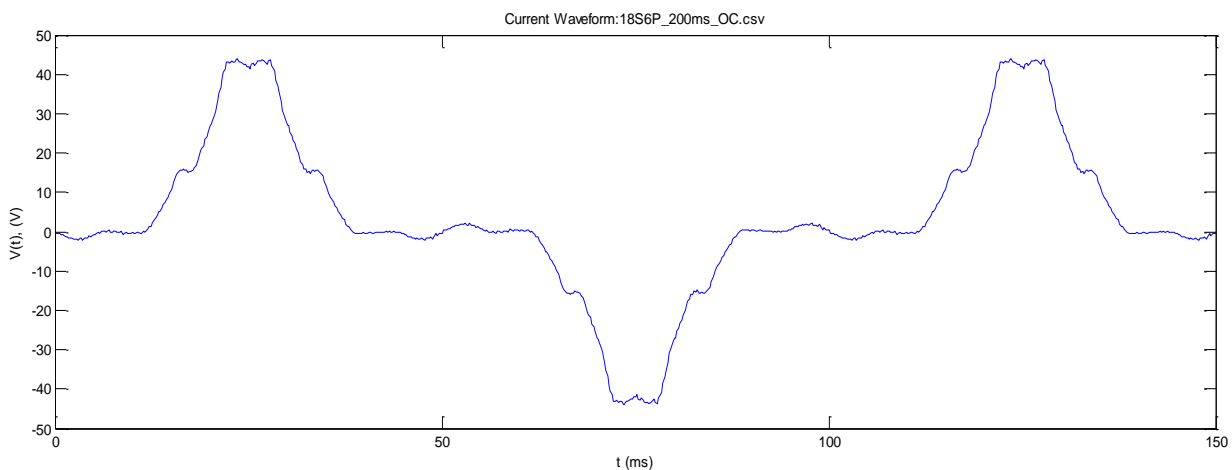


Figure 151: Open circuit phase voltage waveform generated at 200 rpm

Frequency	10 Hz
Voltage (Peak)	44.7 V
Voltage (RMS)	19.7 V
THD_{MATLAB}	-
THD_{ANSYS}	71.2 %

6-Pole Machine (500 rpm)

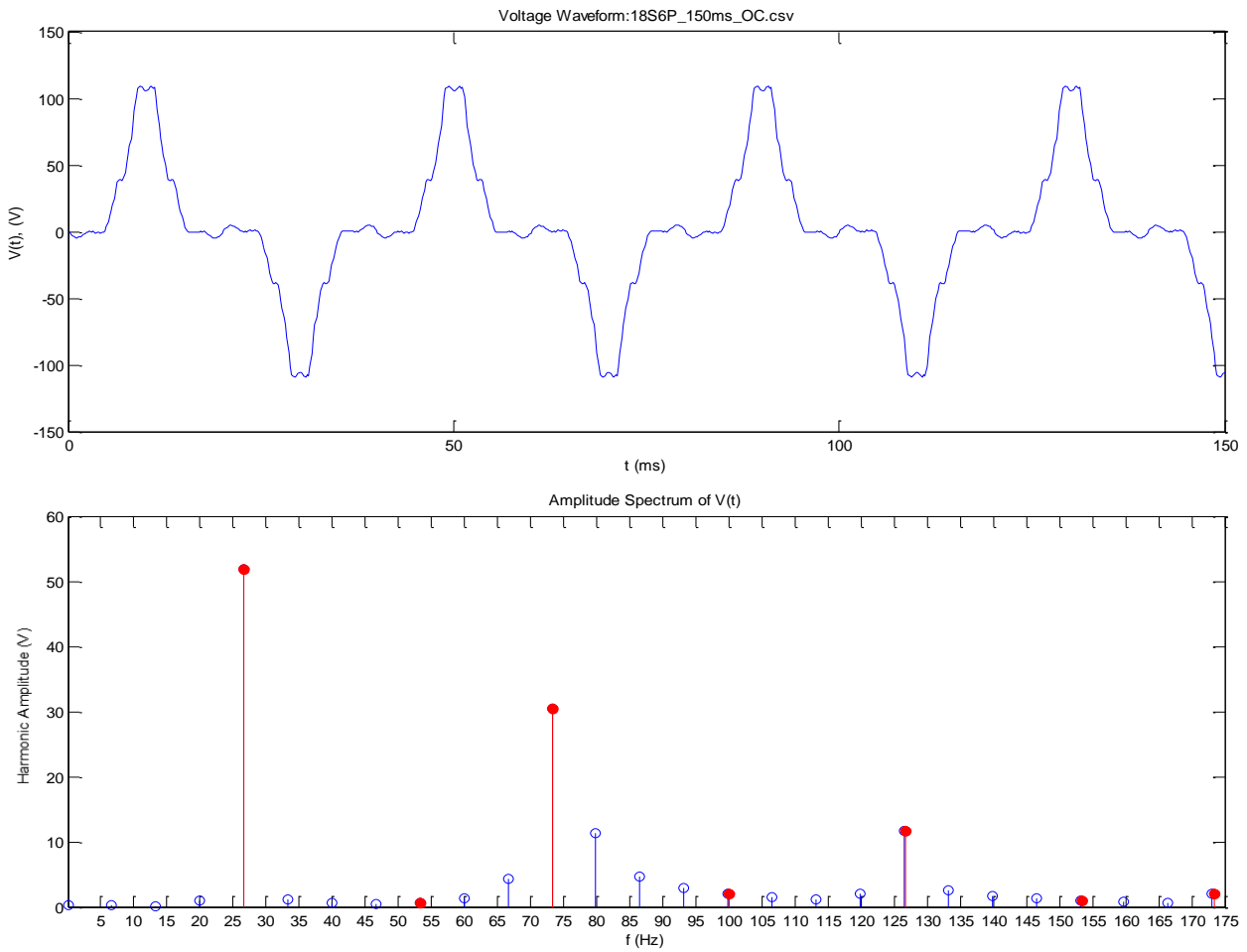


Figure 152: (top) Open circuit waveform voltages (bottom) Waveform spectrum

Frequency	25 Hz
Voltage (Peak)	109 V
Voltage (RMS)	49.5 V
THD_{MATLAB}	63.3 %
THD_{ANSYS}	71.1 %

Harmonic	1	2	3	4	5	6	7
Frequency (Hz)	25.0	50.0	75.0	100	125	150	175
Amplitude (V) (MATLAB)	51.8	0.583	30.5	1.99	11.7	1.04	1.97
Amplitude (V) (ANSYS)	58.9	-	-	-	-	-	-

14-Pole Machine

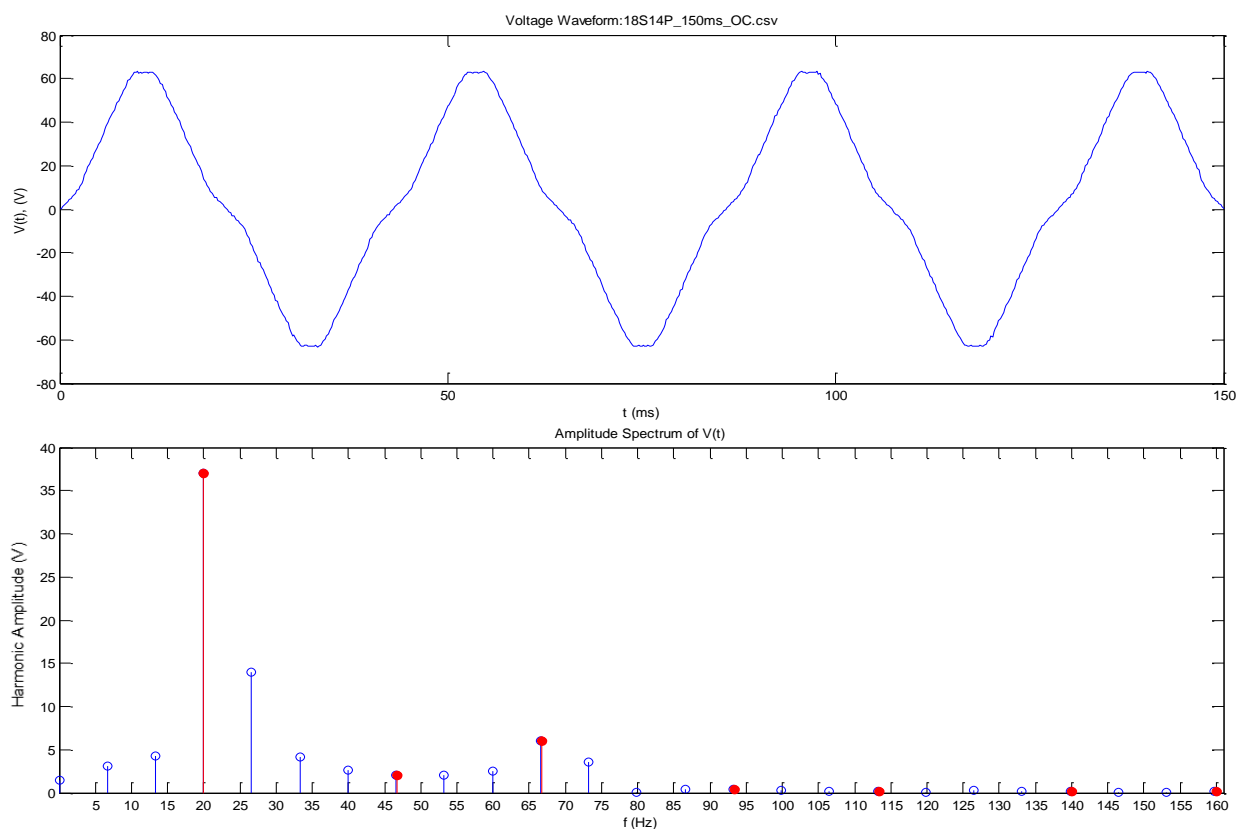


Figure 153: (top) Open circuit waveform voltages (bottom) Waveform spectrum

Frequency	23.3 Hz
Voltage (Peak)	63.4 V
Voltage (RMS)	40.4 V
THD_{MATLAB}	17.3 %
THD_{ANSYS}	17.1 %

Harmonic	1	2	3	4	5	6	7
Frequency (Hz)	23.3	46.6	70.0	93.3	117	140	163
Amplitude (V) (MATLAB)	37.0	2.11	6.04	0.375	0.235	0.0809	0.246
Amplitude (V) (ANSYS)	55.3	-	-	-	-	-	-

20-Pole Machine

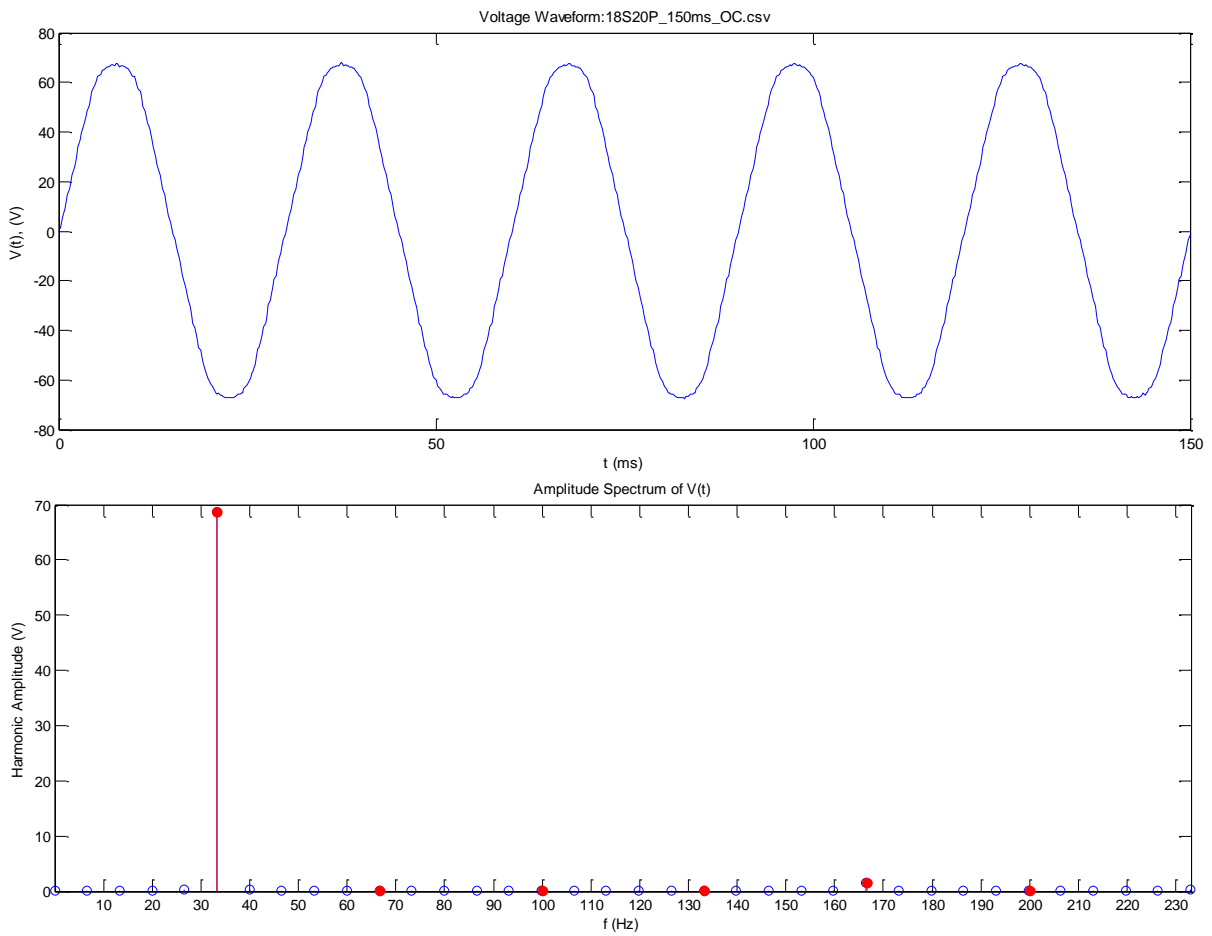


Figure 154: (top) Open circuit waveform voltages (bottom) Waveform spectrum

Frequency	33.3 Hz
Voltage (Peak)	67.9 V
Voltage (RMS)	48.4 V
THD_{MATLAB}	2.40 %
THD_{ANSYS}	7.35 %

Harmonic	1	2	3	4	5	6	7
Frequency (Hz)	33.3	66.6	100	133	166	200	233
Amplitude (V) (MATLAB)	68.8	0.0941	0.112	0.0468	1.63	0.0096	0.222
Amplitude (V) (ANSYS)	68.7	-	-	-	-	-	-

24-Pole Machine

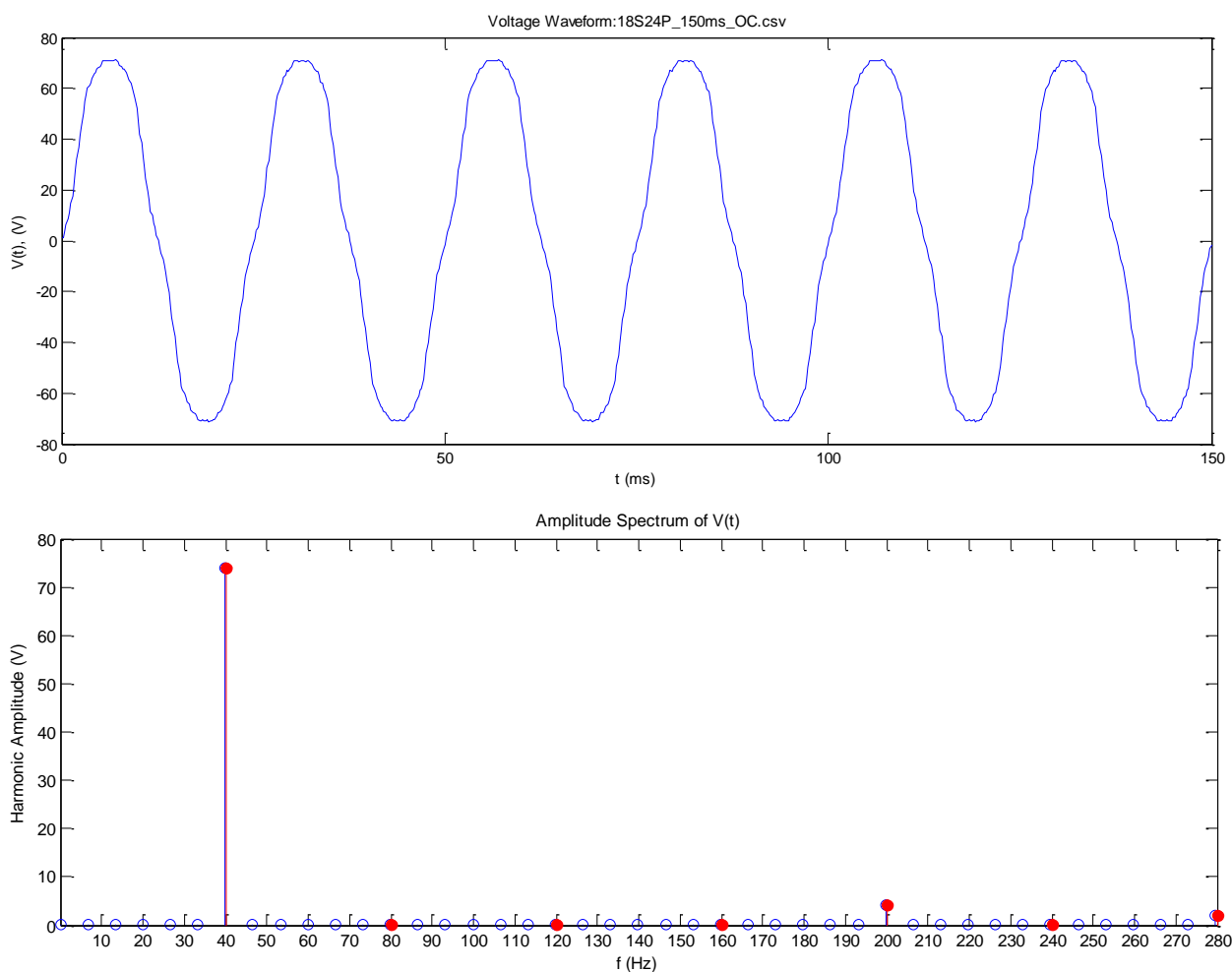


Figure 155: (top) Open circuit waveform voltages (bottom) Waveform spectrum

Frequency	40 Hz
Voltage (Peak)	71.1 V
Voltage (RMS)	50.3 V
THD_{MATLAB}	6.30 %
THD_{ANSYS}	9.00 %

Harmonic_{MATLAB}	1	2	3	4	5	6	7
Frequency (Hz)	40	80	120	160	200	240	280
Amplitude (V) (MATLAB)	73.9	0.00520	0.0942	0.0368	4.25	0.0106	1.90
Amplitude (V) (ANSYS)	74.2	-	-	-	-	-	-

26-Pole Machine

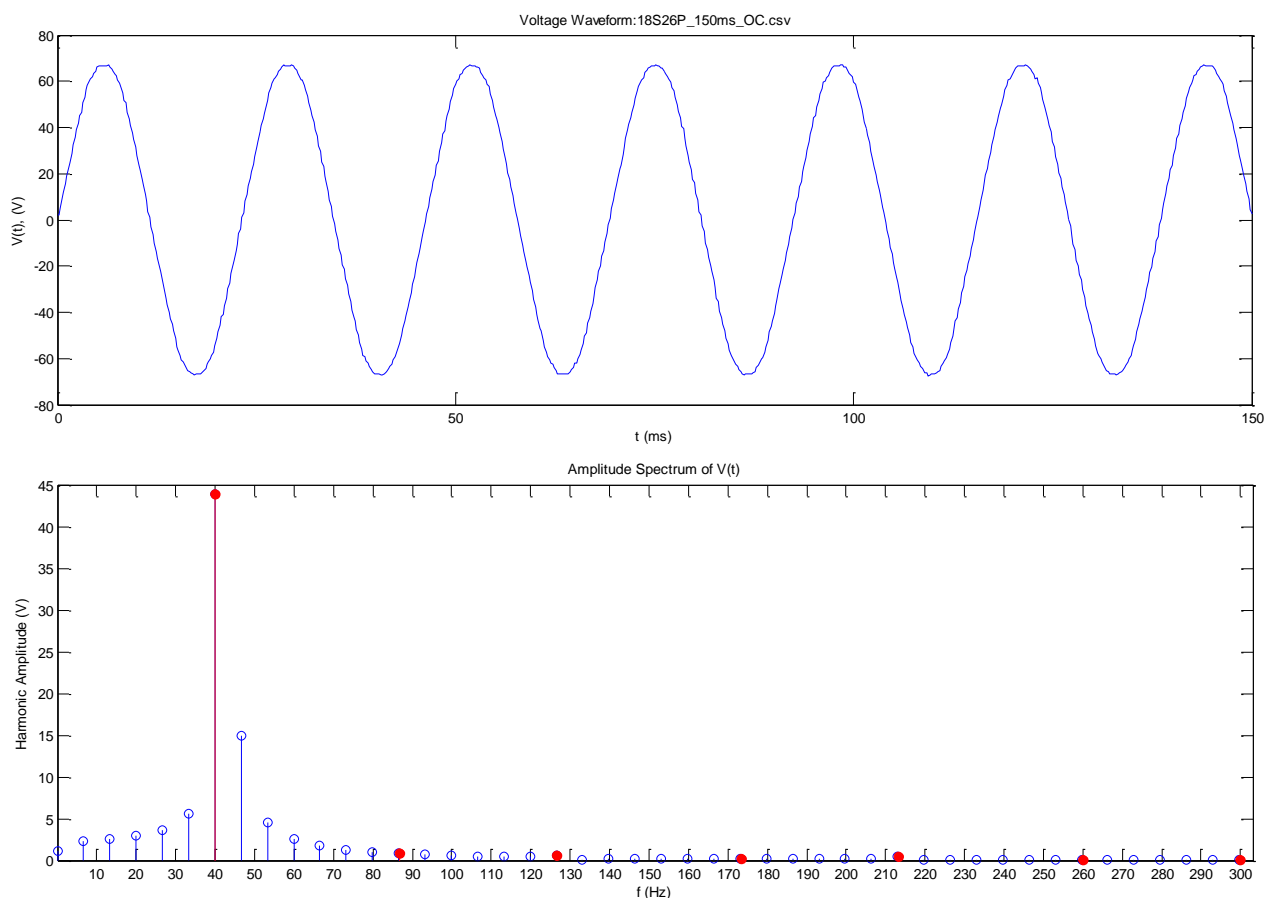


Figure 156: (top) Open circuit waveform voltages (bottom) Waveform spectrum

Frequency	43.3 Hz
Voltage (Peak)	67.3 V
Voltage (RMS)	47.6 V
THD_{MATLAB}	2.61 %
THD_{ANSYS}	7.10 %

Harmonic	1	2	3	4	5	6	7
Frequency	43.3	86.6	130	173	217	260	303
Amplitude (V) (MATLAB)	43.8	0.802	0.627	0.156	0.488	0.0039	0.07
Amplitude (V) (ANSYS)	67.3	-	-	-	-	-	-

*The ANSYS analysis shows the RMS voltage and the RMS of the fundamental component to be identical indicating a THD of 0%

Process Observations

The measurements for the THD from the MATLAB script and the ANSYS function varied significantly in some cases, and are essentially identical in others. The spectral plots from both methods show that the ANSYS method typically contained slightly higher levels of non-harmonic frequency components. This may be due to the settings of the internal FFT, such as the type of window used in the operation, as well as the effects of the sampling frequency. The THD measurement for the 26-pole machine from ANSYS was 7.10%, while MATLAB returned 2.61%. The very bottom plot shown below uses an overlay of a pure sine wave to demonstrate that the MATLAB plot is likely to be more accurate, as the perceived distortion is incredibly low.

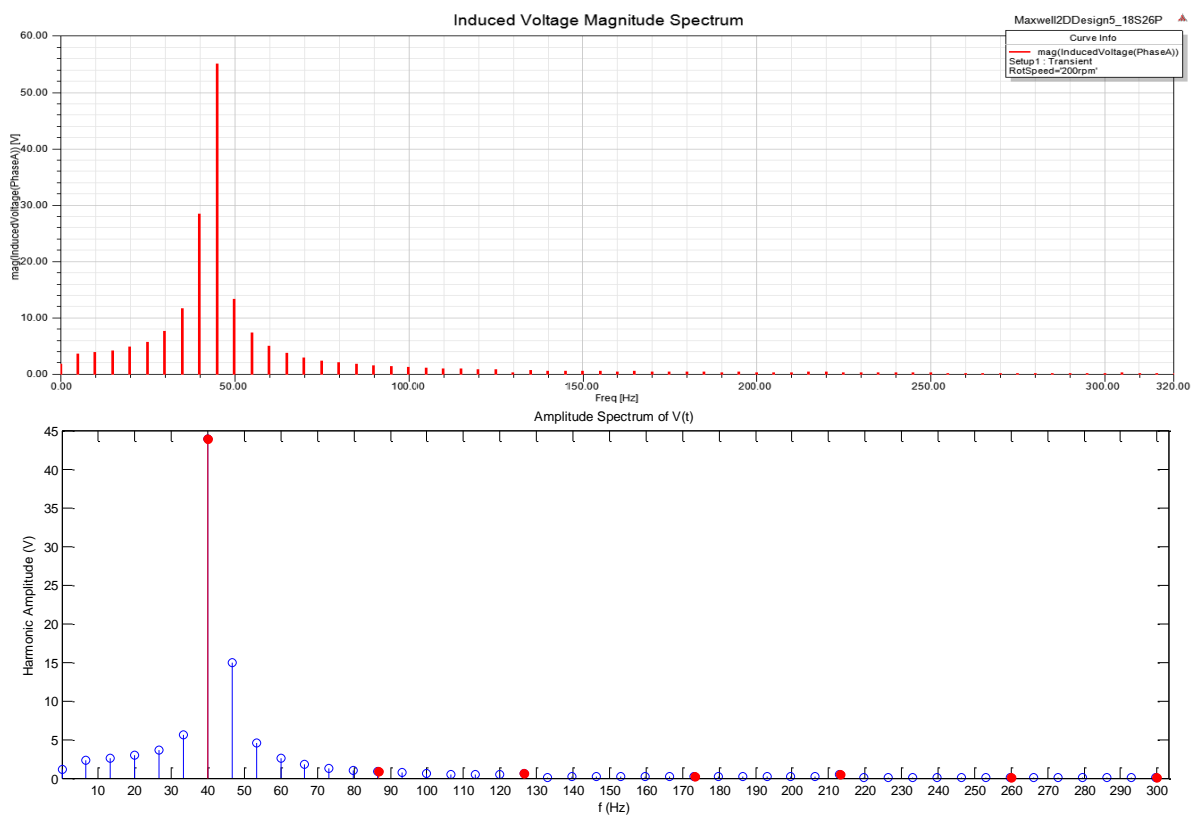


Figure 158: Spectral plots obtained in ANSYS (top) and MATLAB (bottom)

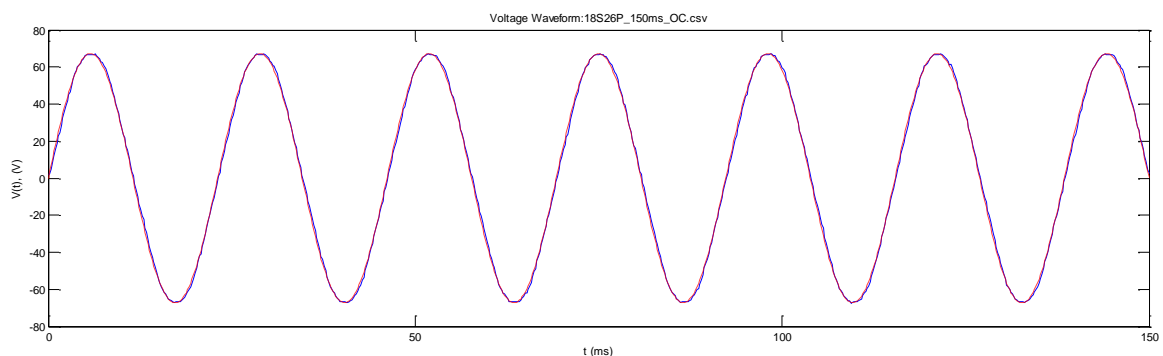


Figure 157: Overlay of the measured voltage waveform (blue) and a pure sine wave (red)

Although the MATLAB script was found to give more accurate THD measurements, the magnitude of the harmonic voltage components was more accurately measured using the ANSYS tools. This was mainly due to the x-axis frequency resolution which caused quantisation errors. The x-axis resolution was set by the FFT operation in MATLAB as a function of the sampling rate.

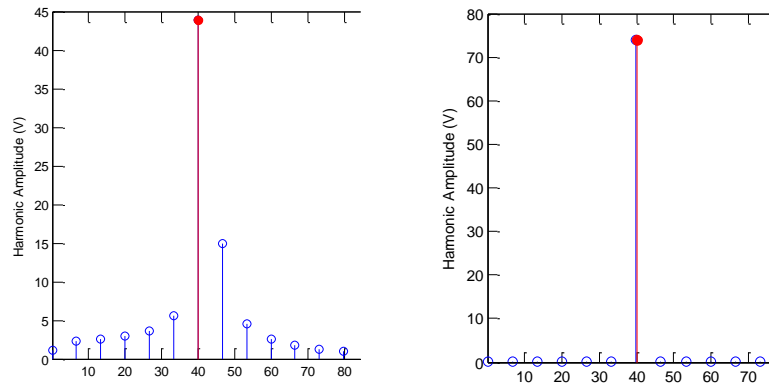


Figure 159: (left) Quantisation error (right) Correctly displayed fundamental at 40 Hz

Both methods, when used together, provided accurate results. Therefore, the THD measurement was taken from the MATLAB calculation, while the magnitude of the harmonic components was calculated using ANSYS Maxwell.

Appendix F: Three-Phase Resistive Load Test

6-Pole Machine

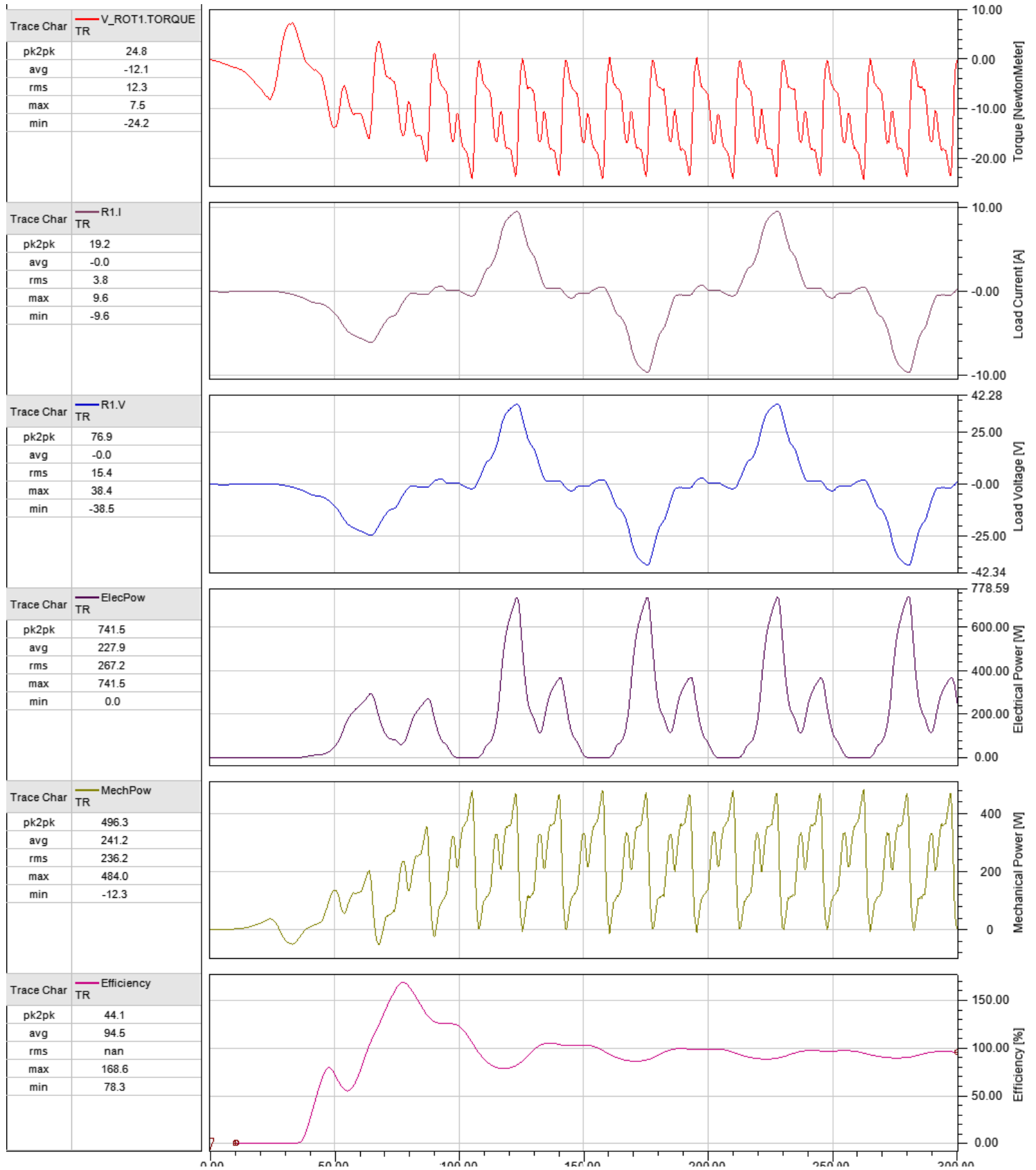


Figure 160: Collected plots from the three-phase resistive test for a 6-pole machine

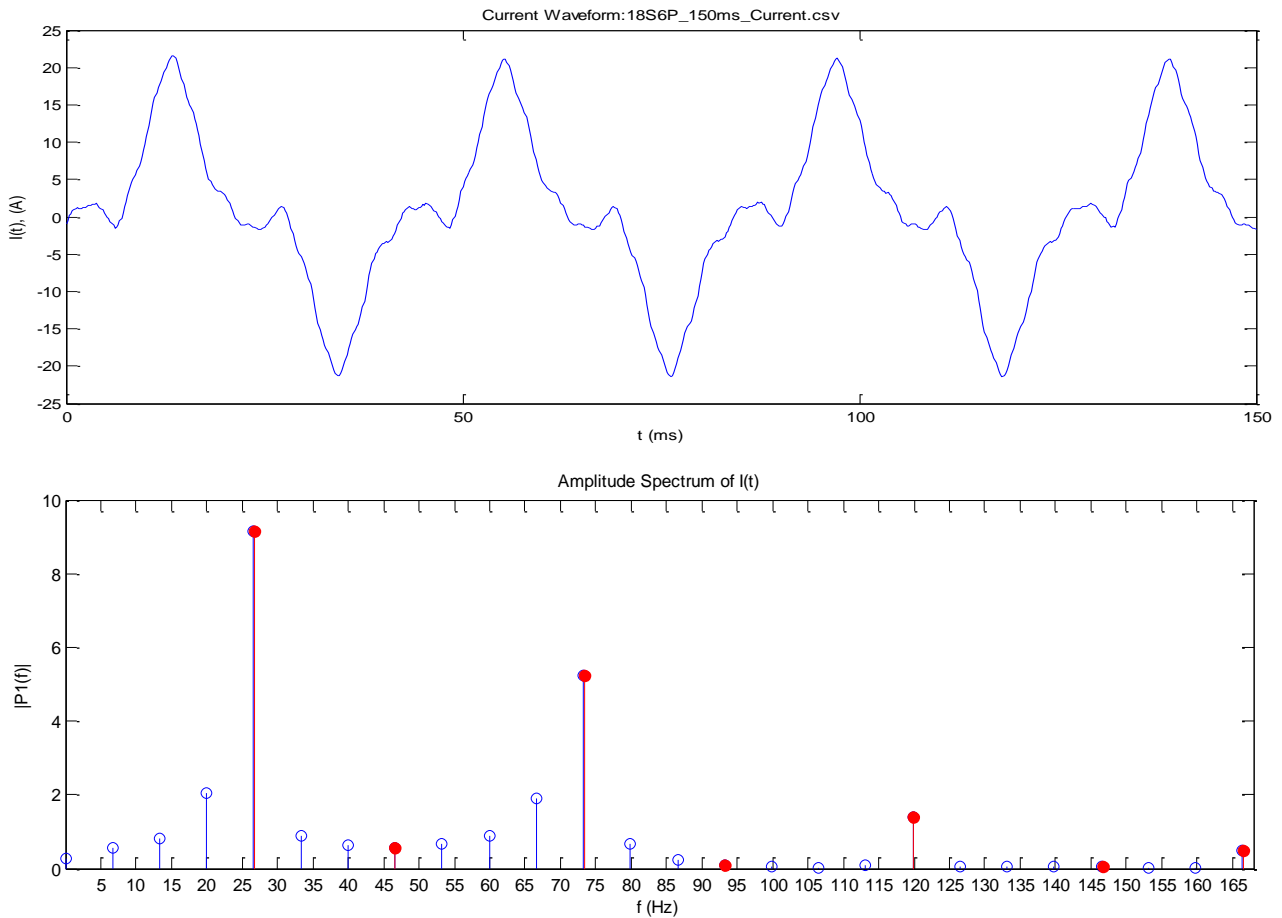


Figure 161: (top) Load current waveform (bottom) Amplitude spectrum

Frequency	25	Hz
Current (Peak)	21.6	A
Current (RMS)	15.3	A
THD	57.0	%

Observations

The results of the test show that the 6-pole machine is unsuitable for this speed. The electrical power is discontinuous, while the torque ripple is exceedingly high. The efficiency briefly reaches above 100%, but this is due to the simulation reacting to the acceleration, and returns to below 100%. The THD is also exceedingly high.

14-Pole Machine

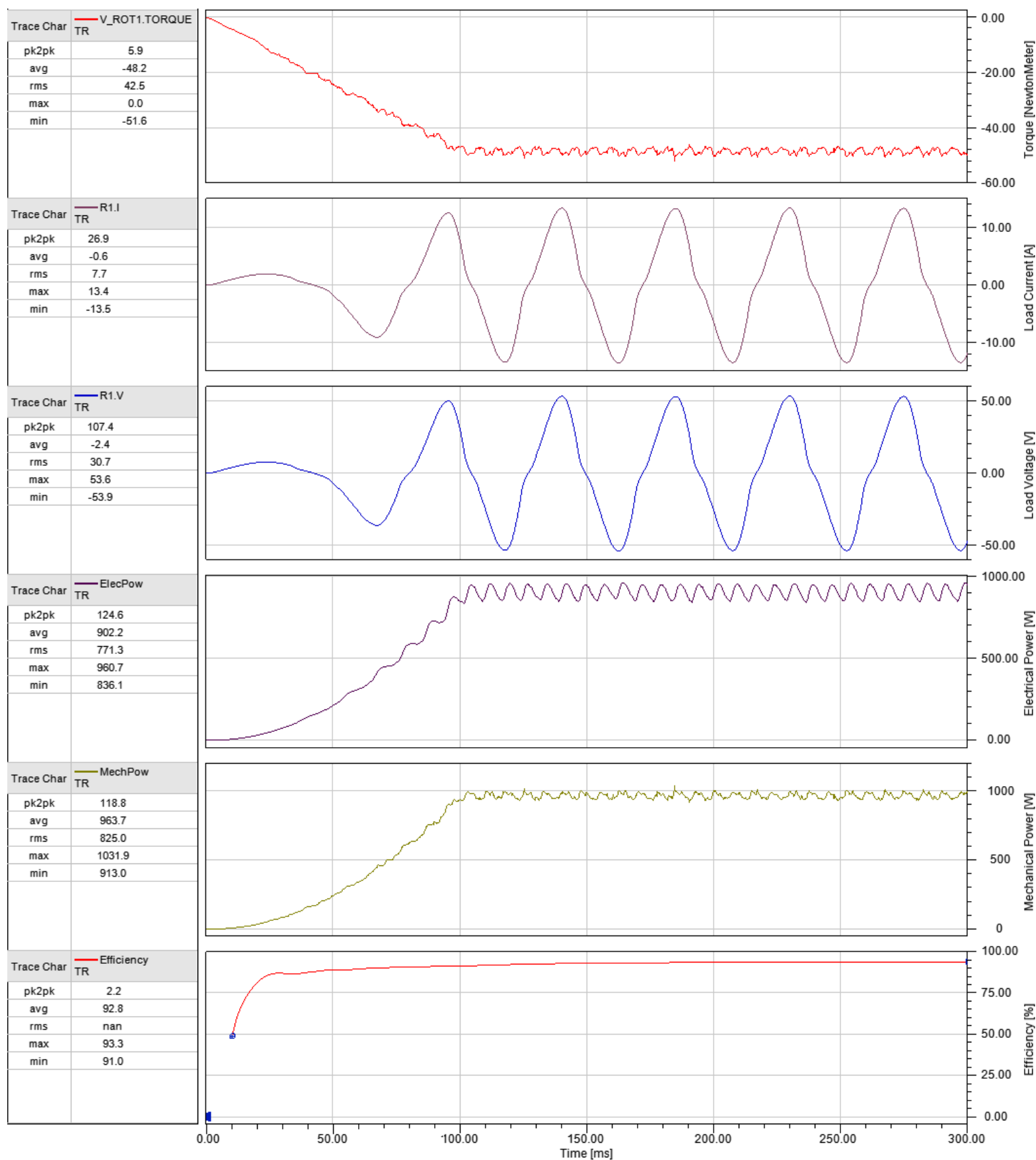


Figure 162: Collected plots from the three-phase resistive test for a 14-pole machine

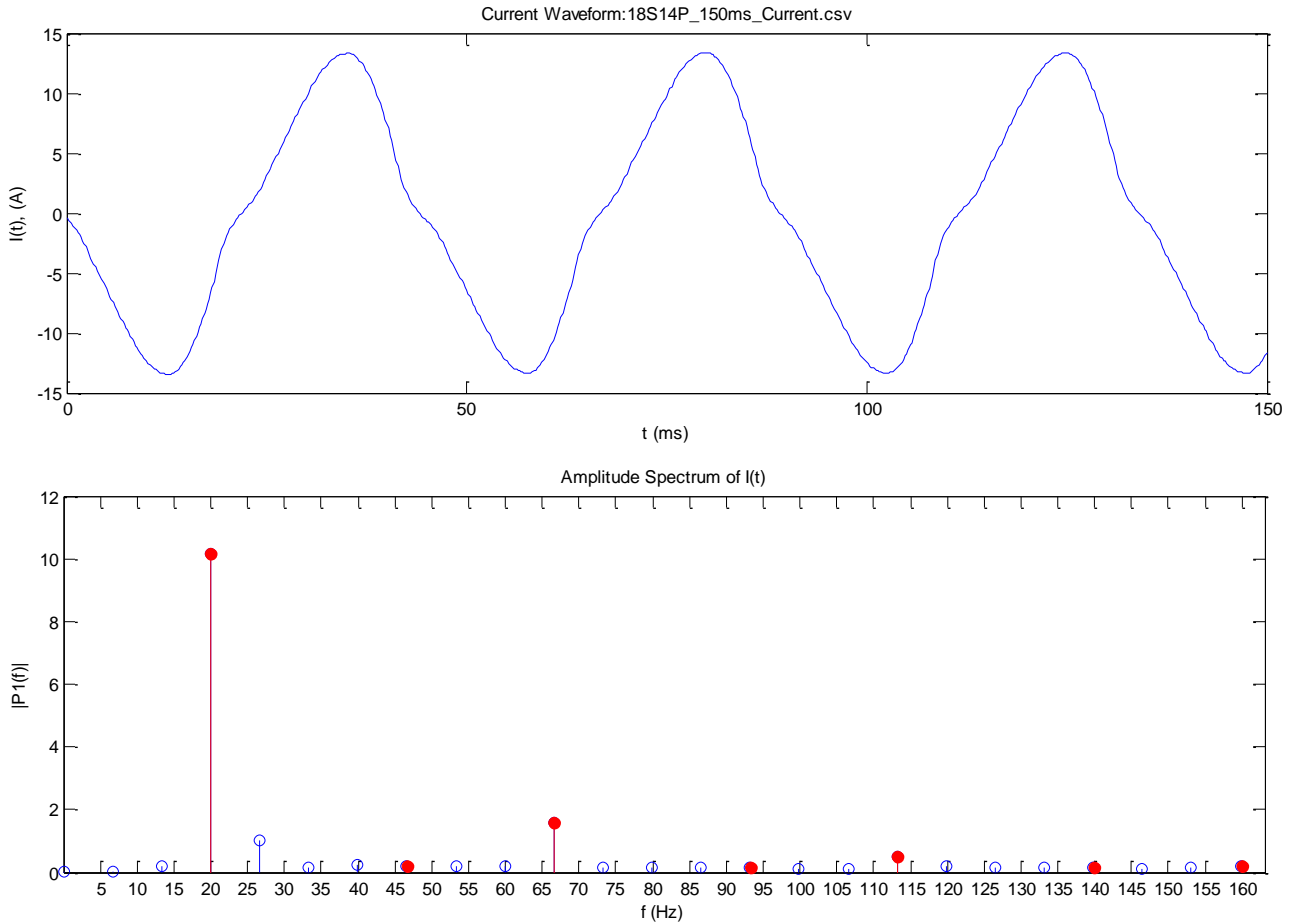


Figure 163: (top) Load current waveform (bottom) Amplitude spectrum

Frequency	23.3 Hz
Current (Peak)	13.4 A
Current (RMS)	7.7 A
THD	16.7 %

Observations

The 14-pole machine performs well, and generates a continuous power of $\approx 900\text{W}$ with minimal torque ripple. It has a high efficiency of 93.3%. However, there is distortion with significant components at the third and fifth harmonics.

20-Pole Machine

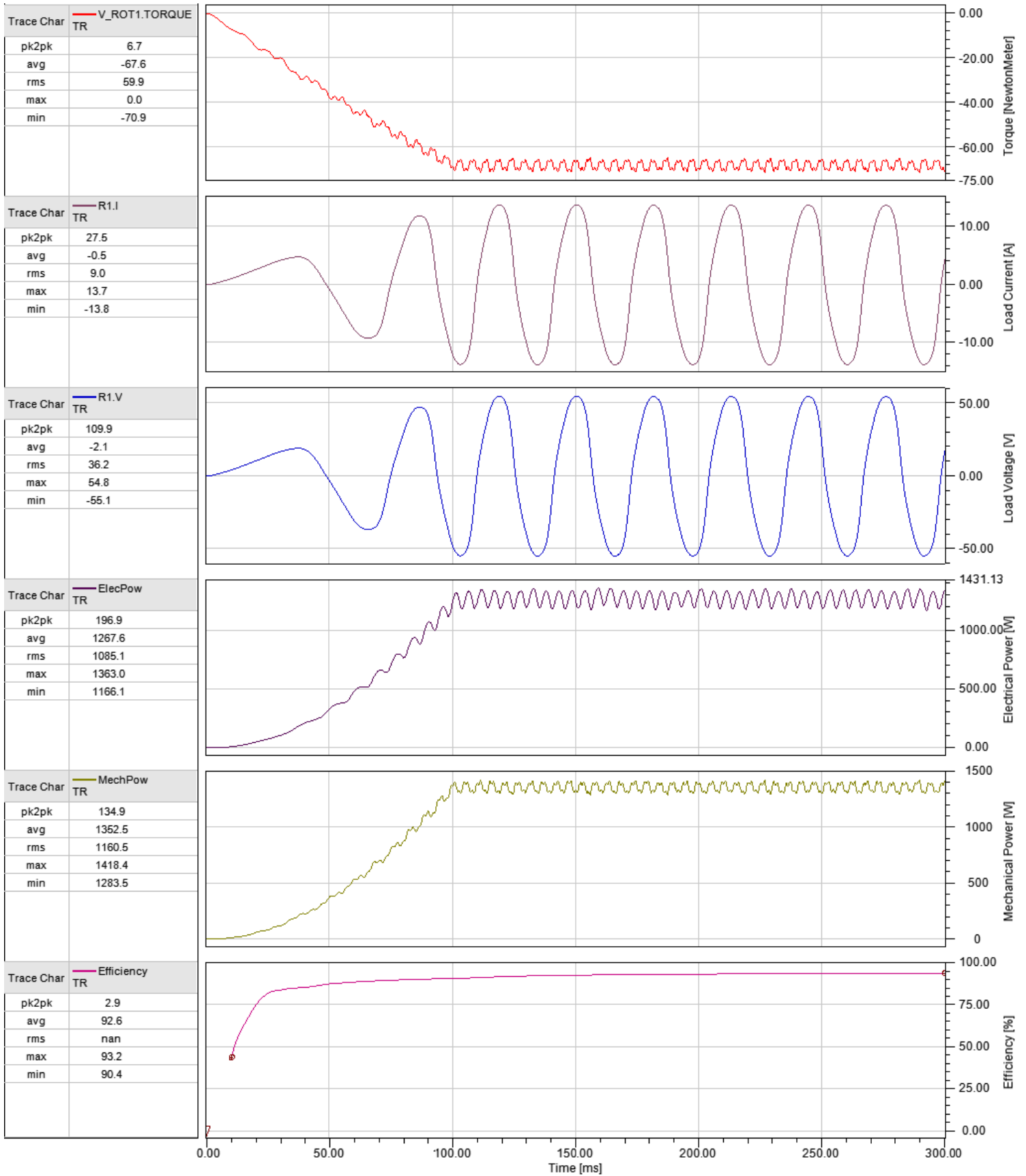


Figure 164: Collected plots from the three-phase resistive test for a 20-pole machine

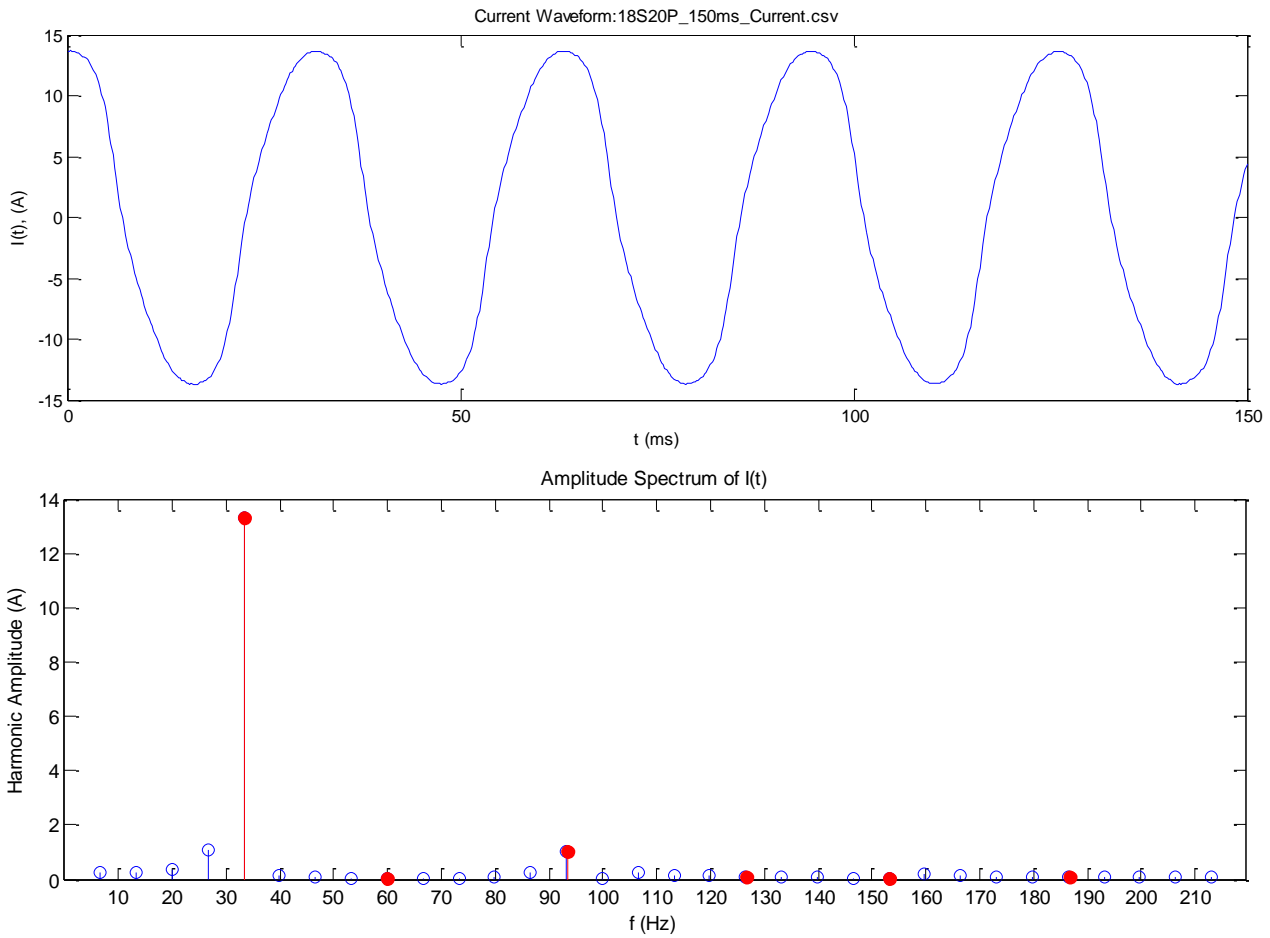


Figure 165: (top) Load current waveform (bottom) Amplitude spectrum

Frequency	33.3	Hz
Current (Peak)	13.7	A
Current (RMS)	9.0	A
THD	7.62	%

Observations

The 20-pole generator performs well with $\approx 1300\text{W}$ with low torque ripple. The THD is reasonable, with significant energy in the third harmonic.

24-Pole Machine

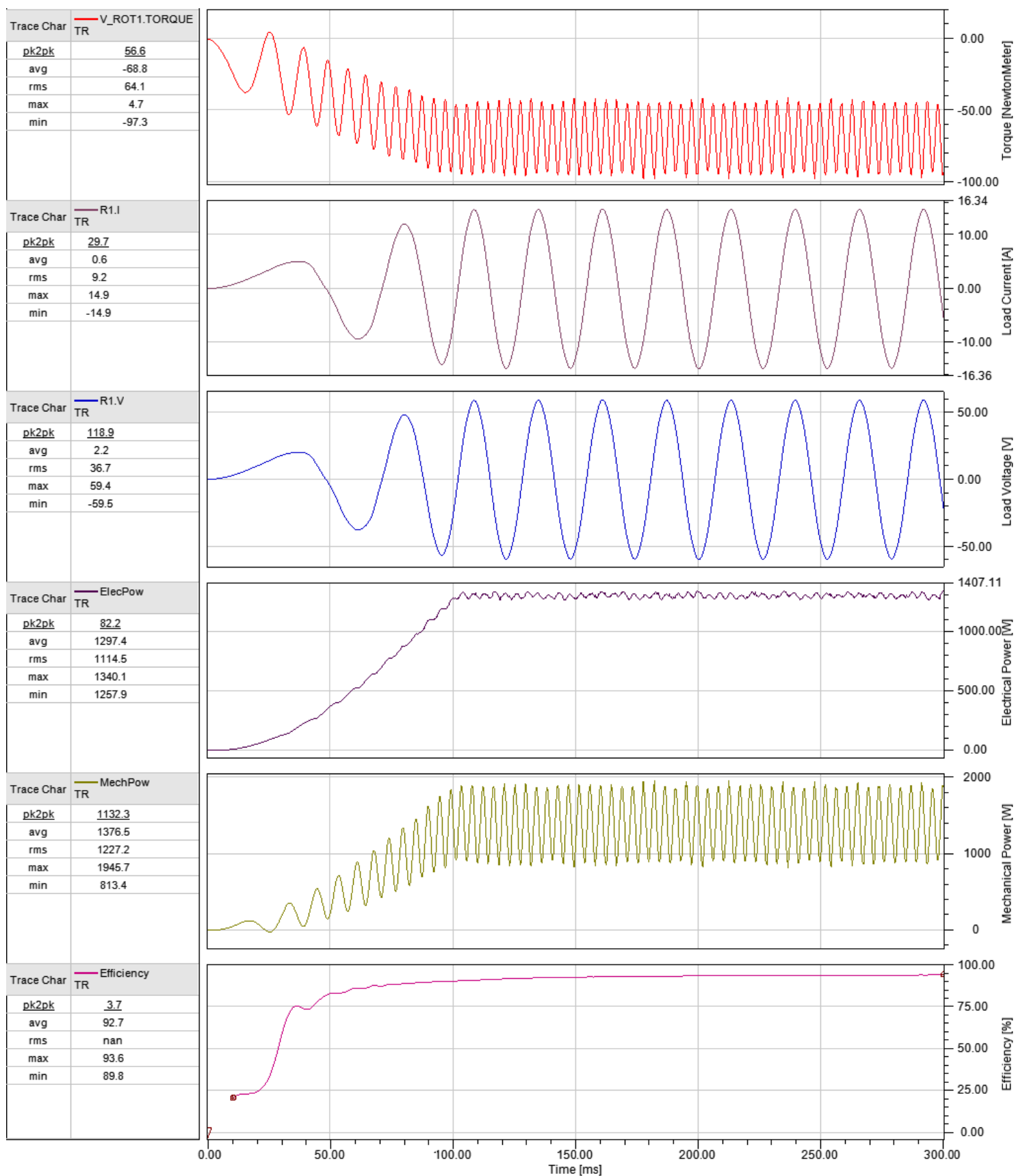


Figure 166: Collected plots from the three-phase resistive test for a 24-pole machine

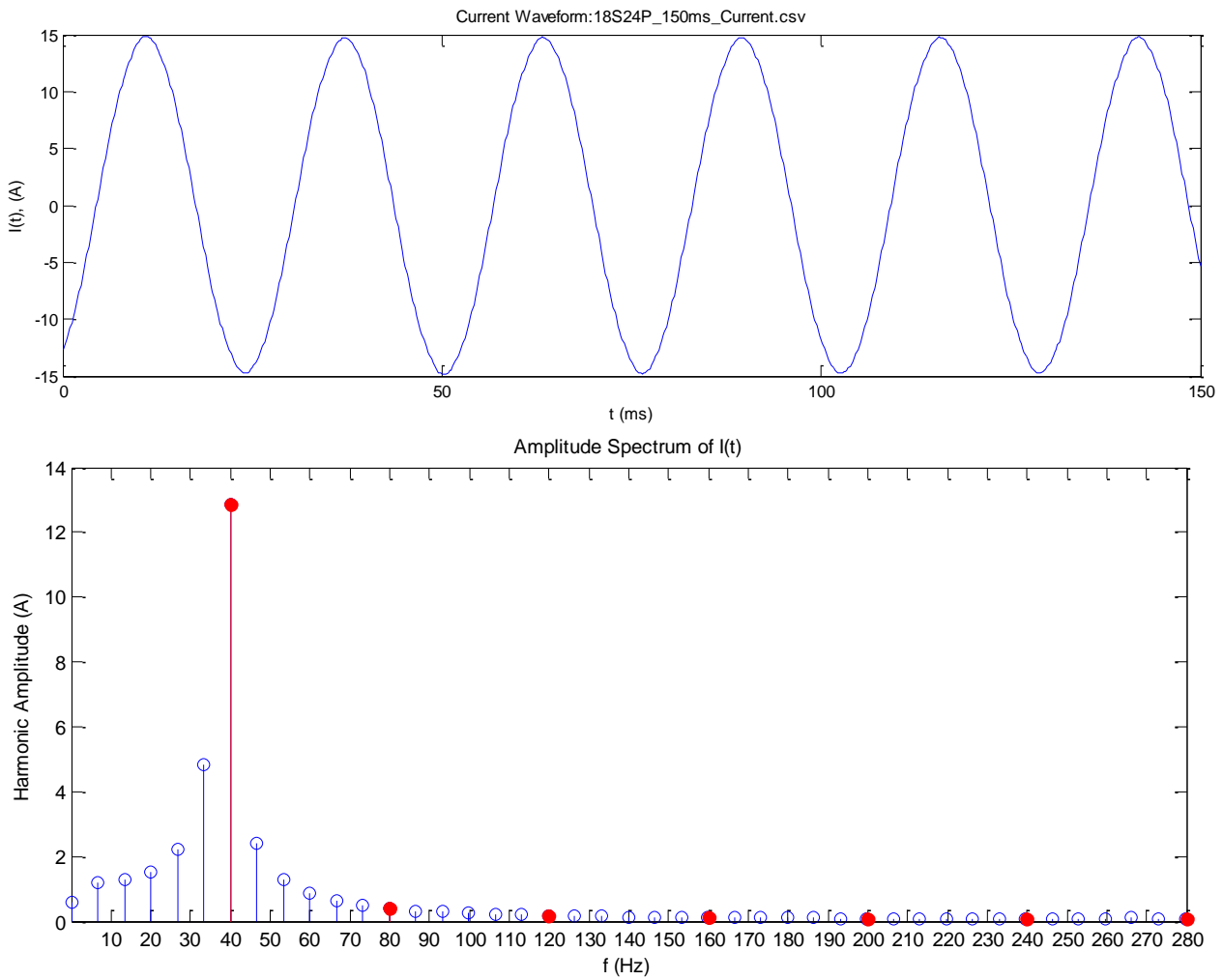


Figure 167: (top) Load current waveform (bottom) Amplitude spectrum

Frequency	40 Hz
Current (Peak)	14.9 A
Current (RMS)	9.2 A
THD	3.55 %

Observations

The 24-pole machine has a high power output of $\approx 1300\text{W}$, a very low distortion current waveform, and a very low-ripple power output. However, the cogging torque is exceedingly high, and restricts the practicality of this machine.

26-Pole Machine

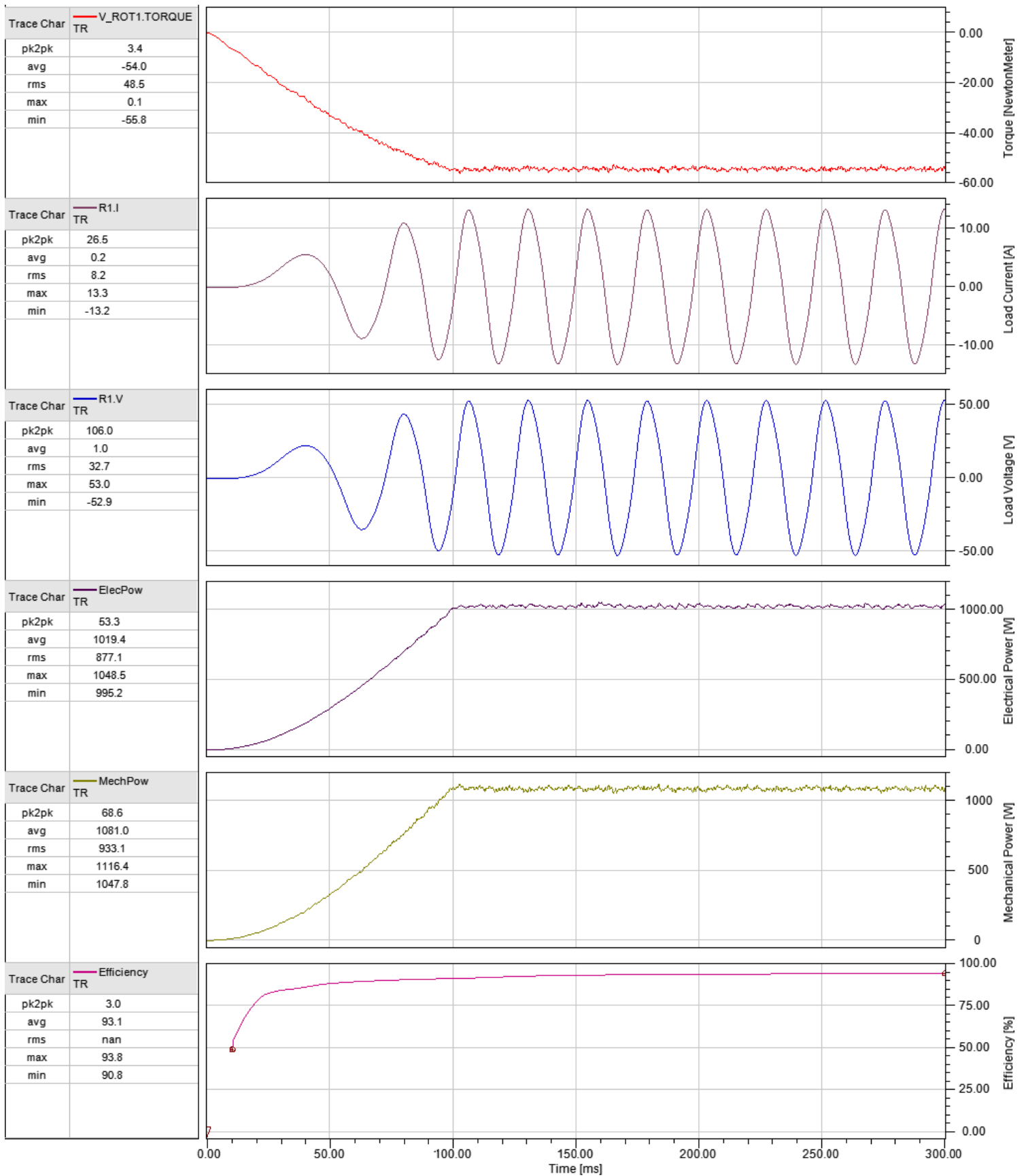


Figure 168: Collected plots from the three-phase resistive test for a 26-pole machine

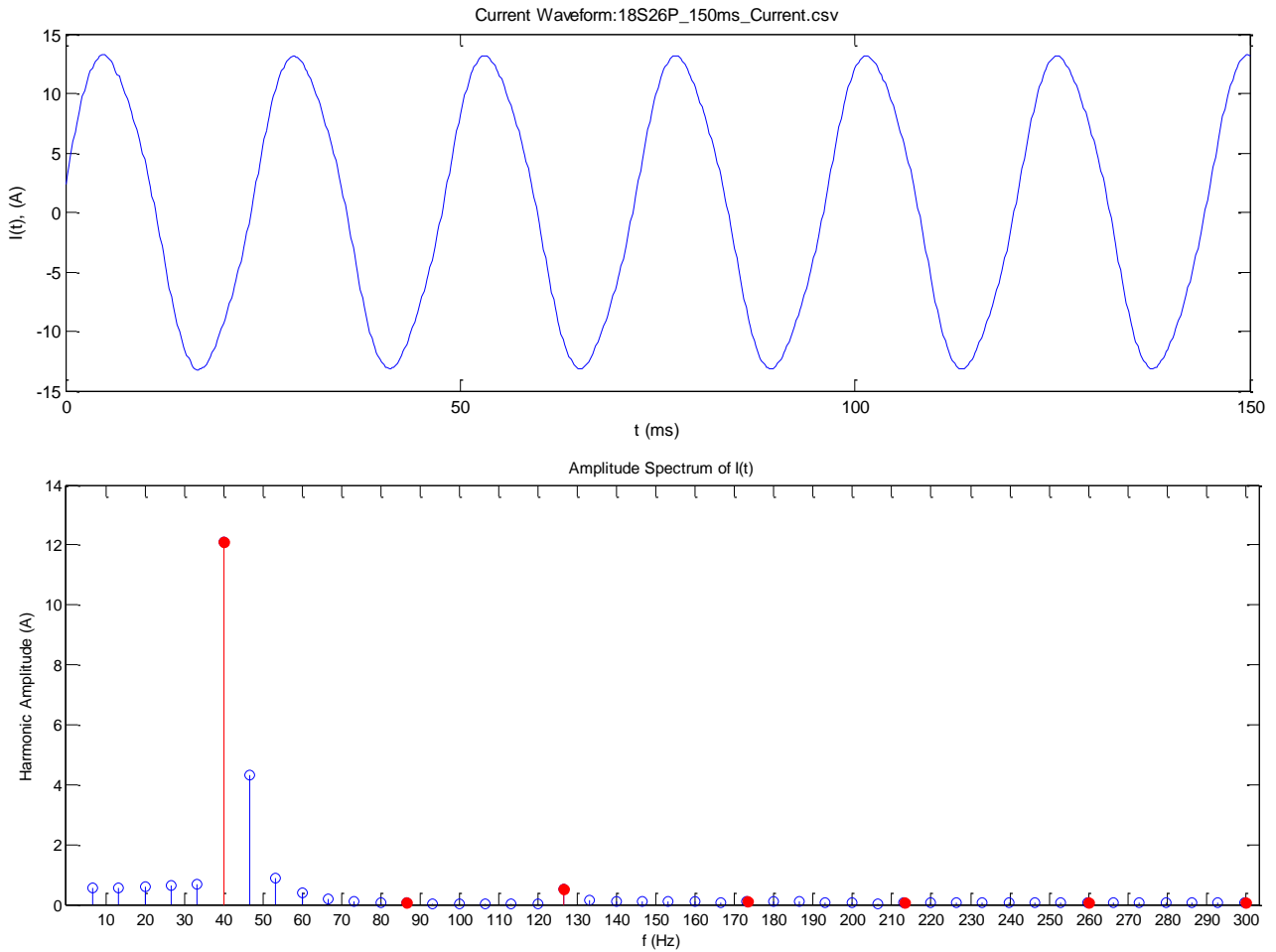


Figure 169: (top) Load current waveform (bottom) Amplitude spectrum

Frequency	43.3 Hz
Current (Peak)	13.3 A
Current (RMS)	8.2 A
THD	4.48 %

Observations

The 26-pole machine has an adequate power output of 1kW, but has extremely low torque ripple, extremely low power ripple, and efficiency of 93.8%. The THD is relatively low, with significant energy in the third harmonic.

Appendix G: Rectified Output Load Resistive Test

6-Pole Machine

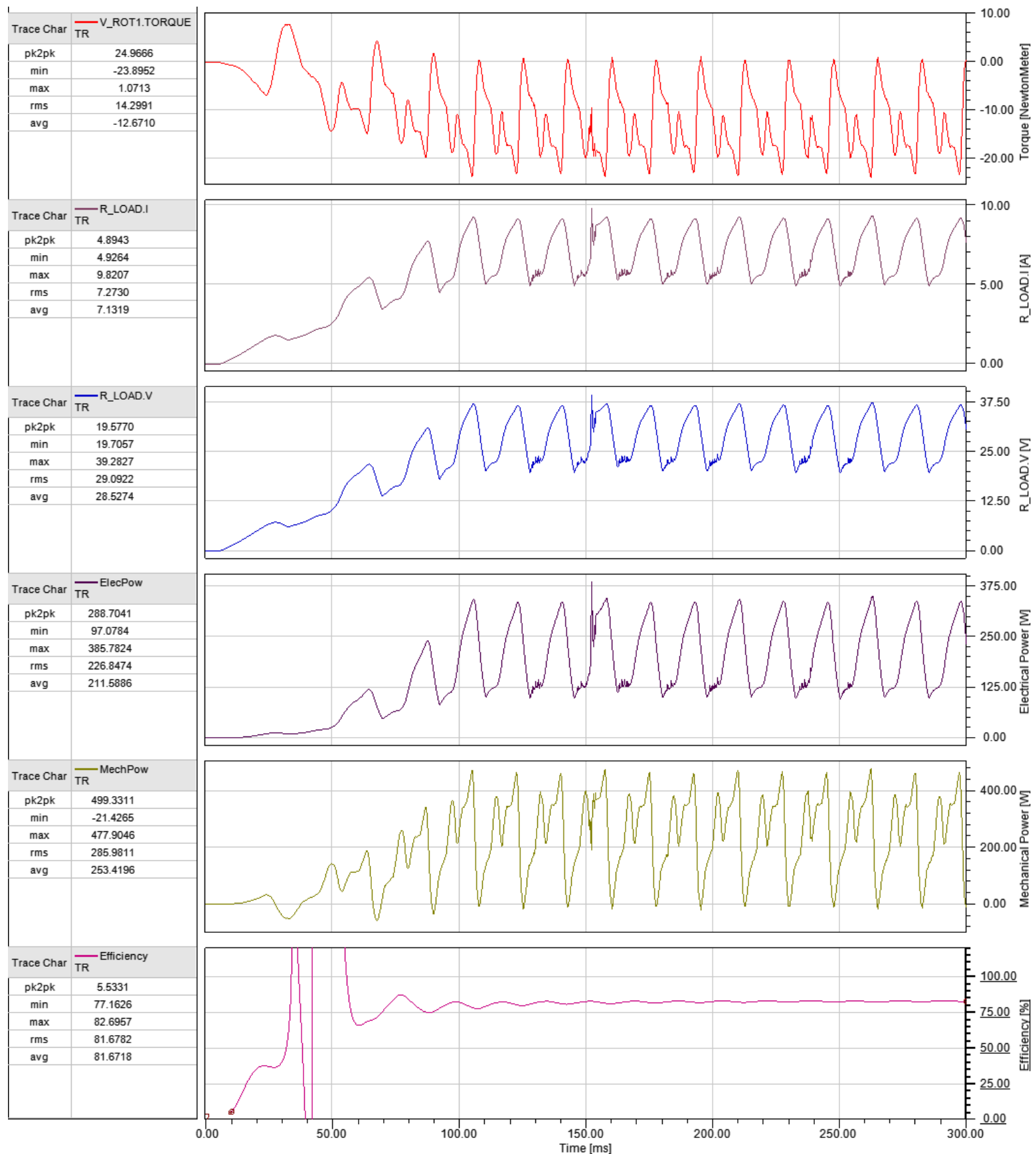


Figure 170: Collected plots from the rectifier test with resistive load [6-pole machine]

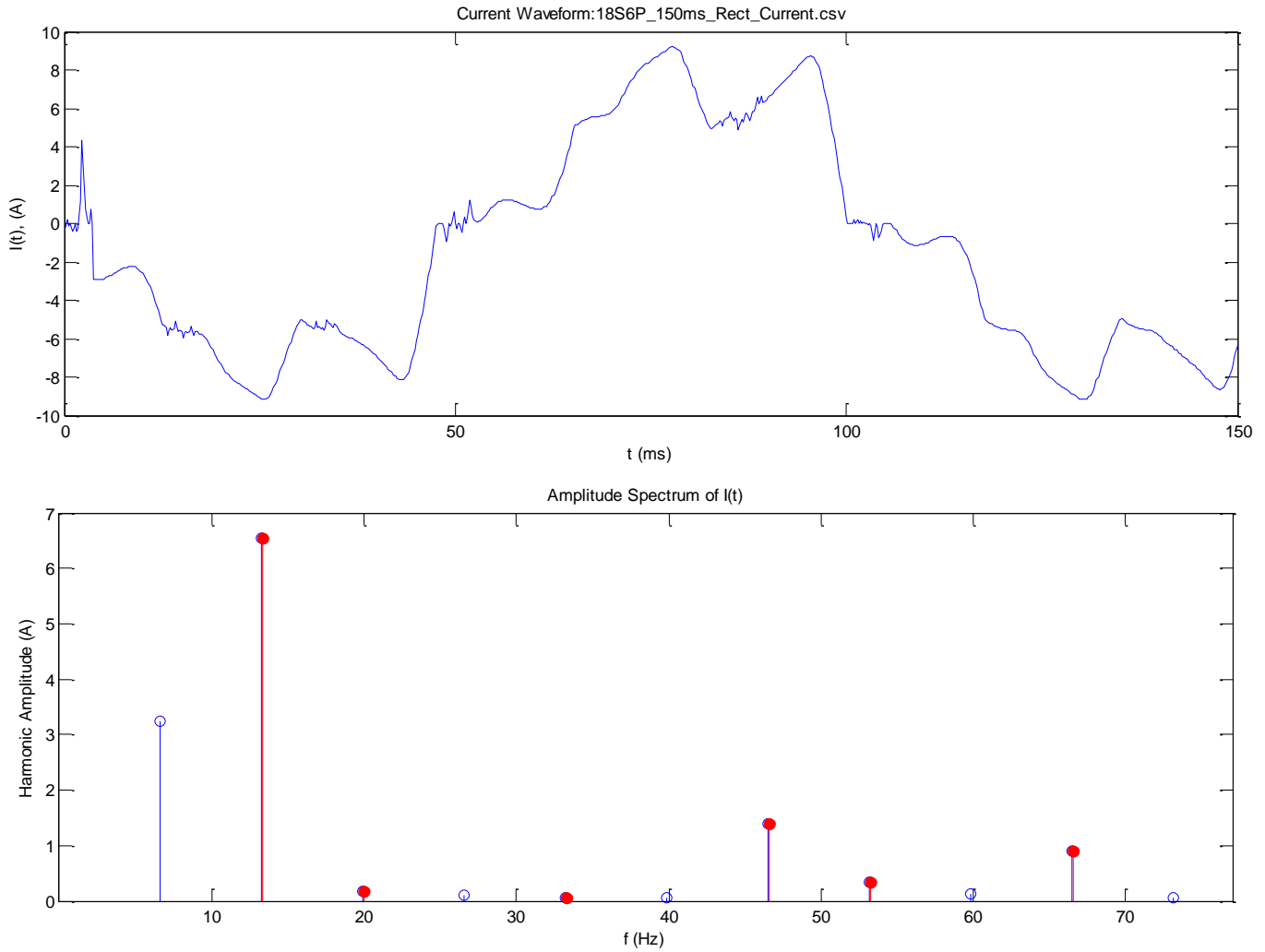


Figure 171: (top) Load current waveform (bottom) Amplitude spectrum)

Frequency	25.0	Hz
Current (Peak)	9.19	A
Current (RMS)	5.74	A
THD	26.4	%

Observations

The 6-pole machine has very high levels of distortion in the windings. This may lead to excessive heating of the generator. The torque ripple of the generator is unacceptably high, and the power generated is almost discontinuous. This machine is operating very poorly at low speeds.

14-Pole Machine

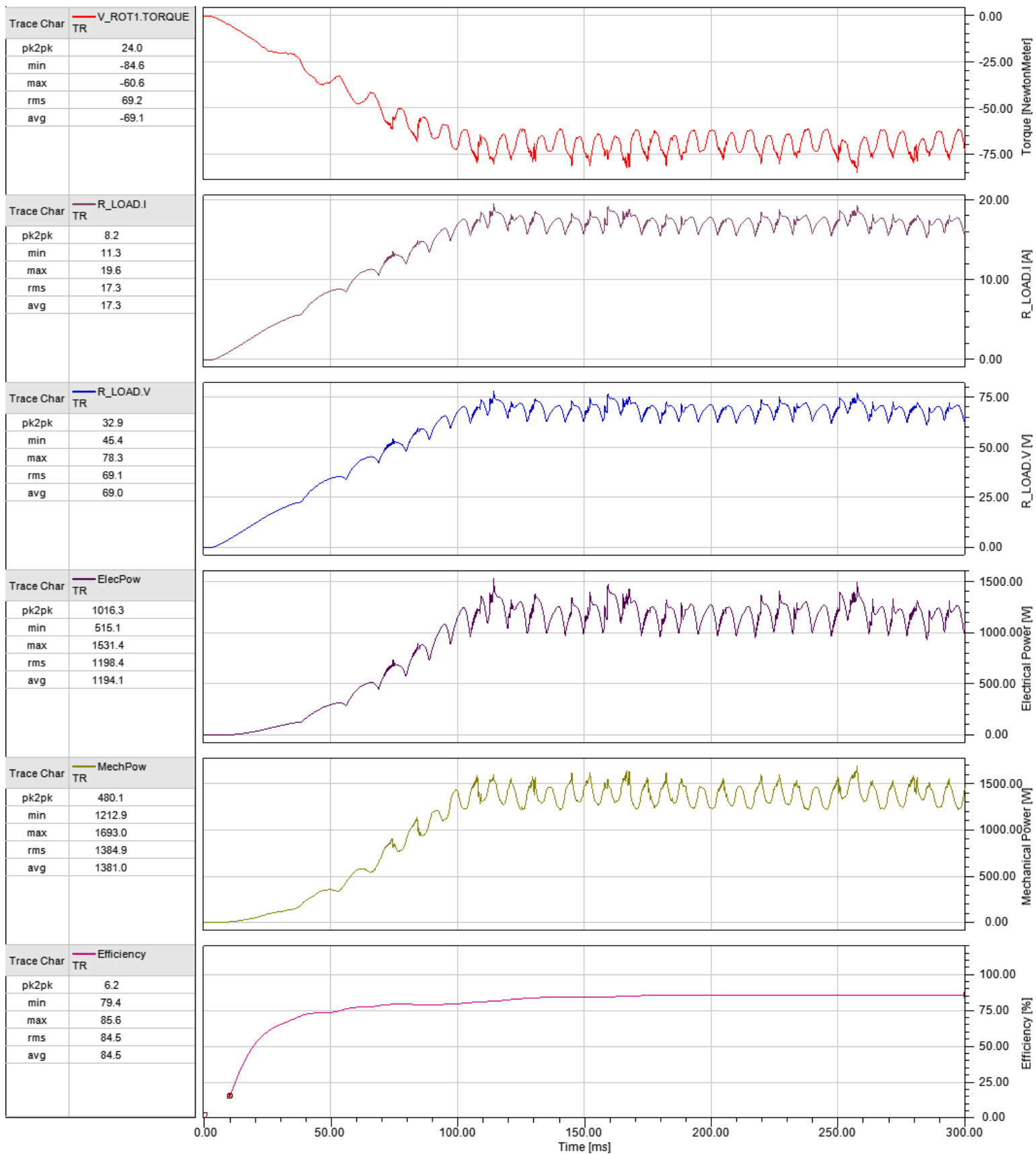


Figure 172: Collected plots from the rectifier test with resistive load [14-pole machine]

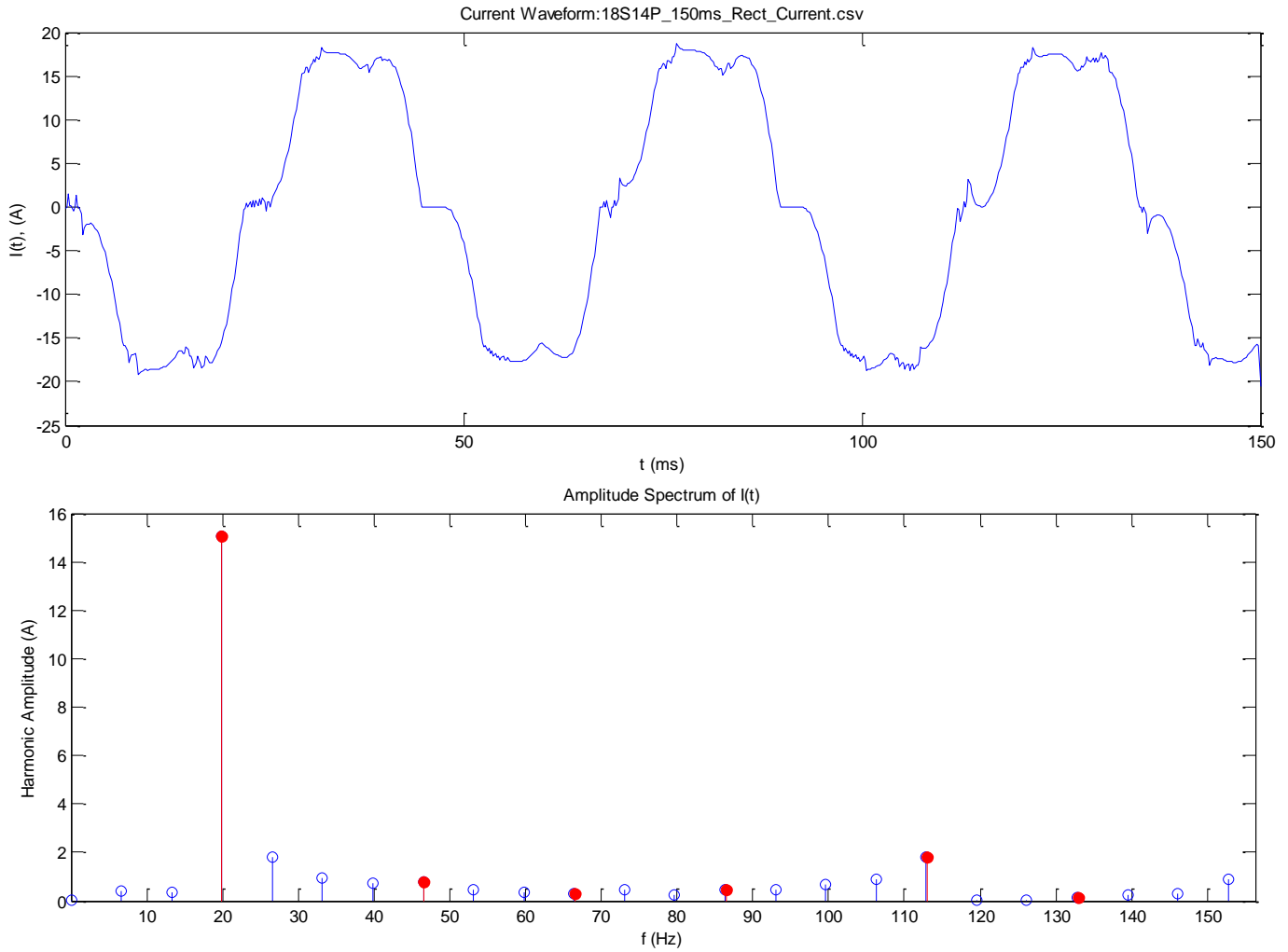


Figure 173: (top) Load current waveform (bottom) Amplitude spectrum)

Frequency	23.33	Hz
Current (Peak)	18.8	A
Current (RMS)	13.4	A
THD	13.9	%

Observations

The 14-pole generator achieves 1kW at the rated speed. The torque ripple is low, and has a relatively high combined efficiency with the rectifier. There are slight transient fluctuations in the torque which may be a result of harmonics generated in the stator currents by the rectifier. The spectral analysis shows that there is significant energy at anharmonic frequencies. Although this may be noise, the current waveform can also be observed to contain irregular transients.

20-Pole Machine

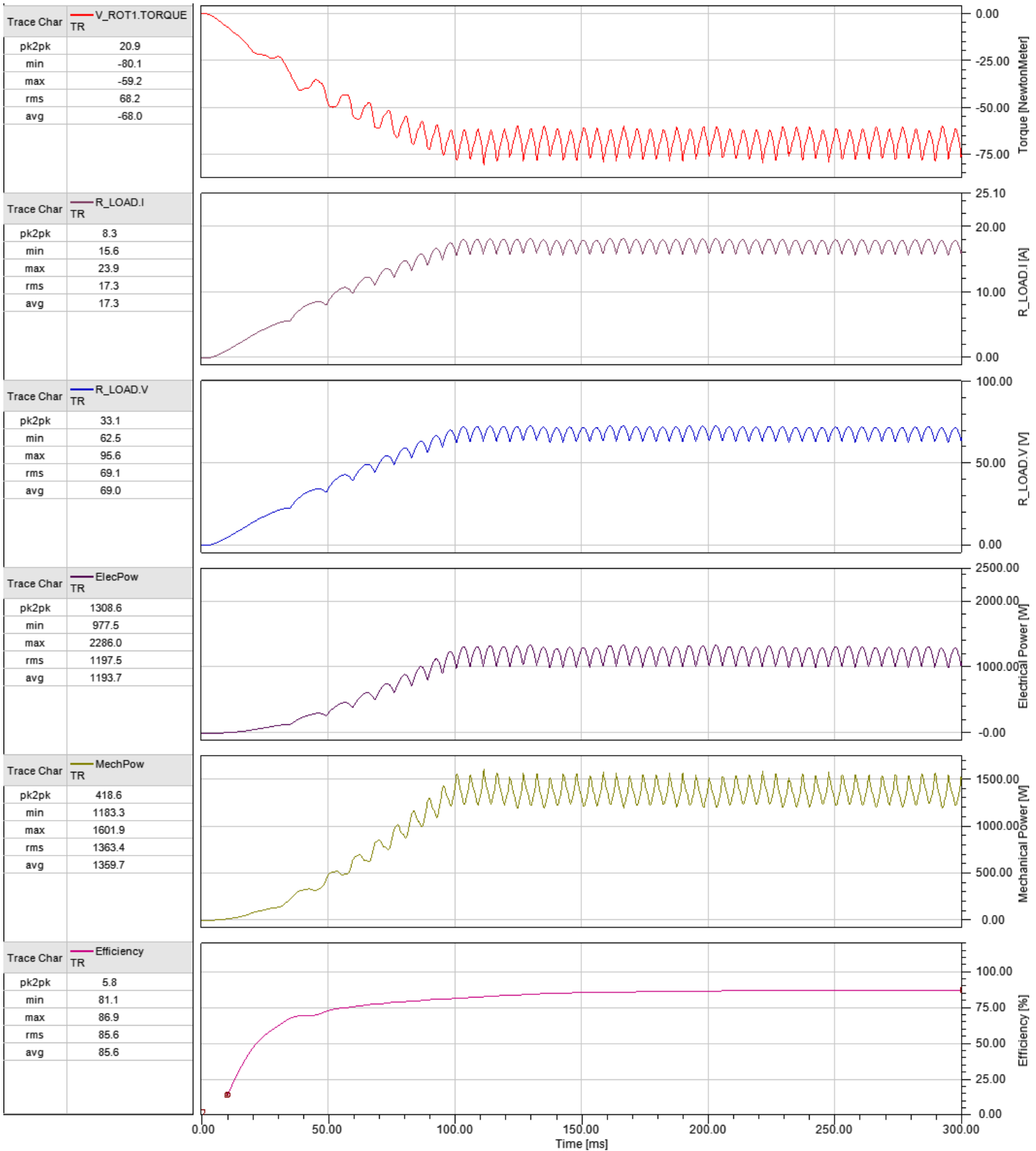


Figure 174: Collected plots from the rectifier test with resistive load [20-pole machine]

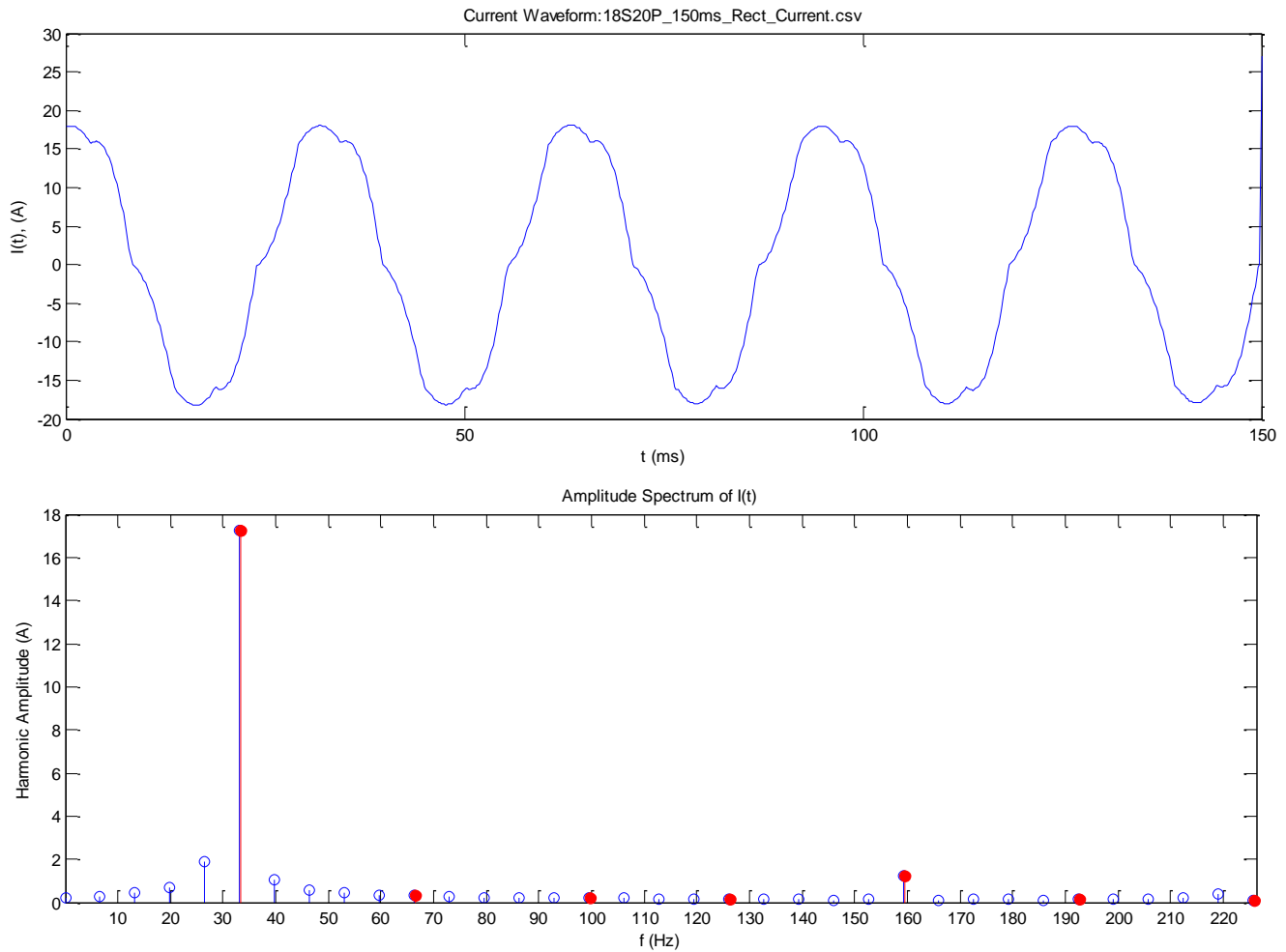


Figure 175: (top) Load current waveform (bottom) Amplitude spectrum

Frequency	33.33	Hz
Current (Peak)	18.1	A
Current (RMS)	13.1	A
THD	7.65	%

Observations

The 20-pole machine generates a similar power output as the 14-pole machine, however, does not suffer the torque fluctuations. The current waveform through the windings can be seen to be much smoother, although still having significant distortion. The spectral analysis shows that most of the distortion is caused by the fifth harmonic.

24-Pole Machine

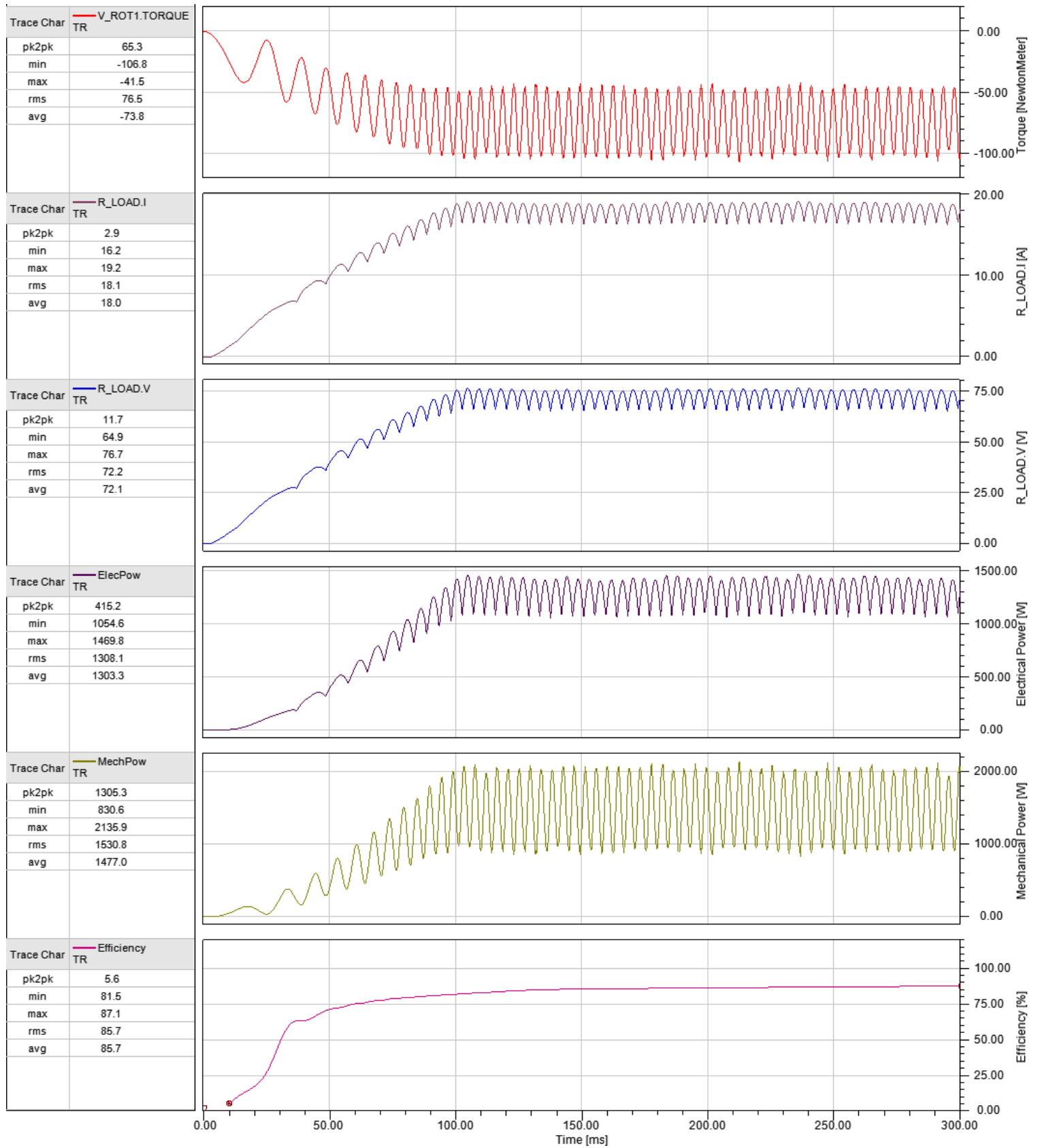


Figure 176: Collected plots from the rectifier test with resistive load [24-pole machine]

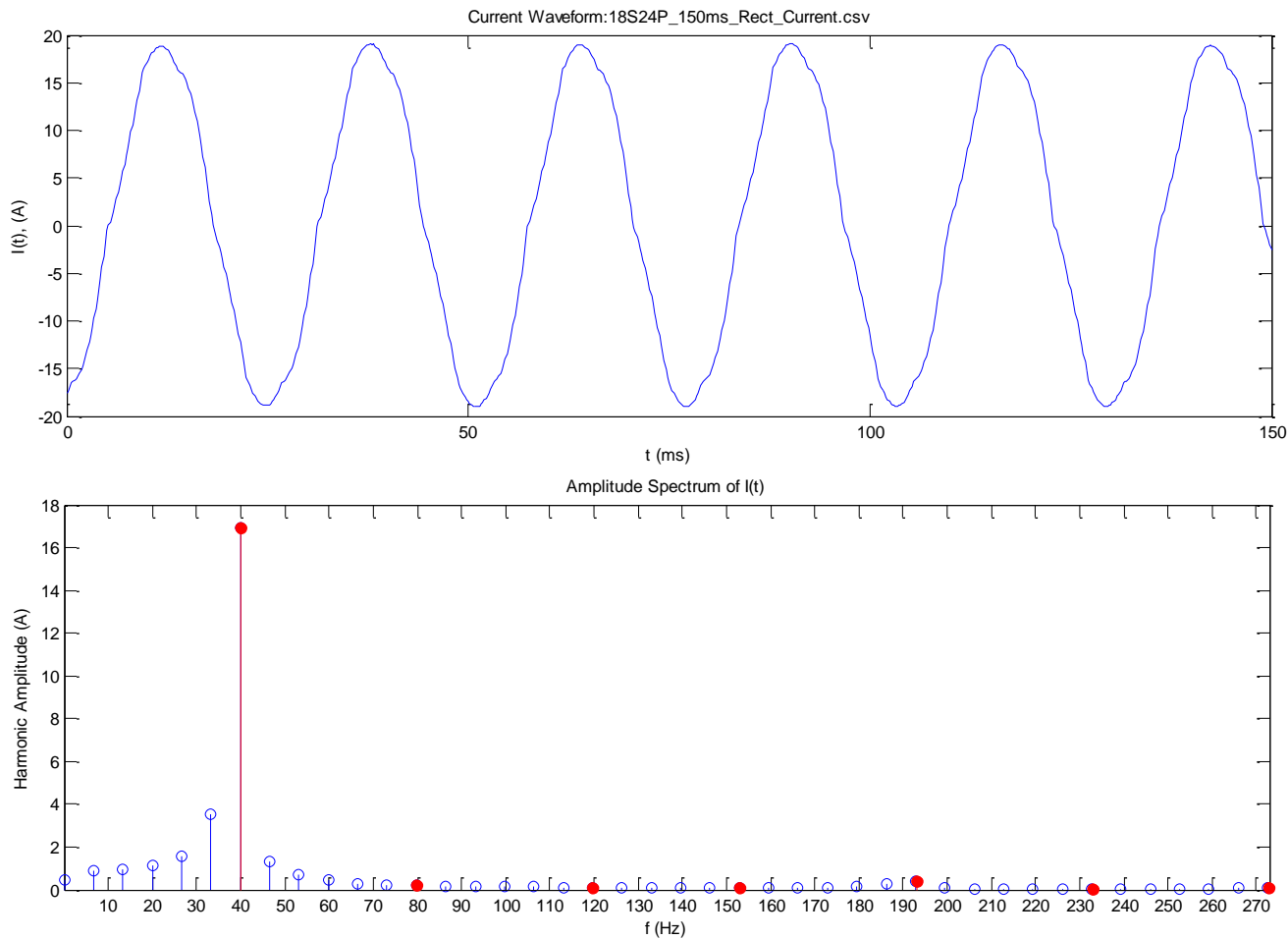


Figure 177: (top) Load current waveform (bottom) Amplitude spectrum

Frequency	40.0	Hz
Current (Peak)	19.1	A
Current (RMS)	13.4	A
THD	2.89	%

Observations

Although the harmonic distortion in the windings is very low, the 24-pole generator performance is greatly impeded by its large cogging torque. The generated power is slightly higher than 1 kW.

26-Pole Machine

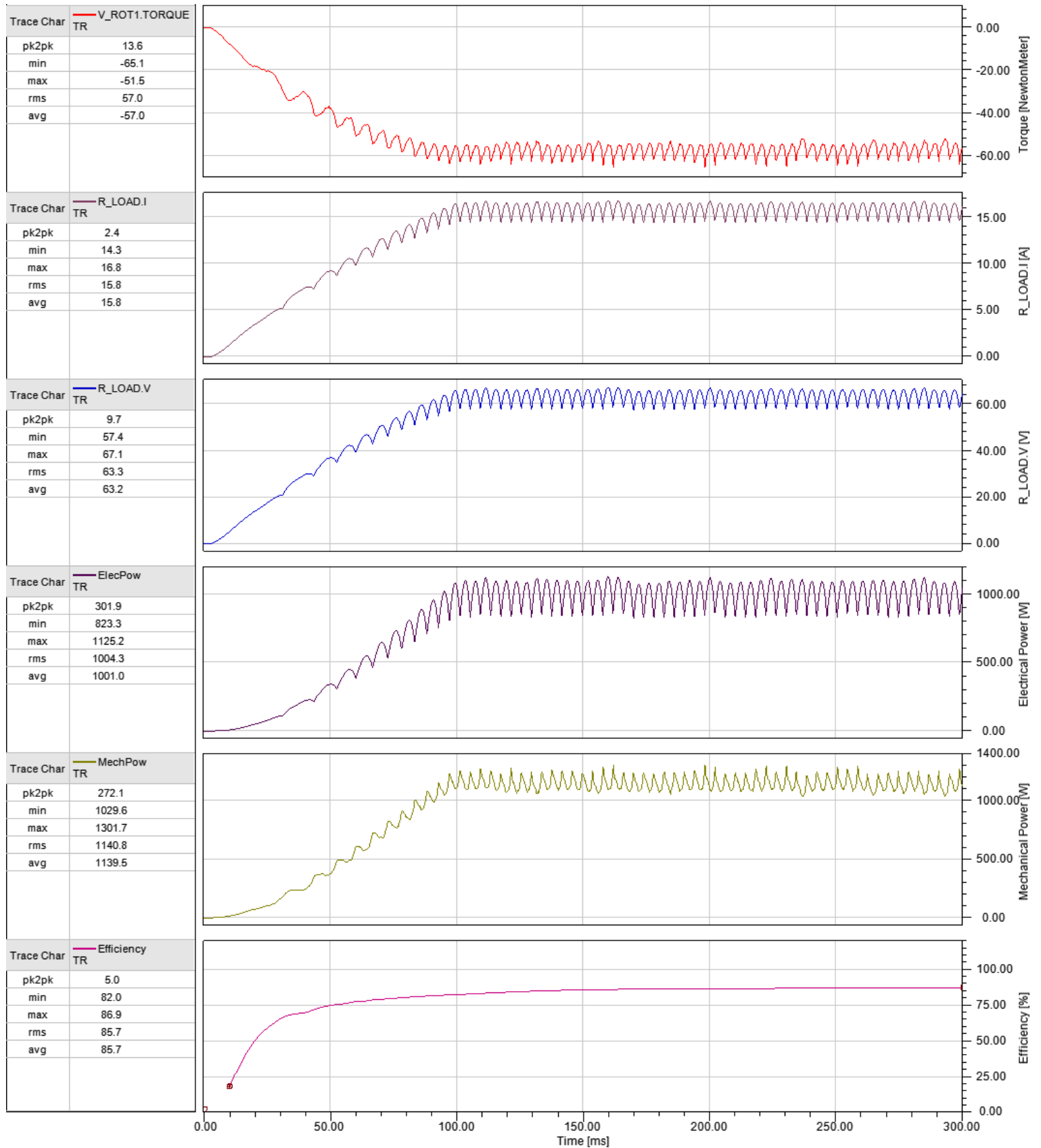


Figure 178: Collected plots from the rectifier test with resistive load [26-pole machine]

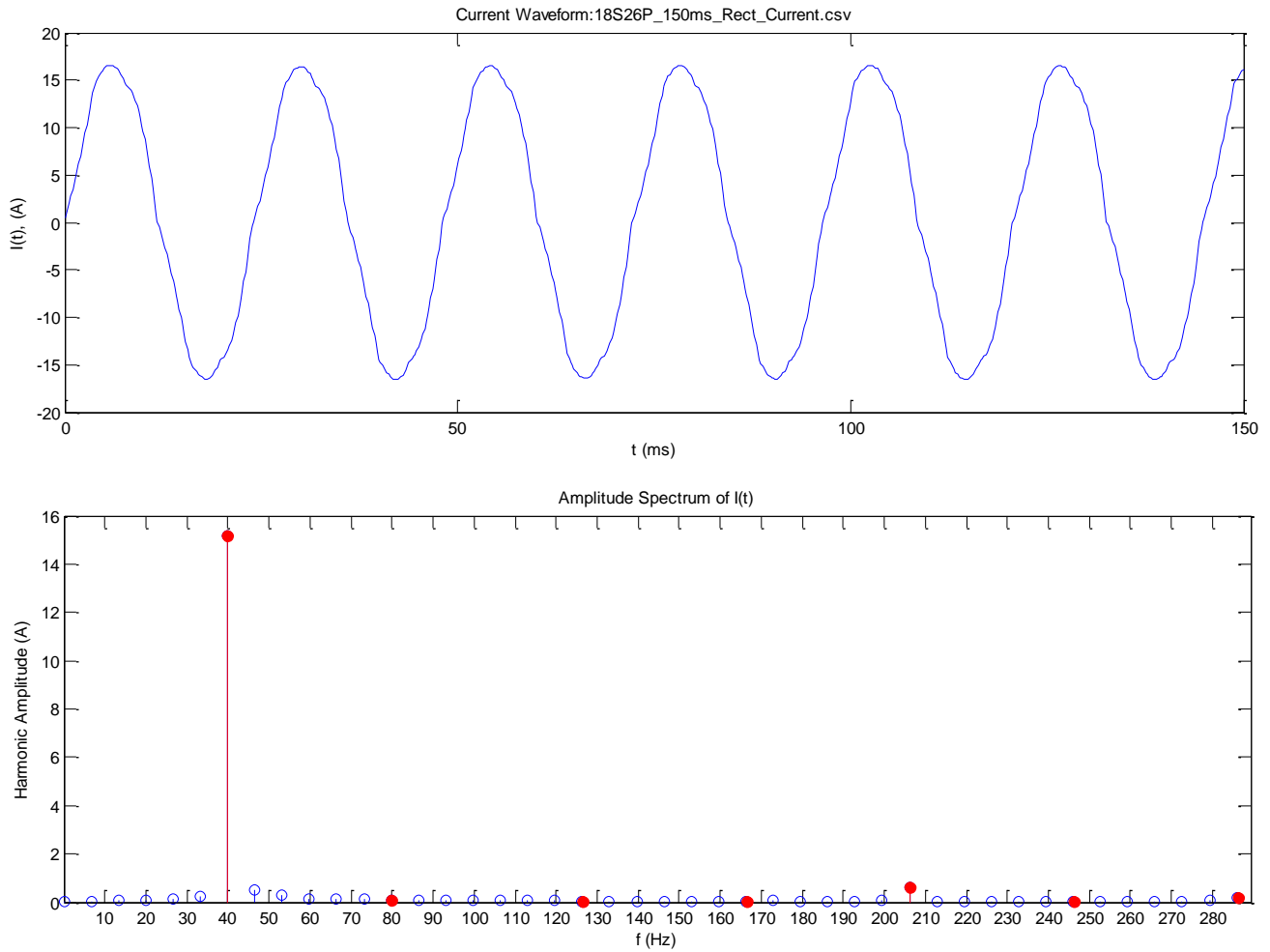


Figure 179: (top) Load current waveform (bottom) Amplitude spectrum

Frequency	10.0	Hz
Current (Peak)	16.6	A
Current (RMS)	11.7	A
THD	4.32	%

Observations

The 26-pole generator exhibits slightly lower power output than most of the other machines, however, it has low THD in the winding currents, and the lowest value of torque ripple.

Appendix H: Maxwell 2D Meshing Result

The mesh used for the simulations is almost identical throughout the tests and use identical meshing parameters. Therefore only the 24-pole machine mesh is presented.

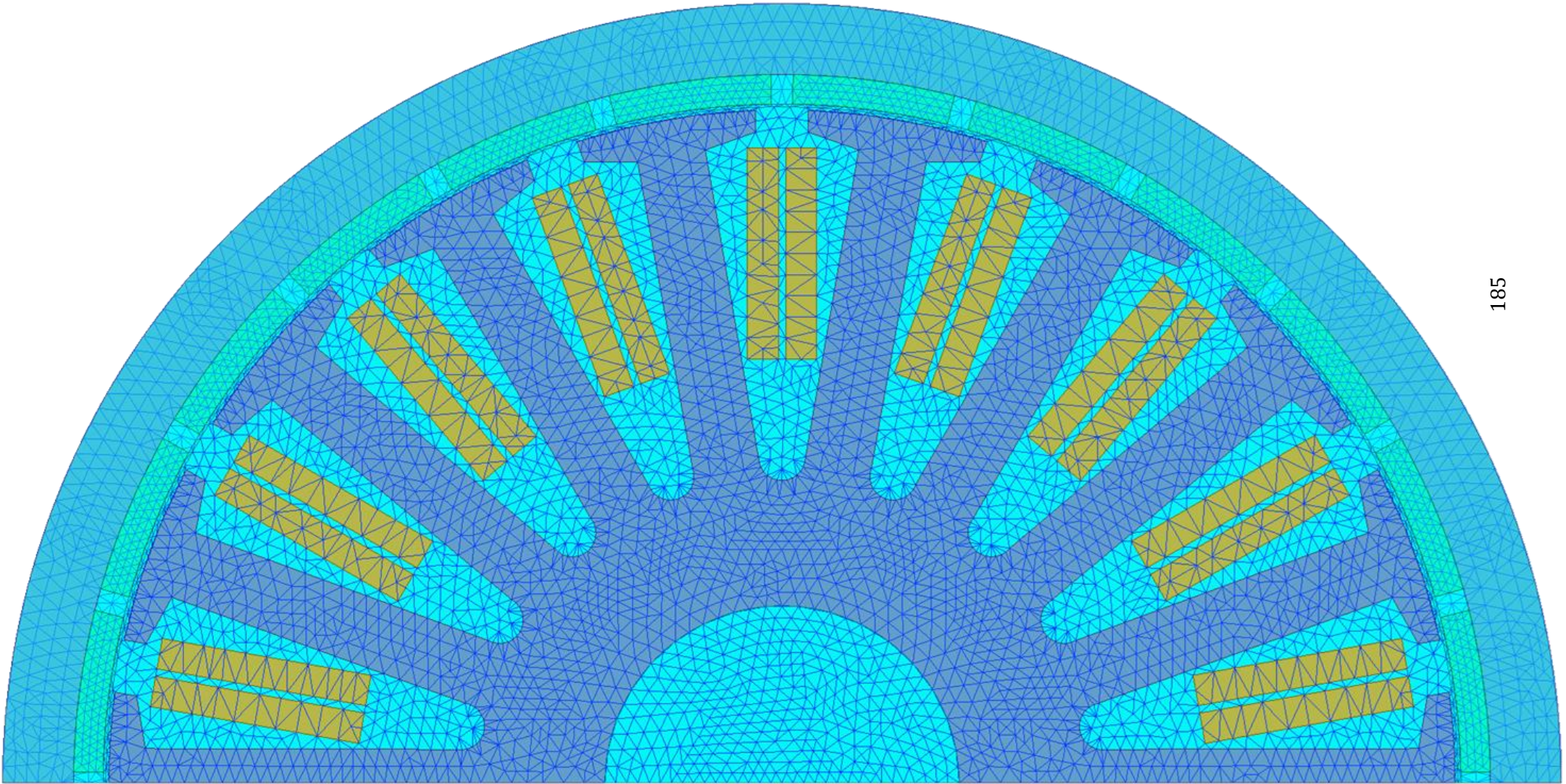


Figure 180: Meshing result for the 18-slot 24-pole machine

Appendix J: Simplorer Circuit Diagrams

Three-Phase Load Test

The first test focused on the effect of a resistive load at rated speed (200 rpm). The basic Simplorer setup is shown in Figure 181.

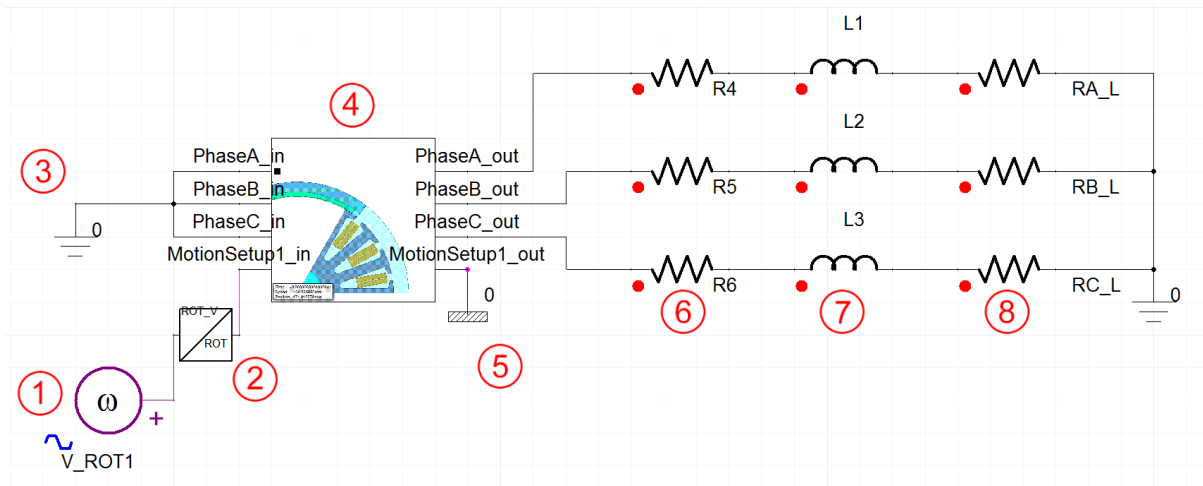


Figure 181: Three-phase load test setup in Simplorer

In this setup the following features are displayed:

1. The input angular velocity waveform generated in Simplorer. This specifies the profile of the input speed, and supplies as much torque as needed to maintain the speed specified.
2. A conversion element that changes the type of variable such that the generator in Maxwell can use the signal.
3. The electrical grounding point for the generator. The generator is arranged in a Wye configuration with this point as the central ground.
4. The cosimulation element that represents the Maxwell 2D simulation.
5. A mechanical ground that specifies that the angular velocity supplied is an absolute value, rather than a relative motion between two rotating objects.
6. Resistors to model the resistance of the windings. The copper loss values are generated from this.
7. Inductors are used to model the inductance associated with the windings.
8. The load resistors simulating the use of a three-phase heating element or similar device.

Rectifier Load Test (Resistive)

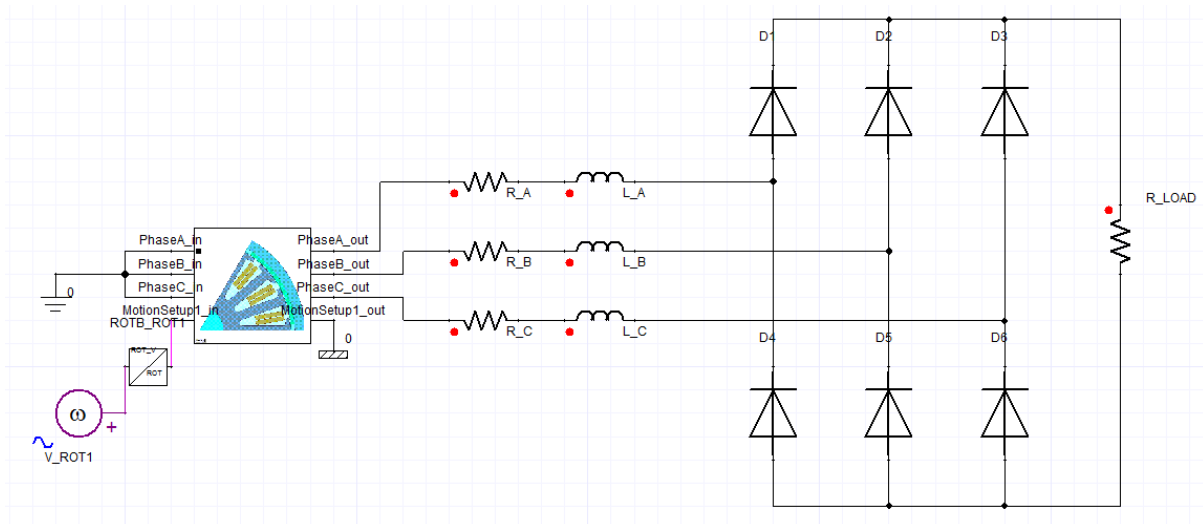


Figure 182: Three-phase bridge rectifier and resistive load

Rectifier Load Test (Battery)

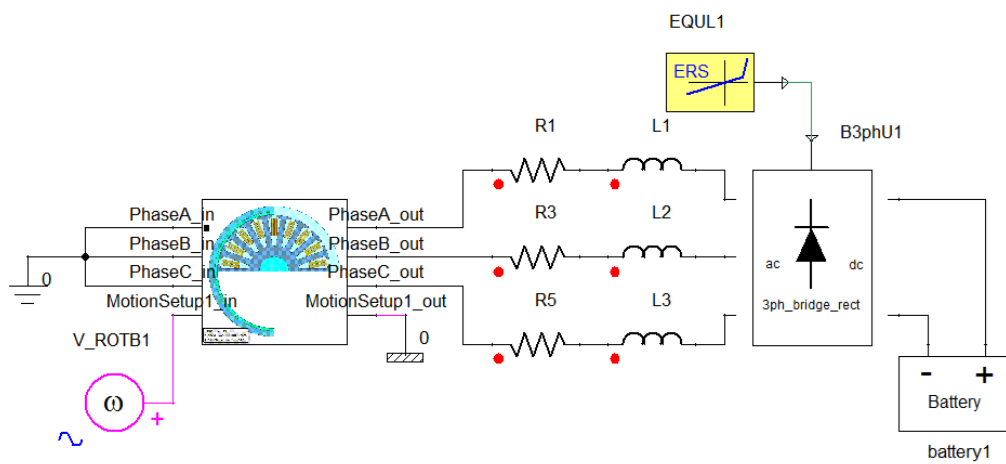


Figure 183: Three-phase bridge rectifier and battery load